# Isospin asymmetry in stable and exotic nuclei

by

Xavier Roca-Maza

TESI
PRESENTADA PER A OPTAR AL GRAU DE
**DOCTOR**

DATA
23 de Març del 2010

Programa de Doctorat
*Física Avançada*
del Departament d'Estructura i Constituents de la Matèria.
Bienni 2005-2007.

Universitat de Barcelona.

Els Doctors Xavier Viñas i Gausí i Mario Centelles i Aixalà, del Departament d'Estructura i Constituents de la Matèria de la Universitat de Barcelona

CERTIFIQUEN:

Que la memòria presentada pel llicenciat Xavier Roca Maza amb títol "Isospin asymmetry in stable and exotic nuclei" ha estat realitzada sota la seva direcció i constitueix la Tesi Doctoral de l'esmentat llicenciat, autoritzant-ne la presentació mitjançant el present escrit.

Barcelona a 15 de Març del 2010.

Dr. Xavier Viñas i Gausí

Dr. Mario Centelles i Aixalà

# Acknowledgments

Opposite to the main topic of this Thesis, no "asymmetries" have been present with respect to the great people with whom I have worked, lived or enjoyed the free time during this four years of PhD. First of all, I would like to thank my PhD advisors Xavier Viñas i Gausí and Mario Centelles i Aixalà. I am deeply grateful to them. With their experience, patience and wisdom they have guided me during the last five years ending with the Thesis I am presenting here. I have also benefited of different collaborations with exceptional researchers. I am indebted and profoundly grateful to Jorge Piekarewicz with whom I have worked in different periods of my PhD. He introduced me into the "neutron-star-world" and into the "Garvey-Kelson relations". I am indebted also to Michal Warda that together with my PhD advisors have enriched me during our collaborations and, surely, most of the works presented in this Thesis had not been possible without them. I have also got profit from a nice collaboration with Francesc Salvat in which we studied elastic electron scattering processes. I would also like to express my gratitude to Peter Ring. Without his invaluable help, the last chapter had never been included in this Thesis. Next, I must thank Peter Schuck with whom I have few but enlightening discussions related to the "Density Functional Theory". I am obliged also to Marcello Baldo who has provided me with a crucial ingredient for the last chapter of this Thesis.

I have shared most of the time during the period of my PhD Thesis with fantastic friends and colleagues inside a very stimulating environment in the Department of "Estructura i Consituents de la Materia" at the University of Barcelona. To all of them: professors, researchers and students, I am also deeply grateful. Especially, I would like to mention Marta Abad, Manuel Barranco, Octavi Boada, David Bote, Alessandro Camboni, Joan Camps, Alesio Celi, Cristian Chumillas, Dani Dagnino, Martí Duocastella, José María Escartín, Noela Fariña, Javier Grande, Muntsa Guilleumas, Alberto Hernando, Estela Jiménez, Bruno Juliá-Diaz, Maria Khoury, David Lopez, Toni Luque, Francesc Malet, Paolo Margaretti, David Mateos, Mariona Moreno, Paolo Moretti, Assumpta Parreño, Martí Pí, Vicent Picó, Artur Polls, Angels Ramos, Arnau Riera, Arnau Ríos, Jordi Salvado and Jaume Tarrús with whom I have shared unforgettable moments.

Finally, I would like to express my deepest gratitude to my family and especially in the last three years also to Benedetta. Without them I had never found my way.

The fantastic front cover of this Thesis have been designed by Alberto Hernando to

whom I am very grateful. This Thesis have been supported by the grant AP2005-4751 of the Spanish Government and by the FAN group of the Department “Estructura i Consitituents de la Materia”.

*A mis padres*

# Contents

# Introduction

The nucleus is a many-body system constituted by a strongly interacting and self-bound ensemble of protons and neutrons also considered as the same particle, namely nucleon, with two possible isospin states (for basical properties of the nucleon see Table 1). Nuclei in which more neutrons than protons exist, *i.e.* nuclei with a certain isospin asymmetry, can be stable nuclei, exotic nuclei, heavy nuclei or nuclei under extreme conditions such as those thought to exist in star interiors and neutron stars. The properties of such systems are related to the isospin dependence of the nuclear interaction and are nowadays a stimulating and active topic of research in nuclear physics and nuclear astrophysics [St05, Bao8]. Generally, isospin dependent properties of nuclei are not completely characterized by existent nuclear models not fully understood by the nuclear community yet. The physical properties of nuclei, such as the mass, neutron and proton distributions, collective excitations, fission properties, matter and momentum flows in heavy ion collisions, etc. are affected in general by the isospin dependence of the nuclear strong interaction. In this sense, the isospin asymmetry contributions should be taken into account for a quantitative description of the experiment. This has stimulated much interest and a lot of activity in this new research direction, namely isospin physics. All in all have motivated the different works presented in this Thesis made of a compilation of four publications, two works accepted for publication and a final chapter including a work planned to be submitted for publication in the near future. In all of these works, the non-negligible effects on different nuclear observables due to the neutron-proton number differences in a nucleus is studied and discussed. Most of the publications presented are focused on the density dependence of the symmetry energy, an important property of the nuclear Equation of State (EoS). Specifically, it is the leading contribution to the energy of an infinite system of protons and neutrons due to its isospin asymmetry. The accurate characterization of this property has been identified as one of the most outstanding questions in Nuclear Physics [Br00, Bao8, Ty01, Hor1, To05, St05, La07, Ba05, Ch05, Che5, Li08, Sh07, Fa06, Pi07].

Since almost the entire last century experiments on stable nuclei have provided a wealth of nuclear data on ground and excited state properties of nuclei leading the Nuclear community to huge advances in the description and understanding of the nucleus. However, only recently, it has been possible to develop new experimental techniques to synthesize and perform measurements of nuclear properties on radioactive nuclei. This new techniques have been or will be soon implemented in facilities such as HIRFL@CSR [Xi02,

| Particle | $m$ (MeV/$c^2$) | $q$ ($e$) | $S$ | $I$ | $I_3$ |
|---|---|---|---|---|---|
| proton | 938.2723($\pm$3) | 1 | $\frac{1}{2}$ | $\frac{1}{2}$ | $+\frac{1}{2}$ |
| neutron | 939.5656($\pm$3) | 0 | $\frac{1}{2}$ | $\frac{1}{2}$ | $-\frac{1}{2}$ |

Table 1: Properties of the proton and the neutron: mass, net electric charge, spin, isospin and third component of isospin. The isospin formalism assumes the same mass for protons and neutrons ($m_n/m_p \approx 1.001$) and, then, they are considered as the same particle in different isospin states with different electric charge.

Xi05], (China) Spiral2@GANIL [Sa01] (France), FAIR@GSI [FAIR, Si04] (Germany), FRIB@MSU [FRIB] (USA) orRIBF@RIEKEN [Su01] (Japan) where the study of nuclei far from the stability valley starts to become feasible. Those nuclei, not present naturally on Earth, are commonly called exotic nuclei. They usually are short-lived, more dilute —as the outermost nucleons are less bound— and present larger isospin asymmetries than Earth-nuclei. Nowadays, the experimental situation has already revealed phenomena such as the displacement or disappearance of magic numbers, skin and halo structures in proton- and neutron-rich nuclei, etc. Experimental studies on neutron-rich nuclei will allow to determine the astrophysical conditions for the formation of neutron-rich stable isotopes as though to exist in the crust of neutron stars. This promising situation will provide useful information to better understand the physics of exotic nuclei. Furthermore, observational data from astrophysical objects and processes, such as the above mentioned neutron stars, proto-neutron stars, astrophysical nucleosynthesis, cooling processes, supernova dynamics, etc., could be crucial in constraining the nuclear EoS in density ranges and isospin asymmetries unreachable in Earth-Laboratories. As most of exotic nuclei planned to be studied experimentally present non-negligible isospin asymmetries, the symmetry energy and its density dependence will have an important role on describing the EoS related to the bulk properties of all these systems. All those ingredients: experimental, observational and theoretical are schematically related in Figure 1. Some of the connections shown in this scheme are discussed along the publications presented in this Thesis.

From a historical point of view, to tackle the (modern) description of the nucleus established in 1932 after the discovery of the neutron by James Chadwick [Ch32], different nuclear models of very different nature have been proposed to describe the ground and excited state properties of nuclei [We35, Be37, Ha49, Ma49, My69, Va72, My74, My77, De80, Mo95, Du95, Fu97, La97, Ty99, Ni02, Go03, Sa03, To05, La05, Ba08]. The most successful approaches in describing the experimental results are, up to date, phenomenological. The models based on such approach are usually built trying to keep the important symmetries of the problem but, as the descriptions are not derived from first principles, their parameters: the coupling constants, masses, etc. are free and, therefore, a fit to measured data should be performed in order to check the suitability of the model. On the

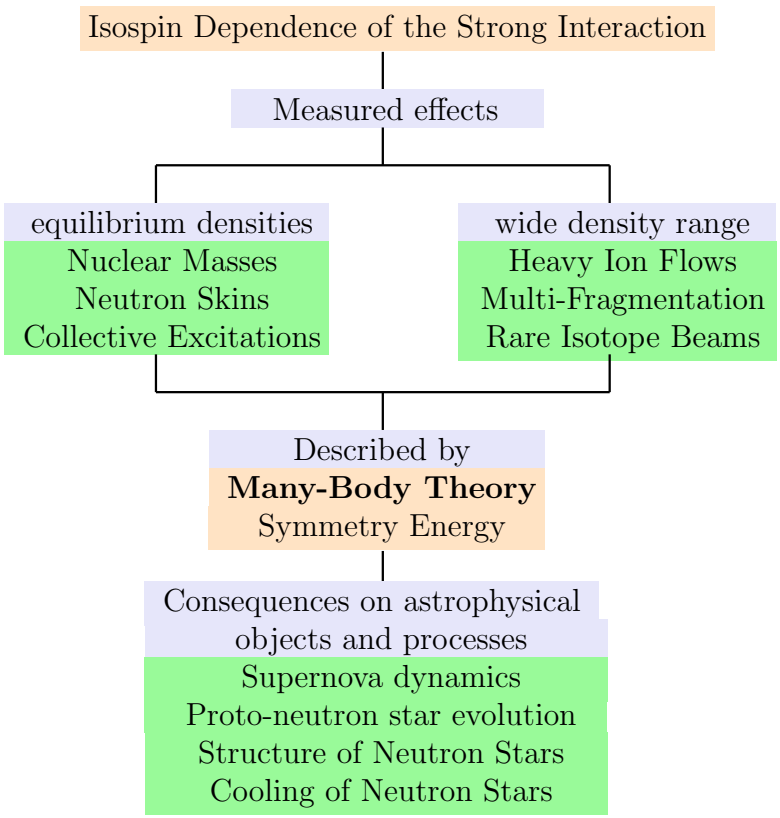


Figure 1: Schematic tree relating several observables and physical processes where the isospin dependence of the strong interaction has shown important implications.

other hand, calculations from first principles exist but they are still not able to achieve the accuracy required to properly describe the experiment. This more fundamental approach consists of deriving in-medium interactions microscopically using realistic nucleon-nucleon potentials that reproduce measured scattering processes. Although these calculations reproduce properties of the EoS reasonably well, full-scale calculations for finite nuclei are not feasible yet. A great effort in this direction have been done in the past and continues in the present since those *ab initio* calculations allow the most direct connection —to our knowledge— to the underlying paradigm: Quantum Chromodynamics.

Regarding the most successful phenomenological approaches, there are two main trends. The *microscopic-macroscopic* approach pioneered by Myers and Świątecki [My69, My74, My77, Mo95] which consists of various refinements to the *Liquid Drop Model* (LDM) of Bethe and Weizsäcker formulated in 1935-1937 [We35, Be37]. The versatility of the LDM arises from the fact that the baryon density and the binding energy per nucleon are, approximately, the same for all nuclei. Then, assuming that the protons and neutrons are exacltly the same particle (nucleon) and that the nuclear strong interaction between them is also the same (*i.e.* the total force only differ due to the electromagnetic interaction), enables a comparison of the nucleus with a liquid drop which also has a constant density independent of the number of molecules. The energy to remove a nucleon, in analogy to

the case of molecules in a drop, is proportional to the number of nucleons in the nucleus. Using this analogy, Weizsäcker developed the so-called *semi-empirical mass formula* able to describe properly the average trends of measured nuclear masses. Despite its simplicity, the semi-empirical mass formula accounts for the essential physics of the gross contribution to the nuclear binding energy. Namely the macroscopic contribution. The formula attempts to describe the mass of a nucleus in terms of the proton and neutron numbers.

As a first qualitative approach to the nucleus and because along different publications presented here we have employed this model and the Droplet Model (DM) [My69, My74] which is based on the same grounds, is interesting now to shortly discuss the most important features paying special attention on the asymmetry energy term which accounts for systems with different neutron-proton numbers. The formula, reads as follows,

$$M(N,Z) \equiv m_{\mathrm{H}} Z + m_n N - B(N,Z) \tag{1}$$

where $m_{\mathrm{H}} = m_p + me - B_e$ is the Hydrogen mass and $B(N,Z)$ is the binding energy of the system with $Z$ protons and $N$ neutrons which in its most elementary version can be written as,

$$B(N,Z) \equiv a_{\mathrm{v}} A - a_{\mathrm{s}} A^{2/3} - a_{\mathrm{c}} \frac{Z^2}{A^{1/3}} - a_{\mathrm{a}} \frac{(N-Z)^2}{A} \tag{2}$$

where $A = N + Z$ is the total number of nucleons in a nucleus of $Z$ protons and $N$ neutrons and $a_i$ for $i =$ v, s, c and a are the volume, surface, Coulomb and asymmetry coefficients respectively. All of them should be fitted to experimental nuclear masses.

Considering the neutron-neutron, proton-proton and neutron-proton strong interaction as equal, one can justify the volume and surface terms of Equation 2 recalling the liquid drop analogy. Assuming that all nucleons are homogeneously distributed and surrounded by the same number of nucleons and that the radius of a nucleus scales with $A^{1/3}$, the volume term should be roughly proportional to $A$. This is true as far as one is not in the surface of the nucleus. For that reason, the surface term —proportional to $A^{2/3}$— is a correction of the over-binding produced by the volume term. Furthermore, it is needed to account for the difference between protons and neutrons arising from the electromagnetic interaction. Protons carry net electric charge and neutrons do not. It is the role of the Coulomb energy term. This term should be proportional to $\frac{Q^2}{R}$ (Coulomb energy of a uniform charged sphere apart from a coefficient) that can be re-written as $\frac{Z^2}{A^{1/3}}$.

Finally, we have assumed that all nucleons contribute equal to the volume energy term and this, apart from the surface effects, neglects the Pauli Exclusion Principle. The Pauli Exclusion Principle states that two equal fermions (same particles with the same quantum numbers) cannot occupy the same energy level. As clearly shows Figure 2 for different $N$ and $Z$ numbers, higher energy levels for one type of particle should be fulfilled while leaving lower energy levels vacant for the other type according to the Pauli Exclusion Principle. Therefore, the unique situation where all nucleons contribute with the same energy is the symmetric case ($N = Z$). This term, namely asymmetry energy term,

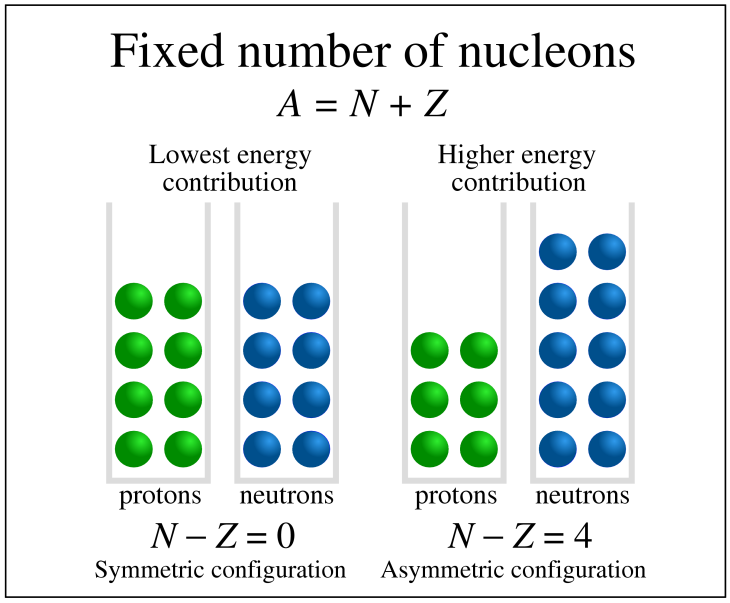


Figure 2: Schematic picture of the energy levels as should be filled due to the Pauli Exclusion Principle for a fixed mass number $A$ in two cases: symmetric configuration $N - Z = 0$ (left-hand-side) and an asymmetric configuration $N - Z = 4$ (right-hand-side).

contributes when a neutron-proton number difference is present in a nucleus. Within this approach, the asymmetry term will contribute equally to a system with the same excess of protons or neutrons. So a term proportional to $(N-Z)^2$ seems the more natural way to formulate it. Then, as it is a correction to the volume term one has to divide by $A$ to keep the scale of this term as the volume one, *i.e.* $\frac{(N-Z)^2}{A} = A\left(1 - 2\frac{Z}{A}\right)^2$ where $0 < \frac{Z}{A} < 1/2$. Summarizing, all the terms assume that the nuclear force is isospin independent but the asymmetry coefficient naturally entangle effects coming form a more real interpretation of the nucleus, *i.e.* coming form its isospin dependence. The asymmetry energy, as the Coulomb energy, is against bounding the nucleus. Specifically, while the Coulomb energy pushes the system to a neutron-rich configuration, the asymmetry term does it to a symmetric one. Deducing from the last statement that the more stable number of protons and neutrons to form a nucleus will correspond to an intermediate situation depending on the competition between the Coulomb and asymmetry terms. Note that the volume and surface terms do not disable this reasoning since their contribution is homogeneous for all nucleons. The most stable nuclei is known to be $^{56}$Fe and with this simple nuclear model one is able to reproduce this experimental observation.

After the formulation of the LDM, tests comparing its predictions to experimental data were done realizing systematic deviations for some neutron and proton numbers (see middle pannel of Figure 3 for an illustrative example). These effects were early taken as an evidence of the existence of shell structure in nuclei: the magic numbers

were discovered. In 1949, Haxel *et al.* [Ha49] and Mayer [Ma49] achieve a great success reproducing such magicity after including the spin-orbit contribution to the nuclear shell model —see left panel of Figure 4, later on we will explain other features of the spin-orbit interaction. The shell or independent particle model is based on the idea that all nucleons in a nucleus create a common average field in which all of them move independently from each other. Under this approximation, the nuclear many-body problem is feasible since the single-particle equations of motion become decoupled and the problem reduces to solve each equation separately using a unique mean field potential. The summation of the energy levels based on the shell model were not able to provide a quantitative picture of the nuclear masses yet. It was on 1966-68 when Strutinsky introduced a successful methodology in many nuclear applications which consists of subtracting the smooth part of the total energy predicted by the shell model ($E_{\rm sm} = E_{\rm smooth} + E_{\rm shell}$) and uses instead the phenomenological LDM results ($E_{\rm Strutinsky} = E_{\rm LDM} + E_{\rm shell}$; see Figure 3). Hence, both ingredients combined constitute the so-called microscopic-macroscopic approach [Lu03]. In all formulations, different approximations under the same basis are considered leading to models containing several free parameters fitted to measured ground state properties. Results are the most accurate in nuclear masses and radii known to date. For this reason, its predictions on the saturation properties of the nuclear EoS have been commonly used as a guideline for other models when experimental data is not available.

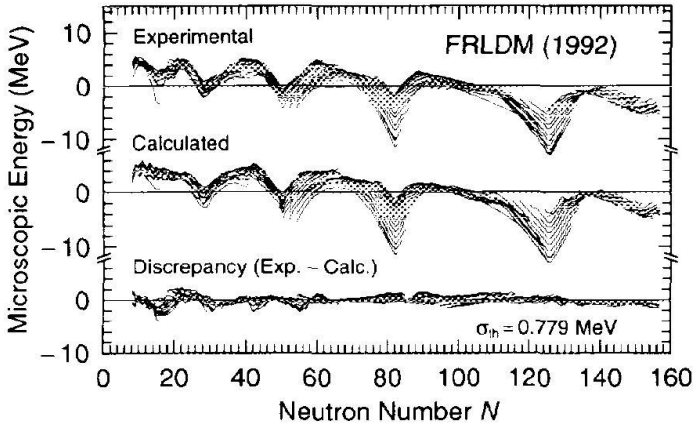


Figure 3: Comparison of experimental masses once subtracted the (average) macroscopic contribution calculated through a spherical Finite Range Liquid Drop Model (upper panel) with the calculated microscopic energies (middle panel) for 1654 nuclei. In the bottom panel is shown the difference between these two quantities —*i.e.* the difference between the macroscopic-microscopic calculations of Reference [Mo95] and the measured ground-state masses—. [This figure was published in Reference [Mo95]]

The other successful methodology in describing the nucleus which also have been studied along most of the works presented here corresponds to the self-consistent *mean-*

*field* approach. The central concept behind them is an *effective interaction* or *energy density functional*. The Density Functional Theory (DFT) is a powerful and general approach used successfully in other fields in Physics as condensed matter. It is possible to describe, for example, with an exquisite accuracy many-electron systems. The reason relies in the possibility of derive such functionals from *ab initio* calculations from electron gas theories. As it have been already pointed out, this kind of calculations are not feasible yet for many-nucleon systems. Instead, one can derive such functionals from a phenomenological approach as it is done within the self-consistent mean field one. Mean-field theory is, as mentioned, a phenomenological description of the nuclear many-body problem in which, as in the case of the independent particle model, the nucleons are assumed to be point-like and moving independently in a mean field potential created by all of them. Relativistic and non-relativistic versions of such models exist providing, in general, an accurate description of measured ground state properties of finite nuclei and of the EoS of symmetric nuclear matter at saturation —mean-field models are usually fitted to these data— but differ on their predictions of isospin sensitive properties, i.e. in the description of the isovector sector of the interaction. While in the non-relativistic case, a phenomenological ansatz concerning the density dependence of the different terms in the energy functional is adopted and variational calculations of the Hartree-Fock type are performed —Skyrme [Va72] or Gogny [De80] forces are examples used to derive such functionals. The relativistic one, starts from a covariant Lagrangian with mesonic and nucleonic degrees of freedom and, as the approach is relativistically invariant, it preserves causality and provides a self-consistent description of the spin-orbit term of the nuclear interaction [Ri96]. The spin-orbit term, included "*ad hoc*" in non-relativistic models, is crucial for the description of the shell-structure of the nucleus (see left panel of Figure 4 for a textbook example). On the contrary, this term and the finite range effects of the nuclear interaction appears naturally from relativistic formulations. To illustrate the influence of the isospin asymmetry contribution on this important ingredient of the nuclear force, one can recall the famous shifts in the charge radii of the Pb isotopic chain. The experimental values show a kink at $N = 126$ which have its origin in the isospin dependence of the spin-orbit term. This is accounted properly by RMF models as can be seen in Figure 4 (right panel). Finally, for comparison with the microscopic-macroscopic approach, Mean Field models have the advantage of avoiding huge number of free parameters, around ten is the usual situation and, thus, have a higher predictive power.

Implicit to the nature of phenomenological approaches, the agreement between different parametrizations is generally restricted to the area where the experiment can provide precise constraints. This situation should hold generally in such models leading to disagreements in extrapolations. Moreover, it is known that stable nuclei are constituted by similar number of neutrons and protons and, therefore have small isospin asymmetries, as it is illustrated in Figure 5. This makes the asymmetric nuclear EoS a magnitude poorly constrained by experimental measurements as compared with the symmetric one. An illustrative example of the latter statement is the incompressibility of symmetric nuclear

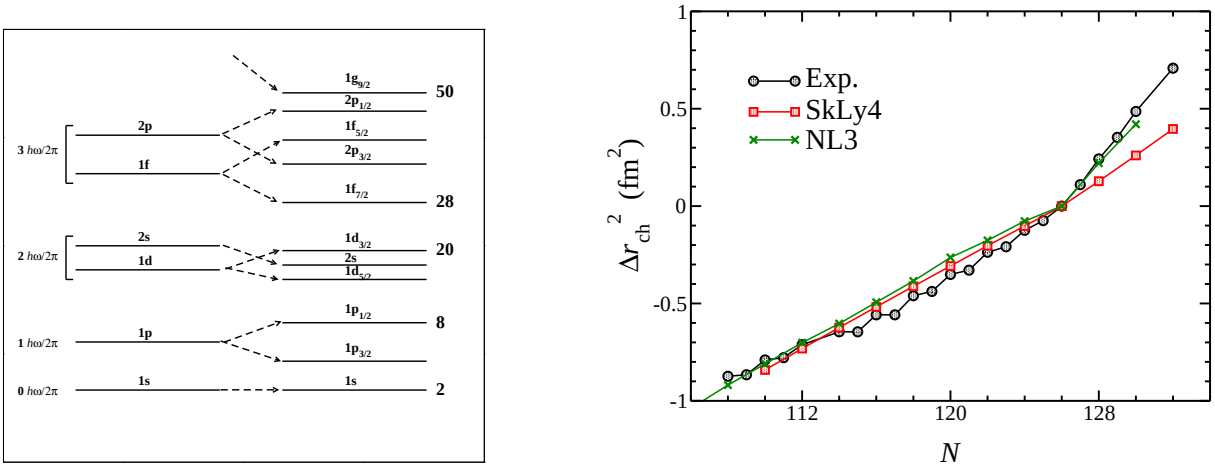


Figure 4: Left panel: schematic nuclear levels of the shell model including the spin-orbit splittings (right hand side). Properly accounting for the spin-orbit interaction allows one to predict the enhancement of the energy-gaps for magic numbers —*i.e.* $n = 2, 8, 20, 28, 50$— observed experimentally. Right panel: Charge radii along the Pb isotopic chain referred to $^{208}$Pb. It is defined as $\Delta r^2_{\rm ch} \equiv r^2_{\rm ch}(N) - r^2_{\rm ch}(126)$ in terms of the neutron number $N$. The measured radii show a kink in $N = 126$ which is reproduced by the relativistic model NL3 [La97] but not for the non-relativistic one SLy4 [Ch98].

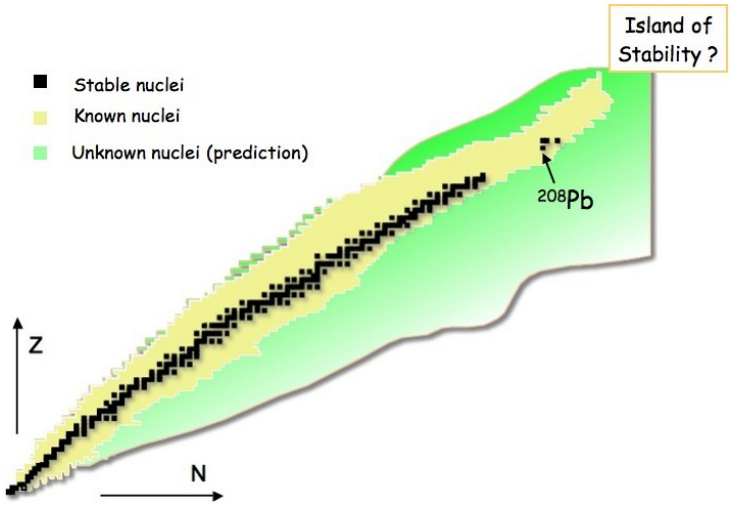


Figure 5: Nuclear chart. In black, roughly following the $N = Z$ line, one finds the stable nuclei. In yellow, are shown unstable measured nuclei. And, in green is depicted the area where unstable nuclei can be theoretically formed [figure from: www.csnsm.in2p3.fr/IMG/jpg/chart.jpg].

matter at its saturation density ($\rho_0$) which has been determined to be $K_0 = 231 \pm 5$ MeV from the nuclear Giant Monopole Resonance [Yo77] —a nuclear collective excitation. But as was already pointed out [Da02, Pi04, Co04], the remaining uncertainties in the deter-

mination of this property are closely related to those of the density dependence of the symmetry energy. In one of the works presented here we will study this nuclear resonance along isotopic chains.

Theoretical studies of the EoS of isospin asymmetric nuclear matter were pioneered by Brueckner *et al.* [Br67] in 1967. Since then, there have been many studies on this subject based on different many-body theories. However, because of our lack of knowledge of the in-medium isospin dependence of the nuclear interaction and the difficulties in solving the many-body problem from *ab initio* calculations, predictions of different models differ widely at supra-saturation densities. A common way to theoretically disentangle the effects of the isospin asymmetry in the nuclear EoS is to perform a Taylor expansion of the energy per particle of the infinite system considering small neutron-proton number differences,

$$e(\rho,\delta) = e(\rho,0) + c_{\rm sym}(\rho)\delta^2 + \mathcal{O}\left[\delta^4\right] \tag{3}$$

where $\rho = \rho_{\rm neutrons} + \rho_{\rm protons}$ is the baryon density, $\delta \equiv (\rho_{\rm neutrons} - \rho_{\rm protons})/\rho$ defines the asymmetry of the system and $c_{\rm sym}(\rho)$ is the symmetry energy. The symmetry energy of an infinite nuclear system of protons and neutrons can be understood as the penalty-energy to the binding for replacing a neutron (proton) by a proton (neutron) in the symmetric configuration ($N = Z$). In the astrophysical context, the symmetry energy drives the difference between the neutron and proton chemical potentials, $\mu_n - \mu_p \approx 4c_{\rm sym}(\rho)\delta$, a quantity which has an important impact on supernova dynamics, proto-neutron star evolution (early stage of evolution of a neutron star), cooling and structure of neutron stars. The magnitude and density dependence of the symmetry energy $c_{\rm sym}(\rho)$ is, as have already been stated, correlated to the neutron-proton difference and, for that, its properties remain partially elusive as it can be seen from Figure 6. In these two plots, it is shown a wide collection of different predictions for the density dependence of the symmetry energy of different and successful nuclear models based on very different theoretical grounds [Fu06]. Within them, there are *ab initio* calculations as DBHF, mean-field predictions as SkM* (non-relativistic) or NL3 (relativistic) and effective interactions based on Chiral Perturbation Theory as ChPT. This representative set of nuclear models show a rather spread behavior for the whole range of represented densities. Especially for densities well below or above $\rho/\rho_0 = 1$.

The publications included in this Thesis have been focused on theoretical aspects of the isospin dependence of the nuclear interaction that are still under debate. The connecting thread along works presented in the three first chapters is the symmetry energy and its density dependence. As mentioned, the accurate characterization of this property entails profound consequences in studying the neutron distribution in stable and exotic nuclei and neutron-rich matter having also an important impact on heavy ion reactions, nuclear astrophysics, and on diverse areas such as tests of the Standard Model via atomic parity violation [Si05]. Hence, connections of the density dependence of the symmetry energy with isospin-sensitive nuclear observables are studied throughout this former works. In

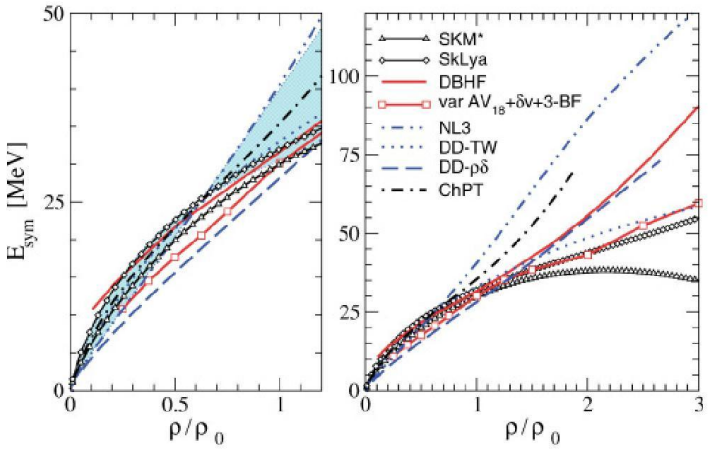


Figure 6: Symmetry energy coefficient as a function of density divided by the saturation density ($\rho_0 = \rho_0$) as predicted by different models including *ab initio* and mean field calculations. The left panel shows the low-density region, while the right panel displays the high-density range [figure from [Fu06]].

the first chapter, three publications are presented. Two of them indicating important constrains on the density dependence of the symmetry energy with the *neutron skin thickness* of nuclei and a third one analyzing the bulk and surface contributions of the proton and neutron distributions in nuclei to the same observable. The neutron skin thickness is commonly defined as the neutron-proton root mean square radius difference in a nucleus,

$$\Delta R_{np} \equiv \langle {r_n}^2 \rangle^{1/2} - \langle {r_p}^2 \rangle^{1/2} \tag{4}$$

This observable is very sensitive to the pressure difference between protons and neutrons in a nucleus. Large values of the pressure difference will favor the formation of a skin-type structure in the nucleus since neutrons will show a strongest resistance to be close from protons than if the pressure difference is small. Furthermore, knowing that the density dependence of the symmetry energy has direct implications on the pressure ($P$),

$$\begin{aligned} P(\rho) &= \rho^2 \frac{\partial e(\rho,\delta)}{\partial \rho} \\ &\approx \rho^2 \frac{\partial}{\partial \rho}\left(e(\rho,0) + c_{\rm sym}(\rho)\delta^2\right) \\ &\approx \rho^2 \frac{\partial e(\rho,0)}{\partial \rho} + \rho^2\delta^2 \frac{\partial c_{\rm sym}(\rho)}{\partial \rho} \end{aligned} \tag{5}$$

where have been introduced Equation 3, one can realize that a certain relation should hold between the neutron skin thickness of nuclei and the density derivative of the symmetry energy. This connection was already noticed by A. Brown [Br00]. Therefore, an accurate calibration of this observable would constrain the isospin dependence of nuclear models. Measurements of observables related with neutron properties, as it is the case

of the neutron skin, use to be based on indirect derivations from the experimental result. Consequently, to disentangle the relevant quantity from such measurements may be a difficult task and the result uses to be model dependent. That is one of the general reasons why properties related with neutrons are poorly constrained by the experiment as compared with other observables, as for example, the nuclear charge radius which is basically determined by the proton distribution through purely electromagnetic probes as it is the case of elastic electron scattering experiments [Ho56]. However, there are some direct measurements sensitive to the neutron distributions using electroweak probes as it is the case of atomic parity violation experiments in elastic electron scattering processes [Ho01, Mi02]. Furthermore, observables showing important effects due to neutrons are usually far from the stability valley and have, for that reason, large asymmetries and short half-lives —another source of difficulties for experimentalists. Measurements on short-lived nuclei will be possible in the near future, as stated, with the help of the Rare Ion Beam facilities [RBFa]. In 2001, although with the usual uncertainties of observables dependent on the neutron distribution, were measured the largest collection of neutron skins within the same experimental set up using antiprotonic atom techniques. From Calcium to Uranium measuring a total of 26 neutron skins [Tr01]. In this respect, we were interested on how far these uniformly measured neutron skins could help in constraining the density dependence of the symmetry energy and its compatibility with determinations based on other physical observables. For these reasons, we took the experimental results of [Tr01] as a baseline for our studies along works presented in chapter one.

In the following chapter, a publication devoted to understand the impact of the symmetry energy on the structure of the outer crust of a neutron star is presented. A neutron star is one of the densest objects in the Universe. In its outer layers, or which is equivalent at sub-nuclear densities, the abundance of neutrons is dominant in front of the one of protons, electrons and muons. Deeper inside the star, when the interface between the outer layers (namely inner and outer crust) and the inner ones (namely inner and outer core) occurs, one is well above the nuclear saturation density and exotic states of matter may appear (see Figure 7). Strange baryons, condensed mesons or even deconfined quarks are possible candidates to be present. Regarding the outer crust, it comprises a region spanning about seven orders of magnitude in density: from about $10^4$ g/cm$^3$ to a neutron drip density of about $4 \times 10^{11}$ g/cm$^3$ [Ba71]. These densities are far from the saturation density of nuclear matter $\rho_0 \approx 2.5 \times 10^{14}$ g/cm$^3$ but are larger enough to ionize the electrons —present to ensure the charge neutrality in the star— from nuclei. Although we calculated the composition of the crust using among some of the more sophisiticated nuclear mass tables available in the literature, we also introduced a "Toy Model" based on the LDM [We35, Be37] to illustrate in a simple way the essential physics of the outer crust, *i.e.* the competition of the electron density —which drives the system toward more neutron-rich nuclei via $\beta$-equilibrium— against the symmetry energy that opposes such a change. This competition arise from the same origin as the one mentioned between the Coulomb and asymmetry terms of the semi-empirical mass formula. The neutron-rich

nuclei present in the outer crust are on average more dilute than their more symmetric counterparts because of the development of a neutron skin. As a result, these nuclei become sensitive to the symmetry energy below nuclear matter saturation density and affect the composition of the crust. In particular, the realistic mass tables showed that models with a smaller derivative of the symmetry energy respect to the baryon density at nuclear sub-saturation predicts nuclei more neutron rich than models with a bigger derivative. From the observational point of view, this study was also motivated by recent observations of multiple oscillations exhibited after giant flares in neutron stars. This oscillations depend on the nuclear EoS and are expected for some specific shear waves of the crust. Further observations and modelizations would provide a powerful probe for its structure [Du98, Pi05].

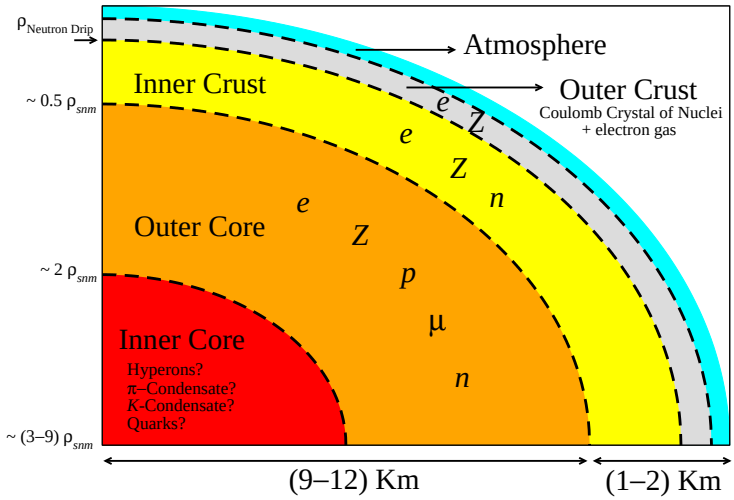


Figure 7: Rendition of a neutron star structure and composition. Standing for $e$ or $\mu$ a degenerate free fermi gas of electrons or muons respectively, for $Z$ a nuclei with this proton number arranged in a Coulomb lattice and for $n$ or $p$ a free system of neutrons or protons respectively. Finally, the constitutive particles inside the region named inner core can not be constrained neither for nuclear theory nor for observational data yet.

In the third chapter, is analyzed the influence of the symmetry energy on the *Giant Monopole Resonance* (GMR) in stable, neutron-rich and along Zr and Pb isotopic chains, from the proton to neutron theoretical drip lines. A GMR is a collective excitation of atomic nuclei which can be understood as an excitation in terms of a radial oscillation of all protons and neutrons expanding and contracting. The frequency of this collective excitation is one of the most direct ways to access to the compressibility modulus of the symmetric EoS provided that GMR have been measured on nuclei with moderate isospin asymmetries ($(N-Z)/A < 0.25$). It is defined as,

$$K_0 \equiv 9\rho_0^2 \left( \frac{\partial^2 e(\rho, \delta = 0)}{\partial \rho^2} \right)_{\rho=\rho_0} \tag{6}$$

By studying the GMR along isotopic chains we were investigating how the density dependence of the symmetry energy affects this frequency in more asymmetric systems. In terms of the compressibility modulus of asymmetric nuclear matter —characterized by the asymmetry parameter $\delta = (N - Z)/A$— at its saturation point, $\rho_\delta$, the approximate relation could be written as follows,

$$\begin{aligned} K_\delta &\equiv 9\rho_\delta^2 \left( \frac{\partial^2 e(\rho,\delta)}{\partial \rho^2} \right)_{\rho=\rho_\delta} \\ &\approx 9\rho_\delta^2 \left( \frac{\partial^2 e(\rho,\delta=0)}{\partial \rho^2} + \frac{\partial^2 c_{\rm sym}(\rho)}{\partial \rho^2}\delta^2 \right)_{\rho=\rho_\delta} \end{aligned} \tag{7}$$

The study pointed that for large isospin asymmetries —present in nuclei which have not been measured its mass yet— the excitation energy could differ considerably between models depending on the stiffness of its symmetry energy. In this respect, we should stress that other collective modes as the Giant Dipole Resonance (GDR) or the Pygmy Dipole Resonance (PDR) have recently allowed to obtain valuable constraints on the density dependence of the symmetry energy [Tr08, Kl07] and that further measurements of this nuclear collective excitations along isotopic chains are expected to constrain more tightly the density dependence of the symmetry energy.

In chapter four a theoretical study on *elastic electron scattering* off stable and exotic nuclei is laid. We focus our analysis of exotic nuclei to the study of Ca and Sn isotopic chains, from the proton to the neutron drip lines, *i.e.* from small to large isospin asymmetries. Elastic scattering processes using electron beams and stable nuclei as a target have been for many years a very useful tool to investigate the size and shape of stable nuclei. Electrons interact with nuclei basically through the electromagnetic force providing accurate information about the charge distribution of atomic nuclei. Therefore, as the electric charge distribution is constrained basically by the proton distribution and this, depends indirectly, on the neutron distribution —through the strong interaction—, it is straight forward to understand that different isospin asymmetries could, and in fact will, affect the measured differential cross section of the scattering process. Motivated by future studies of electron scattering off exotic nuclei intended in new facilities such as ELISe [Si07] and SCRIT [Su05, Wa08], we provided theoretical predictions along isotopic chains allowing us to identify correlations of potential interest.

Finally, in chapter five we present a novel relativistic mean-field (RMF) interaction with explicit density dependence of the meson-nucleon vertices. The adjusted relativistic mean field model is based on the Density Dependent Relativistic Hadron Field Theory which enables an effective description of the nuclear many-body problem as an energy density functional. A RMF model, as have been already explained, starts from a Lagrangian with mesonic and nucleonic degrees of freedom. After that, one derives the mean-field equations and solve them self-consistently. The standard version of a RMF model, contains three mesons carrying the nuclear interaction between protons and neutrons, namely the $\sigma$, $\omega$ and $\rho$ mesons. These models are usually fitted to some selected

finite nuclei properties as masses and charge radii and to some properties of the nuclear EoS at saturation. In chapter five, we present a functional which, in addition, include an extra degree of freedom suggested by fully microscopical calculations of asymmetric nuclear matter: the $\delta$ meson [Hu96, Hu98]. The extension included in this new interaction allows a theoretical improvement with respect to standard RMF models in the description of the isospin dependent part of the nuclear strong interaction. Furthermore, we propose to fix the density dependence of the $\delta$-nucleon vertex to the effective mass splitting as predicted by Dirac-Brueckner calculations of pure neutron matter [Da07]. And, to include in our fitting procedure one of the microscopical calculations of the nuclear EoS believed to be among the most accurate in the literature [Ba04] in density ranges between zero and two times the nuclear saturation density.

The different studies presented in this Thesis have been organized in five chapters. The first one contains two published works in *Physical Review Letters* and *Physical Review C* and one accepted for publication in *Physical Review C*. The sencond and fourth chapters are devoted to different works that have been already published in *Physical Review C*. The third one contains a work accepted for publication in *Journal of Physics G* and the fifth one is devoted to a work which is still on progress. A brief introduction specific to each chapter is included. Although works presented in chapters four and five are more general and does not study exclusively the effects of the isospin asymmetry on different nuclear observables and on properties of the nuclear EoS, all works are devoted to investigate some aspect of the isospin dependence of the nuclear strong interaction.

# 1 Symmetry energy and the neutron skin of a nucleus

## 1.1 Introduction

The neutron skin thickness of nuclei is generally defined as the neutron-proton root mean square radius difference (see Equation 4). It is, thus, an isospin sensitive observable as it has been discussed in the general introduction. Isospin dependent properties of nuclei are usually difficult to measure or to derive model-independently from the experiment. However, it is well stablished that the neutron skin of a heavy nucleus accommodates a linear correlation with the density derivative of the neutron EoS at $\rho_n = 0.10$ fm$^{-3}$ universally in mean-field models [Br00]. This type of correlation with the neutron skin thickness also holds in the case of the density derivative of the symmetry energy at saturation ($L$) [Fu04]. In Figure 8, this correlation is displayed for the case of $^{208}$Pb. This important property of mean-field models, which on the other hand have widely

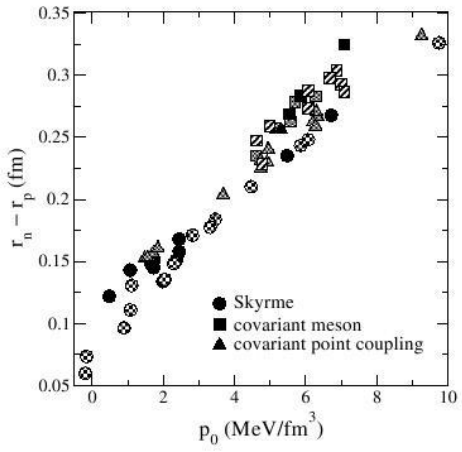


Figure 8: Neutron skin thickness in $^{208}$Pb for different mean-field models as a function of the density derivative of the symmetry energy at saturation. Where $p_0 = L\rho_0/3$. Figure taken from Reference [Fu04].

demonstrated its accuracy on describing the nucleus, will be exploited in the high precision experiment of the neutron skin of $^{208}$Pb planned at the Jefferson Laboratory in the present

year [Mi02]. The accurate characterization of the density dependence of the symmetry energy entails important consequences in the study of the neutron distribution in stable and exotic nuclei. Therefore, the study of the symmetry energy and its density dependence is a timely and challenging problem.

In the first publication presented in this Thesis, "Nuclear Symmetry Energy Probed by Neutron Skin Thickness of Nuclei", we show that the bulk symmetry energy $c_{\rm sym}(\rho)$ at a given density $\rho_A$ equals in very good approximation the symmetry energy of a heavy nucleus ($a_4(A)$) universally in mean-field models. This relation is very important since it allows to connect isospin dependent properties of finite nuclei and nuclear matter. We, then, take advantage of this relation and study possible constraints on $c_{\rm sym}(\rho)$ arising from neutron skin measurements. Awaiting for high precision measurements of the neutron distribution in nuclei, we use instead the largest and uniformely measured data set available in the literature on neutron skins [Tr01] employing antiprotonic atom techniques. The main point of using this data is to know how far uniformly measured data on neutron skins over the periodic table may help in constraining the density dependence of the bulk symmetry energy. We base our study on the grounds of the Droplet Model (DM) [My74, My77] in order to work with analytical expressions. This study turned out to be very helpful to elucidate correlations between this isospin dependent observable and different parameters of the nuclear EoS (see Figures 1 and 3 of that publication). Interestingly, we learn that in spite of the relatively large error bars in this data, the size of the final uncertainties in the different properties of the symmetry energy are comparable to other analysis. This highlights the value of having skin data consistently measured across the mass table while high precision measurements are not available yet.

In a second publication under the title: "Neutron skin thickness in the droplet model with surface width dependence: Indications of softness of the nuclear symmetry energy", we analyze the bulk and surface contributions to the neutron skin thickness in finite nuclei with the DM approach and a representative set of nuclear effective interactions. In the grounds of the DM, the neutron skin thickness of nuclei is driven by the ratio of the bulk symmetry energy at saturation $J$ and the surface stiffness coefficient $Q$. The former can be understood as the penalty energy to the system to convert all protons into neutrons in symmetric nuclear matter and the latter accounts for the resistance of the system against the separation of neutrons from protons to form a neutron skin. Plotting the $J/Q$ value as predicted by the different effective interactions employed in this work against the neutron skin thickness of $^{208}$Pb, one notes a linear correlation between such quantities and, as a consequence, between the $L$ and $J/Q$. Next, motivated by the fact that the analysis of the experiments in antiprotonic atoms [Tr01] assumed a halo-type structure for the derivation of the neutron skin thickness and that was also showed in [Sw05] that the skin-type structure can reproduce with similar quality the same experiment (see 9 for a schematic example), we study the bulk and surface contributions to the neutron skin thickness on the above mentioned nuclei with the same set of mean-field interactions used to state the linear correlation between $L$ and $J/Q$. Our conclusion is that both, surface

and bulk contributions are needed for a proper description of the neutron skin thickness as predicted by these models and that the leading term in the surface contribution is also driven by the $J/Q$ value. Hence, we suggest a DM-based formula for the neutron skin thickness consistent with our results and fit with it the data of antiprotonic atoms to determine the value of $J/Q$ derived from such experiment. Furthermore, taking advantage of the linear correlation between $L$ and $J/Q$, we also estimate the value of $L$ suggested by the same experiment. The results obtained with this new constraint on the density dependence of the symmetry energy —in harmony with our previous work— favored a relatively soft symmetry energy (small value of $L$) as compared with other experimental indications (see Figure 6 of our publication). Finally, we took the derivations for the $L$ parameter estimated with other observables and methods and calculate the mean and standard deviation provided that all values where extracted independently. The result, indicates a relatively narrow window for the possible values of $L$ ranging form 45 MeV to 75 MeV.

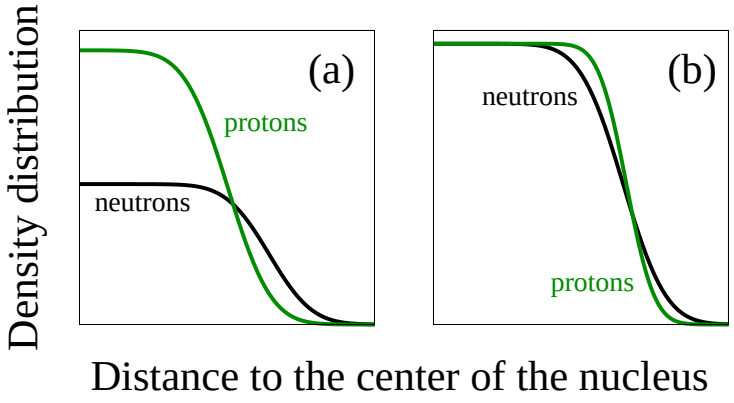


Figure 9: Schematic picture of Skin (a) and halo (b) structures due to differences in the proton-neutron distributions

In the third section of this Chapter, we present a work devoted to the "Analysis of bulk and surface contributions in the neutron skin of nuclei". This work have been accepted for publication in *Physical review C*. As have been already explained, experimental studies on properties related to the neutron distribution are not usually free of theoretical or phenomenological assumptions. Experimentalists, commonly use approximate analytical expressions for the neutron and proton density distributions and, depending on the specific difficulties in the derivation of the nuclear property, they add also some "theoretical" constrains on these distributions. For example, to assume halo or skin structure of the neutron skin thickness have been a common practice in experimental studies(see *e.g.* [Tr01]). Here, as in the previous work, we study the surface and bulk contributions to the neutron skin thickness taking as a baseline a representative set of nuclear effective interactions but from a different point of view. We explain some aspects of the methods employed in antiprotonic atoms to better understand their results. Next, in analogy to

the frequent situation found in experiments, we fit a two-parameter Fermi function to reproduce the self-consistent calculations of the neutron and proton distributions. We also analyze some possible definitions of the nuclear radius with the aim of precisely characterize which one best discern between the bulk and surface contributions of the nuclear density distribution. In this respect, we notice that the equivalent sharp radius is a more suitable quantity than the half-density radius of the Fermi distribution. Finally, we investigate the neutron skin thickness in stable nuclei and how its bulk and surface contributions evolves along the Sn and Pb isotopic chains. This study bring us to notice that the density distribution in mean-field results for nuclei with isospin asymmetries —$(N - Z)/A$— higher than 0.1 clearly show a mixed halo and skin structures.

# 1.2 Nuclear Symmetry Energy Probed by Neutron Skin Thickness of Nuclei

PRL 102, 122502 (2009) PHYSICAL REVIEW LETTERS week ending 27 MARCH 2009

## Nuclear Symmetry Energy Probed by Neutron Skin Thickness of Nuclei

M. Centelles,[1] X. Roca-Maza,[1] X. Viñas,[1] and M. Warda[1,2]

[1]*Departament d'Estructura i Constituents de la Matèria and Institut de Ciències del Cosmos, Facultat de Física, Universitat de Barcelona, Diagonal 647, 08028 Barcelona, Spain*

[2]*Katedra Fizyki Teoretycznej, Uniwersytet Marii Curie–Skłodowskiej, ul. Radziszewskiego 10, 20-031 Lublin, Poland*

(Received 3 June 2008; revised manuscript received 1 February 2009; published 26 March 2009)

We describe a relation between the symmetry energy coefficients $c_{\rm sym}(\rho)$ of nuclear matter and $a_{\rm sym}(A)$ of finite nuclei that accommodates other correlations of nuclear properties with the low-density behavior of $c_{\rm sym}(\rho)$. Here, we take advantage of this relation to explore the prospects for constraining $c_{\rm sym}(\rho)$ of systematic measurements of neutron skin sizes across the mass table, using as example present data from antiprotonic atoms. The found constraints from neutron skins are in harmony with the recent determinations from reactions and giant resonances.

DOI: 10.1103/PhysRevLett.102.122502 PACS numbers: 21.10.Gv, 21.60.−n, 21.65.Ef, 26.60.−c

A wealth of measured data on densities, masses, and collective excitations of nuclei has allowed to resolve basic features of the equation of state (EOS) of nuclear matter, like the density $\rho_0 \approx 0.16$ fm$^{-3}$, energy per particle $a_v \approx -16$ MeV, and incompressibility $K_v \approx 230$ MeV [1] at saturation. However, the symmetry properties of the EOS due to differing neutron and proton numbers remain more elusive to date. The quintessential paradigm is the density dependence of the symmetry energy [1–10]. The accurate characterization of this property entails profound consequences in studying the neutron distribution in stable and exotic nuclei and neutron-rich matter [2–4]. It impacts on heavy ion reactions [5–9], nuclear astrophysics [3,4,10], and on diverse areas such as tests of the Standard Model via atomic parity violation [11].

The general expression $e(\rho,\delta) = e(\rho,0) + c_{\rm sym}(\rho)\delta^2 + \mathcal{O}(\delta^4)$ for the energy per particle of nuclear matter of density $\rho = \rho_n + \rho_p$ and asymmetry $\delta = (\rho_n - \rho_p)/\rho$ defines the symmetry energy coefficient $c_{\rm sym}(\rho)$ of a nuclear EOS. It is customary and insightful to characterize the behavior of an EOS around the saturation density $\rho_0$ in terms of a few bulk parameters, like $e(\rho,0) \simeq a_v + \frac{1}{2}K_v\epsilon^2$ and $c_{\rm sym}(\rho) \simeq J - L\epsilon + \frac{1}{2}K_{\rm sym}\epsilon^2$ where $\epsilon = (\rho_0 - \rho)/(3\rho_0)$ [5–7,12]. The value of $J = c_{\rm sym}(\rho_0)$ is acknowledged to be about 32 MeV. The values of $L = 3\rho\partial c_{\rm sym}(\rho)/\partial\rho|_{\rho_0}$ and $K_{\rm sym} = 9\rho^2\partial^2 c_{\rm sym}(\rho)/\partial\rho^2|_{\rho_0}$ govern the density dependence of $c_{\rm sym}$ around $\rho_0$. They are less certain, and the predictions vary largely among nuclear theories, see, e.g., Ref. [7] for a review.

In experiment, recent research in intermediate-energy heavy ion collisions (HIC) is consistent with a dependence $c_{\rm sym}(\rho) = c_{\rm sym}(\rho_0)(\rho/\rho_0)^\gamma$ at $\rho < \rho_0$ [6–9]. Isospin diffusion predicts $\gamma = 0.7$–$1.05$ ($L = 88 \pm 25$ MeV) [6,7], isoscaling favors $\gamma = 0.69$ ($L \sim 65$ MeV) [8], and a value closer to 0.55 ($L \sim 55$ MeV) is inferred from nucleon emission ratios [9]. Nuclear resonances are another hopeful tool to calibrate $c_{\rm sym}(\rho)$ below $\rho_0$ [13–16]. Indeed, the giant dipole resonance (GDR) of $^{208}$Pb analyzed with Skyrme forces suggests a constraint $c_{\rm sym}(0.1\ {\rm fm}^{-3}) = 23.3$–$24.9$ MeV [14], implying $\gamma \sim 0.5$–$0.65$. Note that the Thomas-Fermi model fitted very precisely to binding energies of 1654 nuclei [17] predicts an EOS that yields $\gamma = 0.51$. With the caveat that the connection of experiments to the EOS often is not at all trivial [6–9,13], it is important to seek further clues from the above and other isospin-sensitive signals, such as the neutron skin thickness $S = R_n - R_p$ of nuclei (difference of neutron and proton rms radii). Because $S$ of heavy nuclei correlates linearly with the slope $L$ of $c_{\rm sym}$ in mean field theories of nuclear structure [2–7,18,19], these studies have far-reaching implications for nuclear theory.

In this Letter, we show that $c_{\rm sym}(\rho)$ of the EOS equals at $\rho \approx 0.1$ fm$^{-3}$ the value of the symmetry energy coefficient $a_{\rm sym}(A)$ of heavy *finite* nuclei, universally in mean field theories. The observed correlations of $S$ [2–7] and of the excitation energy of the GDR [14] with the density dependence of $c_{\rm sym}$ can be deduced naturally from this relation. We resort to the nuclear droplet model (DM) [12] to work out the analytical formulas. The result derived for $S$ is applied to investigate limits to the slope and curvature of $c_{\rm sym}$ from neutron skins measured for 26 stable nuclei, from $^{40}$Ca to $^{238}$U, in antiprotonic atoms [20]. A main point is ascertaining how far *uniformly* measured neutron skins *over* the periodic table may help constrain the density dependence of $c_{\rm sym}$. We provide the first evidence that the constraints from skins are in consonance with the recent observations from reactions and giant resonances, though the probed densities and energies are not necessarily the same.

The symmetry energy coefficient $a_{\rm sym}(A)$ of finite nuclei is smaller than the bulk value $J$. Given a nuclear force, the DM allows one to extract $a_{\rm sym}(A)$ as [12,21]

$$a_{\rm sym}(A) = \frac{J}{1 + x_A}, \quad \text{with} \quad x_A = \frac{9J}{4Q}A^{-1/3}. \qquad (1)$$

The so-called surface stiffness $Q$ measures the resistance

 

of the nucleus against separation of neutrons from protons to form a neutron skin. One can obtain $Q$ of nuclear forces by asymmetric semi-infinite nuclear matter (ASINM) calculations [12,21,22]. The contribution of $a_{\rm sym}(A)$ to the nucleus energy is $a_{\rm sym}(A)(I + x_A I_C)^2 A$, where $I = (N - Z)/A$ and $I_C = e^2 Z/(20JR)$ is due to Coulomb. One has $R = r_0 A^{1/3}$. A small correction to $a_{\rm sym}(A)$ from surface compression [12] is neglected here. Let us mention that (1) may be derived also from the notion of surface symmetry energy [4,19].

The neutron skin thickness of nuclei is obtained as

$$S = \sqrt{3/5}[t - e^2 Z/(70J)] + S_{\rm sw} \tag{2}$$

in the DM [12,23]. The quantity $t$ gives the distance between the neutron and proton mean surface locations:

$$t = \frac{3r_0}{2}\frac{J/Q}{1 + x_A}(I - I_C) = \frac{2r_0}{3J}[J - a_{\rm sym}(A)]A^{1/3}(I - I_C), \tag{3}$$

where in the right side we have introduced the surface symmetry term $a_{\rm ss}(A) = [J - a_{\rm sym}(A)]A^{1/3}$ using Eq. (1). The second term in Eq. (2) is due to Coulomb repulsion, and $S_{\rm sw} = \sqrt{3/5}[5(b_n^2 - b_p^2)/(2R)]$ is a correction caused by an eventual difference in the surface widths $b_n$ and $b_p$ of the neutron and proton density profiles.

We first illustrate the aforesaid correlation of $S$ of heavy nuclei with $L$ in Fig. 1(a). It depicts the *quantal* self-consistent value of $S$ in $^{208}$Pb against $L$ for multiple Skyrme, Gogny, and covariant models of different nature [2–7,18,21,24]. In Fig. 1(b), we show that a similar correlation exists with the ratio $L/J$, which is proportional to $\gamma$ if a scaling $(\rho/\rho_0)^\gamma$ holds for $c_{\rm sym}(\rho)$. And in Fig. 1(c), we show that the close dependence of $S$ on $J - a_{\rm sym}(A)$ predicted by the DM is borne out in the quantal $S$ value, using

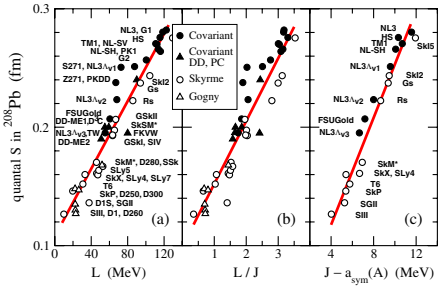


FIG. 1 (color online). Correlation of the quantal self-consistent $S$ value in $^{208}$Pb with the slope of the symmetry energy $L$ (a), the ratio $L/J$ (b), and with $J - a_{\rm sym}(A)$ (c), for various nuclear models (DD and PC stand for density dependent and point coupling models). From left to right, the correlation factors are $r = 0.961$, 0.945, and 0.970.

forces where we have computed $Q$ in ASINM. It reassures one that the DM expression incorporates the proper elements for the study. Many of the given nuclear interactions are accurately fitted to experimental binding energies, single-particle data, and charge radii of a variety of nuclei. However, their isospin structure is not sufficiently firmed up as seen, e.g., in the differing predictions for $S(^{208}\text{Pb})$. There is thus a need to deepen our knowledge of isospin-sensitive observables like $S$ and of their constraints on $c_{\rm sym}(\rho)$.

We bring into notice a genuine relation between the symmetry energy coefficients of the EOS and of nuclei: $c_{\rm sym}(\rho)$ equals $a_{\rm sym}(A)$ of a heavy nucleus like $^{208}$Pb at a density $\rho \approx 0.1$ fm$^{-3}$. Indeed, the relation holds similarly down to medium mass numbers, at lower $\rho$ values and a little more spread. Table I exemplifies this fact with several nuclear models, where we show the density fulfilling $c_{\rm sym}(\rho) = a_{\rm sym}(A)$ for $A = 208$, 116, and 40. We find that this density can be parametrized as

$$\rho_A = \rho_0 - \rho_0/(1 + cA^{1/3}) \tag{4}$$

with $c$ fixed by $\rho_{208} = 0.1$ fm$^{-3}$ (which gives $\rho_{116} \approx 0.093$ fm$^{-3}$ and $\rho_{40} \approx 0.08$ fm$^{-3}$ for the models of Table I).

The relation "$c_{\rm sym}(\rho) = a_{\rm sym}(A)$" can be very helpful to elucidate other correlations of isospin observables with $c_{\rm sym}(\rho)$ and to gain deeper insights into them. For example, it allows one to replace $a_{\rm sym}(A)$ in Eq. (3) for a heavy nucleus by $c_{\rm sym}(\rho) \simeq J - L\epsilon + \frac{1}{2}K_{\rm sym}\epsilon^2$ with $\epsilon$ computed at $\rho \approx 0.1$ fm$^{-3}$ [25]:

$$t = \frac{2r_0}{3J}L\left(1 - \epsilon\frac{K_{\rm sym}}{2L}\right)\epsilon A^{1/3}(I - I_C). \tag{5}$$

The imprint of the density content of the symmetry energy on the neutron skin appears now explicitly. The leading proportionality of (5) with $L$ explains the observed linear-

TABLE I. Value of $J$, $a_{\rm sym}(A)$, and density $\rho$ that fulfils $c_{\rm sym}(\rho) = a_{\rm sym}(A)$ for $A = 208$, 116, and 40, in various nuclear models. $J$ and $a_{\rm sym}$ are in MeV and $\rho$ is in fm$^{-3}$. Here, $c_{\rm sym}(\rho)$ was computed exactly as $\frac{1}{2}\partial^2 e(\rho,\delta)/\partial\delta^2|_{\delta=0}$ from the EOS of the models.

| | | $A = 208$ | | $A = 116$ | | $A = 40$ | |
|---|---|---|---|---|---|---|---|
| Model | $J$ | $a_{\rm sym}$ | $\rho$ | $a_{\rm sym}$ | $\rho$ | $a_{\rm sym}$ | $\rho$ |
| NL3 | 37.4 | 25.8 | 0.103 | 24.2 | 0.096 | 21.1 | 0.083 |
| NL-SH | 36.1 | 26.0 | 0.105 | 24.6 | 0.099 | 21.3 | 0.086 |
| FSUGold | 32.6 | 25.4 | 0.099 | 24.2 | 0.092 | 21.9 | 0.078 |
| TF [17] | 32.6 | 24.2 | 0.094 | 22.9 | 0.086 | 20.3 | 0.071 |
| SLy4 | 32.0 | 25.3 | 0.100 | 24.2 | 0.093 | 22.0 | 0.079 |
| SkX | 31.1 | 25.7 | 0.103 | 24.8 | 0.096 | 22.8 | 0.084 |
| SkM* | 30.0 | 23.2 | 0.101 | 22.0 | 0.094 | 19.9 | 0.079 |
| SIII | 28.2 | 24.1 | 0.093 | 23.4 | 0.088 | 21.8 | 0.078 |
| SGII | 26.8 | 21.6 | 0.104 | 20.7 | 0.098 | 18.9 | 0.084 |

PRL 102, 122502 (2009) PHYSICAL REVIEW LETTERS week ending 27 MARCH 2009

ity of $S$ of a heavy nucleus with $L$ in nuclear models [2,4,7]. The correction with $K_{\rm sym}$ does not alter the situation as $\epsilon \sim 1/9$ is small. One can use Eq. (5) in other mass regions by calculating $\epsilon$ from $\rho_A$ of Eq. (4). We have checked numerically in multiple forces that the results closely agree with Eq. (3) for the $40 \leq A \leq 238$ stable nuclei given in Fig. 2.

With the help of Eq. (5) for $t$ (using $\rho_A$ to compute $\epsilon$), we next analyze constraints on the density dependence of the symmetry energy by optimization of (2) to experimental $S$ data. We employ $c_{\rm sym}(\rho) = 31.6(\rho/\rho_0)^\gamma$ MeV [6–9] and take as experimental baseline the neutron skins measured in 26 antiprotonic atoms [20] (see Fig. 2). These data constitute the largest set of uniformly measured neutron skins over the mass table till date. With allowance for the error bars, they are fitted linearly by $S = (0.9 \pm 0.15)I + (-0.03 \pm 0.02)$ fm [20]. This systematics renders comparisons of skin data with DM formulas, which by construction average the microscopic shell effect, more meaningful [26]. We first set $b_n = b_p$ (i.e., $S_{\rm sw} = 0$) as done in the DM [12,23,26] and in the analysis of data in Ref. [19]. Following the above, we find $L = 75 \pm 25$ MeV ($\gamma = 0.79 \pm 0.25$). The range $\Delta L = 25$ MeV stems from the window of the linear averages of experiment. The $L$ value and its uncertainty obtained from neutron skins with $S_{\rm sw} = 0$ is thus quite compatible with the quoted constraints from isospin diffusion and isoscaling observables in HIC [6–8]. On the other hand, the symmetry term of the incompressibility of the nuclear EOS around equilibrium ($K = K_v + K_\tau \delta^2$) can be estimated using information of the symmetry energy as $K_\tau \approx K_{\rm sym} - 6L$ [5–7]. The constraint $K_\tau = -500 \pm 50$ MeV is found from isospin diffusion [6,7], whereas our study of neutron skins leads to $K_\tau = -500^{+125}_{-100}$ MeV. A value $K_\tau = -550 \pm 100$ MeV seems to be favored by the giant monopole resonance (GMR) measured in Sn isotopes as is described in [13]. Even if the present analyses may not be called definitive, significant consistency arises among the values extracted for $L$ and $K_\tau$ from seemingly unrelated sets of data from reactions, ground-states of nuclei, and collective excitations.

To assess the influence of the correction $S_{\rm sw}$ in (2), we compute the surface widths $b_n$ and $b_p$ in ASINM [22]. This yields the $b_{n(p)}$ values of a finite nucleus if we relate the asymmetry $\delta_0$ in the bulk of ASINM to $I$ by $\delta_0(1 + x_A) = I + x_A I_C$ [21–23]. In doing so, we find that Eq. (2) reproduces trustingly $S$ (and its change with $I$) of self-consistent Thomas-Fermi calculations of finite nuclei made with the same nuclear force. Also, $S_{\rm sw}$ is very well fitted by $S_{\rm sw} = \sigma_{\rm sw} I$. All slopes $\sigma_{\rm sw}$ of the forces of Fig. 1(c) lie between $\sigma_{\rm sw}^{\rm min} = 0.15$ fm (SGII) and $\sigma_{\rm sw}^{\rm max} = 0.31$ fm (NL3). We then reanalyze the experimental neutron skins including $S_{\rm sw}^{\rm min}$ and $S_{\rm sw}^{\rm max}$ in Eq. (2) to simulate the two conceivable extremes of $S_{\rm sw}$ according to mean field models. The results are shown in Fig. 3. Our above estimates of $L$ and $K_\tau$ could be shifted by up to $-25$ and $+125$ MeV, respectively, by nonzero $S_{\rm sw}$. This is on the soft side of the HIC [6–8] and GMR [13] analyses of the symmetry energy, but closer to the alluded predictions from nucleon emission ratios [9], the GDR [14], and nuclear binding systematics [17]. One should mention that the properties of $c_{\rm sym}(\rho)$ derived from terrestrial nuclei have intimate connections to astrophysics [3,4,10]. As an example, we can estimate the transition density $\rho_t$ between the crust and the core of a neutron star [3,10] as $\rho_t/\rho_0 \sim 2/3 + (2/3)^\gamma K_{\rm sym}/2K_v$, following the model of Sect. 5.1 of Ref. [10]. The constraints from neutron skins hereby yield $\rho_t \sim 0.095 \pm 0.01$ fm$^{-3}$. This value would not support the direct URCA process of cooling of a neutron star that requires a higher $\rho_t$ [3,10]. The result is in accord with $\rho_t \sim 0.096$ fm$^{-3}$ of the microscopic EOS of Friedman and Pandharipande [27], as well as with $\rho_t \sim 0.09$ fm$^{-3}$ pre-

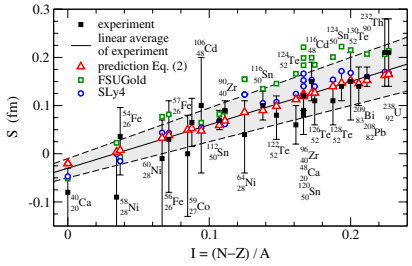


FIG. 2 (color online). Comparison of the fit described in the text of Eq. (2) with the experimental neutron skins from antiprotonic measurements and their linear average $S = (0.9 \pm 0.15)I + (-0.03 \pm 0.02)$ fm [20]. Results of the modern Skyrme SLy4 and relativistic FSUGold forces are also shown.

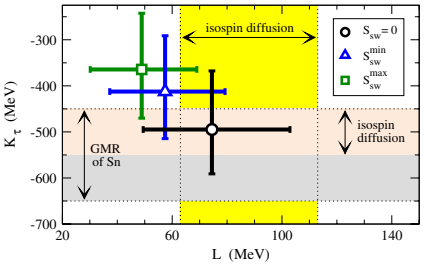


FIG. 3 (color online). Constraints on $L$ and $K_\tau$ from neutron skins and their dependence on the $S_{\rm sw}$ correction of Eq. (2). The crosses express the $L$ and $K_\tau$ ranges compatible with the uncertainties in the skin data. The shaded regions depict the constraints on $L$ and $K_\tau$ from isospin diffusion [6,7] and on $K_\tau$ as determined in [13] from the GMR of Sn isotopes.

dicted by a recent analysis of pygmy dipole resonances in nuclei [15].

We would like to close with a brief comment regarding the GDR. As mentioned, Ref. [14] very interestingly constrains $c_{\rm sym}(0.1)$ from the GDR of $^{208}$Pb. The analysis notes that the mean excitation energy of the GDR depends on $g(A) = J/\{1 + \frac{5}{3}a_{\rm ss}(A)A^{-1/3}/J\}$ [4,14] and shows numerically that the values of $g(208)$ and $c_{\rm sym}(0.1)$ are correlated in Skyrme forces. Inserting $a_{\rm ss}(A)$ given below Eq. (3), one has $g(A) = J/\{1 + \frac{5}{3}[J - a_{\rm sym}(A)]/J\}$. Immediately, the equivalence $a_{\rm sym}(208) \approx c_{\rm sym}(0.1)$ explains why $g(208)$ has a dependence on $c_{\rm sym}(0.1)$, gives it analytically, and validates it for any type of mean field model [28]. One could extend it to other $A$ values through Eq. (4). In conclusion, the discussed relation of $c_{\rm sym}(\rho)$ with $a_{\rm sym}(A)$ can be much valuable to link different problems depending upon $a_{\rm sym}(A)$ of nuclei to the symmetry properties of the EOS.

Summarizing, we have described a generic relation between the symmetry energy in finite nuclei and in nuclear matter at subsaturation. It plausibly encompasses other prime correlations of nuclear observables with the density content of the symmetry energy. We take advantage of this relation to explore constraints on $c_{\rm sym}(\rho)$ from neutron skins measured in antiprotonic atoms [20]. We discuss the $L$ and $K_\tau$ values that skins favor vis-à-vis most recent observations from reactions and giant resonances. The difficult experimental extraction of neutron skins limits their potential to constrain $c_{\rm sym}(\rho)$. Interestingly, we learn that in spite of present error bars in the data of [20], the size of the final uncertainties in $L$ or $K_\tau$ is comparable to the other analyses. This highlights the value of having skin data consistently measured across the mass table, and calls for pursuing extended measurements of neutron radii and skins with "conventional" hadronic probes. Combined with a precision extraction of $R_n$ of $^{208}$Pb through electroweak probes [29], they would contribute to cast uniquely tight constraints on $c_{\rm sym}(\rho)$.

Work supported by the Spanish Consolider-Ingenio 2010 Programme CPAN CSD2007-00042 and Grants Nos. FIS2008-01661 from MEC (Spain) and FEDER, 2005SGR-00343 from Generalitat de Catalunya, and N202 179 31/3920 from MNiSW (Poland). X. R. acknowledges Grant No. AP2005-4751 from MEC (Spain).

[1] J. Piekarewicz, Phys. Rev. C **76**, 031301(R) (2007), and references therein.
[2] B. A. Brown, Phys. Rev. Lett. **85**, 5296 (2000); S. Typel and B. A. Brown, Phys. Rev. C **64**, 027302 (2001).
[3] C. J. Horowitz and J. Piekarewicz, Phys. Rev. Lett. **86**, 5647 (2001); B. G. Todd-Rutel and J. Piekarewicz, Phys. Rev. Lett. **95**, 122501 (2005).
[4] A. W. Steiner *et al.*, Phys. Rep. **411**, 325 (2005).
[5] V. Baran, M. Colonna, V. Greco, and M. Di Toro, Phys. Rep. **410**, 335 (2005).
[6] L. W. Chen, C. M. Ko, and B. A. Li, Phys. Rev. Lett. **94**, 032701 (2005); Phys. Rev. C **72**, 064309 (2005).
[7] B. A. Li, L. W. Chen, and C. M. Ko, Phys. Rep. **464**, 113 (2008).
[8] D. V. Shetty, S. J. Yennello, and G. A. Souliotis, Phys. Rev. C **76**, 024606 (2007).
[9] M. A. Famiano *et al.*, Phys. Rev. Lett. **97**, 052701 (2006).
[10] J. M. Lattimer and M. Prakash, Phys. Rep. **442**, 109 (2007).
[11] T. Sil, M. Centelles, X. Viñas, and J. Piekarewicz, Phys. Rev. C **71**, 045502 (2005).
[12] W. D. Myers and W. J. Świątecki, Ann. Phys. (N.Y.) **55**, 395 (1969); **84**, 186 (1974); W. D. Myers, *Droplet Model of Atomic Nuclei* (Plenum, New York, 1977).
[13] T. Li *et al.*, Phys. Rev. Lett. **99**, 162503 (2007).
[14] L. Trippa, G. Colò, and E. Vigezzi, Phys. Rev. C **77**, 061304(R) (2008). We thank a referee for bringing this paper to our attention.
[15] A. Klimkiewicz *et al.*, Phys. Rev. C **76**, 051603(R) (2007).
[16] H. Liang, N. Van Giai, and J. Meng, Phys. Rev. Lett. **101**, 122502 (2008).
[17] W. D. Myers and W. J. Świątecki, Nucl. Phys. A **601**, 141 (1996); Phys. Rev. C **57**, 3020 (1998).
[18] R. J. Furnstahl, Nucl. Phys. A **706**, 85 (2002).
[19] P. Danielewicz, Nucl. Phys. A **727**, 233 (2003).
[20] A. Trzcińska *et al.*, Phys. Rev. Lett. **87**, 082501 (2001); J. Jastrzębski *et al.*, Int. J. Mod. Phys. E **13**, 343 (2004).
[21] M. Brack, C. Guet, and H.-B. Håkansson, Phys. Rep. **123**, 275 (1985).
[22] M. Centelles, M. Del Estal, and X. Viñas, Nucl. Phys. A **635**, 193 (1998).
[23] W. D. Myers and W. J. Świątecki, Nucl. Phys. A **336**, 267 (1980).
[24] J. P. Blaizot *et al.*, Nucl. Phys. A **591**, 435 (1995).
[25] The expression $J - L\epsilon + \frac{1}{2}K_{\rm sym}\epsilon^2$ differs from the exact value of $c_{\rm sym}(\rho)$ by less than 1% at $\rho = 0.1$ fm$^{-3}$ in all forces tested, thus being of sufficient accuracy.
[26] W. J. Świątecki, A. Trzcińska, and J. Jastrzębski, Phys. Rev. C **71**, 047301 (2005).
[27] C. P. Lorenz, D. G. Ravenhall, and C. J. Pethick, Phys. Rev. Lett. **70**, 379 (1993).
[28] In practice, this dependence becomes almost linear: using for calculation the forces of Fig. 1(c) as well as the TF model of [17], we find that $g(208)$ has a correlation factor 0.991 with $a_{\rm sym}(208)$ and 0.983 with $c_{\rm sym}(0.1)$.
[29] R. Michaels, P. A. Souder, and G. M. Urciuoli, spokespersons, http://hallaweb.jlab.org/parity/prex.

# 1.3 Neutron skin thickness in the droplet model with surface width dependence: Indications of softness of the nuclear symmetry energy

PHYSICAL REVIEW C **80**, 024316 (2009)

**Neutron skin thickness in the droplet model with surface width dependence: Indications of softness of the nuclear symmetry energy**

M. Warda,[1,2,*] X. Viñas,[1,†] X. Roca-Maza,[1,‡] and M. Centelles[1,§]

[1]*Departament d'Estructura i Constituents de la Matèria and Institut de Ciències del Cosmos, Facultat de Física, Universitat de Barcelona, Diagonal 647, 08028 Barcelona, Spain*

[2]*Katedra Fizyki Teoretycznej, Uniwersytet Marii Curie–Skłodowskiej, ul. Radziszewskiego 10, 20-031 Lublin, Poland*

(Received 4 June 2009; revised manuscript received 21 July 2009; published 28 August 2009)

We analyze the neutron skin thickness in finite nuclei with the droplet model and effective nuclear interactions. The ratio of the bulk symmetry energy $J$ to the so-called surface stiffness coefficient $Q$ has in the droplet model a prominent role in driving the size of neutron skins. We present a correlation between the density derivative of the nuclear symmetry energy at saturation and the $J/Q$ ratio. We emphasize the role of the surface widths of the neutron and proton density profiles in the calculation of the neutron skin thickness when one uses realistic mean-field effective interactions. Next, taking as experimental baseline the neutron skin sizes measured in 26 antiprotonic atoms along the mass table, we explore constraints arising from neutron skins on the value of the $J/Q$ ratio. The results favor a relatively soft symmetry energy at subsaturation densities. Our predictions are compared with the recent constraints derived from other experimental observables. Though the various extractions predict different ranges of values, one finds a narrow window $L \sim 45$–$75$ MeV for the coefficient $L$ that characterizes the density derivative of the symmetry energy that is compatible with all the different empirical indications.

DOI: 10.1103/PhysRevC.80.024316 PACS number(s): 21.60.−n, 21.65.Ef, 21.10.Gv, 36.10.−k

## I. INTRODUCTION

Neutron skin thickness is the name in common usage to refer to the difference between the root-mean-square (rms) radii of the neutron and proton density distributions of atomic nuclei:

$$\Delta R_{np} = \langle r^2 \rangle_n^{1/2} - \langle r^2 \rangle_p^{1/2}. \quad (1)$$

Experimentally, the value of the proton rms radius $\langle r^2 \rangle_p^{1/2}$ is obtained from the charge radius. The latter has been measured by electron-nucleus elastic scattering with high accuracy (often the accuracy in charge radii is better than 1% [1]). In contrast, our knowledge of the neutron distribution in nuclei and of its rms radius $\langle r^2 \rangle_n^{1/2}$, as well as our knowledge of $\Delta R_{np}$, is to date less precise. This situation looks inadequate in anticipation of the next generation of rare ion accelerator facilities that are planned for the synthesis and study of exotic nuclei, as in RIKEN centers (Japan), in FAIR at GSI (Germany), in the CSR at HIRFL (China), or in FRIB at MSU (U.S.A.). Without securing sufficient knowledge of the neutron distribution in stable nuclei, the prospects of nuclear structure theory in this thriving domain may be compromised. It is expected that parity-violating electron scattering will provide in the nearby future a leap forward in the quest for high-precision determinations of the neutron radius in heavy nuclei [2].

The calibration of the neutron skin thickness of nuclei also is one of the problems at the forefront of nuclear structure by reason of being intimately correlated with the nuclear symmetry energy. Indeed, the symmetry energy is a fundamental quantity in nuclear physics and astrophysics, because it governs at the same time important properties of very small entities like atomic nuclei and of very large objects like neutron stars [3]. One of the crucial properties of the symmetry energy, which still is not sufficiently well constrained, is its dependence on the nuclear density. It is relevant in the astrophysical context to understand a wealth of phenomena [3–5], including supernova explosions, neutrino emission, and the cooling mechanism of protoneutron stars, as well as mass-radius relations in neutron stars. Moreover, the density content of the symmetry energy eventually relates to basic issues in physics. This is the case of precision tests of the standard model through atomic parity nonconservation observables [6], and even of studies on constraining a possible time variation of the gravitational constant [7]. In terrestrial laboratories, the available tools to delineate the density dependence of the symmetry energy at saturation and subsaturation densities include the interaction potential between neutron-rich nuclei [8], observables like isospin diffusion and isoscaling in heavy-ion reactions at intermediate energies [9–21], different modes of collective excitations of nuclei [22–26], and, of course, data on the binding and structure of neutron-rich nuclei and on their neutron skin thickness.

In the literature there exist several theoretical formulations to investigate the neutron skin thickness of neutron-rich nuclei and its connections with the symmetry energy. This is the case, for instance, of methods based on the droplet model [27,28], on the concept of surface symmetry energy [5,29,30], thermodynamical arguments [31], nucleonic density form factors [32], mean-field analyses [33–35], or studies in the spirit of the Landau-Migdal approximation [36]. It has been shown that the neutron skin thickness in heavy nuclei, like $^{208}$Pb, calculated in mean-field models with either nonrelativistic or relativistic effective nuclear interactions, displays a linear correlation with the slope of the neutron

*warda@kft.umcs.lublin.pl
†xavier@ecm.ub.es
‡roca@ecm.ub.es
§mariocentelles@ub.edu

 

equation of state (EOS) obtained with the same interactions at a neutron density $\rho \approx 0.10$ fm$^{-3}$ [37–39]. A similar correlation exists between $\Delta R_{np}$ and the density derivative of the bulk symmetry energy [13–16,33,40,41], as the latter is a measure of the pressure difference between neutrons and protons. These correlations have been exploited in recent years to gain a deeper understanding of the isospin properties of the effective nuclear interaction and to relate them with nuclear and astrophysical observations.

The rms radius of neutron densities in nuclei has been measured with hadronic probes such as proton-nucleus elastic scattering [42–45] or inelastic scattering excitation of the giant dipole and spin-dipole resonances [46,47]. Antiprotonic atoms are helpful to probe the size of the neutron skin of nuclei from the fact that the nuclear periphery is very sensitive to antiprotons in the normally electronic shell. Experimentalists combine two different techniques in this case [48–50], namely the measurement of the antiprotonic x rays that determine the atomic level shifts and widths due to the strong interaction and the radiochemical analysis of the yields after the antiproton annihilation. The values of the neutron skin thickness of 26 stable nuclei from $^{40}$Ca to $^{238}$U deduced from antiprotonic atoms data by Trzcińska *et al.* [48,49] follow a roughly linear trend with the overall relative neutron excess $I = (N - Z)/A$ of these nuclei. This trend can be fitted by the relationship $\Delta R_{np} = (0.90 \pm 0.15)I + (-0.03 \pm 0.02)$ fm as discussed in Refs. [48,49]. As mentioned, all neutron skin thickness measurements have relatively large uncertainties in comparison with charge radii, and sometimes the results from different experimental techniques are not totally consistent among them [47,49]. The neutron skin sizes determined in Refs. [48,49] from the analysis of antiprotonic atoms are to date the largest set of *uniformly* measured values of $\Delta R_{np}$ *all over* the periodic table ($40 \leqslant A \leqslant 238$). Due to this reason, we shall use hereinafter these data as the experimental benchmark for our calculations.

The droplet model (DM) describes in a physically transparent way nuclear radii and relates them directly with basic properties of the nuclear interactions. In the present article we study the neutron skin thickness of atomic nuclei with the DM using various effective nuclear interactions of the Skyrme, Gogny, and relativistic mean-field (RMF) type. The present work extends with a new analysis and perspective a first presentation of our study made in Ref. [51]. Here, we will show that the ratio of the DM parameters $J$ and $Q$, which drives the value of the neutron skin thickness in heavy nuclei, is correlated with the slopes in density of the nuclear symmetry energy and of the EOS of neutron matter. We compare the DM values for the neutron skin thickness with the results obtained in self-consistent extended Thomas-Fermi (ETF) calculations of finite nuclei [52–55], because both methods are free of shell effects. A non-negligible role of the contribution of the difference in the surface widths of the neutron and proton density profiles is noticed. Next, we use the experimental neutron skin thickness measured in antiprotonic atoms to explore the range of possible values of the ratio $J/Q$ that are favored by neutron skins. With these values we can predict some properties of the density dependence of the nuclear symmetry energy. Our results are compared with the constraints recently obtained in the literature using other observables and methods.

The present article is arranged as follows. In the second section we study the neutron skin thickness of heavy nuclei on the basis of the DM [27,56,57] and show a correlation that links the value of the ratio $J/Q$, which governs the neutron skin thickness of nuclei, with the slope of the symmetry energy in bulk matter at saturation. In the third section, the contribution of the surface widths of the neutron and proton density distributions to the neutron skin thickness is analyzed with the DM using nonrelativistic and covariant mean-field nuclear interactions. In the fourth section we estimate possible constraints on the density dependence of the nuclear symmetry energy on the basis of the DM and the experimental data on neutron skin sizes derived from antiprotonic atoms. We discuss the present results in comparison with the recent constraints obtained from various observables and methods. Finally, the summary and our conclusions are laid in the fifth section. We outline the procedure for the calculation of the $Q$ coefficient in the Appendix.

## II. THE FRAMEWORK

### A. Neutron skin thickness in the droplet model

In the DM of average nuclear properties [52,56,57] the neutron skin thickness of a finite nucleus is computed from the expression [27,56]

$$\Delta R_{np} = \sqrt{\frac{3}{5}}\left[t - \frac{e^2 Z}{70J} + \frac{5}{2R}\left(b_n^2 - b_p^2\right)\right], \tag{2}$$

where $e^2 Z/70J$ is a correction due to the Coulomb interaction, $R = r_0 A^{1/3}$ is the nuclear radius, and $b_n$ and $b_p$ are the surface widths of the neutron and proton density profiles. In the "standard" version of the DM it is assumed that $b_n = b_p = 1$ fm [27,28,56], which implies a vanishing surface width correction to the neutron skin thickness.

The quantity $t$ in Eq. (2) represents the distance between the neutron and proton mean surface locations. This distance is computed as [27,56]

$$t = \frac{3}{2} r_0 \frac{J}{Q} \frac{I - \frac{c_1 Z}{12J} A^{-1/3}}{1 + \frac{9}{4}\frac{J}{Q} A^{-1/3}}, \tag{3}$$

where $I = (N - Z)/A$, $J$ is the symmetry energy coefficient at saturation, $Q$ is the surface stiffness coefficient, and $c_1 = 3e^2/5r_0$. The coefficient $J$ represents with a very good accuracy the energy cost per nucleon to convert all protons into neutrons in symmetric infinite nuclear matter at saturation density $\rho_0$. The surface stiffness coefficient $Q$ measures the resistance of the system against separation of neutrons from protons to form a neutron skin. To extract $Q$ from an effective nuclear interaction requires performing calculations of asymmetric semi-infinite nuclear matter (ASINM). Therefore, the calculated value of $Q$ may depend somewhat on the type of approach, such as the Hartree-Fock or Thomas-Fermi methods, employed to describe the nuclear surface [30,52,53,58–60].

From Eq. (3), one sees that the leading contribution to $t$ in large nuclei is the term $\frac{3}{2} r_0 (J/Q) I$. Thus, the DM suggests

TABLE I. Saturation density $\rho_0$ and $J$, $L$, $K_{\rm sym}$, and $Q$ parameters of the Skyrme and Gogny forces as well as RMF parameter sets used in this work.

| Force | $\rho_0$ fm$^{-3}$ | $J$ MeV | $L$ MeV | $K_{\rm sym}$ MeV | $Q$ MeV | $J/Q$ |
|---|---|---|---|---|---|---|
| SGII | 0.158 | 26.83 | 37.7 | −146 | 41.7 | 0.64 |
| SVI | 0.144 | 26.88 | −7.3 | −471 | 78.4 | 0.34 |
| SIII | 0.145 | 28.16 | 9.9 | −394 | 63.6 | 0.44 |
| T6 | 0.161 | 29.97 | 30.9 | −211 | 47.8 | 0.63 |
| SkP | 0.163 | 30.00 | 19.7 | −267 | 52.1 | 0.58 |
| SkM* | 0.160 | 30.03 | 45.8 | −156 | 39.0 | 0.77 |
| SkX | 0.155 | 31.10 | 33.2 | −252 | 56.2 | 0.55 |
| NL3 $\Lambda_v = 0.03$ | 0.148 | 31.68 | 55.3 | −8 | 45.2 | 0.70 |
| D1S | 0.163 | 31.93 | 22.4 | −252 | 53[a] | 0.60 |
| SLy4 | 0.160 | 32.00 | 46.0 | −120 | 46.1 | 0.69 |
| FSUGold | 0.148 | 32.59 | 60.5 | −52 | 43.7 | 0.75 |
| NL3 $\Lambda_v = 0.02$ | 0.148 | 33.15 | 68.2 | −54 | 39.6 | 0.84 |
| NL3 $\Lambda_v = 0.01$ | 0.148 | 34.96 | 87.7 | −46 | 35.2 | 0.99 |
| NL-SH | 0.146 | 36.12 | 113.7 | 80 | 34.5 | 1.05 |
| TM1 | 0.145 | 36.89 | 110.8 | 34 | 34.3 | 1.08 |
| NL3 | 0.148 | 37.40 | 118.5 | 101 | 31.7 | 1.18 |
| NL1 | 0.152 | 43.46 | 140.2 | 143 | 29.4 | 1.48 |
| NL2 | 0.146 | 45.12 | 133.4 | 20 | 41.7 | 1.08 |

[a]Estimated value.

that one can expect a correlation between $\Delta R_{np}$ and $J/Q$ in heavy nuclei. We illustrate this fact in the left panel of Fig. 1. We depict there the neutron skin thickness of $^{208}$Pb obtained from *self-consistent quantal* calculations with the Skyrme and Gogny Hartree-Fock methods as well as with the RMF Hartree approach. The results are shown as a function of the value of the $J/Q$ ratio for various mean-field effective interactions. The $J$ values of the selected interactions (about 27–32 MeV in the nonrelativistic forces and about 32–45 MeV in the covariant forces, see Table I) cover widely the plausible physical range of the bulk symmetry energy. The values of $Q$ used in this work have been extracted from ASINM calculations performed in the extended Thomas-Fermi (ETF) approach as described in the Appendix (see also Ref. [53]). Even if the shell effects, present in the mean-field calculations of $\Delta R_{np}$, are not built in the DM [27], one observes a considerably linear correlation between the values of $\Delta R_{np}$ and $J/Q$. It should be pointed out that while all the effective interactions have been accurately calibrated to data on binding energies and charge radii, and describe these properties very successfully, they predict widely different values of $\Delta R_{np}$, as we see in the present case of $^{208}$Pb. This underlines the fact that the isospin sector of the effective interactions is little constrained.

### B. Properties of the nuclear symmetry energy

Let us consider the energy per particle $e(\rho, \delta)$ in asymmetric infinite nuclear matter of total density $\rho = \rho_n + \rho_p$ and relative neutron excess $\delta = (\rho_n - \rho_p)/\rho$, where $\rho_n$ and $\rho_p$ stand for the neutron and proton densities, respectively. The general expression

$$e(\rho, \delta) = e(\rho, \delta = 0) + c_{\rm sym}(\rho)\delta^2 + \mathcal{O}(\delta^4) \qquad (4)$$

defines the symmetry energy coefficient $c_{\rm sym}(\rho)$ of a nuclear EOS at the density $\rho$. This expression is particularly useful because $c_{\rm sym}(\rho)$ dominates the corrections to the symmetric limit for all values of $\delta$, especially at the subsaturation densities of relevance for finite nuclei [61]. Actually, $c_{\rm sym}(\rho)$ provides with excellent accuracy the difference between the binding energies of pure neutron matter ($\delta = 1$) and symmetric matter ($\delta = 0$).

It is customary, and insightful, to characterize the behavior of an EOS around the saturation density $\rho_0$ by means of a few bulk parameters calculated at the saturation point, as in the formula [10,13–16,56,61–63]

$$e(\rho, \delta) \approx a_v + \frac{K_v}{2}\epsilon^2 + \left[J - L\epsilon + \frac{K_{\rm sym}}{2}\epsilon^2\right]\delta^2, \qquad (5)$$

where $\epsilon = (\rho_0 - \rho)/3\rho_0$ expresses the relative density displacement from $\rho_0$. Here, the quantities $a_v$ and $K_v$ denote the energy per particle and the incompressibility modulus of symmetric nuclear matter. One has $c_{\rm sym}(\rho_0) = J$. The DM coefficients $L$ and $K_{\rm sym}$ are, respectively, proportional to the slope and the curvature of the symmetry energy coefficient $c_{\rm sym}(\rho)$ at saturation density:

$$L = 3\rho_0 \frac{\partial c_{\rm sym}(\rho)}{\partial \rho}\bigg|_{\rho_0}, \quad K_{\rm sym} = 9\rho_0^2 \frac{\partial^2 c_{\rm sym}(\rho)}{\partial \rho^2}\bigg|_{\rho_0}. \qquad (6)$$

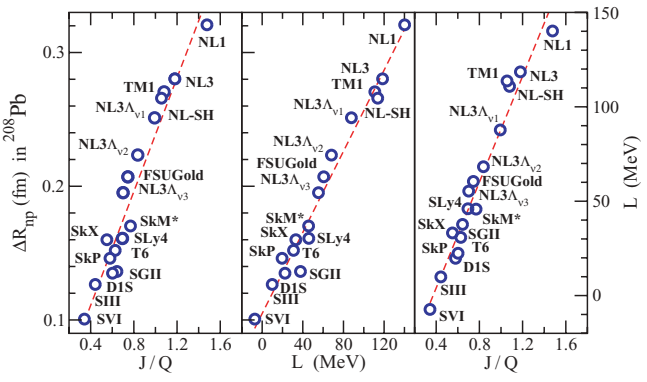


FIG. 1. (Color online) For several nuclear mean-field models, existing correlation between the neutron skin thickness $\Delta R_{np}$ in $^{208}$Pb and the ratio $J/Q$ (left panel) and between $\Delta R_{np}$ in $^{208}$Pb and the slope of the symmetry energy $L$ (middle panel). The correlation between the coefficient $L$ and the ratio $J/Q$ is also shown (right panel). In the present figure, $\Delta R_{np}$ has been computed with Eq. (1) from the rms radii of quantal self-consistent calculations for the indicated mean-field models.

The quadratic expansion $c_{\rm sym}(\rho) \approx J - L\epsilon + \frac{1}{2}K_{\rm sym}\epsilon^2$ in Eq. (5) is often a reliable representation of the actual value of the $c_{\rm sym}(\rho)$ coefficient at densities roughly between $\rho_0/2$ and $2\rho_0$ [61]. For instance, in the case of a typical subsaturation density value $\rho = 0.10$ fm$^{-3}$, one finds that the above quadratic expansion of $c_{\rm sym}(\rho)$ differs from the exact $c_{\rm sym}(\rho)$ by less than 1% in many different nuclear mean field forces [51]. These facts point to the usefulness of investigating parameters such as $L$ and $K_{\rm sym}$ for the characterization of the density dependence of the symmetry energy.

The values of the DM coefficients $J$, $L$, and $K_{\rm sym}$ for the nonrelativistic forces and the RMF parameter sets considered in this work are given in Table I. In the Skyrme and Gogny effective interactions the symmetry energy coefficient at saturation $J$ takes values around 30 MeV. The RMF parametrizations have larger values of $J$, also with a larger spread. The slope ($L$) and the curvature ($K_{\rm sym}$) of the symmetry energy at saturation take even more widely scattered values among the different interactions. The consequence is that all mentioned nuclear models predict a different behavior of the symmetry energy at subsaturation densities, what can be seen, e.g., in Fig. 1 of Ref. [13].

As is known, the density dependence of the symmetry energy near saturation tends to be much softer in the nonrelativistic forces than in the covariant meson-exchange models of nuclear structure (see the values of $L$ in Table I). In particular, taking into account Eq. (5), the slope of the neutron EOS

$$\frac{de(\rho,\delta=1)}{d\rho} = \frac{L}{3\rho_0} - \frac{K_v + K_{\rm sym}}{3\rho_0}\epsilon\,, \tag{7}$$

and of the symmetry energy

$$\frac{dc_{\rm sym}(\rho)}{d\rho} = \frac{L}{3\rho_0} - \frac{K_{\rm sym}}{3\rho_0}\epsilon\,, \tag{8}$$

calculated at densities $\rho$ close to the saturation value $\rho_0$ differ considerably between models. We also know that $\Delta R_{np}$ in $^{208}$Pb shows a linear dependence with these slopes at some subsaturation density $\rho \simeq 0.10$ fm$^{-3}$ [37–40]. Therefore it is reasonable that the neutron skin thickness in $^{208}$Pb and the leading term $L/3\rho_0$ of Eqs. (7) and (8) are related. As far as $\rho_0$ does not change much in the different effective forces, a correlation between $\Delta R_{np}$ in $^{208}$Pb and the DM coefficient $L$ is thus expected [13–15,33,41] and we display it in the middle panel of Fig. 1.

From the discussed results of $\Delta R_{np}$ versus $J/Q$ and of $\Delta R_{np}$ versus $L$ in Fig. 1, a correlation between the DM coefficient $L$ and the $J/Q$ ratio is to be expected too. Note that $L$ rules the density dependence of the symmetry energy of the nuclear equation of state [Eq. (8)] and that $Q$ governs the thickness of the neutron skin of finite nuclei [Eqs. (2) and (3)]. The correlation between $L$ and $J/Q$ can be seen in the right panel of Fig. 1. This correlation shows that the value of the slope $L$ of the symmetry energy at the saturation density increases with the value of the ratio between the bulk symmetry energy coefficient $J$ and the surface stiffness coefficient $Q$. The trend is considerably linear among the various nuclear effective interactions.

Previous literature [53,59] has shown that the systematics of experimental binding energies relates increasing values of $J$ with decreasing values of $Q$ in nuclear effective interactions whose parameters have been adjusted to describe experimental data. We note this same trend in Table I, where the RMF sets that in general have larger $J$ values also tend to have smaller $Q$ values than their nonrelativistic counterparts. A smaller $Q$ coefficient means that it is easier to develop a neutron skin in finite nuclei. Consistently, the neutron skin thickness in $^{208}$Pb (or any other heavy nucleus) is usually larger when computed with a RMF parameter set than when computed with a nonrelativistic force. These facts, and the noticed correlation between $L$ and $J/Q$, allow one to interpret in a qualitative way within the DM, the correlation pointed out in Refs. [37–40] between the slope of the symmetry energy at some subsaturation density $\rho \simeq 0.10$ fm$^{-3}$ and the neutron skin thickness in a heavy nucleus. In a recent work [51] we have investigated further the relations of the neutron skin thickness with the parameters $L$ and $K_{\rm sym}$ that characterize the density dependence of the symmetry energy around saturation.

## III. SURFACE WIDTH CONTRIBUTION TO THE NEUTRON SKIN THICKNESS

The neutron skin thickness values derived from measurements performed in antiprotonic atoms have been obtained in Refs. [48,49]. It is assumed that the neutron skin is due to an enhancement of the neutron surface width with respect to the proton surface width and that the mean location of the proton and neutron surfaces in these nuclei are the same. This situation corresponds to the so-called "neutron halo-type" distribution [48]. It has been shown that the same set of experimental values of neutron skin thickness can be explained with similar quality as in Ref. [48] by means of the "standard" version of the DM (where $b_n = b_p$) [28]. The latter case assumes that the peripheral neutrons are concentrated at the neutron surface, which is shifted with respect to the proton surface and that both the neutron and proton density distributions have the same surface width. This is rather the pattern of the so-called "neutron skin-type" distribution according to Ref. [48].

The analysis of neutron and proton densities calculated with nuclear mean-field interactions carried out in Ref. [32] by means of the Helm model points out that self-consistent mean-field densities show a mixed character between the "neutron halo" and "neutron skin" patterns. This means that, actually, the self-consistent neutron and proton density profiles obtained with nuclear effective interactions differ not only in the mean location of their surfaces but also in their surface widths. In the following we shall see that similar conclusions are found from the calculations of the neutron skin thickness performed in the DM with formula (2). It will turn out that the surface width contribution $\propto (b_n^2 - b_p^2)$ in the DM expression (2) for the neutron skin thickness, which arises from $b_n \neq b_p$, is necessary to reproduce the neutron skin thickness values calculated from the definition (1) using self-consistent densities of finite nuclei obtained with the ETF approach in mean-field theory, for nonrelativistic forces as well as for relativistic parametrizations.

In Fig. 2 we display by empty symbols, as a function of the overall relative neutron excess $I = (N - Z)/A$, the neutron

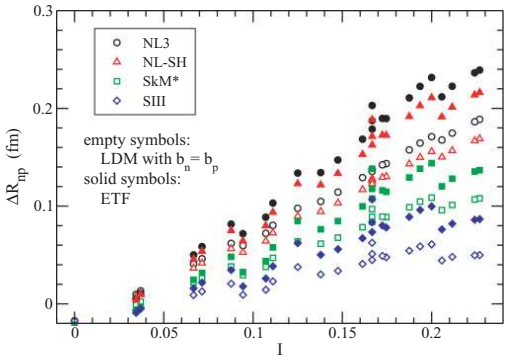


FIG. 2. (Color online) The neutron skin thickness predicted by the "standard" version of the DM [Eq. (2) with $b_n = b_p$] is compared with the result obtained from self-consistent ETF calculations of finite nuclei, in four illustrative mean-field parameter sets. The nuclei considered are those investigated experimentally with antiprotonic atoms in Refs. [48,49] and have masses $40 \leqslant A \leqslant 238$.

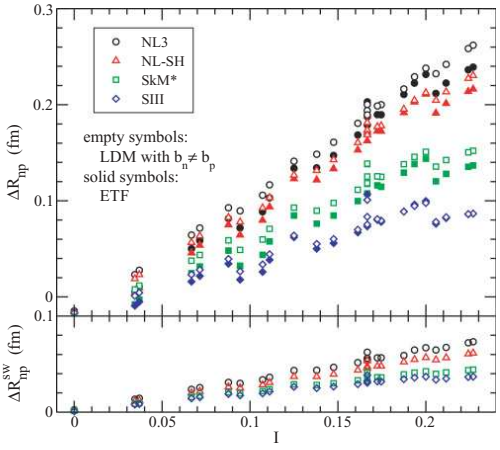


FIG. 3. (Color online) (Upper panel) The same as in Fig. (2) but here the DM values include a nonvanishing surface width contribution $\Delta R_{np}^{\rm sw}$ [Eq. (10)] with $b_n$ and $b_p$ obtained from ASINM calculations as described in the text. (Lower panel) The surface width contribution $\Delta R_{np}^{\rm sw}$ (the vertical scale proportionality is the same as in the upper panel).

skin thickness predicted by the "standard" version of the DM [namely Eq. (2) with $b_n = b_p$] using some well-known effective forces. The nuclei are those from $^{40}$Ca to $^{238}$U measured in the experiments with antiprotonic atoms [48,49], and that were studied with the DM in Ref. [28]. The values shown in Fig. 2 have been computed using the SIII and SkM* Skyrme forces and the NL-SH and NL3 RMF parameter sets, as suitable examples. We have chosen these four parameter sets for display in Fig. 2 because they span the whole range of values of the ratio $J/Q$ of nuclear interactions that describe reasonably well the ground-state properties of finite nuclei, having a bulk symmetry energy coefficient $J$ between 28 and 37 MeV (see Fig. 1 and Table I). The DM results for $\Delta R_{np}$ obtained with the other mean-field interactions considered in this work that have a $J$ coefficient between the values of SIII and NL3, also lie within the window of results delimited by the SIII and NL3 interactions in Fig. 2.

The values of $\Delta R_{np}$ predicted by the DM are compared in Fig. 2 with the values that we obtain from self-consistent ETF calculations in finite nuclei (filled symbols). Both models do not incorporate shell effects. In Fig. 2 we have used the ETF approach in the non-relativistic [54] and relativistic [55] frameworks to compute $\Delta R_{np}$. We have calculated these ETF values of $\Delta R_{np}$ by application of Eq. (1) with the rms radii of the self-consistent neutron and proton densities obtained in each isotope. From Fig. 2 two significant points stem. First, the predictions of the DM in the "standard" form ($b_n = b_p$) systematically undershoot the ETF neutron skin thickness computed in finite nuclei with the selected effective nuclear interactions. In particular, this trend is reinforced with growing neutron excess $I$. Second, it can be observed that for a given nucleus the difference between the ETF value of $\Delta R_{np}$ computed with (1) and the value provided by the "standard" DM prescription is slightly larger in the RMF parameter sets than in the Skyrme forces. Altogether, these facts suggest that in the mean-field interactions the surface width contribution to the DM formula for $\Delta R_{np}$ does not vanish and that this contribution has some dependence on the ratio $J/Q$ of the force.

To apply the full Eq. (2) to compute the neutron skin thickness including the surface width correction, one needs to evaluate the neutron and proton surface widths in finite nuclei. In practice, there is not conclusive experimental evidence on the difference of the surface widths $b_n$ and $b_p$ of the nuclear density distributions [27,28,32,50,52]. To estimate $b_n^2 - b_p^2$ we will therefore rely on theoretical guidance as a surrogate. Within the context related to the DM and the leptodermous expansion of a finite nucleus [52,56,57], the surface properties in finite nuclei can be extracted from ASINM calculations. The semi-infinite geometry does not include shell, Coulomb, or finite-size effects. We will use here the ETF method including $\hbar^2$ corrections for describing ASINM, because the ETF method is free of the Friedel oscillations of the quantal densities [30,60]. We summarize in the Appendix the basic aspects of the procedure. More details can be found in Ref. [53]. From Eqs. (A1)–(A4) of the Appendix, we can obtain the values of the surface widths $b_n$ and $b_p$ in ASINM with a given relative neutron excess in the bulk $\delta_0$. In the DM, these surface widths correspond to the values $b_n$ and $b_p$ in finite nuclei if $\delta_0$ is calculated from the overall relative neutron excess $I$ of the nucleus through the following relation [52,53,56]:

$$\delta_0 = \frac{I + \frac{3}{8}\frac{c_1}{Q}\frac{Z^2}{A^{5/3}}}{1 + \frac{9}{4}\frac{J}{Q}A^{-1/3}}, \tag{9}$$

which takes into account the Coulomb correction.

Once the neutron and proton surface widths in finite nuclei are known, we can compute their contribution to the neutron

skin thickness, which reads [cf. Eq. (2)]

$$\Delta R_{np}^{\rm sw} = \sqrt{\frac{3}{5}}\frac{5}{2R}\left(b_n^2 - b_p^2\right). \tag{10}$$

The corresponding values of $\Delta R_{np}^{\rm sw}$ for the nuclei considered in Fig. 2 are displayed in the bottom panel of Fig. 3. It is worth pointing out that the calculated $\Delta R_{np}^{\rm sw}$ values show, for each nuclear interaction, a well-defined increasing linear trend as a function of the overall relative neutron excess $I$ of the nuclei.

The neutron skin thickness predictions of the DM when one includes the surface width contribution (2) are displayed in the top panel of Fig. 3 by empty symbols. Note that the results correspond to adding the values $\Delta R_{np}^{\rm sw}$ shown in the bottom panel of this figure to the DM values that we have displayed in Fig. 2. As done in Fig. 2, we compare in the top panel of Fig. 3 the DM results with the self-consistent ETF calculations of $\Delta R_{np}$ [54,55]. One now observes an improved and remarkable agreement between the DM predictions and the self-consistent ETF values computed with the same interaction, stemming from the inclusion of the calculated $\Delta R_{np}^{\rm sw}$ contribution. It is interesting to note that the neutron skin thickness obtained with Eq. (1) from the rms radii of the self-consistent ETF calculations in finite nuclei shows a well defined increasing linear tendency with the relative neutron excess $I$, similarly to the case of the results of the DM and in consonance with the trend of the experimental values derived from antiprotonic atoms [48].

The lower panel of Fig. 3 also suggests that, for a given nucleus, $\Delta R_{np}^{\rm sw}$ grows when the $J/Q$ ratio of the nuclear interaction increases (see Table I). To analyze this behavior in more detail, we fit $\Delta R_{np}^{\rm sw}$ by means of a law $\sigma^{\rm sw} I$, which defines the slope $\sigma^{\rm sw}$ of $\Delta R_{np}^{\rm sw}$ with respect to the relative neutron excess $I$. This slope is displayed in Fig. 4 as a function of the $J/Q$ ratio for different interactions. The slopes $\sigma^{\rm sw}$ lie inside a band limited by two straight lines, corresponding to the equations $\sigma^{\rm sw} = 0.3J/Q + 0.07$ fm (left) and $\sigma^{\rm sw} = 0.3J/Q - 0.05$ fm (right). Note that all considered Skyrme forces have slopes $\sigma^{\rm sw}$ below 0.25 fm, whereas the analyzed RMF models have slopes $\sigma^{\rm sw}$ always above this value.

One relevant conclusion is that bulk and finite nuclei properties described through successful theoretical mean-field models constrain the possible values of the surface width contribution to the neutron skin thickness between the limits portrayed in Fig. 4. From this figure it can be deduced that the surface width contribution to the neutron skin thickness $\Delta R_{np}^{\rm sw}$ has, on top of a global increasing trend with $J/Q$, a more involved dependence on the parameters of the effective nuclear interactions. For instance, on the one hand, the RMF force FSUGold and the Skyrme force SkM* have almost the same $J/Q$ ratio (see Table I). However, the predicted values of $\sigma^{\rm sw}$ are clearly different for both interactions as can be seen in Fig. 4. On the other hand, it is possible to find different interactions that have almost the same slope $\sigma^{\rm sw}$, and therefore the same $\Delta R_{np}^{\rm sw}$, but with different values of the $J/Q$ ratio. Some examples of this fact in Fig. 4 are the Skyrme forces SIII and SGII (with slopes of 0.16 and 0.15 fm, respectively) and the RMF parametrizations FSUGold and NL3 (with slopes 0.30 fm and 0.31 fm). These facts suggest that it is possible to find the same total neutron skin thickness by combining a small value of the $J/Q$ ratio in $t$ [see Eq. (3)] with a large $\Delta R_{np}^{\rm sw}$ contribution or, vice versa, by combining a large $J/Q$ ratio in $t$ with a small $\Delta R_{np}^{\rm sw}$ contribution.

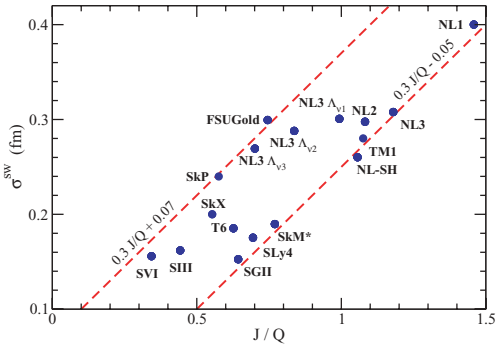


FIG. 4. (Color online) Average slope of $\Delta R_{np}^{\rm sw}$ with respect to $I$ for various nuclear mean-field models as a function of $J/Q$. All the data lie in the area limited by the marked lines $\sigma^{\rm sw} = 0.3J/Q + 0.07$ fm and $\sigma^{\rm sw} = 0.3J/Q - 0.05$.

## IV. ESTIMATES OF THE DENSITY CONTENT OF THE SYMMETRY ENERGY

As we have pointed out, the nuclear symmetry energy and the properties of the EOS of neutron-rich matter are of increasing importance in both nuclear physics and astrophysics. There is a significant recent effort in the community toward constraining the values of the parameters that characterize the density dependence of the symmetry energy in the subsaturation regime of the EOS. The new developments come in particular from the investigation of isospin-sensitive observables in intermediate-energy heavy-ion collisions [9–21] and in nuclear resonances [22–25]. Obviously, the different studies do not deal with exactly the same regimes of density and energy. One also has to keep in mind that the connection of the experiments with the EOS is not at all trivial; it often requires extrapolations of the measured data, which imply a model dependence. Therefore, it is important to further investigate indications from those and other experimental probes of the symmetry energy, with different methodologies, as well as to study the interplay between the constraints derived from the different analyses.

In the present section we want to apply the experience gained in the DM study of the neutron skin thickness performed in the previous sections to estimate possible constraints on the density dependence of the nuclear symmetry energy as suggested by neutron skin data. To this end, we shall first obtain the range of values of the $J/Q$ ratio that are compatible with the neutron skin thickness derived from the experimental data in antiprotonic atoms. We recall that this set of data for 26 stable nuclei is to date the largest set of uniformly measured neutron skins spanning the mass table. Once the estimated range of values for the ratio $J/Q$ will be found, the constraints derived from the neutron skin data on the DM parameter $L$,

related to the density derivative of the symmetry energy, will be determined from the existing linear correlation between the values of $L$ and $J/Q$. This correlation has been displayed in Fig. 1 and is a general feature of mean-field interactions that have been adjusted to reproduce with good accuracy binding energies and charge radii (often among other properties) of nuclei across the periodic table.

### A. Constraints on the $J/Q$ ratio

From the previous section we know that the surface width part in Eq. (2) gives a non-negligible contribution to neutron skins in effective nuclear interactions. This contribution is needed to reproduce the neutron skin thickness values computed self-consistently in ETF calculations of finite nuclei. We have also seen that to leading order, both the mean location of the neutron and proton surfaces (3) and the surface width correction (10) are basically driven by the value of the $J/Q$ ratio. The discussions in the previous sections suggest to fit the experimental $\Delta R_{np}^{\rm exp}$ data by means of the following DM inspired ansatz:

$$\Delta R_{np} = \sqrt{\frac{3}{5}}\left(t - \frac{e^2 Z}{70J}\right) + \left(0.3\frac{J}{Q} + c\right) I, \qquad (11)$$

where $t$ is given by Eq. (3). The second term is the surface width contribution. It is parameterized to reproduce the dashed lines on Fig. 4, with $c = -0.07$ fm or $c = -0.05$ fm.

With the ansatz (11), we will use $J/Q$ as an open parameter. It will be constrained by a least-squares minimization from the experimental values $\Delta R_{np}^{\rm exp}$ derived from the analysis of antiprotonic atoms [48,49]. We note that Eq. (11), as well as $t$ given by Eq. (3), depends on the particular values of the symmetry energy at saturation $J$ and of the nuclear matter radius $r_0$. We fix these quantities to the empirical values $J = 31.6$ MeV and $r_0 = 1.143$ fm (the latter corresponds to a saturation density $\rho_0 = 0.16$ fm$^{-3}$). We consider the values $c = 0.07$ fm and $c = -0.05$ fm in Eq. (11), discussed in connection with Fig. 4, to simulate the upper and lower bounds of the window of the theoretical predictions for $\sigma^{\rm sw}$ obtained according to mean-field models of nuclear structure. In the $\chi^2$ minimization we have weighted each $\Delta R_{np}^{\rm exp} - \Delta R_{np}$ difference by the inverse of the associated experimental uncertainties. That is, in practice we have minimized the quantity

$$\sum_i \left[\frac{\Delta R_{np}(i) - \Delta R_{np}^{\rm exp}(i)}{\xi_i}\right]^2, \qquad (12)$$

where $\Delta R_{np}$ is calculated with Eq. (11) and the $\xi_i$ denote the uncertainties of the experimental data.

The fits to experiment give $J/Q = 0.667 \pm 0.047$ with $c = 0.07$ fm and $J/Q = 0.791 \pm 0.049$ with $c = -0.05$ fm (i.e., a range $0.62 \lesssim J/Q \lesssim 0.84$). The quoted uncertainties in the $J/Q$ predictions correspond to the value of one standard deviation associated with the fit made through Eq. (12). To check our method of minimization and error estimation, we have applied the same procedure to make a linear fit $mI + n$ of the experimental data $\Delta R_{np}^{\rm exp}$. In this case we have obtained $\Delta R_{np} = (0.901 \pm 0.147)I + (-0.034 \pm 0.023)$ fm, which fully agrees with the result quoted by the experimentalists [48,49].

The results for $\Delta R_{np}$ from our fits compared with the experimental data $\Delta R_{np}^{\rm exp}$ are displayed as a function of $I$ in Fig. 5. Both extractions of $J/Q$, for $c = 0.07$ and $c = -0.05$ fm, predict basically the same total neutron skin thickness with a similar quality and they are close to the average $\Delta R_{np} = (0.90 \pm 0.15)I + (-0.03 \pm 0.02)$ fm [48,49] of the experimental data. However, the splitting of the neutron skin thickness into a part coming from the distance $t$ and another part coming from the surface width $\Delta R_{np}^{\rm sw}$ is different in both cases, as we have discussed in the previous section. Therefore, it becomes clear that the experimental neutron skin thickness data, by themselves, may be able to constrain the total value but not its partition into a bulk and a surface width contribution.

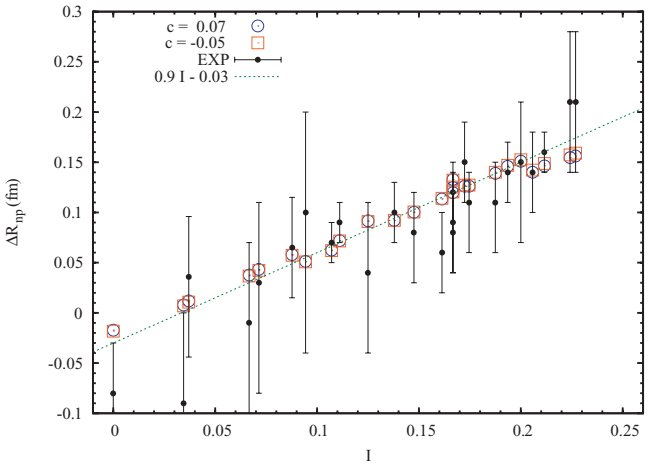


FIG. 5. (Color online) The values of $\Delta R_{np}$ obtained from Eq. (11) by fitting the $J/Q$ ratio, using $c = 0.07$ fm (circles) and $c = -0.05$ fm (squares) to reproduce the $\Delta R_{np}^{\rm exp}$ values measured in antiprotonic atoms (dots with error bars). The average value of $\Delta R_{np}^{\rm exp}$ is marked by the dotted line.

It is generally acknowledged that the value of the bulk nuclear symmetry energy coefficient $J$ is about 30–32 MeV, but there is some uncertainty. To assess the dependence of the extraction of $J/Q$ on the assumed value for the $J$ coefficient (which in the above we have taken as 31.6 MeV), we have repeated the fit of Eq. (11) to the neutron skin data for $J = 35$ MeV and for $J = 28$ MeV. The results are, respectively, $J/Q = 0.642 \pm 0.046$ and $J/Q = 0.701 \pm 0.048$ if $c = 0.07$ fm and $J/Q = 0.764 \pm 0.048$ and $J/Q = 0.829 \pm 0.051$ if $c = -0.05$ fm. All in all, it seems safe to consider that within the present model the $J/Q$ values compatible with the data from antiprotonic atoms span a window from about $J/Q = 0.59$ to $J/Q = 0.88$ or $0.6 \lesssim J/Q \lesssim 0.9$ in round figures.

We recall that the DM of nuclei does not incorporate shell effects and averages the corresponding quantal magnitudes. With the method described we have fitted $\Delta R_{np}^{\rm exp}$ that in general contains shell effects and possible correlation and deformation contributions. But, as mentioned, the neutron skin data analyzed show a well-defined linear trend with the relative neutron excess $I$ (namely $\Delta R_{np} = (0.90 \pm 0.15)I + (-0.03 \pm 0.02)$ fm [48,49]). This trend, and the agreement of the DM values for $\Delta R_{np}$ with the self-consistent ETF calculations in finite nuclei, which also are free of shell effects and have a linear trend with $I$ (Figs. 2 and 3), gives more reliability to the predictions obtained with the DM formula from the experimental data.

### B. Constraints on the $L$ parameter

As we have discussed previously, the parameter $L$ has a direct relation with the slope of the symmetry energy of the nuclear EOS, see Eq. (8). Having determined the values of the $J/Q$ ratio compatible with the experimental neutron skins measured in antiprotonic atoms, we can use the linear correlation between $L$ and $J/Q$ found in mean-field effective nuclear interactions to obtain an insight on the values of the parameter $L$ favored by neutron skins.

We have displayed the linear correlation $L = mJ/Q + n$ in the rightmost panel of Fig. 1 (the linear correlation coefficient for the shown interactions is $r = 0.978$). The values of the $m$ and $n$ coefficients have some dependence on the set of interactions chosen to make the linear regression. We have checked that this dependence is rather weak. Namely we have tested the correlation of $L$ with $J/Q$ by taking into account successively 10, 14, 18, and 24 interactions and we have found the linear regressions to be comprised between $L = 139J/Q - 52$ MeV and $L = 150J/Q - 57$ MeV. Considering these two limiting cases and the constraint $0.6 \lesssim J/Q \lesssim 0.9$ found in the previous section, leads to a variation of $L$ between 31 and 78 MeV. Thus, our estimate for the $L$ coefficient, which takes into account the surface width correction in $\Delta R_{np}$ obtained in the calculations with mean-field interactions, basically lies in the range $30 \lesssim L \lesssim 80$ MeV. Had we kept the value of $J$ fixed at 31.6 MeV, the extracted range for $L$ would be a little narrower: $35 \lesssim L \lesssim 70$ MeV.

In a previous work [51] we have investigated the correlations between the symmetry energy coefficient in finite nuclei and in the EOS at subsaturation densities. These correlations allow one to derive an aproximate formula for the neutron skin thickness with explicit dependence on the $L$ coefficient. By comparison of that result for the neutron skin thickness with the experimental data set of Refs. [48,49], in Ref. [51] we found a range of values $L = 55 \pm 25$ MeV (displayed in Fig. 3 of Ref. [51]) when one includes the surface width contribution $\Delta R_{np}^{\rm sw}$ in the calculations. That prediction is consistent with the values obtained here by the present procedure. A somewhat higher range $L = 75 \pm 25$ MeV was obtained [51] when one neglects $\Delta R_{np}^{\rm sw}$. Although a vanishing $\Delta R_{np}^{\rm sw}$ value, corresponding to $b_n = b_p$ in the nucleon density distributions, is not favored by the mean-field interactions (see Sec. III), it cannot be discarded without having more experimental evidence on the value of $b_n$ as we have noted in Sec. III (see also Refs. [28,48]).

In recent years, considerable advances in probing experimentally the density dependence of the symmetry energy at subsaturation have been achieved in heavy-ion collisions (HIC) at intermediate energies. It has been found that the symmetry energy can be modelized around the saturation density with reasonable good approximation by [11–20]

$$c_{\rm sym}(\rho) = J\left(\frac{\rho}{\rho_0}\right)^{\gamma}. \tag{13}$$

From Eq. (13), one can estimate the parameter $L$ defined in Eq. (6) from the stiffness $\gamma$ of the symmetry energy, as $L = 3\gamma J$. The values for $\gamma$ extracted in the literature from different HIC observables fall in the range $\gamma \sim 0.55$–$1.05$, which implies $L$ values roughly between 50 and 100 MeV. In these studies, the value of $J$ in Eq. (13) normally has been taken equal to 31.6 or 32 MeV. The extraction of the equation of state of cold nuclear matter from HIC data is a very complicated task and requires model assumptions [9–21,64–66]; the indicated estimates for $\gamma$ and $L$ may be somewhat modified as more measurements and analyses be performed. The range $30 \lesssim L \lesssim 80$ MeV of $L$ values determined here from neutron skins, assuming the dependence of Eq. (13), favors a constraint $0.32 \lesssim \gamma \lesssim 0.84$ for the $\gamma$ exponent. Thus, the result points toward a soft symmetry energy.

Our estimates for the stiffness $\gamma$ can be compared with alternative predictions derived in the recent literature. For instance, our range $0.32 \lesssim \gamma \lesssim 0.84$ overlaps with the values $\gamma \sim 0.55$–$0.77$ that Danielewicz [29] obtains from the study of binding energies, neutron skins, and isospin analog states of selected nuclei. It also contains the value $\gamma \sim 0.55$ that is inferred from the analysis of neutron-proton emission ratios in HIC carried out by Famiano *et al.* [20], as well as with the value $\gamma \sim 0.69$ obtained by Shetty *et al.* [17–19] from isotopic scaling in intermediate-energy nuclear reactions.

The stiffness of the symmetry energy at subsaturation densities also has been investigated from isospin diffusion data in HIC, by means of simulations with an isospin- and momentum-dependent transport model with in-medium nucleon-nucleon cross sections [12–16]. In this case the prediction is $0.69 \lesssim \gamma \lesssim 1.05$. It corresponds to a behavior of $c_{\rm sym}(\rho)$ that nearly ranges between the familiar $\rho^{2/3}$ dependence of the purely kinetic symmetry energy of a free Fermi gas, in the lower limit, and linearity in the density

$\rho$, in the upper limit. The constraints on the stiffness of the symmetry energy derived from isospin diffusion, combined with an analysis of the properties of Skyrme interactions, are found to lead to a constraint $63 \lesssim L \lesssim 113$ MeV [12–16]. The predictions from isospin diffusion are thus a little stiffer, though the lower limits of $\gamma$ and $L$ obtained using this method are in agreement with the upper limits of $\gamma$ and $L$ obtained from our study of neutron skins with inclusion of the surface width contribution.

Another valuable reference comes from the celebrated Thomas-Fermi model of Myers and Świątecki [67,68]. This model was fitted very precisely to the binding energies of a comprehensive set of 1654 nuclei. It predicts an EOS that leads to a coefficient $L = 49.9$ MeV. Note that if we compare $c_{\rm sym}(\rho)$ calculated from the EOS of the Thomas-Fermi model with Eq. (13), an exponent $\gamma = 0.51$ is obtained. Additional information on the density content of the symmetry energy arises from the constraints on the symmetry pressure $P_{\rm sym} = \rho_0 L/3$ extracted by Klimkiewicz *et al.* [24] from the properties of pygmy dipole resonances in nuclei. These are indicative of a value $\gamma \sim 0.35$–$0.65$ if one assumes $P_{\rm sym} = \rho_0 \gamma J$ following from Eq. (13) given above. Trippa *et al.* [25] have obtained the constraint $23.3 < c_{\rm sym}(\rho = 0.1\ {\rm fm}^{-3}) < 24.9$ MeV from consideration of the giant dipole resonance in $^{208}$Pb, which implies a range $\sim 0.5$–$0.65$ for the $\gamma$ exponent. We depict in Fig. 6 the estimated ranges of values for the $L$ parameter from the discussed analyses.

In summary, in spite of the discrepancies in the details, the various findings from experimental isospin-sensitive signals, including ours, all agree on a rather soft nuclear symmetry energy at subsaturation densities. Recent studies of pure neutron matter at low densities based on universal properties of dilute Fermi gases lead to a similar conclusion [69,70]. One may mention that there exists recent circumstantial evidence [71], derived from $\pi^-/\pi^+$ ratios in central HIC collisions at SIS/GSI energies, hinting at that the nuclear symmetry energy is soft also in the region of suprasaturation densities ($\rho \geqslant 2\rho_0$). However, further experimental and theoretical confirmations of this fact need to be done [71].

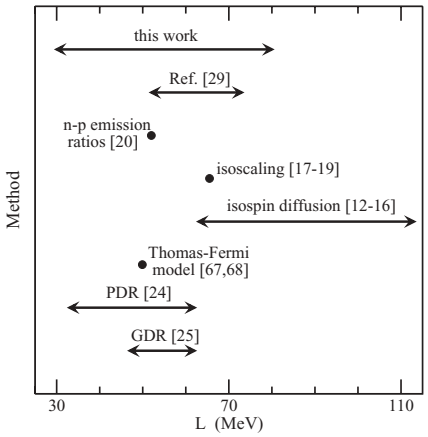


FIG. 6. Comparison of the estimated values of the parameter $L$ from different observables and methods. Some of the estimates have been analyzed through Eq. (13) for $c_{\rm sym}(\rho)$.

## V. SUMMARY AND CONCLUSIONS

The droplet model predicts that the neutron skin thickness of atomic nuclei is correlated with the ratio $J/Q$, where $J$ is the symmetry energy in bulk matter and $Q$ is the surface stiffness coefficient. We have shown that the $J/Q$ ratio displays a linear relationship with the DM parameter $L$ in nuclear mean-field models that are calibrated to experimental ground-state properties such as binding energies, charge radii, and single-particle data. In this way, the known correlation between the neutron skin thickness in a heavy nucleus and the density derivative of the symmetry energy (or of the neutron equation of state) evaluated at a subsaturation density, can be interpreted in the context of the DM.

According to the droplet model, the neutron skin thickness is correlated with the overall relative neutron excess $I = (N - Z)/A$ of nuclei. This fact is in agreement with the experimental findings using information from antiprotonic atoms. The DM expression for the neutron skin thickness contains "bulk" and "surface" parts. The bulk part corresponds to the contribution proportional to the distance $t$ between the neutron and proton mean surface locations. This part is quite dependent on the Skyrme force or RMF parametrization used to compute it (see Fig. 2). In finite nuclei, this DM bulk contribution systematically underestimates the neutron skin thickness extracted directly as the difference of the neutron and proton rms radii of the nucleus from self-consistent ETF calculations with effective forces. This evidence indicates that the surface part, due to the $b_n \neq b_p$ contribution, is necessary in the DM formula to properly estimate the neutron skin thickness in finite nuclei in mean-field models using effective nuclear interactions.

The DM surface contribution $\Delta R_{np}^{\rm sw}$ to the neutron skin thickness is smaller than the bulk part and shows a well-defined linear increasing tendency with the overall relative neutron excess $I$. We have investigated the dependence of the slope $\sigma^{\rm sw}$ with respect to $I$ of this surface contribution using various Skyrme and RMF forces. We have found that the slopes $\sigma^{\rm sw}$ lie in a region of the $\sigma^{\rm sw}$–$J/Q$ plane that can be roughly limited by two straight lines as a function of the $J/Q$ value. It implies that nuclear properties, which are included in the calibration of the free parameters of the Skyrme and RMF interactions, constrain the possible values of the surface width contribution to the neutron skin thickness in the DM. If the same nuclear interaction is used, a good agreement between both the DM formula and the self-consistent ETF calculations of $\Delta R_{np}$ in finite nuclei is found along the whole periodic table when the contribution $\Delta R_{np}^{\rm sw}$ is included in the DM.

To analyze possible bounds suggested by experimental neutron skin data on the value of the $J/Q$ ratio, we have adjusted the DM neutron skin thickness formula to the neutron skin sizes measured in antiprotonic atoms [48,49]. We have determined a window $0.6 \lesssim J/Q \lesssim 0.9$ for the $J/Q$

ratio by using the largest and smallest surface contributions $\Delta R_{np}^{\rm sw}$ obtained from successful Skyrme forces and RMF parametrizations. These two fits reproduce the experimental data with almost the same quality. In other words, the experimental data of the neutron skin thickness in finite nuclei constrain the total theoretical estimate but not its partition into a bulk and a surface contribution. Once the window of $J/Q$ values is known, the compatible range of values of the parameter $L$ can be estimated from the linear correlation between $L$ and $J/Q$ shown in Fig. 1. From our analysis we find the constraints $30 \lesssim L \lesssim 80$ MeV.

If a model symmetry energy $c_{\rm sym}(\rho) = J(\rho/\rho_0)^\gamma$ is assumed, a prediction for the value of the stiffness $\gamma$ of the symmetry energy can be obtained, with use of the empirical values of $J$ and $\rho_0$. In this way we find the estimate $0.32 \lesssim \gamma \lesssim 0.84$. Thus, our analysis of the experimental neutron skins deduced from antiprotonic atoms suggests a relatively soft symmetry energy, in good accord with the recent indications from pygmy [24] and giant [25] dipole resonances. Our prediction for the stiffness $\gamma$ of the symmetry energy also is in reasonable agreement with the constraints derived by Danielewicz [29], by Famiano *et al.* [20], and by Shetty *et al.* [19] using different observables, as well as with the value $\gamma = 0.51$ of the EOS of the Thomas-Fermi model of Myers and Świątecki [67,68]. In the upper limit, our prediction overlaps with the lower limit provided by the analysis of isospin diffusion data in intermediate-energy heavy-ion collisions [12–16].

In summary, different techniques of extracting the parameters that describe the density dependence of the symmetry energy predict different values. However, taking the average of the central values of the predictions displayed in Fig. 6, with account of their uncertainties when available, there exist narrow windows of the parameters $L \sim 45$–$75$ MeV and $\gamma \sim 0.5$–$0.8$ which are, actually, compatible with all the different methods mentioned to obtain them. These ranges of values of the indicated parameters for describing the leading density dependence of the symmetry energy in bulk matter seem to be the "optimal" ones according to present experimental evidence from nuclear data.

To conclude, we are aware that the neutron skin thickness data derived from antiprotonic atoms are to some extent model dependent and have for some nuclei large error bars. Also, our theoretical method represents just an average approximation. In spite of these limitations, we hope to have shown that from neutron skin data it is possible to make a reasonable estimate of the density dependence of the symmetry energy with uncertainties that are not significantly much larger than those currently obtained from other experimental observables. One expects that future data from the planned parity-violating electron scattering experiment for measuring the neutron radius in $^{208}$Pb [2] will contribute to narrow down the constraints derived here from the thickness of neutron skins of nuclei.

## ACKNOWLEDGMENTS

The authors are very grateful to W. J. Świątecki for valuable discussions during the XIV Nuclear Physics Workshop held in Kazimierz-Dolny (Poland). Helpful correspondence with A. Trzcińska is gratefully acknowledged. Work partially supported by Grant Nos. FIS2005-03142 and FIS2008-01661 from MEC (Spain) and FEDER, No. 2009SGR-1289 from Generalitat de Catalunya, and by the Spanish Consolider-Ingenio 2010 Programme CPAN CSD2007-00042. X.R. also was supported by grant AP2005-4751 from MEC (Spain). M.W. gratefully acknowledges the warm hospitality extended to him by the Nuclear Theory Group and the Departament d'Estructura i Constituents de la Matèria at the University of Barcelona during his stay in Barcelona.

## APPENDIX

To compute the surface stiffness coefficient $Q$ and also the neutron and proton surface widths $b_n$ and $b_p$ that appear in the contribution $\Delta R_{np}^{\rm sw}$ of Eq. (10) to the neutron skin thickness, we obtain the self-consistent neutron and proton density profiles in asymmetric semi-infinite nuclear matter (ASINM). To do that we consider a semi-infinite slab with a plane interface separating a mixture of protons and neutrons at the left, whose densities decrease smoothly to zero at the right as empty space is reached. The axis perpendicular to the interface is taken to be the $z$ axis. Thus, the relative neutron excess $\delta = (\rho_n - \rho_p)/(\rho_n + \rho_p)$ depends locally on the $z$ coordinate. When $z$ goes to minus infinity, the neutron and proton densities approach the values of asymmetric uniform nuclear matter in equilibrium, corresponding to an interior bulk neutron excess $\delta_0$.

To obtain the proton and neutron densities in ASINM one has to minimize the total energy per unit area with respect to arbitrary variations of the densities, with the constraint of conservation of the number of protons and neutrons. When $\delta_0$ is not very large, so that occurrence of drip nucleons does not take place (which is the situation in all cases considered in the present work), the constrained energy per unit area reads [53,59,72]

$$\frac{E}{S} = \int_{-\infty}^{\infty} [\varepsilon(z) - \mu_n \rho_n(z) - \mu_p \rho_p(z)] dz. \qquad \text{(A1)}$$

In this equation, $\varepsilon(z)$ represents the energy density functional of the nuclear effective interaction under investigation, and $\mu_n$ and $\mu_p$ are the neutron and proton chemical potentials. The explicit expressions of $\varepsilon(z)$ in the extended Thomas-Fermi (ETF) method for Skyrme forces and relativistic mean-field interactions can be found in, e.g., Appendix A of Ref. [53]. The proton and neutron densities obey the coupled local Euler-Lagrange equations

$$\frac{\delta\varepsilon(z)}{\delta\rho_n} - \mu_n = 0, \qquad \frac{\delta\varepsilon(z)}{\delta\rho_p} - \mu_p = 0. \qquad \text{(A2)}$$

We solve them fully self-consistently by numerical iteration [54]. We note in this respect that we have not used any parameterized form of the densities such as, e.g., Fermi shapes. In the relativistic model the variational equations (A2) are supplemented with additional field equations for the meson fields; the calculational details for the relativistic problem can be found in Refs. [53–55].

From the calculated density profiles, one obtains the mean locations of the surfaces, $z_{0q}$ ($q = n, p$), as

$$z_{oq} = \frac{\int_{-\infty}^{\infty} z\rho_q'(z)dz}{\int_{-\infty}^{\infty} \rho_q'(z)dz}, \tag{A3}$$

where the primes indicate a derivative with respect to the $z$ coordinate. The proton and neutron surface widths in ASINM are obtained as the second moment of $\rho'(z)$:

$$b_q^2 = \frac{\int_{-\infty}^{\infty}(z - z_{0q})^2\rho_q'(z)dz}{\int_{-\infty}^{\infty} \rho_q'(z)dz}. \tag{A4}$$

The distance $t = z_{0n} - z_{0p}$ between the mean surface locations of the neutron and proton density profiles allows one to extract the surface stiffness coefficient $Q$ from the relation [56]

$$t = z_{0n} - z_{0p} = \frac{3r_0}{2}\frac{J}{Q}\delta_0, \tag{A5}$$

which is valid in the limit of small asymmetries. For each given nuclear interaction we solve the ASINM problem for five different values of $\delta_0$, between 0.005 and 0.025, and we then evaluate $Q$ from the slope of $t$.

There exists a second way of computing $Q$. It is based on the fact that in dividing the energy in bulk and surface parts, as soon as $\delta_0 \neq 0$, there are two possibilities to define the bulk reference energy [53,72]. One definition is based on the chemical potentials $\mu_n$ and $\mu_p$ of each nucleon species; this definition is thermodynamically consistent and it is the one that we have given in Eq. (A1). The second definition of the reference energy is based on taking the value of the energy per particle in bulk asymmetric nuclear matter. Accordingly, on the bulk reference energy chosen, there exist two forms of the surface energy in ASINM, which are called $E_{\mathrm{surf},\mu}$ and $E_{\mathrm{surf,e}}$ [53,72]. In the small asymmetry limit, it can be shown that the difference between these two quantities behaves as

$$E_{\mathrm{surf,e}} - E_{\mathrm{surf},\mu} = \frac{9J^2}{2Q}\delta_0^2. \tag{A6}$$

Thus, the slope of $E_{\mathrm{surf,e}} - E_{\mathrm{surf},\mu}$ with respect to $\delta_0^2$ provides another means to extract the value of the surface stiffness coefficient $Q$. We have computed $Q$ from Eq. (A5) and have used Eq. (A6) to confirm the validity of our calculated values.


[1] I. Angeli, At. Data Nucl. Data Tables **87**, 185 (2004).
[2] R. Michaels, P. A. Souder, and G. M. Urciuoli, Jefferson Laboratory Experiment E06002, http://hallaweb.jlab.org/parity/prex.
[3] J. M. Lattimer and M. Prakash, Science **304**, 536 (2004); Phys. Rep. **442**, 109 (2007).
[4] H. Heiselberg and M. Hjorth-Jensen, Phys. Rep. **328**, 237 (2000).
[5] A. W. Steiner, M. Prakash, J. M. Lattimer, and P. J. Ellis, Phys. Rep. **411**, 325 (2005).
[6] T. Sil, M. Centelles, X. Viñas, and J. Piekarewicz, Phys. Rev. C **71**, 045502 (2005), and references therein.
[7] P. Jofré, A. Reisenegger, and R. Fernández, Phys. Rev. Lett. **97**, 131102 (2006); P. G. Krastev and Bao-An Li, Phys. Rev. C **76**, 055804 (2007).
[8] Dao T. Khoa, W. von Oertzen, and A. A. Ogloblin, Nucl. Phys. **A602**, 98 (1996).
[9] T. Gaitanos, M. Di Toro, S. Typel, V. Baran, C. Fuchs, V. Greco, and H. H. Wolter, Nucl. Phys. **A732**, 24 (2004).
[10] V. Baran, M. Colonna, V. Greco, and M. Di Toro, Phys. Rep. **410**, 335 (2005).
[11] M. B. Tsang *et al.*, Phys. Rev. Lett. **92**, 062701 (2004).
[12] A. W. Steiner and B. A. Li, Phys. Rev. C **72**, 041601(R) (2005).
[13] L. W. Chen, C. M. Ko, and B. A. Li, Phys. Rev. Lett. **94**, 032701 (2005).
[14] L. W. Chen, C. M. Ko, and B. A. Li, Phys. Rev. C **72**, 064309 (2005).
[15] L. W. Chen, C. M. Ko, and B. A. Li, Phys. Rev. C **76**, 054316 (2007).
[16] B. A. Li, L. W. Chen, and C. M. Ko, Phys. Rep. **464**, 113 (2008).
[17] G. A. Souliotis, D. V. Shetty, A. Keksis, E. Bell, M. Jandel, M. Veselsky, and S. J. Yennello, Phys. Rev. C **73**, 024606 (2006).
[18] D. V. Shetty, S. J. Yennello, and G. A. Souliotis, Phys. Rev. C **75**, 034602 (2007).
[19] D. V. Shetty, S. J. Yennello, and G. A. Souliotis, Phys. Rev. C **76**, 024606 (2007).
[20] M. A. Famiano *et al.*, Phys. Rev. Lett. **97**, 052701 (2006).
[21] M. B. Tsang, Y. Zhang, P. Danielewicz, M. Famiano, Z. Li, W. G. Lynch, and A. W. Steiner, Phys. Rev. Lett. **102**, 122701 (2009).
[22] J. Piekarewicz, Phys. Rev. C **66**, 034305 (2002); **69**, 041301(R) (2004).
[23] T. Li *et al.*, Phys. Rev. Lett. **99**, 162503 (2007).
[24] A. Klimkiewicz *et al.*, Phys. Rev. C **76**, 051603(R) (2007).
[25] L. Trippa, G. Colò, and E. Vigezzi, Phys. Rev. C **77**, 061304(R) (2008).
[26] H. Liang, N. Van Giai, and J. Meng, Phys. Rev. Lett. **101**, 122502 (2008).
[27] W. D. Myers and W. J. Świątecki, Nucl. Phys. **A336**, 267 (1980).
[28] W. J. Świątecki, A. Trzcińska, and J. Jastrzębski, Phys. Rev. C **71**, 047301 (2005).
[29] P. Danielewicz, Nucl. Phys. **A727**, 233 (2003).
[30] P. Danielewicz and J. Lee, Nucl. Phys. **A818**, 36 (2009).
[31] C. J. Pethick and D. G. Ravenhall, Nucl. Phys. **A606**, 173 (1996).
[32] S. Mizutori, J. Dobaczewski, G. A. Lalazissis, W. Nazarewicz, and P.-G. Reinhard, Phys. Rev. C **61**, 044326 (2000).
[33] R. J. Furnstahl, Nucl. Phys. **A706**, 85 (2002).
[34] J. Treiner and H. Krivine, Ann. Phys. **170**, 406 (1986).
[35] M. Warda, B. Nerlo-Pomorska, and K. Pomorski, Nucl. Phys. **A635**, 484 (1998).
[36] A. E. L. Dieperink, Y. Dewulf, D. Van Neck, M. Waroquier, and V. Rodin, Phys. Rev. C **68**, 064307 (2003).
[37] B. A. Brown, Phys. Rev. Lett. **85**, 5296 (2000).
[38] S. Typel and B. A. Brown, Phys. Rev. C **64**, 027302 (2001).
[39] M. Centelles, M. Del Estal, X. Viñas, and S. K. Patra, in *The Nuclear Many-Body Problem 2001*, Vol. 53 of NATO Advanced Studies Institute Series B: Physics, edited by W. Nazarewicz and D. Vretenar (Kluwer, Dordrecht, 2002), p. 97.
[40] M. Baldo, C. Maieron, P. Schuck, and X. Viñas, Nucl. Phys. **A736**, 241 (2004).
[41] S. S. Avancini, J. R. Marinelli, D. P. Menezes, M. M. W. Moraes, and C. Providência, Phys. Rev. C **75**, 055805 (2007).

[42] L. Ray, G. W. Hoffmann, G. S. Blanpied, W. R. Coker, and R. P. Liljestrand, Phys. Rev. C **18**, 1756 (1978); L. Ray and G. W. Hoffmann, Phys. Rev. C **31**, 538 (1985).
[43] V. E. Starodubsky and N. M. Hintz, Phys. Rev. C **49**, 2118 (1994).
[44] S. Karataglidis, K. Amos, B. A. Brown, and P. K. Deb, Phys. Rev. C **65**, 044306 (2002).
[45] B. C. Clark, L. J. Kerr, and S. Hama, Phys. Rev. C **67**, 054605 (2003).
[46] A. Krasznahorkay *et al.*, Phys. Rev. Lett. **82**, 3216 (1999).
[47] A. Krasznahorkay *et al.*, Nucl. Phys. **A731**, 224 (2004).
[48] A. Trzcińska, J. Jastrzębski, P. Lubiński, F. J. Hartmann, R. Schmidt, T. von Egidy, and B. Kłos, Phys. Rev. Lett. **87**, 082501 (2001).
[49] J. Jastrzębski, A. Trzcińska, P. Lubiński, B. Kłos, F. J. Hartmann, T. von Egidy, and S. Wycech, Int. J. Mod. Phys. E **13**, 343 (2004).
[50] B. Kłos *et al.*, Phys. Rev. C **76**, 014311 (2007).
[51] M. Centelles, X. Roca-Maza, X. Viñas, and M. Warda, Phys. Rev. Lett. **102**, 122502 (2009).
[52] M. Brack, C. Guet, and H.-B. Håkansson, Phys. Rep. **123**, 275 (1985).
[53] M. Centelles, M. Del Estal, and X. Viñas, Nucl. Phys. **A635**, 193 (1998).
[54] M. Centelles, M. Pi, X. Viñas, F. Garcias, and M. Barranco, Nucl. Phys. **A510**, 397 (1990).
[55] M. Centelles, X. Viñas, M. Barranco, and P. Schuck, Ann. Phys. (NY) **221**, 165 (1993).
[56] W. D. Myers and W. J. Świątecki, Ann. Phys. (NY) **55**, 395 (1969); **84**, 186 (1974).
[57] W. D. Myers, *Droplet Model of Atomic Nuclei* (Plenum, New York, 1977).
[58] M. Farine, J. M. Pearson, and B. Rouben, Nucl. Phys. **A304**, 317 (1978); M. Farine, J. Côté, and J. M. Pearson, *ibid.* **A338**, 86 (1980); Phys. Rev. C **24**, 303 (1981).
[59] K. Kolehmainen, M. Prakash, J. M. Lattimer, and J. Treiner, Nucl. Phys. **439**, 535 (1985).
[60] M. Centelles and X. Viñas, Nucl. Phys. **A563**, 173 (1993).
[61] J. Piekarewicz and M. Centelles, Phys. Rev. C **79**, 054311 (2009).
[62] M. Lopez-Quelle, S. Marcos, R. Niembro, A. Bouyssy, and Nguyen Van Giai, Nucl. Phys. **A483**, 479 (1988).
[63] I. Bednarek and R. Manka, J. Phys. G **36**, 095201 (2009).
[64] S. Kowalski *et al.*, Phys. Rev. C **75**, 014601 (2007).
[65] S. K. Samaddar, J. N. De, X. Viñas, and M. Centelles, Phys. Rev. C **76**, 041602(R) (2007); **78**, 034607 (2008).
[66] S. R. Souza, M. B. Tsang, R. Donangelo, W. G. Lynch, and A. W. Steiner, Phys. Rev. C **78**, 014605 (2008).
[67] W. D. Myers and W. J. Świątecki, Nucl. Phys. **A601**, 141 (1996).
[68] W. D. Myers and W. J. Świątecki, Phys. Rev. C **57**, 3020 (1998).
[69] A. Schwenk and C. J. Pethick, Phys. Rev. Lett. **95**, 160401 (2005).
[70] J. Piekarewicz, Phys. Rev. C **76**, 064310 (2007).
[71] Z. Xiao, B. A. Li, L. W. Chen, G. C. Yong, and M. Zhang, Phys. Rev. Lett. **102**, 062502 (2009).
[72] W. D. Myers, W. J. Świątecki, and C. S. Wong, Nucl. Phys. **A436**, 185 (1985).

# 1.4 Analysis of bulk and surface contributions in the neutron skin of nuclei

CQ10223 PRC May 17, 2010 10:58

PHYSICAL REVIEW C **00**, 004300 (2010)

## Analysis of bulk and surface contributions in the neutron skin of nuclei

M. Warda,[1,2,*] X. Viñas,[1,†] X. Roca-Maza,[1,‡] and M. Centelles[1,§]

[1]*Departament d'Estructura i Constituents de la Matèria and Institut de Ciències del Cosmos, Facultat de Física, Universitat de Barcelona, Diagonal 647, E-08028 Barcelona, Spain*

[2]*Katedra Fizyki Teoretycznej, Uniwersytet Marii Curie–Skłodowskiej, ul. Radziszewskiego 10, PL-20031 Lublin, Poland*

(Received 26 March 2010; published xxxxx)

The neutron skin thickness of nuclei is a sensitive probe of the nuclear symmetry energy and has multiple implications for nuclear and astrophysical studies. However, precision measurements of this observable are difficult to obtain. The analysis of the experimental data may imply some assumptions about the bulk or surface nature of the formation of the neutron skin. Here we study the bulk or surface character of neutron skins of nuclei following from calculations with Gogny, Skyrme, and covariant nuclear mean-field interactions. These interactions are successful in describing nuclear charge radii and binding energies but predict different values for neutron skins. We perform the study by fitting two-parameter Fermi distributions to the calculated self-consistent neutron and proton densities. We note that the equivalent sharp radius is a more suitable reference quantity than the half-density radius parameter of the Fermi distributions to discern between the bulk and surface contributions in neutron skins. We present calculations for nuclei in the stability valley and for the isotopic chains of Sn and Pb.

DOI: 10.1103/PhysRevC.00.004300 PACS number(s): 21.10.Gv, 36.10.Gv, 21.60.−n, 21.30.Fe

### I. INTRODUCTION

The description of the sizes and shapes of atomic nuclei is among the oldest problems in nuclear physics. The rms radius of the charge distribution in nuclei surely is the most prominent example of this kind of observable. Owing to the high degree of accuracy achieved by the elastic electron-nucleus and muon-nucleus scattering experiments, the nuclear charge radius is nowadays known with uncertainties that are for many nuclei smaller than 1% [1,2]. In contrast, our knowledge about the neutron distribution and its rms radius in nuclei is not so precise. Actually, accurate determinations of the rms radius of the neutron density are still lacking. This implies that the so-called neutron skin thickness, generally defined as the neutron-proton rms radius difference in the atomic nucleus,

$$\Delta R_{np} = \langle r^2 \rangle_n^{1/2} - \langle r^2 \rangle_p^{1/2}, \tag{1}$$

is not precisely known either.

The neutron skin thickness observable, Eq. (1), is a very sensitive probe of the pressure difference that exists between neutrons and protons in the atomic nucleus. As such, $\Delta R_{np}$ is intimately correlated with the density dependence of the nuclear symmetry energy and with the equation of state of pure neutron matter [3–12]. Owing to this fact, the accurate calibration of $\Delta R_{np}$ is a problem of significant implications for studies that embrace diverse facets of both nuclear physics and nuclear astrophysics (see, for example, Refs. [13–23]). It should be mentioned that Eq. (1) is not the only useful prescription to characterize the different spatial extension of the neutron and proton densities in a nucleus. The neutron-proton radius difference has also been computed using Helm radii instead of rms radii for the discussion of nuclear halos in the literature [24,25]. Nevertheless, in the present work we use the conventional and more frequent definition for $\Delta R_{np}$, Eq. (1).

Because neutrons are uncharged particles, the measurement of their spatial distribution in the nucleus is more difficult than for the positively charged protons (see, e.g., Ref. [26]). The experimental access to neutron densities and neutron rms radii usually involves strongly interacting hadronic probes, for example, in the case of experiments that perform proton-nucleus elastic scattering [27–31], $\alpha$-particle elastic scattering [32], and techniques based on the inelastic scattering excitation of the giant dipole and spin-dipole resonances [33,34]. The neutron skin thickness of nuclei has also been investigated through radiochemical and x-ray techniques in antiprotonic atoms [35–40], taking advantage of the fact that the nuclear periphery is very sensitive to antiprotons in the normally electronic shell. Although the scope of our analysis of neutron skins is theoretical, in this article we refer to some extent to the experimental investigations in antiprotonic atoms to set the stage for our calculations.

A few years ago, Trzcińska *et al.* [38,39] extracted the neutron skin thickness of a large set of nuclei in experiments with antiprotons conducted at the former LEAR facility of CERN. The measurements were made for 26 stable isotopes distributed across the mass table, from the light and symmetric nucleus $^{40}$Ca to the heavy and asymmetric nucleus $^{238}$U. Because of the fact that the antiproton-nucleon interaction is very strong, antiprotons are able to interact with the atomic nucleus at distances where the nuclear density is much smaller than its central value. Slow enough antiprotons can form a hydrogen-like atom with the nucleus. When the antiproton

*warda@kft.umcs.lublin.pl
†xavier@ecm.ub.es
‡roca@ecm.ub.es
§mariocentelles@ub.edu

 

CQ10223 PRC May 17, 2010 10:58



annihilates with a nucleon, producing pions that may miss the nucleus, it leaves a residue that is one neutron or proton fewer. From the analysis of these yields, information about the neutron distribution in the nucleus can be obtained [35–39]. A second experimental method measures antiprotonic x rays from where the atomic level widths and shifts owing to the strong interaction are determined [38–40]. By combining the results obtained with these two experimental techniques, the neutron-proton rms difference $\Delta R_{np}$ can be deduced provided that the charge density of the nucleus is known [38–40].

The extraction of $\Delta R_{np}$ values from antiprotonic atoms assumes nucleon densities in the form of two-parameter Fermi (2pF) distributions. The procedure involves interpreting whether the difference between the peripheral neutron and proton densities arises from an increase of the mean location of the surface of the neutron density (i.e., from an increase of the bulk radius of neutrons) or, rather, from an increase of the surface diffuseness of the neutron density. This question is also instrumental in studies of properties of nuclei by parity-violating electron scattering [41]. The radiochemical data in antiprotonic atoms were shown to be in favor of interpreting $\Delta R_{np}$ as an increase of the neutron surface diffuseness [38,39] but with the caveat that some room existed within assigned errors for an intermediate situation [38]. Indeed, a comparison with the droplet model [42] suggests that the neutron skin sizes of the antiprotonic measurements can be described similarly well in the droplet model theory by a difference in the diffuseness as by a difference in the bulk radius of the neutron and proton densities.

In the present work we theoretically investigate the bulk and surface components in the neutron skin thickness of nuclei by parametrizing self-consistently calculated nucleon densities by 2pF distributions. The 2pF form is also common in experimental analyses. Our calculations are performed with some representative effective nuclear forces. These are the finite-range Gogny D1S interaction and the zero-range Skyrme SLy4 force from the nonrelativistic framework, and the NL3 and FSUGold parameter sets from the relativistic mean-field (RMF) framework. We discuss the predictions that these mean-field models make for the decomposition of the neutron skin thickness in bulk and surface contributions for the set of stable nuclei that were analyzed in the experiments in antiprotonic atoms. We also study the theoretical predictions along the isotopic chains of Sn and Pb and the variation of the results as one moves from the proton to the neutron drip line in these isotopic chains.

The structure of this article is the following. In Sec. II we present a brief summary of the experimental methodology and results in antiprotonic atoms to highlight some interesting aspects for our study. In Sec. III we discuss the common definitions of nuclear radii and characterize the bulk and surface contributions in the neutron skin thickness of nuclei. In Sec. IV we analyze the theoretical mean-field results in stable isotopes and the predictions for nuclei across the Sn and Pb isotopic chains. We present the summary and conclusions in Sec. V. Some relations for 2pF functions are collected in the Appendix.

## II. SOME ASPECTS OF THE METHODS AND RESULTS IN ANTIPROTONIC ATOMS

The radiochemical study of antiprotonic atoms [35–39,43–45] consists of the analysis of the nuclei with a mass number one unit smaller than the target mass number $A_t$ where the antiproton annihilation takes place. These products that have one less neutron or proton are short lived and their decay is followed by emission of $\gamma$ rays. Standard nuclear spectroscopy methods allow one to determine the absolute number of these residual nuclei with mass number $A_t - 1$. The probability of producing a cold product with mass number $A_t - 1$ is calculated by using the antiproton-nucleus optical potential fitted to reproduce the x-ray experimental data (atomic level shifts and level widths) [38,40,46]. The probability distribution for obtaining a nucleus with mass number $A_t - 1$ has a maximum located about 2–3 fm outside the half-density radius $R_{1/2}$ of the target nucleus.

To compare the experimental data for any target, it is convenient to introduce the peripheral halo factor [47]:

$$f_{\rm halo}^{\rm expt} = \left[\frac{N(\bar{p}n)}{N(\bar{p}p)}\frac{Z_t}{N_t}\right] \Big/ \left[\frac{{\rm Im}(\delta_{\bar{p}n})}{{\rm Im}(\delta_{\bar{p}p})}\right]. \tag{2}$$

The first term in brackets on the right-hand side of this equation gives the ratio of the $\bar{p}$ annihilations on peripheral neutrons to the $\bar{p}$ annihilations on peripheral protons, normalized with the $Z_t/N_t$ value of the target nucleus. The quantities $\delta_{\bar{p}n}$ and $\delta_{\bar{p}p}$ are the $\bar{p}$-$n$ and $\bar{p}$-$p$ scattering amplitudes, respectively, and the factor $F = {\rm Im}(\delta_{\bar{p}n})/{\rm Im}(\delta_{\bar{p}p})$ gives the ratio of the $\bar{p}$ annihilation probabilities on a neutron and on a proton. Consequently, halo factor (2) essentially measures the change of the ratio of the neutron-to-proton concentration in the peripheral region with respect to the bulk value represented by the $N_t/Z_t$ ratio in the target nucleus. A halo factor larger (smaller) than 1 means an increase of the relative neutron (proton) concentration in the nuclear periphery. Assuming the ratio $F$ is known, the measurement of the $N_t - 1$ and $Z_t - 1$ product yields allows one to obtain the experimental value of the halo factor. It was concluded that the comparison of the results from the antiprotonic x-ray method with the radiochemical method favors a value of $F \approx 1$ [38].

The number of nuclei with one fewer neutron or proton is proportional to the quantities ${\rm Im}(\delta_{\bar{p}n})\rho_n$ or ${\rm Im}(\delta_{\bar{p}p})\rho_p$, respectively, integrated over the region where the annihilation process takes place. Thus, approximately, one can estimate theoretically the halo factor as [37,48]

$$f_{\rm halo}^{\rm theor}(r) \approx \frac{\rho_n(r)}{\rho_p(r)}\frac{Z_t}{N_t}. \tag{3}$$

This factor reaches the experimental value $f_{\rm halo}^{\rm expt}$ at a distance $r \approx R_{1/2} + 2.5$ fm beyond the half-density radius of the charge distribution, where the antiproton annihilation takes place. One can use this fact to reproduce the neutron density distribution from some experimental observables.

The charge distribution in many stable nuclei is known very precisely. Usually the experimental charge density is given in some analytical form that is or may be converted to a 2pF

CQ10223 PRC May 17, 2010 10:58



distribution [49,50]. The simple 2pF formula

$$\rho(r) = \frac{\rho_0}{1 + \exp[(r - C)/a]} \tag{4}$$

has only two free parameters with clear physical meaning: on the one hand, $a$ describes the diffuseness of the surface of the density profile; on the other hand, the half density or central radius $C$ describes the mean location of this surface (i.e., $C$ is indicative of the extension of the bulk part of the density distribution). The other, more sophisticated, parametrizations of the density distributions [49,50] describe better the central part of the nucleus or modify the surface part with higher-order terms. We do not use them because the interpretation of the multiple parameters is harder and less direct.

To study the differences at the nuclear periphery between the neutron and proton densities in the antiprotonic atoms experiments, the authors of Ref. [38] used 2pF functions. They used the notation "neutron skin-type" distribution and "neutron halo-type" distribution to describe the two extreme cases of 2pF shapes having either $C_n > C_p$ and $a_n = a_p$ or $C_n = C_p$ and $a_n > a_p$, respectively. As we mentioned in the Introduction, the radiochemical data gave support to understanding the difference between the neutron and proton rms radii in the antiprotonic atoms from an increase of $a_n$ rather than from an increase of $C_n$, compared to the $a_p$ and $C_p$ values. Thus, the neutron halo-type distribution ($C_n - C_p = 0$) was assumed [38]. (Note that here "halo type" is a useful notation, but the nuclei in the antiprotonic experiments are stable isotopes and it is not meant that they have halos like very light or exotic nuclei, such as $^{11}$Li [24,25]). It was noted in the same work [38] that some room was left, nevertheless, within the error bars for intermediate cases with $C_n > C_p$ and $a_n > a_p$.

The 2pF shape can be applied for the description of charge, proton, or neutron densities. Indeed, if the charge density is known in the 2pF form, the corresponding point proton density can be easily found and it also takes a 2pF form, with the parameters obtained through the deconvolution procedure [51,52]. The more relevant expressions are given in the Appendix. From these proton density profiles, one can try to deduce the neutron density profiles with some additional information. For instance, if one knows the $C_p$ and $a_p$ parameters of the proton density and the value of the neutron skin thickness $\Delta R_{np}$ defined in Eq. (1) (e.g., from independent experimental measurements), a relationship between the half-density radius $C_n$ and the diffuseness $a_n$ of the neutron 2pF distribution can be found (see the Appendix). Such a procedure creates a family of neutron density profiles that depend on one free parameter, which can be chosen to be either $C_n - C_p$ or $a_n - a_p$. Now it is possible to check which set of values of $C_n$ and $a_n$ reproduces the experimental halo factor (2). This allows one to determine the 2pF neutron distribution. Next we apply this idea to the $^{208}$Pb nucleus as an illustrative test case.

In Fig. 1 we display the halo factor, Eq. (3), for the $^{208}$Pb nucleus computed with 2pF density distributions. The 2pF neutron densities are obtained from the experimental charge density taken from Ref. [53], which we convert to a 2pF proton density using the formulas given in the Appendix. We consider

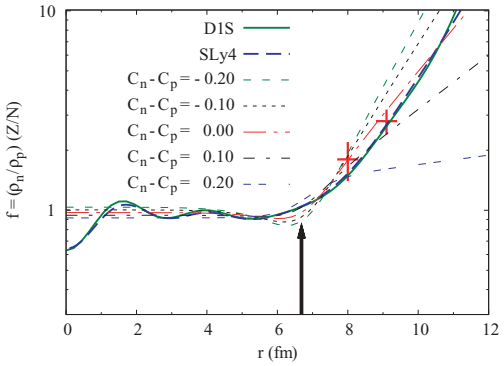


FIG. 1. (Color online) The halo factor in $^{208}$Pb as a function of the distance from the center of the nucleus, calculated using the 2pF formulas from the experimental charge density [53] assuming a neutron skin thickness $\Delta R_{np} = 0.16$ fm and different values of $C_n - C_p$ (thin lines). The results of the theoretical predictions with the Gogny D1S and Skyrme SLy4 nuclear forces are also shown. The values of the halo factor deduced from experiment [38,40] are marked by crosses. The value of the proton half-density radius $C_p$ is indicated by an arrow.

a family of 2pF neutron densities that differ one from the other in the half-density radius $C_n$ and diffuseness $a_n$, but they all have the same value for the neutron skin thickness: $\Delta R_{np} = 0.16$ fm (which corresponds to the value extracted from the results of the x-ray method in the $^{208}$Pb antiprotonic atom [40]). We allow the difference $C_n - C_p$ to vary in the range from $-0.20$ to 0.20 fm. The value of the diffuseness $a_n$ of the 2pF neutron density is then obtained using Eq. (A10) from the Appendix.

The values of the 2pF parameters in our present calculation are given in Table I. Agreement with the results from previous experiments [38,40] (indicated by crosses in Fig. 1) is found

TABLE I. The parameters $C$ and $a$ of the 2pF distributions for $^{208}$Pb obtained from the experimental charge density [53] as described in the text and from mean-field calculations. All values are given in femtometers.

| | $C_q$ | $a_q$ | $C_n - C_p$ | $a_n - a_p$ |
|---|---|---|---|---|
| Proton | 6.704 | 0.438 | | |
| Neutron | 6.504 | 0.659 | −0.20 | 0.221 |
| | 6.604 | 0.614 | −0.10 | 0.176 |
| | 6.704 | 0.565 | 0.00 | 0.127 |
| | 6.804 | 0.511 | 0.10 | 0.073 |
| | 6.904 | 0.449 | 0.20 | 0.011 |
| Fit to D1S density profile | | | | |
| Proton | 6.645 | 0.467 | | |
| Neutron | 6.686 | 0.548 | 0.041 | 0.081 |
| Fit to SLy4 density profile | | | | |
| Proton | 6.683 | 0.470 | | |
| Neutron | 6.755 | 0.555 | 0.072 | 0.085 |

CQ10223 PRC May 17, 2010 10:58



for the parameters of the 2pF distributions in the range from the values $C_n - C_p = 0$ fm and $a_n - a_p = 0.13$ fm to the values $C_n - C_p = 0.10$ fm and $a_n - a_p = 0.07$ fm. In the first limit, the neutron skin thickness $\Delta R_{np}$ is basically due to an enhancement of the diffuseness of the neutron density, whereas the second limit corresponds to a mixed configuration where both the neutron diffuseness and the neutron half-density radius are larger than the values of the proton density. We have to stress that even small differences between $C_n$ and $C_p$ may have a meaningful influence on the value of the neutron skin thickness. The discussed results indicate an intermediate character of the neutron skin thickness in $^{208}$Pb, but with a preference for the density pattern where $C_n \approx C_p$ and $a_n > a_p$. A more precise conclusion is difficult because of the large experimental error bars.

For comparison, in Fig. 1 we also plot the theoretical halo factor (3) in $^{208}$Pb calculated directly from the neutron and proton densities of the Gogny D1S [54] and Skyrme SLy4 [55] effective nuclear forces. At the distances relevant for antiproton annihilation, the halo factor obtained with these theoretical mean-field densities agrees considerably well with the experimental data. The numerical values of the half-density radius $C$ and of the diffuseness parameter $a$ of the D1S and SLy4 equivalent 2pF neutron and proton densities for $^{208}$Pb are reported in Table I. For either force, one observes that the half-density radii $C_n$ and $C_p$ of the 2pF distributions are different and that the values of $a_n$ and $a_p$ are also different. Thus, the results of these models correspond to some intermediate situation between the "neutron halo-type" 2pF distribution (where $C_n = C_p$ and $a_n > a_p$) and the "neutron skin-type" 2pF distribution (where $C_n > C_p$ and $a_n = a_p$) discussed in Ref. [38]. In any case, the two forces, D1S and SLy4, show some preference, as do the calculations considered earlier, for the "neutron halo-type" distribution in $^{208}$Pb, especially in the case of the D1S force, where $C_n - C_p = 0.04$ fm and $a_n - a_p = 0.08$ fm.

From the discussions of this section it is easily seen that the characterization of the "bulk" or "surface" formation of the neutron skin thickness in nuclei is a nontrivial problem. In the following, we wish to analyze this question according to the predictions derived from mean-field models of nuclear structure that are tested to be successful for charge radii, binding energies, and a wealth of phenomena in nuclei. First, we need to establish a prescription to separate bulk and surface contributions in neutron skins calculated with mean-field nuclear densities.

## III. DISCERNING BULK FROM SURFACE IN NEUTRON SKINS

Nuclear radii can be defined in several independent ways. The most popular formulas and their relations are discussed in the book by Hasse and Myers [49] and we recall and analyze them in this section. One of the simplest ways to describe the size of nuclei is to define a *central radius* $C$ in terms of the integral of the nuclear density profile $\rho(r)$ (for either neutrons or protons) as

$$C = \frac{1}{\rho(0)} \int_0^\infty \rho(r) dr. \tag{5}$$

Another option is the *half-density radius* $R_{1/2}$, which is defined from the local condition

$$\rho(R_{1/2}) = \tfrac{1}{2}\rho(0). \tag{6}$$

For density profiles that have a symmetric surface, such as the 2pF distribution defined in Eq. (4), the central radius $C$ and the half-density radius $R_{1/2}$ coincide.

The *equivalent sharp radius* $R$ is the radius of a uniform sharp distribution that has a constant density equal to the bulk value of the actual density and that contains the same number of nucleons as the considered nucleus:

$$\frac{4}{3}\pi R^3 \rho(\text{bulk}) = 4\pi \int_0^\infty \rho(r) r^2 dr. \tag{7}$$

For its importance in experimental techniques, the *equivalent rms radius* $Q$ is commonly used. It describes a uniform sharp distribution with the same rms radius as the given density profile:

$$\tfrac{3}{5} Q^2 = \langle r^2 \rangle. \tag{8}$$

Because the neutron skin thickness (1) is defined through rms radii, it can be expressed easily with $Q$:

$$\Delta R_{np} = \sqrt{\frac{3}{5}} (Q_n - Q_p). \tag{9}$$

In uniform, sharp-edge nuclear distributions, all of the above-mentioned definitions coincide, but in realistic leptodermous density profiles, they give distinct values. The relation between the $C$, $Q$, and $R$ radii can be expressed by expansion formulas in powers of $b/R$, where $b$ is the so-called surface width of the density profile. The latter quantity is defined by

$$b^2 = -\frac{1}{\rho(0)} \int_0^\infty (r - C)^2 \frac{d\rho(r)}{dr} dr. \tag{10}$$

To leading order, one has the relationships [49]

$$C \simeq R \left(1 - \frac{b^2}{R^2}\right) \tag{11}$$

and

$$Q \simeq R \left(1 + \frac{5}{2}\frac{b^2}{R^2}\right). \tag{12}$$

These expansions are useful as long as $b/R$ is small. This condition is well fulfilled in many nuclei because $b \sim 1$ fm and $R \sim r_0 A^{1/3}$; therefore, $b^2/R^2$ is typically no larger than $A^{-2/3}$. Moreover, to consider no further corrective terms in the above relations of the $C$ and $Q$ radii with $R$ may be quite accurate for specific shapes. For example, in the case of 2pF distributions, the first nonvanishing corrections to the terms within brackets in Eqs. (11) and (12) are of order $(b/R)^6$ and $(b/R)^4$, respectively.

The multiple definitions of nuclear radii may sometimes cause misleading conclusions, especially if nuclear properties sensitive to the nuclear matter distribution in nuclei are concerned or two different models are compared. Therefore, one has to be careful about the suitable choice of the radius definition. To compare the foregoing definitions of radii for heavy nuclei, in Fig. 2 we plot the neutron densities obtained in a self-consistent mean-field calculation and the fitted 2pF

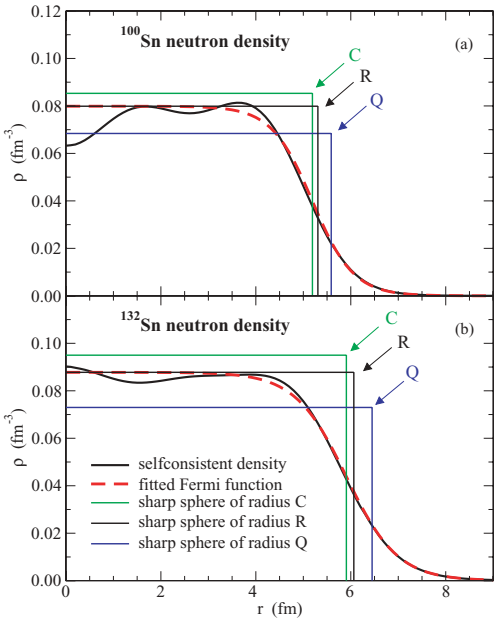


FIG. 2. (Color online) Comparison of sharp surface density profiles that have central ($C$), equivalent sharp ($R$), and equivalent rms ($Q$) radii with the self-consistent and 2pF profiles corresponding to the neutron density of (a) $^{100}$Sn and (b) $^{132}$Sn obtained in the RMF theory (the NL3 interaction [56] has been used).

distributions for the neutron-deficient nucleus $^{100}$Sn and the neutron-rich nucleus $^{132}$Sn. These profiles are compared with sharp-edge density distributions having radii $C$, $R$, and $Q$ calculated from the above expressions with the 2pF function. The central densities of the sharp surface spheres are fixed to fulfill the particle number normalization.

Figure 2 illustrates the fact that the central radius $C$ does not allow the bulk density to be reproduced. A sharp sphere of radius $C$ overestimates the self-consistent density in the whole nuclear interior. The equivalent rms radius $Q$ also fails, because it clearly underestimates the original density in the bulk. Only the equivalent sharp radius $R$ is able to properly reproduce the bulk part of the self-consistent and 2pF density profiles of the nucleus. As discussed in Ref. [49], the equivalent sharp radius $R$ is the quantity of basic geometric importance of the three radii $C$, $R$, and $Q$. A sharp distribution of radius $R$ has the same volume integral as the actual density of the finite nucleus and differs from it only in the surface region. Therefore, the radius $R$ appears to be the suitable quantity to be used to measure the size of the bulk part of the nucleus.

On account of Eq. (9) for the neutron skin thickness and relationship (12) between $Q$ and $R$, one obtains the expression

$$\Delta R_{np} = \sqrt{\frac{3}{5}}\left[(R_n - R_p) + \frac{5}{2}\left(\frac{b_n^2}{R_n} - \frac{b_p^2}{R_p}\right)\right] \tag{13}$$

up to terms of order $O(b^4/R^3)$. Thus, one can make a meaningful distinction between a *bulk* contribution and a *surface* (*diffuseness*) contribution to the neutron skin thickness of nuclei as follows:

$$\Delta R_{np} = \Delta R_{np}^{\text{bulk}} + \Delta R_{np}^{\text{surf}}, \tag{14}$$

with

$$\Delta R_{np}^{\text{bulk}} \equiv \sqrt{\frac{3}{5}}(R_n - R_p) \tag{15}$$

independent of surface properties and

$$\Delta R_{np}^{\text{surf}} \equiv \sqrt{\frac{3}{5}}\frac{5}{2}\left(\frac{b_n^2}{R_n} - \frac{b_p^2}{R_p}\right). \tag{16}$$

The nucleus may develop a neutron skin by separation of the bulk radii $R$ of neutrons and protons or by modification of the diffuseness $b$ of the neutron and proton surfaces. In the general case, a combination of both effects can be found. To which degree the different patterns arise in mean-field calculations of finite nuclei is a question we address in the following sections.

Experimental [50] and theoretical mean-field density distributions present oscillations in their inner bulk region, which implies that some suitable average is needed to determine the bulk density value $\rho$(bulk) of Eq. (7) to compute the equivalent sharp radius $R$. The difficulty may be easily solved by fitting a Fermi function to the original density, as we have illustrated in Fig. 2. In this case, the bulk density value, that is, $\rho_0/[1+\exp(-C/a)]$, is, to excellent accuracy, the $\rho_0$ parameter of the Fermi function. An effect not described by functions like the 2pF distribution is the occurrence of a nonsymmetric surface shape, which is possible in real nuclear densities. However, one plausibly expects that neutron skins of nuclei are dominated by the difference existing between neutrons and protons in the location of the surface (i.e., $R$) and/or in the spatial extent of this surface (i.e., $b$); the difference in the degree of asymmetry between the shapes of the neutron and proton surfaces is expected to be a less important, higher-order correction.

It may be practical to rewrite expressions (15) and (16) for the bulk and surface contributions to the neutron skin thickness directly in terms of the parameters of the 2pF function of Eq. (4). Using the fact that the diffuseness parameter $a$ in a 2pF function is related to the surface width $b$ by the formula

$$b = \frac{\pi}{\sqrt{3}}a \tag{17}$$

and inverting relation (11) between $C$ and $R$, one easily finds to the given order of approximation that Eqs. (15) and (16) become, respectively,

$$\Delta R_{np}^{\text{bulk}} = \sqrt{\frac{3}{5}}\left[(C_n - C_p) + \frac{\pi^2}{3}\left(\frac{a_n^2}{C_n} - \frac{a_p^2}{C_p}\right)\right] \tag{18}$$

and

$$\Delta R_{np}^{\text{surf}} = \sqrt{\frac{3}{5}}\frac{5\pi^2}{6}\left(\frac{a_n^2}{C_n} - \frac{a_p^2}{C_p}\right). \tag{19}$$

CQ10223 PRC May 17, 2010 10:58



We note from these results that

$$\Delta R_{np}^{\text{bulk}} = \sqrt{\frac{3}{5}}(C_n - C_p) + \frac{2}{5}\Delta R_{np}^{\text{surf}}; \tag{20}$$

that is, the quantities $C_n - C_p$ (easily obtained from the 2pF distributions themselves) and $R_n - R_p$ [obtained through Eq. (7)] differ by surface diffuseness terms and should not be mixed. We have seen in Fig. 2 that a sharp sphere having a radius $C$ significantly distorts the appearance of the actual nuclear density by overshooting it in the whole bulk region. It is thus preferable to use $\sqrt{3/5}(R_n - R_p)$ rather than $\sqrt{3/5}(C_n - C_p)$ as a measure of the bulk contribution to the neutron skin thickness.

## IV. DECOMPOSITION OF NEUTRON SKIN THICKNESS IN SELECTED NUCLEI: MEAN-FIELD RESULTS

### A. Nuclei of the experiments in antiprotonic atoms

To get information about the "bulk" or "surface" character of the thickness of neutron skins in theoretical mean-field calculations, we parametrize the self-consistently calculated proton and neutron densities with 2pF distributions. This procedure can be applied very suitably for many heavy nuclei and gives a clear distinction between bulk and surface properties of nuclei. However, there is no universal method to do this parametrization. A popular prescription is to use a $\chi^2$ minimization of the differences between the density to be reproduced and the 2pF profile, or of the differences between their logarithms. These methods may somewhat depend on conditions given during minimization (number of mesh points, limits, etc.). We prefer to extract the parameters of the 2pF profiles by imposing that they reproduce the same quadratic $\langle r^2 \rangle$ and quartic $\langle r^4 \rangle$ moments of the self-consistent mean-field densities. These two conditions, together with the normalization to the proton and neutron numbers, allow us to determine in a unique way the equivalent 2pF densities. This method can be applied to any density distribution. Its focus is on a good reproduction of the surface region of the original density because the local distributions of the quantities $r^2\rho(r)$ and $r^4\rho(r)$ are peaked at the periphery of the nucleus. As an example of the results of the present determination of the 2pF profiles, in Fig. 3 we display in logarithmic scale the self-consistent neutron and proton densities for $^{208}$Pb together with their equivalent 2pF distributions calculated with the NL3 interaction. It can be seen that there is overall good agreement in the central and surface regions of the nucleus. In particular, the 2pF densities reproduce the mean-field densities well at the distances that are relevant for antiproton annihilation.

In this section, we would like to get some insight about the "bulk" or "surface" character of the neutron skin predicted by the mean-field approach in the nuclei for which the neutron skin thickness values were extracted in Refs. [38,39] from the measurements in antiprotonic atoms. These nuclei range from $^{40}$Ca to $^{238}$U and all lie along the valley of stability. We carry out the calculations with the aforementioned nonrelativistic interactions D1S [54] and SLy4 [55] plus the relativistic interactions NL3 [56] and FSUGold [57] as representative examples of successful nuclear mean-field models. We impose

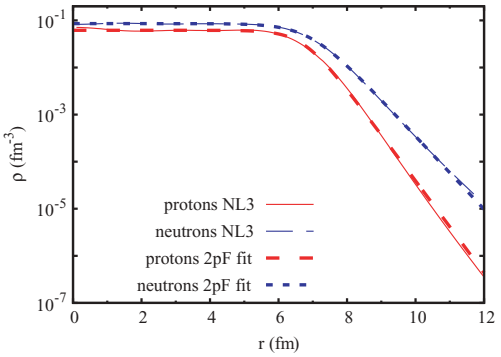


FIG. 3. (Color online) The proton and neutron densities of $^{208}$Pb calculated with the NL3 parameter set as a function of the distance from the center of this nucleus in logarithmic scale. The 2pF densities fitted to the NL3 results are also shown.

spherical symmetry in all nuclei described in this article. The effect of deformation on the neutron skin thickness was discussed elsewhere [58]. The two nonrelativistic forces have a soft symmetry energy [15,18]. On the contrary, the covariant NL3 parameter set has a stiff symmetry energy, which is usual in the relativistic models [15,18]. Note that the notation soft or stiff refers to whether the symmetry energy of the model increases slowly or rapidly as a function of the nuclear density. The covariant parameter set FSUGold was devised to have a softer density dependence of the symmetry energy [57] than the typical relativistic models. Thus, FSUGold is, in this aspect, closer to the nonrelativistic models than NL3.

In Fig. 4 we display the experimental data with error bars determined from the antiprotonic atoms. There is a relatively clear correlation between the experimental value of the neutron skin thickness of these 26 stable nuclei and the overall relative neutron excess $I = (N - Z)/A$ of the nucleus. This trend has been fitted by the linear relationship $\Delta R_{np} = (0.90 \pm 0.15)I + (-0.03 \pm 0.02)$ fm with a $\chi^2$ factor of 0.5 [38,39]. In the same figure, we plot the theoretical $\Delta R_{np}$ value calculated according to Eq. (1) using the mean-field densities of the indicated effective nuclear models for the 23 even-even nuclei that exist in the experimental data set. It is obvious that the theoretical models make largely different predictions for the neutron skin thickness. This is especially visible at large values of $I$. It is seen that the models that have a softer symmetry energy give smaller $\Delta R_{np}$ values, whereas the models with a stiffer symmetry energy give larger $\Delta R_{np}$ values [11,12]. Note that as soon as $I \neq 0$, even when it is small, discrepancies arise among the $\Delta R_{np}$ values of the models. In contrast, all of the considered interactions make an almost identical prediction of $\Delta R_{np} \approx -0.05$ fm for the $^{40}$Ca nucleus.

One observes in Fig. 4 that, similarly to the situation in the experimental data set, the theoretical neutron skin values computed with each nuclear interaction show an average linear behavior as a function of the neutron excess $I$. Actually, the linear correlation factor of $\Delta R_{np}$ with $I$ in the present models

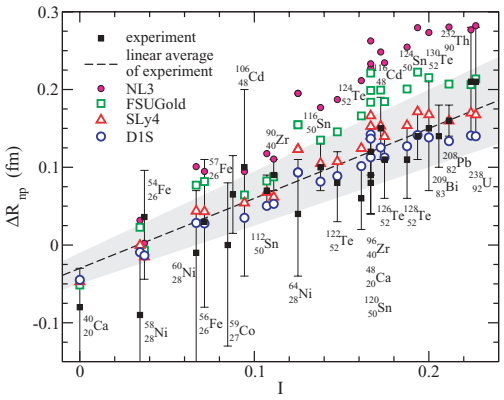


FIG. 4. (Color online) The results of the covariant NL3 and FSUGold parameter sets and of the nonrelativistic Skyrme SLy4 and Gogny D1S forces compared with the experimental neutron skin values $\Delta R_{np}$ deduced from antiprotonic atoms (solid squares with errorbars) and their linear average $\Delta R_{np} = (0.90 \pm 0.15)I + (-0.03 \pm 0.02)$ fm (shaded region) [38,39].

is considerably high (between 0.95 and 0.97). The fit of the neutron skin values calculated with the Skyrme SLy4 force yields $\Delta R_{np} = 1.01I - 0.035$ fm, whereas $\Delta R_{np} = 0.88I - 0.04$ fm is obtained in the case of the Gogny D1S interaction. We find a linear fit of $\Delta R_{np} = 1.20I - 0.03$ fm using the values of the neutron skin thickness computed with the relativistic FSUGold model. If we consider the relativistic NL3 parameter set, which has a stiffer symmetry energy than the other models, we find the linear fit $\Delta R_{np} = 1.50I - 0.03$ fm. Compared with the slope of 0.90 for the fit of the experimental data [38,39], the slopes in forces like D1S and SLy4 are much closer to it, whereas the agreement deteriorates as the model has a stiffer symmetry energy. Thus, one can conclude that the comparison of the slopes of $\Delta R_{np}$ with $I$ between theory and the antiprotonic measurements for nuclei across the mass table favors the models that have a soft symmetry energy.

In Fig. 5 we display the bulk and surface contributions to the theoretical neutron skin thickness that are computed by applying Eqs. (15) and (16), respectively, against the neutron excess $I$. These values are obtained from the 2pF distributions associated with the mean-field neutron and proton densities calculated with the D1S force as well as with the Skyrme SLy4 force and the two RMF parameter sets, FSUGold and NL3. The numerical calculations show that the value of $\Delta R_{np}^{\rm bulk} + \Delta R_{np}^{\rm surf}$ obtained through Eqs. (18) and (19) can be slightly less accurate in some nuclei [compared to the exact value of Eq. (1)] than the result obtained through Eqs. (15) and (16). The small differences, whenever they arise, are due almost entirely to the replacement of $a_q^2/R_q$ by $a_q^2/C_q$ ($q = n, p$) in Eqs. (18) and (19). Of course, Eqs. (18) and (19) are quite practical because they do not require the additional calculation of the $R_q$ values and they can be applied straightforwardly using the $C_q$ and $a_q$ parameters of the 2pF distributions themselves.

The four panels presented in Fig. 5, as a consequence of the differences between models, predict a slightly different splitting of the neutron skin thickness into their bulk and surface contributions for each considered nucleus. Therefore, the values of the bulk and surface contributions to $\Delta R_{np}$ are to some extent model dependent. The total neutron skin thickness roughly follows an increasing tendency with the relative neutron excess $I$, as discussed previously. This tendency is also seen in the bulk contribution $\Delta R_{np}^{\rm bulk}$, especially in the nonrelativistic interactions. However, the surface contribution

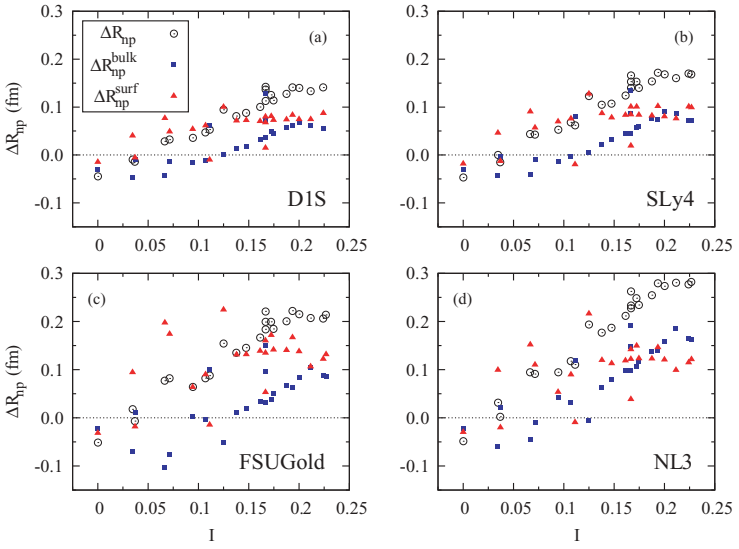


FIG. 5. (Color online) The neutron skin thickness $\Delta R_{np}$ as well as its bulk $\Delta R_{np}^{\rm bulk}$ and surface $\Delta R_{np}^{\rm surf}$ parts [given by Eqs. (15) and (16), respectively] for the nuclei presented in Fig. 4, calculated in various models.

CQ10223 PRC May 17, 2010 10:58



does not clearly follow the same trend and shows a less definite behavior as a function of $I$.

From Fig. 5 we see that, for relatively neutron-rich nuclei ($I \gtrsim 0.15$), the surface part generally contributes 50% or more to the total neutron skin thickness. If the nuclear model has a stiff symmetry energy and $I$ is large, the bulk part of $\Delta R_{np}$ may become larger than the surface part, as can be seen in the NL3 panel of Fig. 5 at $I > 0.2$. More symmetric nuclei ($I \lesssim 0.15$) do not present a definite tendency. The theoretical calculations show that in these nuclei the sharp radius is larger for protons than for neutrons ($R_p > R_n$), while the surface width is larger for neutrons than for protons ($b_n > b_p$). Consequently, the bulk contribution to the neutron skin thickness becomes negative, as can be seen in Fig. 5, and the relatively small value of the neutron skin thickness is basically because of a strong cancellation between the bulk and surface parts. In the lightest nuclei, both contributions are negative and produce a "proton skin" rather than a neutron skin.

### B. Medium and heavy mass isotopic chains

The set of nuclei chosen in Sec. IV A have given us some insight into the bulk and surface contributions to the neutron skin thickness in stable isotopes. To investigate in a systematic way how the bulk and surface contributions evolve with the neutron number, we study the chains of even-even Sn and Pb isotopes from the proton to the neutron drip line.

First, Fig. 6 displays the neutron skin thickness $\Delta R_{np}$ along the Sn and Pb isotopic chains computed in the mean-field approximation with the Gogny D1S and Skyrme SLy4 forces and using the relativistic mean-field models NL3 and FSUGold. For small and moderate values of the relative neutron excess ($I \lesssim 0.2$), the neutron skin thickness grows almost linearly with $I$ in each isotopic chain, as in the case of the stable nuclei analyzed in the previous section. However, $\Delta R_{np}$ shows a rather pronounced kink at $I \approx 0.20 - 0.25$. Beyond this value, it increases again almost linearly as a function of the relative neutron excess, but with a larger slope. Finally, a new departure from the linear behavior of $\Delta R_{np}$ as a function of $I$ can be observed when the isotopes are on the edge of the neutron drip line. The kinks and changes of slope in the neutron skin thickness as a function of the relative neutron excess are clearly connected with the doubly magic nuclei $^{132}$Sn ($I \approx 0.24$) and $^{208}$Pb ($I \approx 0.21$) in the stable nuclei region and with another two doubly magic nuclei, namely $^{176}$Sn ($I \approx 0.43$) and $^{266}$Pb ($I \approx 0.38$), near the neutron drip line. Therefore, it is obvious that these changes of slope are produced by quantal effects, which modify the linear trend of $\Delta R_{np}$ as a function of $I$ in a non-negligible way. The average slope of $\Delta R_{np}$ with $I$ for various forces is clearly different. As has been shown in Refs. [11,12], for each nuclear model, $\Delta R_{np}$ is strongly correlated with the slope of the symmetry energy with respect to the density computed at saturation.

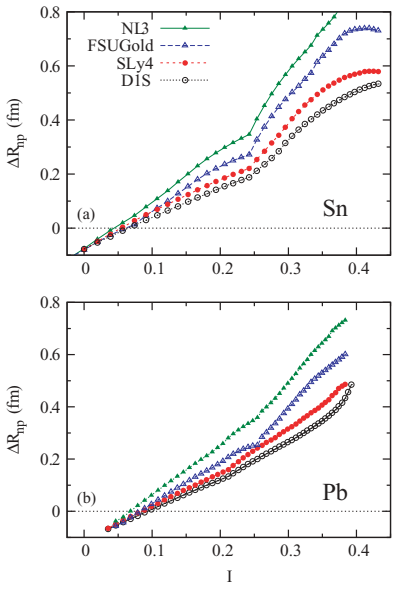


FIG. 6. (Color online) The neutron skin $\Delta R_{np}$ for (a) Sn and (b) Pb isotopes calculated with several mean-field models.

As in Sec. IV A, we fit the mean-field proton and neutron densities by 2pF distributions to investigate the bulk and surface contributions to the neutron skin. To analyze the changes that occur in $\Delta R_{np}$, first we look at the parameters that characterize the 2pF distributions. In Fig. 7 we display the central density $\rho_0$, the half-density radius $C$, and the diffuseness $a$, which are obtained from the D1S densities along the Sn and Pb isotopic chains. The 2pF parameters show an overall smooth behavior as a function of the relative neutron excess $I$ but with local modulations near the shell closures. The central density $\rho_0$ grows (for neutrons) or declines (for protons) almost linearly as a function of $I$ in both isotopic chains. It is just a simple consequence of the increasing asymmetry along the isotopic chains. The central radii $C_n$ and $C_p$ both show a global increasing tendency with the neutron number. One can notice that $C_n$ grows faster with $I$ than $C_p$. However, the $a_n$ and $a_p$ diffuseness parameters behave in a completely different way. Whereas $a_n$ grows on average with increasing neutron excess, $a_p$ remains roughly constant with $I$ in the two isotopic chains. On top of these general trends, we see that the 2pF parameters associated with the neutron densities show kinks around the shell closures at $N = 82$ in Sn and $N = 126$ in Pb (that is, in the region $I \simeq 0.20 - 0.25$), as well as changes of slope near the neutron drip lines. One observes that some signature of the neutron shell effect also appears in the 2pF parameters of the proton densities around magic neutron numbers.

Figure 8 shows the evolution with $I$ of the 2pF parameters corresponding to the quantal densities computed with the SLy4 Skyrme force and with the relativistic mean-field NL3 parameter set. In the two models, the global trends are similar to the ones discussed before for 2pF parameters of D1S distribution. However, they show some differences that can be attributed in part to the different properties of the isovector channel of the interaction.

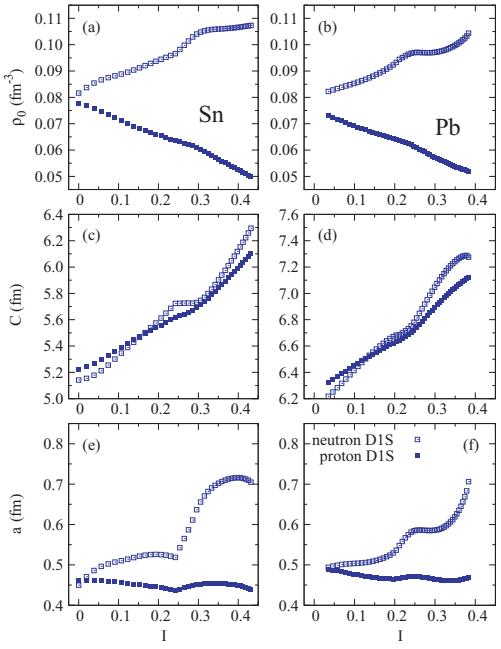


FIG. 7. (Color online) Proton and neutron 2pF parameters (a) $\rho_0$ for Sn, (b) $\rho_0$ for Pb, (c) $C$ for Sn, (d) $C$ for Pb, (e) $a$ for Sn, and (f) $a$ for Pb isotopes. 2pF parameters are fitted to the Gogny D1S density distributions.

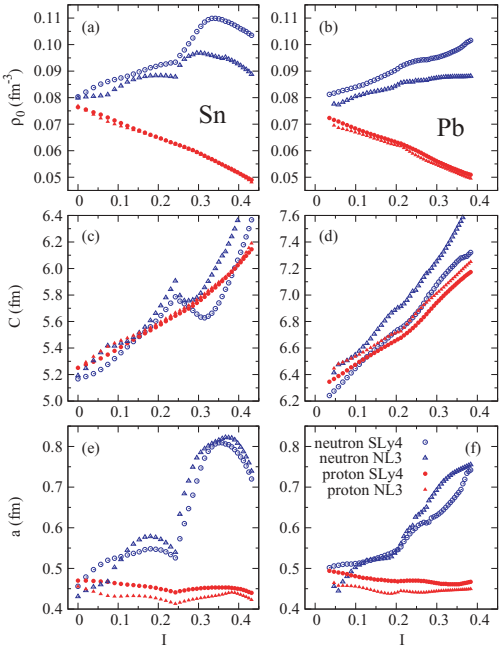


FIG. 8. (Color online) The same as in Fig. 7 but for the Skyrme SLy4 force and relativistic NL3 parameter set.

In Figs. 9(a) and 9(b), we display the bulk and the surface contributions to the nuclear skin thickness calculated with the D1S force along the Sn and Pb isotopic chains. These contributions show for Sn isotopes two well-defined regions as a function of $I$. One of them covers the neutron major shell between $^{100}$Sn and $^{132}$Sn (i.e., $0 \leqslant I \lesssim 0.25$), and the other region corresponds to the next major shell between $^{132}$Sn and $^{176}$Sn in the range $0.25 \lesssim I \lesssim 0.43$. For nearly symmetric Sn isotopes close to $^{100}$Sn, which are neutron deficient, $C_p$ is larger than $C_n$ (see Fig. 7) and, consequently, the bulk part of the neutron skin is negative or at most it takes very small positive values. For these values of $I$, the surface contribution is positive and relatively small, reducing the opposite effect of "proton skin" due to negative values of the bulk part. Looking at more asymmetric isotopes, one can see that, in the magic nuclei $^{132}$Sn and $^{176}$Sn, the bulk and the surface contributions are roughly equal. This implies a rather compact neutron density distribution with a relatively stiff surface as a consequence of the kinks exhibited by the neutron diffuseness parameter $a_n$ around the neutron magic numbers, which can be seen in Fig. 7. In the regions between magic numbers, the surface contribution to the neutron skin thickness is larger than the bulk contribution. The splitting between the surface and bulk contributions reaches its maximum value roughly at midshell. This behavior of the bulk and surface contributions to the neutron skin thickness points out that Sn isotopes in the middle of major shells develop a larger surface region in the density distribution than the magic ones. In other words, these isotopes with neutron number in between magic values are more of "halo" type than the limiting magic nuclei which show a mixed character between "halo" and "neutron skin."

The bulk and the surface contributions to the neutron skin of the Pb isotopes calculated with the D1S force show a similar behavior to the case of the Sn isotopes analyzed before. However, for this heavy isotopic chain, the bulk part gives a more important contribution to the total neutron skin for nuclei in between the magic $^{208}$Pb and $^{266}$Pb nuclei.

The discussed differences in the behavior of the neutron skin and its bulk and surface contributions along the neutron-rich Sn and Pb isotopes can be qualitatively understood as follows. Within a major shell, the rms radii of the different single-particle orbits are spread around their average value. The rms radius of orbits with low angular momentum $l$ are larger than the average, while the rms radius of orbits with high $l$ are slightly smaller but close to the average in the shell. Consequently, the outermost region of the density is basically provided by the orbits with low $l$ in the last populated major shell. On the contrary, orbits with high $l$ in this major shell have their most important contribution at shorter distances from the center of the nucleus, increasing more the bulk than the surface part of the nuclear density. Hence, the filling order of the last single-particle orbits is crucial to determine if the growing of

CQ10223 PRC May 17, 2010 10:58



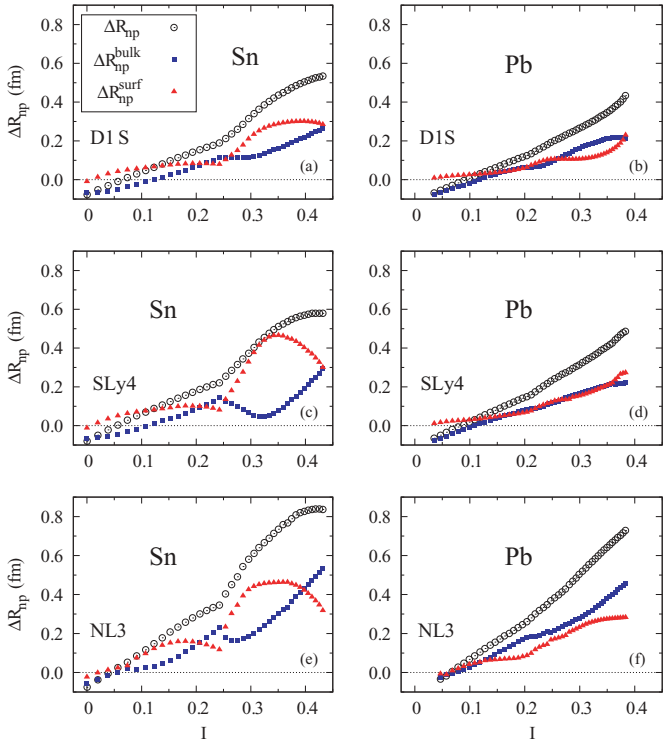


FIG. 9. (Color online) The same as in Fig. 5 but for Sn and Pb isotopes calculated with the Gogny D1S force, Skyrme SLy4 force, and relativistic NL3 parameter set.

the neutron radius, and consequently the neutron skin, is due to an increase of the surface or the bulk of the density. In the case of neutron-rich isotopes of Sn above $N = 82$, the first filled orbits are $2f_{7/2}$, $3p_{3/2}$, and $3p_{1/2}$. This ordering produces an important enhancement of the nuclear surface, which can be appreciated from Figs. 7 and 9. Once midshell is filled, the $1h_{9/2}$ and $1i_{13/2}$ orbits start to be appreciably populated, increasing the bulk more than the surface of the densities and hence of the neutron skin, as can be seen in the aforementioned figures. The situation in Pb isotopes is just the contrary; above $N = 126$, the first occupied levels are $2g_{9/2}$ and $1j_{15/2}$, which increase the bulk more than the surface. Only near the drip line, $N = 184$, are the low-momentum orbits $3d_{5/2}$, $4s_{1/2}$, and $3d_{3/2}$ relevant, increasing the surface and quenching the bulk contributions to the density and consequently of the neutron skin. This behavior in Pb isotopes can also be seen in Figs. 7 and 9.

In Figs. 9(c)–9(f), we display the results calculated with the Skyrme SLy4 force and the NL3 parameter set. The bulk and surface contributions qualitatively behave as the ones computed with the D1S force discussed previously. Of course, some differences are found in comparing the results obtained with the different models because of their different isovector properties. In models with a stiff density dependence of the symmetry energy (for instance, NL3), the bulk contribution to the neutron skin is more important than in models with a soft symmetry energy, as in the case of the SLy4 and D1S forces. This tendency can be especially noted in the Pb isotonic chain.

## V. CONCLUSIONS

Ground-state properties of stable nuclei, such as charge radii and binding energies, can be reproduced fairly well by using mean-field models with effective interactions such as the Skyrme or Gogny forces and with relativistic Lagrangians. Although the isoscalar part of these models is well constrained, their isovector properties are much less determined and the predictions in this sector can differ considerably, even for stable nuclei. A typical example is the neutron skin thickness of nuclei. For this observable, theoretical predictions for $^{208}$Pb using nonrelativistic forces give a value around 0.15 fm while relativistic mean-field parametrizations predict values that are almost twice as large.

The neutron skin thickness of a set of 26 nuclei, distributed over the whole periodic table, has been obtained from the analysis of experiments with antiprotonic atoms [38,39] combined with the charge radii obtained from electron scattering data. One important result of these experiments with antiprotonic atoms is that there exists a rather clear linear correlation between the neutron skin thickness and the overall neutron excess $I$. Theoretical mean-field calculations of the neutron

CQ10223 PRC May 17, 2010 10:58



skin also show this tendency even more clearly. It is found that the relativistic parametrizations systematically predict larger neutron skins than the ones computed with nonrelativistic interactions. This is because the symmetry energy is stiffer in the relativistic models than in the nonrelativistic models.

To analyze the experimental data of antiprotonic atoms, an ansatz of the nuclear densities is needed. The two-parameter Fermi distributions have been used often to this end. It is found that the experimental data can be reproduced by a variety of these Fermi distributions with different values of $C_n - C_p$ and $a_n - a_p$. The experimental values of the halo factor in $^{208}$Pb are well reproduced by distributions with $C_n \approx C_p$ (halo model) and by Fermi densities with both halo and neutron skin ($a_n \approx a_p$) contributions. This latter scenario is also well predicted by the nonrelativistic mean-field densities obtained with the D1S and SLy4 forces.

We have also parametrized the mean-field densities via two-parameter Fermi distributions. We do this by imposing that both mean-field and parametrized densities give the same quadratic and quatric moments. This parametrization of the mean-field densities also allows the neutron skin thickness to be split easily into two contributions, namely the bulk part and the surface part. It is found that the mean-field neutron skins computed in nuclei with $I > 0.1$ can be shared between non-negligible surface and bulk parts. This applies both for stable nuclei investigated in antiprotonic experiments and for drip line isotopes in all the theoretical models considered in this work.

To analyze the neutron skin in neutron-rich nuclei, we have theoretically studied its variation along the Sn and Pb isotopic chains up to the neutron drip line using selected mean-field models. As expected, $\Delta R_{np}$ shows a generally linear growing trend with $I$. However, shell effects, which are always present in mean-field calculations, produce noticeable departures from this linear dependence in nuclei with large neutron excesses.

Regarding the bulk and surface contributions to the neutron skin thickness in Sn isotopes, it can be seen that the considered mean-field models point toward more of a surface character in stable nuclei. This effect is reinforced in the neutron-rich region. In the case of the Pb isotopic chain, bulk and surface contributions have similar values in stable isotopes, whereas the bulk part is larger than the surface part in the more neutron-rich region of this isotopic chain.

## ACKNOWLEDGMENTS

This work was partially supported by the Spanish Consolider-Ingenio 2010 Programme Centro Nacional de Física de Partículas, Astropartículas y Nuclear CSD2007-00042 and by Grant Nos. FIS2005-03142 and FIS2008-01661 from Ministerio de Educación y Ciencia (Spain) and Fondo Europeo de Desarrollo Regional, Grant No. 2009SGR-1289 from Generalitat de Catalunya (Spain), and Grant No. N N202 231137 from Ministerstwo Nauki i Szkolnictwa Wyższego (Poland). X.R. also acknowledges Grant No. AP2005-4751 from MEC (Spain).

## APPENDIX

In two-parameter Fermi (2pF) density distributions

$$\rho_q(r) = \frac{\rho_{0q}}{1 + \exp\left[(r - C_q)/a_q\right]}, \tag{A1}$$

the number of particles and the mean square radii can be approximated, respectively, by the relationships

$$N_q = \frac{4}{3}\pi C_q^3 \rho_{0q}\left(1 + \frac{\pi^2 a_q^2}{C_q^2}\right) \tag{A2}$$

and

$$\langle r^2\rangle_q = \frac{3}{5}C_q^2\left(1 + \frac{7}{3}\frac{\pi^2 a_q^2}{C_q^2}\right), \tag{A3}$$

where $q = n, p, c$ denotes the neutron, proton, and charge distributions, respectively. The result of Eq. (A3) can be easily derived by recalling Eqs. (8), (11), (12), and (17) given in Sec. III.

From the relation existing between the charge and proton rms radii,

$$\langle r^2\rangle_c = \langle r^2\rangle_p + 0.64\ \text{fm}^2, \tag{A4}$$

together with normalization condition (A2), one can derive the parameters $a_p$ and $C_p$ of the 2pF point proton distribution if the parameters $a_c$ and $C_c$ of the experimental charge distribution are known (assuming that the central density is the same for charge and protons). The result for $a_p$ is

$$a_p = \frac{C_p}{\pi}\sqrt{\frac{3Z}{4\pi C_c^3 \rho_{0c}} - 1} \tag{A5}$$

and $C_p$ is obtained as

$$C_p = S_1 + S_2, \tag{A6}$$

where $S_1$ and $S_2$ are given by the equations

$$S_1^3 = T_1 + \sqrt{T_1^2 + T_2^3}, \tag{A7}$$

$$S_2^3 = T_1 - \sqrt{T_1^2 + T_2^3}, \tag{A8}$$

with

$$T_1 = \frac{21Z}{32\pi\rho_{0c}}, \qquad T_2 = \frac{5}{12}(\langle r^2\rangle_c - 0.64\ \text{fm}^2). \tag{A9}$$

Once $a_p$, $C_p$, and the rms radius of the point proton density are available, the following relationship between the parameters $a_n$ and $C_n$ of the neutron distribution can be applied:

$$a_n^2 = \frac{5}{7\pi^2}\left(\Delta R_{np} + \langle r^2\rangle_p^{1/2}\right)^2 - \frac{3}{7}\frac{C_n^2}{\pi^2}. \tag{A10}$$

This expression is obtained by inserting the neutron skin thickness $\Delta R_{np} = \langle r^2\rangle_n^{1/2} - \langle r^2\rangle_p^{1/2}$ of the nucleus in Eq. (A3) for $q = n$. Therefore, for the same $\langle r^2\rangle_p^{1/2}$ and $\Delta R_{np}$ values, one has a degenerate family of 2pF neutron densities depending on one parameter, which can be taken to be either $C_n - C_p$ or $a_n - a_p$ (recall that $C_p$ and $a_p$ are known). Alternatively, if the values of $\langle r^2\rangle_p^{1/2}$ and $C_n - C_p$ are given, one obtains a

family of $\Delta R_{np}$ values depending on the parameter $a_n - a_p$. As mentioned in the main text, the experiments in antiprotonic atoms were shown to preferentially support the situation of 2pF density distributions having $C_n - C_p \approx 0$ [38,39].

[1] G. Fricke, C. Bernhardt, K. Heilig, L. A. Schaller, L. Schellenberg, E. B. Shera, and C. W. de Jager, At. Data Nucl. Data Tables **60**, 177 (1995).
[2] I. Angeli, At. Data Nucl. Data Tables **87**, 185 (2004).
[3] B. A. Brown, Phys. Rev. Lett. **85**, 5296 (2000).
[4] S. Typel and B. A. Brown, Phys. Rev. C **64**, 027302 (2001).
[5] M. Centelles, M. Del Estal, X. Viñas, and S. K. Patra, in *The Nuclear Many-Body Problem 2001*, NATO Advanced Studies Institute Series B: Physics Vol. 53, edited by W. Nazarewicz and D. Vretenar (Kluwer, Dordrecht, 2002), p. 97.
[6] R. J. Furnstahl, Nucl. Phys. A **706**, 85 (2002).
[7] P. Danielewicz, Nucl. Phys. A **727**, 233 (2003).
[8] A. E. L. Dieperink, Y. Dewulf, D. Van Neck, M. Waroquier, and V. Rodin, Phys. Rev. C **68**, 064307 (2003).
[9] M. Baldo, C. Maieron, P. Schuck, and X. Viñas, Nucl. Phys. A **736**, 241 (2004).
[10] S. S. Avancini, J. R. Marinelli, D. P. Menezes, M. M. W. Moraes, and C. Providência, Phys. Rev. C **75**, 055805 (2007).
[11] M. Centelles, X. Roca-Maza, X. Viñas, and M. Warda, Phys. Rev. Lett. **102**, 122502 (2009).
[12] M. Warda, X. Viñas, X. Roca-Maza, and M. Centelles, Phys. Rev. C **80**, 024316 (2009).
[13] C. J. Horowitz and J. Piekarewicz, Phys. Rev. Lett. **86**, 5647 (2001); Phys. Rev. C **64**, 062802(R) (2001).
[14] T. Sil, M. Centelles, X. Viñas, and J. Piekarewicz, Phys. Rev. C **71**, 045502 (2005).
[15] A. W. Steiner, M. Prakash, J. M. Lattimer, and P. J. Ellis, Phys. Rep. **411**, 325 (2005).
[16] J. M. Lattimer and M. Prakash, Phys. Rep. **442**, 109 (2007).
[17] A. Klimkiewicz *et al.*, Phys. Rev. C **76**, 051603(R) (2007).
[18] B. A. Li, L. W. Chen, and C. M. Ko, Phys. Rep. **464**, 113 (2008).
[19] J. Piekarewicz and M. Centelles, Phys. Rev. C **79**, 054311 (2009).
[20] J. Xu, L. W. Chen, B. A. Li, and H. R. Ma, Astrophys. J. **697**, 1549 (2009).
[21] X. Y. Sun, D. Q. Fang, Y. G. Ma, X. Z. Cai, J. G. Chen, W. Guo, W. D. Tian, and H. W. Wang, Phys. Lett. B **682**, 396 (2010).
[22] I. Vidaña, C. Providência, A. Polls, and A. Rios, Phys. Rev. C **80**, 045806 (2009).
[23] A. Carbone, G. Coló, A. Bracco, L.-G. Cao, P. F. Bortignon, F. Camera, and O. Wieland, Phys. Rev. C **81**, 041301(R) (2010).
[24] S. Mizutori, J. Dobaczewski, G. A. Lalazissis, W. Nazarewicz, and P.-G. Reinhard, Phys. Rev. C **61**, 044326 (2000).
[25] N. Schunck and J. L. Egido, Phys. Rev. C **78**, 064305 (2008).
[26] C. J. Batty, E. Friedman, H. J. Gils, and H. Rebel, Adv. Nucl. Phys. **19**, 1 (1989).
[27] L. Ray, G. W. Hoffmann, G. S. Blanpied, W. R. Coker, and R. P. Liljestrand, Phys. Rev. C **18**, 1756 (1978).
[28] L. Ray and G. W. Hoffmann, Phys. Rev. C **31**, 538 (1985).
[29] V. E. Starodubsky and N. M. Hintz, Phys. Rev. C **49**, 2118 (1994).
[30] S. Karataglidis, K. Amos, B. A. Brown, and P. K. Deb, Phys. Rev. C **65**, 044306 (2002).
[31] B. C. Clark, L. J. Kerr, and S. Hama, Phys. Rev. C **67**, 054605 (2003).
[32] H. J. Gils, H. Rebel, and E. Friedman, Phys. Rev. C **29**, 1295 (1984).
[33] A. Krasznahorkay, M. Fujiwara, P. van Aarle, H. Akimune, I. Daito, H. Fujimura, Y. Fujita, M. N. Harakeh, T. Inomata, J. Jänecke, S. Nakayama, A. Tamii, M. Tanaka, H. Toyokawa, W. Uijen, and M. Yosoi, Phys. Rev. Lett. **82**, 3216 (1999).
[34] A. Krasznahorkay, H. Akimune, A. M. van den Berg, N. Blasi, S. Brandenburg, M. Csatlós, M. Fujiwara, J. Gulyaś, M. N. Harakeh, M. Hunyadi, M. de Huu, Z. Máte, D. Sohler, S. Y. van der Werf, H. J. Wörtche, and L. Zolnai, Nucl. Phys. A **731**, 224 (2004).
[35] P. Lubiński, J. Jastrzębski, A. Grochulska, A. Stolarz, A. Trzcińska, W. Kurcewicz, F. J. Hartmann, W. Schmid, T. von Egidy, J. Skalski, R. Smolańczuk, S. Wycech, D. Hilscher, D. Polster, and H. Rossner, Phys. Rev. Lett. **73**, 3199 (1994).
[36] P. Lubiński, J. Jastrzębski, A. Trzcińska, W. Kurcewicz, F. J. Hartmann, W. Schmid, T. von Egidy, R. Smolańczuk, and S. Wycech, Phys. Rev. C **57**, 2962 (1998).
[37] R. Schmidt, F. J. Hartmann, B. Ketzer, T. von Egidy, T. Czosnyka, J. Jastrzębski, M. Kisieliński, P. Lubiński, P. Napiorkowski, L. Pieńkowski, A. Trzcińska, B. Kłos, R. Smolańczuk, S. Wycech, W. Pöschl, K. Gulda, W. Kurcewicz, and E. Widmann, Phys. Rev. C **60**, 054309 (1999).
[38] A. Trzcińska, J. Jastrzębski, P. Lubiński, F. J. Hartmann, R. Schmidt, T. von Egidy, and B. Kłos, Phys. Rev. Lett. **87**, 082501 (2001).
[39] J. Jastrzębski, A. Trzcińska, P. Lubiński, B. Kłos, F. J. Hartmann, T. von Egidy, and S. Wycech, Int. J. Mod. Phys. E **13**, 343 (2004).
[40] B. Kłos, A. Trzcińska, J. Jastrzębski, T. Czosnyka, M. Kisieliński, P. Lubiński, P. Napiorkowski, L. Pieńkowski, F. J. Hartmann, B. Ketzer, P. Ring, R. Schmidt, T. von Egidy, R. Smolańczuk, S. Wycech, K. Gulda, W. Kurcewicz, E. Widmann, and B. A. Brown, Phys. Rev. C **76**, 014311 (2007).
[41] T. Dong, Y. Chu, Z. Ren, and Z. Wang, Phys. Rev. C **79**, 014317 (2009).
[42] W. J. Świątecki, A. Trzcińska, and J. Jastrzębski, Phys. Rev. C **71**, 047301 (2005).
[43] E. Friedman, A. Gal, and J. Mares, Nucl. Phys. A **761**, 283 (2005).
[44] S. Wycech, F. J. Hartmann, J. Jastrzębski, B. Kłos, A. Trzcińska, and T. von Egidy, Phys. Rev. C **76**, 034316 (2007).
[45] E. Friedman, Hyperfine Interact. **193**, 33 (2009).
[46] C. J. Batty, E. Friedman, and A. Gal, Nucl. Phys. A **592**, 487 (1995).
[47] W. M. Bugg, G. T. Condo, E. L. Hart, H. O. Cohn, and R. D. McCulloch, Phys. Rev. Lett. **31**, 475 (1973).
[48] A. Baran, K. Pomorski, and M. Warda, Z. Phys. A **357**, 33 (1997).
[49] R. W. Hasse and W. D. Myers, *Geometrical Relationships of Macroscopic Nuclear Physics* (Springer-Verlag, Heidelberg, 1988).
[50] H. De Vries, C. W. De Jager, and C. De Vries, At. Data Nucl. Data Tables **36**, 495 (1987).

[51] C. Garcia-Recio, J. Nieves, and E. Oset, Nucl. Phys. A **547**, 473 (1992).
[52] J. D. Patterson and R. J. Peterson, Nucl. Phys. A **717**, 235 (2003).
[53] G. Fricke, C. Bernhardt, K. Heilig, L. A. Schaller, L. Schellenberg, E. B. Shera, and C. W. de Jager, At. Data Nucl. Data Tables **60**, 177 (1995).
[54] J. F. Berger, M. Girod, and D. Gogny, Comput. Phys. Commun. **63**, 365 (1991).
[55] E. Chabanat, P. Bonche, P. Haensel, J. Meyer, and R. Schaeffer, Nucl. Phys. A **635**, 231 (1998).
[56] G. A. Lalazissis, J. König, and P. Ring, Phys. Rev. C **55**, 540 (1997).
[57] B. G. Todd-Rutel and J. Piekarewicz, Phys. Rev. Lett. **95**, 122501 (2005).
[58] M. Warda, B. Nerlo-Pomorska, and K. Pomorski, Nucl. Phys. A **635**, 484 (1998).

# 2 Symmetry energy and the outer crust of non-accreting neutron stars

## 2.1 Introduction

In 1934, Walter Baade and Fritz Zwicky proposed the existence of neutron stars as a supernovae remnant [Ba34] only two years after Chadwick's discovery of the neutron. Massive enough red super-giant stars —more than $8M_{\rm Sun}$— at the final stage of their evolution, *i.e.* when all nuclear fuel has been burnt, produce the so-called supernovae explosion whose remnant is a neutron star or a black hole. See Figure 10 for a pictorial representation of the main stages in star evolution including other possibilities as a final astrophysical object. As all the nuclear fuel is burnt, the neutron star cannot compensate

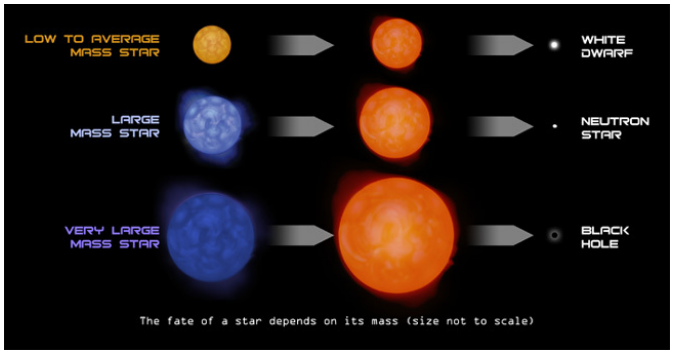


Figure 10: Main stages in star evolution. Scheme taken from NASA/CXC/SAO http://chandra.harvard.edu/graphics/resources/illustrations/stellar_fate2_650.jpg

the gravitational pressure burning light elements into heavier ones like happens in more common stars as the Sun. Then, how can neutron stars become stable? The answer is that as they are composed by fermions and, therefore, the pressure due to the Pauli Exclusion Principle stabilizes the star. This new type of equilibrium impacts on the structure of the neutron star. As a consequence, the ratio between its mass and size is several orders of magnitude larger than in normal stars. A typical neutron star with a mass of $\approx 1.4M_{\rm sun}$ has a radius about 12 km —see Table 2 for more details in its typical properties. These qualitative values of the main properties of a neutron star give us an

idea of the huge densities and intense gravity of this objects. Accounting for this and for the charge neutrality in the star, one could estimate within a simple model the huge pressure exerted by the electrons. Specifically, at the densities found in neutron stars at its outer layers, the electrons can be already treated as a degenerate Fermi gas. The more energetically favorable physical process under this conditions is that a proton captures an electron and form a neutron and an anti-neutrino. The latter gets rid of some energy lowering, in this way, the electron pressure. This process, namely $\beta^-$, are thought to be dominant during the formation of such stars and allow to understand why this stars were called neutron stars.

| $R$ (Km) | $\bar{\rho}$ (gr/cm$^3$) | $v_{\rm scape}/c$ | $g/g_{\rm Earth}$ (surface) | $P$ (dyn/cm$^2$) |
|---|---|---|---|---|
| 10 | $10^{14} - 10^{15}$ | 0.5 | $10^{11}$ | $0 - 10^{35}$ |

Table 2: Orientative properties of a typical neutron star of mass $M = M_{\rm Sun}$. $R$ is the radius, $\bar{\rho}$ is the mean density, $v_{\rm scape}$ is the scape velocity, $c$ is the speed of light, $g$ is the acceleration of the gravity and $P$ is the pressure.

Spanning many orders of magnitude in density, reaching pressures sixteen orders of magnitude higher than in Earth laboratories, spinning at frequencies of almost 1kHz, having magnetic fields twelve orders of magnitude larger than in the Earth surface, a neutron star is an object which requires a deep knowledge of the structure of matter. Furthermore, observers have recently discovered high-frequency oscillations in the tails of giant flares [Ko98] which are believed to be associated with seismic vibrations of the neutron star crust. The frequencies of such vibrations are thought to be very sensitive to the composition of the crust and, therefore, to the symmetry energy and its density dependence [Wa07]. Actually, neutron stars can synthesize very asymmetric nuclei, far asymmetric than produced in terrestrial laboratory conditions. Being, thus, a source for observational studies which could help in constraining nuclear properties in very extreme conditions. Motivated by this possibility, we studied the structure and composition of the outermost layer —apart from the "atmosphere"— of a non-accreting neutron star and present in the next section a publication of our results and conclusions. This layer, namely Outer Crust, is organized into a Coulomb lattice of neutron-rich nuclei embedded in a free electron gas. For its description, we employed among the most accurate nuclear models in nuclear mass predictions. And, as a reference to understand the main physical processes taking place in this layer, we also present a "Toy Model" based on the LDM. We focused our study on the sensitivity of the composition of the crust on the density dependence of the symmetry energy. Roughly, the neutron-richness of nuclei present in the Coulomb lattice is described by the competition between the electron pressure which lead the system to a neutron-pure crust via the $\beta^-$ process and the symmetry energy which opposes such a change. Hence, a precise characterization of the symmetry energy and its density dependence will impact on the structure and composition on the neutron

star crust.

# 2.2 Impact of the symmetry energy on the outer crust of non-accreting neutron stars

PHYSICAL REVIEW C **78**, 025807 (2008)

**Impact of the symmetry energy on the outer crust of nonaccreting neutron stars**

X. Roca-Maza[1] and J. Piekarewicz[2]
[1]*Departament d'Estructura i Constituents de la Matèria, Facultat de Física, Universitat de Barcelona, Diagonal 647, E-08028 Barcelona, Spain*
[2]*Department of Physics, Florida State University, Tallahassee, Florida 32306, USA*
(Received 16 May 2008; published 21 August 2008)

The composition and equation of state of the outer crust of nonaccreting neutron stars is computed by using accurate nuclear mass tables. The main goal of the present study is to understand the impact of the symmetry energy on the structure of the outer crust. First, a simple "toy model" is developed to illustrate the competition between the electronic density and the symmetry energy. Then, realistic mass tables are used to show that models with a stiff symmetry energy—those that generate large neutron skins for heavy nuclei—predict a sequence of nuclei in the stellar environment that is more neutron rich than their softer counterparts. This result may be phrased in the form of a correlation: The larger the neutron skin of $^{208}$Pb, the more exotic the composition of the outer crust.

DOI: 10.1103/PhysRevC.78.025807 PACS number(s): 26.60.Kp, 26.60.Gj, 21.65.Ef, 21.10.Dr

## I. INTRODUCTION

Neutron stars are gold mines for the study of nuclear systems under extreme conditions of density and isospin asymmetry [1,2]. Spanning many orders of magnitude in density, neutron stars display exotic phases that cannot be realized under normal laboratory conditions. Whereas the most common perception of a neutron star is that of a uniform mantle of neutrons packed to densities that may exceed that of normal nuclei by up to an order of magnitude, the reality is far different and much more interesting. First, although the uniform liquid mantle (also known as the outer core) is indeed composed mostly of neutrons, a small fraction of protons and an equal number of charged leptons (i.e., electrons and perhaps even muons) must be present to maintain beta equilibrium. The precise proton fraction in the neutron star is controlled by the *symmetry energy*, a quantity that imposes a penalty on the system as it departs from the isospin symmetric limit of equal number of neutrons and protons. Second, at densities that are below nuclear matter saturation density the uniform phase becomes unstable against density fluctuations. This nonuniform region of the neutron star constitutes the *crust*, which itself is divided into an inner and an outer region (see Fig. 1). In the outer crust—the main focus of the present study—the system is organized into a Coulomb lattice of neutron-rich nuclei embedded in a uniform electron gas [3]. As the density increases, nuclei become progressively more neutron rich until the neutron drip region is reached; this region defines the boundary between the outer and the inner crust. As in the case of the outer crust, the inner crust also consists of a Coulomb lattice of neutron-rich nuclei embedded in a uniform electron gas. Now, however, a uniform neutron vapor permeates the system. As the density continues to increase in the inner crust, the system is speculated to morph into a variety of complex and exotic structures, such as spheres, cylinders, rods, and plates—collectively known as *nuclear pasta* [4–6]. As the density increases even further, uniformity is eventually restored at about one-third of normal nuclear matter saturation density. Finally, at ultra high densities it has been established that the ground state of hadronic matter becomes a color superconductor in a color-flavor-locked (CFL) phase [7,8]. It is unknown, however, whether the density at the core of a neutron star may reach the extreme values required for the CFL phase to develop. Thus, other exotic phases—such as meson condensates, hyperonic matter, and/or quark matter—may be more likely to harbor the core of neutron stars. Figure 1 is believed to represent a plausible rendition of the structure of a neutron star.

As stated earlier, the main focus of our present study is the outer crust of the neutron star. In particular, we are interested in studying the sensitivity of the composition of the outer crust to the model dependence of the symmetry energy. The outer crust comprises a region spanning about seven orders of magnitude in density: from about $10^4$ g/cm$^3$ to a neutron drip density of about $4 \times 10^{11}$ g/cm$^3$ [3]. Although these densities are small relative to nuclear matter saturation density ($2.5 \times 10^{14}$ g/cm$^3$), the electrons (present to maintain charge neutrality) at such densities are no longer bound to nuclei and move freely throughout the crust. Moreover, at these low nuclear densities it is energetically favorable for the nuclei to arrange themselves in a crystalline lattice. At the lowest densities, the electronic contribution is negligible, so the Coulomb lattice is populated by $^{56}$Fe nuclei. However, as the density increases and the electronic contribution becomes important, $^{56}$Fe ceases to be the most energetically favorable nucleus. Instead, it becomes energetically advantageous for the system to lower its electron fraction by having the energetic electrons capture onto protons, with the excess energy carried away by neutrinos. The resulting nuclear lattice is now formed by nuclei having a slightly lower proton fraction than $^{56}$Fe (e.g.,$^{62}$Ni). As the density continues to increase, the nuclear system evolves into a Coulomb lattice of progressively more neutron rich nuclei until the critical neutron drip density is reached. The essential physics of the outer crust is then nicely captured by a "tug-of-war" between an electronic contribution and the nuclear symmetry energy, with the former favoring neutron-rich nuclei and the latter favoring fairly symmetric

 

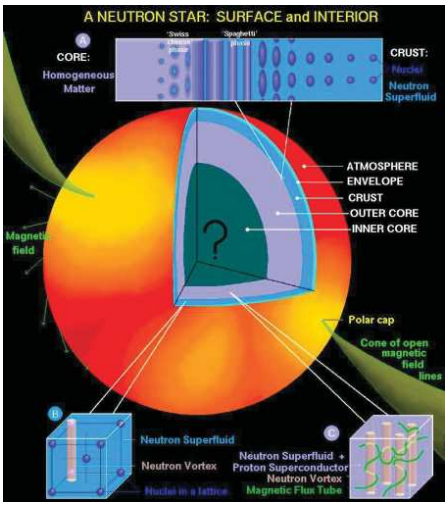


FIG. 1. (Color online) Rendition of the assumed structure and phases of a neutron star. (Figure courtesy of Dany Page.)

ones. The neutron-rich nuclei that populate the Coulomb lattice in the outer crust are on average more dilute than their more symmetric counterparts because of the development of a neutron skin. As a result, these nuclei may become sensitive to the symmetry energy below nuclear matter saturation density. However, whereas the symmetry energy is relatively well known around saturation density, its density dependence (e.g., its slope) is poorly constrained. This may affect the composition of the crust.

Although some theoretical constraints are starting to emerge [9,10], the density dependence of the symmetry energy remains largely unknown. Indicative of this fact is that accurately calibrated models of nuclear structure (both relativistic and nonrelativistic) that reproduce a variety of ground-state properties across the periodic table differ significantly in their predictions for the density dependence of the symmetry energy. Yet these same models have been used to uncover a strong correlation between the pressure of pure neutron matter at saturation density and the neutron skin of heavy nuclei: the larger the pressure the larger the neutron skin [11,12]. (Note that the pressure of pure neutron matter equals that of the symmetry energy at saturation density.) This fact may be illustrated by using the two accurately calibrated models that will be employed throughout this manuscript, namely, NL3 [13,14] and FSUGold [15]. Whereas NL3 predicts a pressure at saturation density of $P_0 \approx 6\,\mathrm{MeV/fm^3}$ and a corresponding neutron skin in $^{208}$Pb of $R_n - R_p \approx 0.28$ fm, FSUGold predicts the significantly lower values of $P_0 \approx 3\,\mathrm{MeV/fm^3}$ and $R_n - R_p \approx 0.21$ fm, respectively. The upcoming Parity Radius Experiment (PREx) at the Jefferson Laboratory will provide a unique experimental constraint on the density dependence of the symmetry by measuring the skin thickness of $^{208}$Pb accurately and model independently via parity-violating electron scattering [16,17]. The correlation between the density dependence of the symmetry energy and the neutron skin of heavy nuclei opened new horizons in nuclear astrophysics. Novel correlations between the neutron skin of $^{208}$Pb and a myriad of neutron-star observables were developed as a result of the similar composition of the neutron skin of a heavy nucleus and the inner crust/outer core of a neutron star [18–23]. One particularly interesting correlation of direct relevance to the crustal region is a "data-to-data" relation between the neutron skin of $^{208}$Pb and the crust-to-core transition density [18].

The recent observations of intense pulses of energetic $\gamma$ rays followed by fainter periodic signals emitted from highly magnetized neutron stars (or "magnetars") are sure to provide an additional new tool in the study of neutron-star structure [24–27]. The discovery of high-frequency oscillations in the tails of giant flares from soft gamma repeaters (i.e., magnetars with magnetic fields in excess of $10^{14}$ gauss [28–30]) are believed to be associated with seismic vibrations of the neutron star crust. Early theoretical models that assume a liquid-core/solid-crust interface suggest torsional shear oscillations of the crust as the most likely modes of excitation in a magnetar. The shear modulus of the crust acts as a restoring force for these modes and such a structural property is highly sensitive to the composition of the crust and, thereby, to the nuclear matter equation of state. Indeed, the shear-mode oscillations depend strongly on the neutron star mass, radius, and *crustal composition*—all properties sensitive to the equation of state [24]. Moreover, *ratios* of frequencies with different nodal structures may be used to determine the thickness of the crust, an observable highly sensitive to the equation of state and particularly to the density dependence of the symmetry energy [25,26]. Hence, as techniques continue to improve, we expect that neutron-star seismology will provide stringent limits on the equation of state of neutron-rich matter.

The manuscript has been organized as follows. The formalism required to compute the composition and equation of state of the outer crust is developed in Sec. II. In Sec. III we employ several realistic nuclear-mass models to compute the structure of the outer crust. Although not nearly as comprehensive as the recent study performed by Rüster, Hempel, and Schaffner-Bielich [31], ours includes a simple "toy model" that provides critical insights into the role played by the symmetry energy. Moreover, in the same section we illustrate the impact of the density dependence of the symmetry energy on the sequence of neutron-rich nuclei present in the outer crust. Our results and conclusions are summarized in Sec. IV.

## II. FORMALISM

In this section we develop the formalism necessary to understand the composition and equation of state of the outer crust of a neutron star. The formalism follows closely the seminal ideas introduced by Baym, Pethick, and Sutherland back in 1971 [3]. For more recent references that employ modern nuclear mass tables see Refs. [31–33]. The central question that one aims to answer is the following: What is the ground state of cold, fully catalyzed matter for densities

between complete ionization ($\rho \approx 10^4$ g/cm$^3$) and "neutron drip" ($\rho \approx 10^{11}$ g/cm$^3$)? Since at these densities uniform matter is unstable against cluster formation, a Coulomb lattice of nuclei embedded in a uniform free Fermi gas of electrons is formed. Thus, the composition of the outer crust is determined by that nucleus (with neutron number $N$, proton number $Z$, and baryon number $A = N + Z$) that minimizes—for each density—the total energy per nucleon of the system. In the outer crust (i.e., before neutron drip) the *energy per nucleon* consists of three different contributions: nuclear, electronic, and lattice. That is,

$$\varepsilon(A, Z; n) = \varepsilon_n + \varepsilon_e + \varepsilon_\ell, \tag{1}$$

where the baryon density is denoted by $n \equiv A_{\rm total}/V$. The nuclear contribution to the total energy per nucleon is simple and independent of the density. It is given by

$$\varepsilon_n(N, Z) \equiv \frac{M(N, Z)}{A},$$

with

$$M(N, Z) = Nm_n + Zm_p - B(N, Z). \tag{2}$$

Here $M(N, Z)$ is the nuclear mass, $B(N, Z)$ is the corresponding binding energy, and $m_n$ and $m_p$ are neutron and proton masses, respectively.

The electronic contribution—at least at the densities of interest ($\rho \gtrsim 10^4$ g/cm$^3$)—is modeled as a degenerate free Fermi gas [3]. That is,

$$\varepsilon_e(A, Z; n) = \frac{\mathscr{E}_e}{n} = \frac{1}{n\pi^2}\int_0^{p_{\rm Fe}} p^2\sqrt{p^2 + m_e^2}\, dp, \tag{3}$$

where $\mathscr{E}_e$, $m_e$, and $p_{\rm Fe}$ are the electronic energy density, mass, and Fermi momentum, respectively. Note that the electronic Fermi momentum and baryon density are related as follows:

$$p_{\rm Fe} = (3\pi^2 n_e)^{1/3} = (3\pi^2 yn)^{1/3} \equiv y^{1/3} p_F, \tag{4}$$

where the electron fraction $y \equiv Z/A$ has been defined. Moreover, for future convenience the following definition of the overall Fermi momentum has been introduced:

$$p_F = (3\pi^2 n)^{1/3}. \tag{5}$$

As the integral in Eq. (3) may be evaluated analytically, the electronic contribution may be computed in closed form. That is,

$$\varepsilon_e(A, Z; n) = \frac{m_e^4}{8\pi^2 n}\left[x_F y_F\left(x_F^2 + y_F^2\right) - \ln(x_F + y_F)\right], \tag{6}$$

where dimensionless Fermi momentum and energy have been defined as follows:

$$x_F \equiv \frac{p_{\rm Fe}}{m_e} \quad \text{and} \quad y_F \equiv \frac{\epsilon_{\rm Fe}}{m_e} = \sqrt{1 + x_F^2}. \tag{7}$$

We now discuss the last term in Eq. (1). Whereas the Coulomb repulsion within the individual nuclei has been properly included in Eq. (2), the Coulomb repulsion among nuclei as well as their interactions with the uniform electron background has not. At the densities and temperatures of relevance to the outer crust, namely, large enough for full ionization but small enough for the Coulomb repulsion among nuclei to dominate over their kinetic energy, Wigner has shown (in the context of the electron gas) that the system will crystallize into a body-centered-cubic lattice [34–36]. The last term in Eq. (1) represents the lattice contribution to the energy per particle. The calculation of the potential energy of the Coulomb lattice is complicated. It consists of divergent contributions that must be canceled as required by the overall charge neutrality of the system. Fortunately, accurate numerical calculations for the electron gas have been available for a long time [37,38] and these results can be readily generalized to the present case [3]. Indeed, the lattice energy per nucleus may be written as

$$\frac{E_\ell}{N_c} = -(1.81962)\frac{(Ze)^2}{a} = -(1.79186)\frac{(Ze)^2}{2r_0}, \tag{8}$$

where $N_c$ is the number of nuclei (i.e., $A$-body clusters), $a$ is the lattice constant, and $r_0$ is a length scale related to the volume per nuclei. For the particular case of a body-centered-cubic lattice, these quantities are related in the following way:

$$n_c a^3 = \frac{N_c}{V}a^3 = 2 \quad \text{or} \quad \left(\frac{a}{2r_0}\right) = \left(\frac{\pi}{3}\right)^{1/3}. \tag{9}$$

Using the fact that the number of nuclei is related to the total baryon number of the system as

$$N_c = \frac{A_{\rm total}}{A} = \frac{N_{\rm total}}{N} = \frac{Z_{\rm total}}{Z}, \tag{10}$$

we can write the lattice contribution to the energy per baryon in closed form as follows:

$$\varepsilon_\ell(A, Z; n) = -\frac{(1.79186)}{A^{4/3}}\frac{(Ze)^2}{2R_0}. \tag{11}$$

Note that here $R_0$ refers to the length scale associated with the volume per *baryon* ($r_0 = A^{1/3}R_0$). That is,

$$R_0 = \left(\frac{3}{4\pi n}\right)^{1/3} = \left(\frac{9\pi}{4}\right)^{1/3} {p_F}^{-1}. \tag{12}$$

By using these definitions, the lattice contribution becomes equal to

$$\varepsilon_\ell(A, Z; n) = -C_\ell \frac{Z^2}{A^{4/3}} p_F \quad (\text{with } C_\ell = 3.40665 \times 10^{-3}). \tag{13}$$

For completeness, the full expression for the energy per baryon is now displayed in terms of the individual *nuclear, electronic,* plus *lattice* contributions:

$$\begin{aligned}\varepsilon(A, Z; n) &= \frac{M(N, Z)}{A} + \frac{m_e^4}{8\pi^2 n}\left[x_F y_F\left(x_F^2 + y_F^2\right) - \ln(x_F + y_F)\right] \\ &\quad - C_\ell \frac{Z^2}{A^{4/3}} p_F.\end{aligned} \tag{14}$$

Note that given $A$, $Z$, and $n = A_{\rm total}/V$, the only unknown quantity in this expression is the nuclear mass $M(N, Z)$. Although experimentally available for a large number of nuclei around the line of stability, nuclear masses near the drip line are unknown, thereby making the need for theoretical extrapolations unavoidable. As crustal properties become

better determined, nuclear masses at the drip line will be strongly constrained. Alternatively, the advent of facilities capable of producing beams of rare isotopes to explore the limits of nuclear existence will place strong constraints on crustal properties.

Having computed the energy per baryon of the system, we are now in a position to compute two additional thermodynamic properties that are essential for the understanding of both the structure and composition of the outer crust. These are the equation of state, namely, the relation between pressure and density, and the chemical potential. Recall that in modeling the outer crust the central assumption is that of thermal, hydrostatic, and chemical equilibrium. Thus, complete equilibrium demands the equality of temperature, pressure, and chemical potential at each layer of the outer crust.

At zero temperature and for a constant number of particles, the pressure of the system may be computed from the total energy of the system. As the individual nuclei do not contribute to the pressure, one must only compute the electronic and lattice contributions. In particular, the electronic contribution at zero temperature is given by

$$P_e \underset{T=0}{=} -\left(\frac{\partial E_e}{\partial V}\right)_Z = \frac{x_F}{3}\left(\frac{\partial \mathscr{E}_e}{\partial x_F}\right) - \mathscr{E}_e = \frac{m_e^4}{3\pi^2}\left(x_F^3 y_F - \frac{3}{8}\left[x_F y_F\left(x_F^2 + y_F^2\right) - \ln(x_F + y_F)\right]\right). \tag{15}$$

Similarly, the lattice contribution to the pressure is given by the following simple expression:

$$P_\ell \underset{T=0}{=} -\left(\frac{\partial E_\ell}{\partial V}\right)_{A,Z} = -\frac{n}{3} C_\ell \frac{Z^2}{A^{4/3}} p_F. \tag{16}$$

In this manner the full (*electronic* plus *lattice*) contribution to the pressure may be written as

$$P(A, Z; n) = \frac{m_e^4}{3\pi^2}\left(x_F^3 y_F - \frac{3}{8}\left[x_F y_F\left(x_F^2 + y_F^2\right) - \ln(x_F + y_F)\right]\right) - \frac{n}{3} C_\ell \frac{Z^2}{A^{4/3}} p_F. \tag{17}$$

As alluded to earlier, full equilibrium in the system is established by demanding that the temperature, pressure, and chemical potential—but not necessarily the baryon density—be continuous throughout the outer crust. As the temperature of the system is assumed to be equal to zero, the only remaining thermodynamic observable to calculate is the chemical potential. At zero temperature, the Gibbs free energy and the total energy of the system are related by a Legendre transform ($G = E + PV$). That is,

$$\mu(A, Z; P) = \frac{G(A, Z; P)}{A_{\text{total}}} = \varepsilon(A, Z; n) + \frac{P}{n} = \frac{M(N, Z)}{A} + \frac{Z}{A}\mu_e - \frac{4}{3} C_\ell \frac{Z^2}{A^{4/3}} p_F, \tag{18}$$

where $\mu_e = \sqrt{p_{\text{Fe}}^2 + m_e^2}$ is the electronic chemical potential. Note that the chemical potential is a function of the pressure whereas the energy per baryon is a function of the baryon density. The transformation from one into the other is accomplished through Eq. (17). Also note that as hydrostatic and chemical equilibrium must be maintained throughout the star, it is convenient to compute the composition of the outer crust by minimizing the Gibbs free energy per particle (i.e., $\mu$) at constant pressure rather than by minimizing the energy per particle at constant baryon density. This procedure will be carried out in the next section.

## III. RESULTS

In this section results will be presented for the structure and composition of the outer crust. The implementation of the ideas developed in the previous section will be carried out by using various models for nuclear masses. Two of these models are based on sophisticated microscopic/macroscopic models that yield root-mean-square (rms) errors of only a fraction of an MeV when compared to large databases of available experimental nuclear masses [39,40]. These two models are the ones by Duflo and Zuker [41–43] and the finite range droplet model of Möller, Nix, and collaborators [44,45]. The other two models are based on accurately calibrated microscopic approaches that employ a handful of empirical parameters to reproduce the ground-state properties of finite nuclei and some collective excitations [13–15]. Although these microscopic approaches are successful, their rms errors are significantly larger than those obtained with the microscopic/macroscopic models. Yet one of the great advantages of the microscopic models is the ability to systematically study the impact of unknown physics on crustal properties. First and foremost, we are interested in understanding how models that are equally successful in describing available ground-state properties of finite nuclei differ in their predictions of exotic (neutron-rich) nuclei.

### A. Toy model of the outer crust

Although the structure and composition of the crust will be ultimately computed using sophisticated mass formulas, we start by introducing a "toy model" that despite its simplicity captures the essential physics of the outer crust, namely, a competition between an electronic density that drives the system toward more neutron rich nuclei and a nuclear symmetry energy that opposes such a change.

The toy model consists of the following two approximations. First, a simple liquid-drop model will be used to compute nuclear masses [see Eq. (2)]. Second, the electronic contribution will be assumed to be that of an extremely relativistic (i.e., $m_e/p_{\text{Fe}} \to 0$) Fermi gas. Although both of these approximations will be relaxed in the next section, we believe that the physical insights that one develops from this analytic treatment are valuable.

The liquid-drop mass formula may be written in the absence of pairing correlations [and by assuming $Z(Z-1) \approx Z^2$] as

follows:

$$\varepsilon_n(x,y) = m_p y + m_n(1-y) - a_v + \frac{a_s}{x} + a_c x^2 y^2 + a_a(1-2y)^2, \tag{19}$$

where $x \equiv A^{1/3}$ and $y \equiv Z/A$ is the proton (or electron) fraction. The various empirical constants ($a_v, a_s, a_c$, and $a_a$) represent volume, surface, Coulomb, and asymmetry contribution, respectively. Using a least-square fit to 2049 nuclei (available online at the UNEDF collaboration Web site `http://www.unedf.org/`) one obtains the following values for the four empirical constants:

$$\begin{aligned} a_v &= 15.71511\,\text{MeV}, \quad a_s = 17.53638\,\text{MeV}, \\ a_c &= 0.71363\,\text{MeV}, \quad a_a = 23.37837\,\text{MeV}. \end{aligned} \tag{20}$$

To understand the competition among the various terms—and to anticipate how this competition will be modified in the presence of a Fermi gas of electrons—we compute the optimal values of $x$ and $y$ using the simple liquid-drop formula by setting both derivatives equal to zero. That is,

$$\left(\frac{\partial \varepsilon_n}{\partial x}\right)_y = -\frac{a_s}{x^2} + 2a_c x y^2 = 0, \tag{21a}$$

$$\left(\frac{\partial \varepsilon_n}{\partial y}\right)_x = -\Delta m + 2a_c x^2 y - 4a_a(1-2y) = 0, \tag{21b}$$

where we have defined $\Delta m \equiv m_n - m_p$. This set of equations has the following simple analytic solution:

$$A = x^3 = \left(\frac{a_s}{2a_c}\right)\frac{1}{y^2}, \tag{22a}$$

$$y = \frac{1+\left(\dfrac{\Delta m}{4a_a}\right)}{2+\left(\dfrac{a_c}{2a_a}\right)x^2} \approx \frac{1/2}{1+\left(\dfrac{a_c}{4a_a}\right)x^2}. \tag{22b}$$

These solutions suggest the following physical interpretation. For a fixed proton fraction $y = Z/A$, the optimal value of $x$ emerges from a competition between the surface contribution (which favors large $x$) and the Coulomb contribution (which favors small $x$). For the set of empirical constants given in Eq. (20), the relevant ratio is given by $a_s/2a_c \approx 12.287$. Conversely, if $A = x^3$ is held fixed, then the optimal proton fraction $y$ results from the competition between Coulomb and asymmetry contributions, with the former favoring $y = 0$ and the latter $y = 1/2$. If both equation are solved simultaneously, then one finds the most stable nucleus for this parameter set. One obtains $x_0 = 3.906$ and $y_0 = 0.454$, or, equivalently,

$$\begin{aligned} A_0 &= 59.598, \quad Z_0 = 27.060, \quad N_0 = 32.538, \\ (B/A)_0 &= 8.784\,\text{MeV}, \quad m_0 = 930.195\,\text{MeV}, \end{aligned} \tag{23}$$

with $m_0 \equiv (M/A)_0$ being the nuclear mass per nucleon.

The second assumption defining the toy model is that of an extremely relativistic Fermi gas of electrons (i.e., $p_{\text{Fe}} \gg m_e$). In this limit one obtains simple expressions for the total energy per baryon, chemical potential, and pressure in terms of the adopted set of variables. That is,

$$\varepsilon(x,y,p_F) = \varepsilon_n(x,y) + \frac{3}{4}y^{4/3}p_F - C_\ell\, x^2 y^2 p_F, \tag{24a}$$

$$\mu(x,y,p_F) = \varepsilon_n(x,y) + y^{4/3}p_F - \frac{4}{3}C_\ell\, x^2 y^2 p_F, \tag{24b}$$

$$P(x,y,p_F) = \frac{n}{4}y^{4/3}p_F - \frac{n}{3}C_\ell\, x^2 y^2 p_F. \tag{24c}$$

Before assessing the quantitative impact of the density-dependent (i.e., electronic and lattice) contributions on the semiempirical mass formula, a few comments are in order. First, at the predicted neutron drip density of about $4 \times 10^{11}$ g/cm$^3$, the Fermi momentum is approximately equal to $p_F^{\max} \approx 40$ MeV. This suggests a large electronic contribution at those densities of about $\varepsilon_e^{\max} \approx 30\, y^{4/3}$ MeV. As the nuclear contribution is independent of density, the electrons will drive the system to small values of $y$. Second, the lattice contribution (perhaps not surprisingly) has the same dependence on $x$ and $y$ as the Coulomb contribution to the semiempirical mass formula. Indeed, the full impact of the lattice contribution can be included through a redefinition, albeit a density-dependent one, of the Coulomb coefficient. That is, $a_c \to \widetilde{a}_c(p_F) \equiv (a_c - C_\ell p_F)$. As the optimal value of the proton fraction $y$ (for fixed $x$) emerges from a competition between Coulomb and asymmetry terms [see Eq. (22b)], the lattice contribution drives the system toward the symmetric $y = 1/2$ limit. Yet the lattice contribution is marginal. Indeed, even at neutron drip densities its contribution provides a meager, although by no means negligible, correction to the dominant Coulomb term. These two facts summarize the main structure of the outer crust, namely, a nuclear lattice embedded in an electron gas that is responsible for driving the system toward progressively more neutron rich nuclei. Thus the outer crust represents a unique laboratory for the study of neutron-rich nuclei in the $Z \approx 20$–$50$ region. As such, it nicely complements rare-isotope facilities worldwide that aim to provide a detailed map of the nuclear landscape.

Incorporating electronic and lattice contributions to the semiempirical mass formula yields the following expression for the total energy per nucleon of the system:

$$\varepsilon(x,y,p_F) = m_p y + m_n(1-y) - a_v + \frac{a_s}{x} + a_c x^2 y^2 + a_a(1-2y)^2 + \frac{3}{4}y^{4/3}p_F - C_\ell\, x^2 y^2 p_F. \tag{25}$$

As done before for the pure nuclear contribution, the optimal values of $x$ and $y$—at fixed density—may be obtained by setting both derivatives equal to zero. That is,

$$\left(\frac{\partial \varepsilon}{\partial x}\right)_{y,p_F} = -\frac{a_s}{x^2} + 2\widetilde{a}_c x y^2 = 0, \tag{26a}$$

$$\left(\frac{\partial \varepsilon_n}{\partial y}\right)_{x,p_F} = -\Delta m + 2\widetilde{a}_c x^2 y - 4a_a(1-2y) + y^{1/3}p_F = 0, \tag{26b}$$

where a "renormalized" Coulomb coefficient has been defined as

$$\widetilde{a}_c(p_F) \equiv (a_c - C_\ell p_F). \tag{27}$$

#### 1. First-order solution

Before providing exact solutions to Eqs. (26), we compute approximate solutions that are accurate to first order in $p_F$. In addition of being analytic, these closed-form expressions provide valuable insights into the composition of the outer crust. The first-order solutions are obtained by incorporating the density dependence in the following form:

$$x(p_F) = x_0(1+\xi) \quad \text{and} \quad y(p_F) = y_0(1+\eta), \tag{28}$$

where both $\xi$ and $\eta$ represent small (i.e., first-order in $p_F$) deviations from the zero-density results. Substituting these equations into Eqs. (26) yields the first-order solutions. One obtains

$$\begin{aligned} x(p_F) &= x_0\left[1+\left(\frac{(C_1-1)C_\ell+2C_2}{3C_1-1}\right)\frac{p_F}{a_c}\right] \\ &= (3.90610+0.03023p_F), \end{aligned} \tag{29a}$$

$$\begin{aligned} y(p_F) &= y_0\left[1-\left(\frac{3C_2-C_\ell}{3C_1-1}\right)\frac{p_F}{a_c}\right] \\ &= (0.45405-0.00419p_F). \end{aligned} \tag{29b}$$

Note that in these expressions the Fermi momentum should be given in MeV. Moreover, for simplicity the following two dimensionless quantities were introduced:

$$C_1 \equiv \frac{4a_a}{x_0^2 a_c} \approx 8.58843 \quad \text{and} \quad C_2 \equiv \frac{1}{2x_0^2 y_0^{2/3}} \approx 0.05547. \tag{30}$$

The first-order equations [Eqs. (29)]—while not necessarily quantitatively accurate—provide useful insights into how the composition of the outer crust evolves with density. As previously suggested, the proton fraction $y$ decreases with density in an effort to minimize the "repulsive" electronic contribution. Indeed, to an excellent approximation Eq. (29b) may be written in the following simple form:

$$y(p_F) = y_0 - \frac{p_{\rm Fe}}{8a_a} = (0.45405 - 0.00411\,p_F). \tag{31}$$

As indicated in Eq. (22b), the optimal value of $y_0$ emerges from a competition between Coulomb and asymmetry terms, with the former driving $y_0$ toward zero and the latter toward one half. This equation indicates that the evolution of $y$ with density is controlled by the dimensionless ratio of $p_{\rm Fe}/a_a$, suggesting that the larger the value of the asymmetry energy, the slower the evolution away from $y_0$, that is, the more symmetric the nucleus will remain. Moreover, as the denominator in Eq. (31) [$8a_a \approx 100$ MeV] is significantly larger than the electronic Fermi momentum over the entire region of interest, the first-order approximation is expected to be fairly accurate over the entire outer crust. Indeed, assuming a realistic value for the drip density of $\rho_{\rm drip} = 4\times10^{11}\,{\rm g/cm^3}$ yields a proton fraction of $y_{\rm drip} = 0.298$. This represents a 2% deviation from the value of $y(^{118}{\rm Kr}) = 0.305$ for the conventionally accepted drip nucleus $^{118}$Kr.

#### 2. Exact solution

The exact solution to the toy-model problem requires (for a fixed value of $p_F$) finding the simultaneous roots of Eqs. (26a) and (26b). Although the exact solution is numerically simple, it cannot be displayed in closed form. Yet the exact solution differs only slightly from the $C_\ell \equiv 0$ solution—which has an analytic, albeit a bit unorthodox, solution. The closed-form solution for the $C_\ell \equiv 0$ case may be obtained by simply rewriting Eqs. (26) as

$$x(y) = \left(\frac{a_s}{2a_c y^2}\right)^{1/3}, \tag{32a}$$

$$p_F(y) = \frac{\Delta m - 2a_c x^2 y + 4a_a(1-2y)}{y^{1/3}}. \tag{32b}$$

This set of equations suggests that rather than looking for a solution of $x$ and $y$ as a function of $p_F$, one should "solve" for $x$ and $p_F$ as a function of $y$, with the maximum value of $y$ given by $y_{\rm max} = y_0 = 0.45405$ and the minimum value of $y$ given by the condition $\mu(y_{\rm min}) = m_n$.

In Fig. 2 the baryon number $x = A^{1/3}$ and proton fraction $y = Z/A$ are displayed as a function of the Fermi momentum $p_F \equiv (3\pi^2 n)^{1/3}$. The black solid line displays the exact numerical solution to the toy-model problem [see Eqs. (26)]. In this simple model, the drip line density is predicted to be at $\rho_{\rm drip} = 4\times10^{11}\,{\rm g/cm^3}$ with the drip line nucleus being $^{154}$Cd (i.e., $Z = 48$ and $N = 106$). The solution obtained by ignoring the lattice contribution is displayed by the red dashed line. Because the lattice contribution to the chemical potential is negative, the $C_\ell \equiv 0$ solution reaches the drip line faster (i.e., at a lower density). Moreover, as the lattice contribution "renormalizes" the Coulomb term in the semiempirical mass formula (or, equivalently, enhances the role of the symmetry energy) the $C_\ell \equiv 0$ solution predicts a lower proton fraction

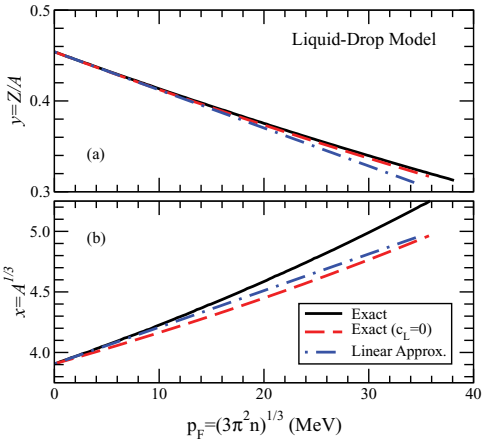


FIG. 2. (Color online) Proton fraction $y = Z/A$ (a) and baryon number $x = A^{1/3}$ (b) displayed as a function of the Fermi momentum $p_F \equiv (3\pi^2 n)^{1/3}$. The black solid lines represent the exact solution to the toy-model problem given in Eqs. (26), the red dashed lines display the corresponding solution in the $C_\ell \equiv 0$ (no lattice) limit [see Eqs. (32)], and the low-density solution [Eqs. (29)] is displayed by the blue dot-dashed lines.

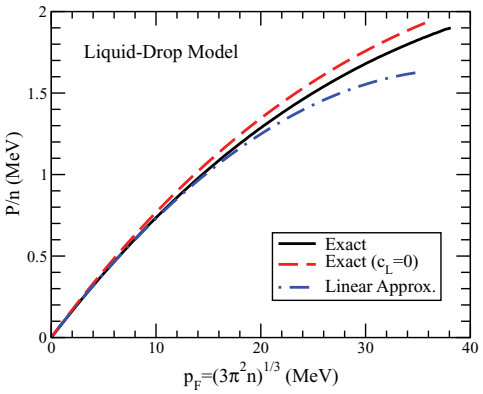


FIG. 3. (Color online) Pressure as a function of the Fermi momentum $p_F \equiv (3\pi^2 n)^{1/3}$. The black solid line represent the exact solution to the toy-model problem, the red dashed line displays the corresponding $C_\ell \equiv 0$ (no lattice) solution, and the low-density solution is displayed by the blue dot-dashed line.

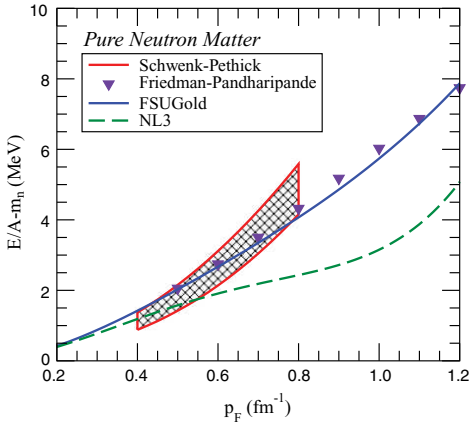


FIG. 4. (Color online) Energy per particle for pure neutron matter as a function of the neutron Fermi momentum. Shown are the microscopic model of Friedman and Pandharipande [46] (purple triangles) and the *model-independent* result based on the physics of resonant Fermi gases by Schwenk and Pethick [9] (red region). Also shown are the predictions from the accurately calibrated NL3 [13,14] (green dashed line) and FSUGold [15] (blue line) parameter sets.

than the exact solution. Finally, the dot-dashed blue line displays the solution correct to first order in $p_F$. In the particular case of the proton fraction $y$, the approximate linear solution $y = y_0 - p_{\rm Fe}/8a_a$ [Eq. (31)] reproduces fairly accurately the behavior of the exact solution.

The equation of state (i.e., pressure versus density) predicted by the toy model is displayed in Fig. 3. Because the lattice provides a negative contribution to the pressure [Eq. (24c)], the equation of state for the $C_\ell \equiv 0$ case is slightly stiffer than the exact one. The first-order solution in $p_F$ provides a quantitatively accurate description of the equation of state up to fairly large values of the density. Note that the first-order approximation to the pressure is defined as follows:

$$\frac{P}{np_F} = \frac{1}{4}y^{4/3} - \frac{1}{3}C_\ell\, x^2 y^2 \approx (0.08367 - 0.00106 p_F). \quad (33)$$

### B. Realistic models of the outer crust

In this section we employ realistic nuclear mass models to compute the structure and composition of the outer crust. Two of the models [41–45] are based on sophisticated mass formulas that have been calibrated to thousands of available experimental masses throughout the periodic table [39,40]. The other two models are based on accurately calibrated microscopic approaches that employ a handful of empirical parameters to reproduce the ground-state properties of finite nuclei and some nuclear collective excitations [13–15].

Whereas the microscopic models have yet to attain the level of precision displayed by the microscopic/macroscopic ones, they are valuable in elucidating various details of the underlying physics. For example, in the previous section we established the critical role played by the symmetry energy in the evolution of the proton fraction with density [see Eq. (31)]. However, it is unknown how the symmetry energy coefficient $a_a$ changes as nuclei move toward the drip line. Presumably, the development of a significant neutron skin makes these nuclei (on average) more dilute than their stable counterparts. If so, one needs to extrapolate the symmetry energy to lower densities, a procedure that is highly uncertain because of our poor knowledge of the slope of the symmetry energy. To illustrate this uncertainty, the equations of state of pure neutron matter predicted by NL3 (green dashed line) and FSUGold (blue solid line) are displayed in Fig. 4. For comparison, we also show the predictions from the microscopic model of Friedman and Pandharipande based on realistic two-body interactions [46] (purple upside-down triangles) and the *model-independent* result based on the physics of resonant Fermi gases by Schwenk and Pethick [9] (red hatched region). Note that, to a very good approximation, the equation of state of pure neutron matter equals that of symmetric nuclear matter plus the symmetry energy. The differences between NL3 and FSUGold displayed in Fig. 4 are all due to the large uncertainties in the symmetry energy. In particular, as NL3 predicts a stiffer equation of state than FSUGold, namely, one whose energy increases faster with density at high densities, the symmetry energy of NL3 is lower than that of FSUGold at subsaturation densities. Thus, FSUGold has been shown to reach the neutron drip lines earlier than NL3 [47]. By the same token, NL3 should predict a sequence of more neutron rich nuclei (lower $y$) in the outer crust than FSUGold.

Shown in the left-hand panel of Fig. 5 is the proton fraction predicted by the two microscopic models, FSUGold (blue solid line) and NL3 (green dashed line). Also shown is the simple prediction obtained from the liquid-drop formula [Eq. (31)]. The proton fraction predicted with the FSUGold parameter

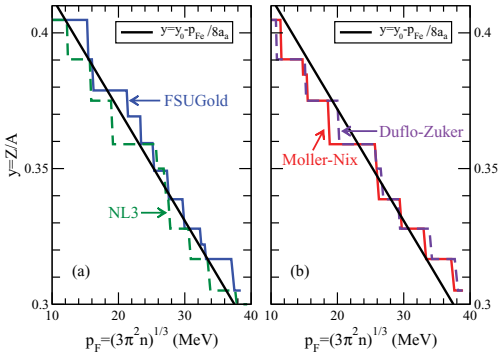


FIG. 5. (Color online) (a) The proton fraction predicted by the accurately calibrated FSUGold (blue solid line) and NL3 (green dashed line) parameter sets along with the simple liquid-drop formula given in Eq. (31). (b) The corresponding proton fraction as predicted by the mass formulas from Moller-Nix (red solid line) and Duflo-Zuker (purple dashed line).

set is consistently higher than for the NL3 set. This is a reflection of the stiffer penalty imposed on the FSUGold set for departing from the symmetric ($N = Z$) limit. The right-hand panel shows the corresponding behavior for the case of the microscopic/macroscopic models of Moller-Nix (red solid line) and Duflo-Zuker (purple dashed line). Differences among these two models are small.

Similar trends may be observed in Figs. 6 and 7, where the composition of the outer crust is displayed as a function of density. As the system makes a rapid jump in neutron number (say to magic number $N = 50$) the proton number

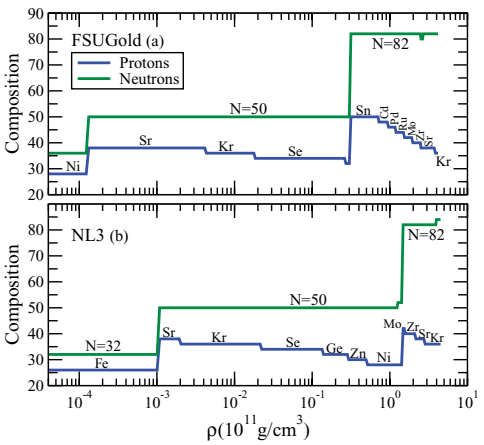


FIG. 6. (Color online) Composition of the outer crust of a neutron star as predicted by the accurately calibrated FSUGold (a) and NL3 (b) parameter sets. Protons are displayed with the (lower) blue line and neutrons with the (upper) green line.

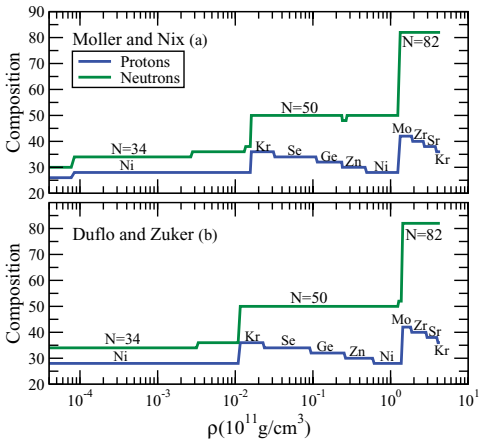


FIG. 7. (Color online) Composition of the outer crust of a neutron star as predicted by using the mass formulas of Moller-Nix (a) and Duflo-Zuker (b). Protons are displayed with the blue (lower) line and neutrons with the green (upper) line.

jumps with it. Along this neutron plateau, the proton fraction decreases systematically with increasing density in an effort to reduce the electronic contribution to the chemical potential. Eventually, the neutron-proton mismatch is too large and the jump to the next neutron plateau ensues—a jump that is driven by the symmetry energy. Clearly, the larger the symmetry energy is at low densities, the smaller is the neutron-proton mismatch and the earlier is the jump to the next neutron plateau. These features are clearly displayed in Fig. 6 as one contrasts the behavior of FSUGold to that of NL3. In contrast,

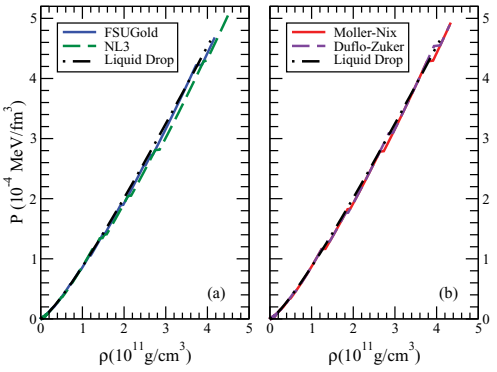


FIG. 8. (Color online) (a) The zero-temperature equation of state (pressure versus density) predicted by the accurately calibrated FSUGold (blue solid line) and NL3 (green dashed line) parameter sets along with the prediction from the simple liquid-drop formula. (b) The corresponding expression as predicted by the mass formulas from Moller-Nix (red solid line) and Duflo-Zuker (purple dashed line).

TABLE I. Equation-of-state observables (mass density, baryon density, pressure, and electronic chemical potential) and composition (nucleus and binding energy per nucleon) at the base of the outer crust.

| Model | $\rho$ ($10^{11}$ g/cm$^3$) | $n$ ($10^{-4}$ fm$^{-3}$) | $P$ ($10^{-4}$ MeV/fm$^3$) | $\mu_e$ (MeV) | Element | $B/A$ (MeV) |
|---|---|---|---|---|---|---|
| Moller-Nix | 4.34 | 2.60 | 4.93 | 26.22 | $^{118}$Kr | 7.21 |
| Duflo-Zuker | 4.32 | 2.58 | 4.89 | 26.17 | $^{118}$Kr | 7.19 |
| FSUGold | 4.17 | 2.50 | 4.68 | 25.88 | $^{118}$Kr | 7.11 |
| NL3 | 4.49 | 2.69 | 5.06 | 26.39 | $^{120}$Kr | 7.13 |

few differences are noticeable in Fig. 7 when comparing the model of Moller-Nix to that of Duflo-Zuker.

We conclude this section by displaying in Fig. 8 equation-of-state (pressure-versus-density) predictions for the outer crust of a neutron star. The left-hand panel shows results from calculations using the FSUGold (blue solid line) and NL3 (green dashed line) parameter sets. Although barely visible, the density shows discontinuities at those places where the composition changes abruptly. It is also noted that the FSUGold parametrization predicts a pressure that rises slightly faster with density than that of NL3. For the NL3 set, the symmetry energy admits lower values of the proton/electron fraction $y$, which, in turn, lowers the pressure of the system. Lower values of $y$ also yield lower values of the chemical potential, thereby delaying the arrival to the neutron drip line. Indeed, whereas FSUGold predicts a drip line density of $\rho_{\rm drip} = 4.17 \times 10^{11}$ g/cm$^3$, with NL3 the transition is delayed by about 8%, or until $\rho_{\rm drip} = 4.49 \times 10^{11}$ g/cm$^3$. A similar plot is shown for the microscopic/macroscopic models of Moller-Nix (red solid line) and Duflo-Zuker (purple dashed line). Differences between these two models are barely noticeable. Indeed, drip line densities in both models are predicted at about $\rho_{\rm drip} = 4.3 \times 10^{11}$ g/cm$^3$. Model predictions for various observables at the base of the outer crust (i.e., in the drip line region) are listed in Table I.

We remark in closing that all nuclei generated with the FSUGold parameter set included pairing correlations but neglected deformation. In regard to pairing correlations, these were included by means of a constant matrix element fitted to reproduce the experimental binding energies of some selected isotopic and isotonic chains, as described in Ref. [48]. However, deformation was ignored, so a spherical approximation was assumed in which all orbitals in the open shell share the same occupation number.

## IV. CONCLUSIONS

Following the seminal work by Baym, Pethick, and Sutherland, as well as the more recent comprehensive work by Rüster, Hempel, and Schaffner-Bielich, we studied the composition and equation of state of the outer crust of nonaccreting neutron stars. The central focus of our study was the sensitivity of crustal properties to the density dependence of the symmetry energy. Four different models were adopted. Two of these models, Moller-Nix and Duflo-Zuker, are based on a combined microscopic/macroscopic approach and yield the most accurate nuclear masses available in the literature. The other two models, NL3 and FSUGold, are of a purely microscopic nature and are based on a relativistic mean-field approach. Although the former are significantly more accurate than the latter, microscopic models have the advantage of making definite predictions on how the symmetry energy changes with density (see Fig. 4). One can then study the impact of various features of the symmetry energy—such as its slope—on crustal properties.

The composition and equation of state of the outer crust emerge from a competition among three relatively simple contributions to the total energy (or chemical potential) of the system: nuclear, electronic, and lattice. The nuclear contribution appears exclusively in the form of nuclear masses and is independent of the baryon density. The electronic contribution is modeled after a zero-temperature free Fermi gas and dominates the behavior of the system with baryon density. Finally, the (body-centered-cubic) lattice contribution is also density dependent and provides a relatively modest correction (of no more than 10%) to the energy of the system. This competition is then primarily driven by an electronic term that favors a small electron fraction (to reduce the electronic Fermi energy) and a nuclear symmetry energy that opposes such a shift toward progressively more neutron rich nuclei. To motivate the discussion and to highlight this competition, we implemented a "toy model" of the outer crust by using a simple semiempirical ("Bethe-Weizsäcker") nuclear mass formula. Volume, surface, Coulomb, and asymmetry terms were extracted from a least-square fit to 2049 nuclei (see `http://www.unedf.org/`). The advantage of such a simple model is that useful insights emerge from the analytic structure of our results. Indeed, a particularly transparent result that illustrates nicely the competition between the electronic contribution and the nuclear symmetry energy was obtained, namely,

$$y(p_F) = y_0 - \frac{p_{\rm Fe}}{8a_a} + \mathcal{O}\big(p_{\rm Fe}^2\big), \tag{34}$$

where $y_0$ is the zero-density proton fraction, $p_{\rm Fe}$ is the electronic Fermi momentum, and $a_a$ is the symmetry energy coefficient. Although illuminating, this (first-order) result is also surprisingly accurate, as the electronic Fermi momentum at the base of the outer crust is very close in value to the symmetry energy coefficient ($p_{\rm Fe} \approx 26$ MeV versus $a_a \approx 23$ MeV). In particular, the toy model predicts a value for the electron fraction at the base of the crust that differs by only a few percent from that of the drip line nucleus $^{118}$Kr.

What is unknown, however, is how the symmetry energy coefficient $a_a$ is modified as nuclei move away from the line of stability. Presumably, the symmetry energy is reduced in

neutron drip nuclei by the development of a dilute neutron skin. To investigate the sensitivity of the outer crust to the density dependence of the symmetry energy we employed two relativistic mean-field models (NL3 and FSUGold) that, although accurately calibrated, predict a significantly different density dependence for the symmetry energy. In particular, NL3 predicts a smaller symmetry energy than FSUGold at the (small) densities of relevance to the outer crust (see Fig. 4). One of the main goals of the present manuscript was to document how such differences impact the composition of the outer crust. One noticed, quite generally, that as the density increases along a fixed neutron-number plateau (say at magic number $N = 50$) the proton fraction decreased systematically in an effort to reduce the electronic contribution to the chemical potential. Eventually, however, the proton fraction becomes too low and the symmetry energy drives the system into the next plateau (say at magic number $N = 82$). How low can the proton fraction get is then a question that must be answered by the symmetry energy. Indeed, whereas NL3 predicts the formation of ${}^{78}_{28}\mathrm{Ni}_{50}$, FSUGold (having a larger symmetry energy) leaves the $N = 50$ plateau with the formation of ${}^{82}_{32}\mathrm{Ge}_{50}$ (or four protons earlier). This result may be stated in the form of a correlation between the neutron radius of ${}^{208}\mathrm{Pb}$ and the composition of the outer crust: *The larger the neutron skin of* ${}^{208}\mathrm{Pb}$, *the more exotic the composition of the outer crust*. Note that by "exotic" we mean nuclei that are unstable under normal laboratory conditions. Finally, and as was done in Ref. [31], we have computed crustal properties using two of the most accurate tables of nuclear masses available today, namely, those of Moller-Nix and Duflo-Zuker. Our results using the model of Moller and Nix agree well with those published in Ref. [31]. These results are practically indistinguishable from the ones obtained using the Duflo-Zuker nuclear mass table, a table that includes 9210 nuclei!

In summary, we have used realistic nuclear mass tables to elucidate the role of the symmetry energy on the structure and composition of the outer crust of neutron stars. Recent observations of crustal modes in magnetars are likely to provide stringent limits on the equation of state of neutron-rich matter. As the field of nuclear astrophysics continues to advance—with the commission of both radioactive beam facilities as well as ground- and space-based telescopes—we enter a new era that promises great hope in the determination of the nuclear matter equation of state.

## ACKNOWLEDGMENTS

The authors are grateful to José Barea, Alejandro Frank, Jorge Hirsch, and their students for useful discussions and for making the Duflo-Zuker mass formula available to us. We are also grateful to George Lalazissis for providing the NL3 mass formula. Xavier Roca-Maza acknowledges support from Grant Nos. AP2005-4751 and FIS2005-03142 from MEC (Spain) and FEDER. This work was supported in part by the Department of Energy Grant No. DE-FD05-92ER40750.

[1] J. M. Lattimer and M. Prakash, Astrophys. J. **550**, 426 (2001).
[2] J. M. Lattimer and M. Prakash, Science **304**, 536 (2004).
[3] G. Baym, C. Pethick, and P. Sutherland, Astrophys. J. **170**, 299 (1971).
[4] D. G. Ravenhall, C. J. Pethick, and J. R. Wilson, Phys. Rev. Lett. **50**, 2066 (1983).
[5] M. Hashimoto, H. Seki, and M. Yamada, Prog. Theor. Phys. **71**, 320 (1984).
[6] C. P. Lorenz, D. G. Ravenhall, and C. J. Pethick, Phys. Rev. Lett. **70**, 379 (1993).
[7] M. G. Alford, K. Rajagopal, and F. Wilczek, Nucl. Phys. **B537**, 443 (1999).
[8] K. Rajagopal and F. Wilczek, The Condensed Matter Physics of QCD, At the Frontier of Particle Physics, Handbook of QCD, edited by M. Shifman (World Scientific, 2000), Vol. 4, hep-ph/0011333.
[9] A. Schwenk and C. J. Pethick, Phys. Rev. Lett. **95**, 160401 (2005).
[10] J. Piekarewicz, Phys. Rev. C **76**, 064310 (2007).
[11] B. A. Brown, Phys. Rev. Lett. **85**, 5296 (2000).
[12] R. J. Furnstahl, Nucl. Phys. **A706**, 85 (2002).
[13] G. A. Lalazissis, J. Konig, and P. Ring, Phys. Rev. C **55**, 540 (1997).
[14] G. A. Lalazissis, S. Raman, and P. Ring, At. Data Nucl. Data Tables **71**, 1 (1999).
[15] B. G. Todd-Rutel and J. Piekarewicz, Phys. Rev. Lett. **95**, 122501 (2005).
[16] C. J. Horowitz, S. J. Pollock, P. A. Souder, and R. Michaels, Phys. Rev. C **63**, 025501 (2001).
[17] Jefferson Laboratory experiment E-00-003, spokespersons R. Michaels, P. A. Souder, and G. M. Urciuoli (2005); http://hallaweb.jlab.org/parity/prex.
[18] C. J. Horowitz and J. Piekarewicz, Phys. Rev. Lett. **86**, 5647 (2001).
[19] C. J. Horowitz and J. Piekarewicz, Phys. Rev. C **64**, 062802(R) (2001).
[20] C. J. Horowitz and J. Piekarewicz, Phys. Rev. C **66**, 055803 (2002).
[21] J. Carriere, C. J. Horowitz, and J. Piekarewicz, Astrophys. J. **593**, 463 (2003).
[22] A. W. Steiner, M. Prakash, J. M. Lattimer, and P. J. Ellis, Phys. Rep. **411**, 325 (2005).
[23] A. W. Steiner, Phys. Rev. C **77**, 035805 (2008).
[24] A. L. Piro, Astrophys. J. **634**, L153 (2005).
[25] T. E. Strohmayer and A. L. Watts, Astrophys. J. **653**, 593 (2006).
[26] A. L. Watts and T. E. Strohmayer, Astrophys. Space Sci. **308**, 625 (2007).
[27] A. L. Watts and T. E. Strohmayer, Adv. Space Res. **40**, 1446 (2007).
[28] C. Thompson and R. C. Duncan, Mon. Not. R. Astron. Soc. **275**, 255 (1995).
[29] C. Kouveliotou *et al.*, Nature (London) **393**, 235 (1998).
[30] C. Kouveliotou, R. C. Duncan, and C. Thompson, Sci. Am. **288N2**, 24 (2003).
[31] S. B. Rüster, M. Hempel, and J. Schaffner-Bielich, Phys. Rev. C **73**, 035804 (2006).
[32] P. Haensel, J. L. Zdunik, and J. Dobaczewski, Astron. Astrophys. **222**, 353 (1989).

[33] P. Haensel and B. Pichon, Astron. Astrophys. **283**, 313 (1994).
[34] E. Wigner, Phys. Rev. **46**, 1002 (1934).
[35] E. Wigner, Trans. Faraday Soc. **34**, 678 (1938).
[36] A. L. Fetter and J. D. Walecka, *Quantum Theory of Many Particle Systems* (McGraw-Hill, New York, 1971).
[37] R. A. Coldwell-Horsfall and A. A. Maradudin, J. Math. Phys. **1**, 395 (1960).
[38] C. A. Sholl, Proc. Phys. Soc. **92**, 434 (1967).
[39] G. Audi and A. H. Wapstra, Nucl. Phys. **A565**, 1 (1993).
[40] G. Audi and A. H. Wapstra, Nucl. Phys. **A595**, 409 (1995).
[41] J. Duflo, Nucl. Phys. **A576**, 29 (1994).
[42] A. Zuker, Nucl. Phys. **A576**, 65 (1994).
[43] J. Duflo and A. P. Zuker, Phys. Rev. C **52**, R23 (1995).
[44] P. Moller, J. R. Nix, W. D. Myers, and W. J. Swiatecki, At. Data Nucl. Data Tables **59**, 185 (1995).
[45] P. Moller, J. R. Nix, and K. L. Kratz, At. Data Nucl. Data Tables **66**, 131 (1996).
[46] B. Friedman and V. R. Pandharipande, Nucl. Phys. **A361**, 502 (1981).
[47] B. G. Todd and J. Piekarewicz, Phys. Rev. C **67**, 044317 (2003).
[48] M. Del Estal, M. Centelles, X. Viñas, and S. K. Patra, Phys. Rev. C **63**, 044321 (2001).

# 3 Symmetry energy effects on the nuclear Giant Monopole Resonance

## 3.1 Introduction

The isoscalar Giant Monopole Resonance (GMR) is a collective excitation of protons and neutrons in nuclei. For a given nucleus, the excitation energy of the GMR can be determined through an inelastic $\alpha$-particle scattering experiment. The GMR was first established in 1977 by Harakeh and Youngblood *et al.* [Ha77, Yo77]. The relevant quantities characterizing the resonance are the angular momentum transferred by the $\alpha$-particle to the nucleus under study, the spin $S$ and the isospin $T$ all associated to the nature of the oscillations. $L$ correspond to the multipole order, $L = 0$ is the monopole, $L = 1$ the dipole, $L = 2$ the quadrupole, etc. The spin $S$ could be either 0 or 1. A giant resonance with $S = 0$ —often called electric— corresponds to a spatial oscillation of the nuclear mass or charge distribution, while $S = 1$ —often called magnetic— corresponds to a spin oscillation. The isospin $T$, which could be also 0 or 1, determines the relative behavior of neutrons versus protons. For $T = 0$ or isoscalar resonance, the neutrons and protons oscillate in phase, whereas for $T = 1$, or isovector resonance, the neutrons and protons oscillate with opposite phase. Figure 11 shows a schematic picture of the isoscalar GMR ($L = 0$, $S = 0$ and $T = 0$) also called breathing mode since the whole nucleus is subject to a radial oscillation —expansion and contraction. The frequency of this breathing mode is directly related to the compressibility of the finite nucleus ($K_A$). For stable nuclei where the neutron-proton asymmetry is not higher than $\alpha \equiv \frac{N-Z}{A} < 0.25$, the determination of the GMR excitation energy is believed to be one of the most direct ways to access to the compressibility modulus of infinite nuclear matter ($K_0$). With the aim of precisely characterize this property, recent studies have pointed out that the GMR of a whole isotopic chain should be measured in order to extract $K_0$ with better accuracy [Kh09]. In that sense, one must also study nuclei with increasing neutron number (along isotopic chains) where the isospin dependent part of the finite nucleus incompressibility plays a non-negligible role. The reason is that the outermost neutrons are more weakly bound as more neutron-rich is the nucleus and, therefore, this peripheral neutrons start to behave almost as extremely asymmetric nuclear matter which is very soft (compressible) as compared with the symmetric one.

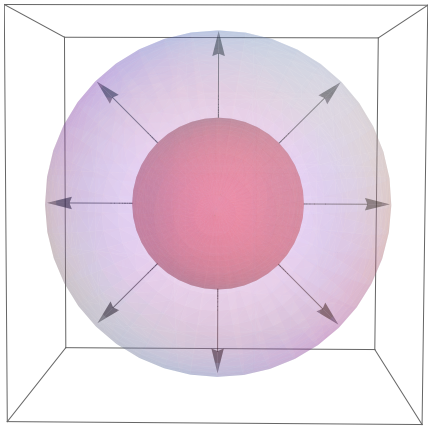

Figure 11: Rendition of a $L = 0$ mode of a collective motion in nuclei or Nuclear Giant Monopole Resonance

Motivated by the study of these effects, we present in this section a work devoted to analyze the influence of the density dependence of the symmetry energy on the average excitation energy of the GMR in stable, neutron-rich nuclei and along the Zr and Pb isotopic chains from the neutron to the proton theoretical drip lines. This work have been already accepted to be published in the *Journal of Physics G*.Our results show that the isospin dependent contribution to the average excitation energy ($E_{\rm M}$) of the GMR in nuclei with large isospin asymmetries can differ considerably between models depending on the softness of their symmetry energy. Therefore the incompressibility modulus of finite nuclei will be affected since $E^2 \propto K_A$. Experiments of inelastic $\alpha$-particle scattering off unstable nuclei such as nuclei with a large neutron excess are not feasible yet. Hence, some of the results enclosed here can not be compared against the experiment. Neither with other calculations since our work contains the first indications on how the density dependence of the symmetry energy will impact on the GMR in heavy and medium mass nuclei with very different isospin asymmetries —along two whole isotopic chains. Despite the above mentioned experimental situation, our calculations could provide useful information on physical processes involving nuclei under extreme isospin asymmetries as it is thought to happen in astrophysical processes [Pa07].

# 3.2 The influence of the symmetry energy on the giant monopole resonance of neutron-rich nuclei analyzed in Thomas-Fermi theory

IOP Publishing Journal of Physics G: Nuclear and Particle Physics

J. Phys. G: Nucl. Part. Phys. **37** (2010) 075107 (22pp) doi:10.1088/0954-3899/37/7/075107

## The influence of the symmetry energy on the giant monopole resonance of neutron-rich nuclei analyzed in Thomas–Fermi theory

**M Centelles[1], S K Patra[2], X Roca-Maza[1], B K Sharma[3], P D Stevenson[4] and X Viñas[1]**

[1] Departament d'Estructura i Constituents de la Matèria and Institut de Ciències del Cosmos, Facultat de Física, Universitat de Barcelona, Diagonal 647, 08028 Barcelona, Spain
[2] Institute of Physics, Bhubaneswar 751 005, India
[3] Department of Nuclear and Atomic Physics, Tata Institute of Fundamental Research, Homi Bhabha Road, Mumbai 400 005, India
[4] Department of Physics, University of Surrey, Guildford, Surrey, GU2 7XH, UK

E-mail: mariocentelles@ub.edu

Received 1 December 2009
Published 19 May 2010
Online at stacks.iop.org/JPhysG/37/075107

**Abstract**

We analyze the influence of the density dependence of the symmetry energy on the average excitation energy of the isoscalar giant monopole resonance (GMR) in stable and exotic neutron-rich nuclei by applying the relativistic extended Thomas–Fermi method in scaling and constrained calculations. For the effective nuclear interaction, we employ the relativistic mean field model supplemented by an isoscalar–isovector meson coupling that allows one to modify the density dependence of the symmetry energy without compromising the success of the model for binding energies and charge radii. The semiclassical estimates of the average energy of the GMR are known to be in good agreement with the results obtained in full RPA calculations. The present analysis is performed along the Pb and Zr isotopic chains. In the scaling calculations, the excitation energy is larger when the symmetry energy is softer. The same happens in the constrained calculations for nuclei with small and moderate neutron excess. However, for nuclei of large isospin the constrained excitation energy becomes smaller in models having a soft symmetry energy. This effect is mainly due to the presence of loosely bound outer neutrons in these isotopes. A sharp increase of the estimated width of the resonance is found in largely neutron-rich isotopes, even for heavy nuclei, which is enhanced when the symmetry energy of the model is soft. The results indicate that at large neutron numbers the structure of the low-energy region of the GMR strength distribution changes considerably with the density dependence of the nuclear symmetry energy, which may be worthy of further characterization in RPA calculations of the response function.

0954-3899/10/075107+22$30.00  

J. Phys. G: Nucl. Part. Phys. **37** (2010) 075107 M Centelles *et al*

## 1. Introduction

The departure of the equation of state (EOS) of neutron-rich matter ($N > Z$) from the symmetric limit ($N = Z$) is governed by the nuclear symmetry energy. This makes the knowledge of the symmetry energy important for a variety of areas of nuclear physics (masses, neutron densities, heavy ion collisions, etc) and of astrophysics (supernovae, neutron stars, nucleosynthesis, etc) [1–6]. However, the available experimental data on nuclei, which correspond mostly to isotopes with small and moderate neutron–proton asymmetries, do not constrain very precisely the value of the symmetry energy at the saturation density. Rather, it seems to be better constrained at a lower density around 0.10 fm$^{-3}$ [7–10], corresponding to an average between the bulk and surface symmetry contributions in the semi-empirical mass formula [11–13]. All in all, the density dependence of the symmetry energy is a basic nuclear property that is still not sufficiently well known [1, 4]. This situation has prompted a recent ongoing effort to characterize more closely the symmetry energy in the regime of subsaturation densities, relevant for finite nuclei, from the phenomenology of different nuclear observables [1, 4, 11–19]. A proper understanding of the symmetry energy is particularly desirable in order to predict the ground-state and excitation properties of atomic nuclei far from the naturally occurring region of stability [20–24].

The study of collective excitations of nuclei near and away from the stability line is a salient source of information for nuclear structure [25–29]. For instance, the isoscalar giant monopole resonance (GMR) constrains the compression modulus $K_0$ of the EOS of symmetric nuclear matter. This resonance has been accurately measured in heavy and medium mass nuclei through recently improved $\alpha$-particle scattering experiments [27, 28]. By comparing the 1p–1h RPA results predicted by Gogny [30], Skyrme [31–33] and relativistic mean field (RMF) interactions [34, 35] with the excitation energy measured in $^{208}$Pb ($14.17 \pm 0.28$ MeV [27]), it is concluded that the value of the nuclear incompressibility $K_0$ must lie in the range of 200–280 MeV. Performing measurements of the GMR in exotic nuclei may deliver other valuable information and enhance our knowledge of the physics of isospin-rich and loosely bound nuclear systems [26, 29, 32, 36, 37]. However, it represents an important experimental challenge due to e.g. the low intensities in the radioactive ion beams. With the advent of new technologies it is hoped that measurements of the breathing mode in short-lived unstable nuclei will become feasible in the future [26]. Note that promising first successes have already been demonstrated [29]. Although the value of the excitation energy of the GMR is driven to a large extent by the compression modulus of symmetric matter, it is known to be influenced also by the density dependence of the symmetry energy in a neutron-rich nucleus such as $^{208}$Pb [33, 38–42]. This influence is expected to be amplified in isotopes with large neutron numbers, but how and to which extent has not actually been assessed.

Our purpose in this paper is to investigate the effects of the density dependence of the symmetry energy on the average excitation energy of the GMR in isospin-rich nuclei, of heavy and medium mass, when moving away from the stability valley. We ought to mention, however, that our aim here is not pursuing to constrain the nuclear EOS from the present calculations, but rather to analyze the effects that arise from the existing uncertainty in the knowledge of the density dependence of the symmetry energy. We advance that the calculations will show that the impact on the excitation energy of the GMR is somehow moderate for isotopes not far from stability, while the more notable effects are found for nuclei with large neutron numbers, thereby (unfortunately) rendering them more difficult to see in experiment. To describe the effective nuclear interaction, we found convenient to use the model of [8–10] that consists of a standard RMF Lagrangian plus an isoscalar–isovector nonlinear interaction between the $\omega$- and

$\rho$-meson fields. This coupling provides an efficient way to change in a controlled manner the density dependence of the symmetry energy without modifying the EOS of symmetric matter. In particular, the compression modulus $K_0$ is not modified. When the model is applied to finite nuclei, the variation of the strength of the isoscalar–isovector coupling changes the properties of the neutron density distribution (for example, the neutron rms radius), which have large experimental uncertainties, but the predicted ground-state binding energies and charge rms radii, which are accurately known in experiment, remain basically unaltered. Thus, this RMF model allows one to modify the density content of the symmetry energy while preserving the agreement with the accurate ground-state information on which the model has been calibrated previously (see [8–10, 41, 43]).

The consistent microscopic framework for the calculation of the properties of the GMR is furnished by the Hartree–Fock plus RPA theory, which corresponds to the small-amplitude limit of the time-dependent Hartree–Fock method. The generalization of this theory to deal with pairing in open-shell nuclei is known as quasiparticle RPA (QRPA). The QRPA provides the full information on the response function and centroid energies of the GMR. These microscopic calculations are manageable but rather demanding if they are fully self-consistent, which is accentuated when they are performed using the canonical basis or in isotopes with large neutron numbers as it has been recently discussed in [37]. We will carry out our analysis by studying the estimates of the average excitation energy of the GMR that can be obtained without performing explicit RPA calculations but which carry meaningful physical information on the RPA strength. The typical example of this procedure is the sum-rule approach to the RPA developed in the nonrelativistic framework using Skyrme forces [44–46]. The sum-rule techniques provide the average properties of the GMR such as the centroid energy and the resonance width and have been successfully applied to study the GMR in different nuclei and isotopic chains [30, 33, 37, 44–48]. In the sum-rule approach one obtains the cubic and inverse energy-weighted moments of the RPA strength function by means of, respectively, scaling and constrained calculations of the uncorrelated Hartree–Fock nuclear ground state. Note that these ground-state scaling and constrained values are the *exact* RPA moments [44–46]. Because highly accurate ground-state calculations are simpler, the sum-rule techniques also have been used in the literature as a means to check the self-consistency of explicit RPA calculations of the strength function [32, 37, 47, 48].

The validity of the sum-rule theorems when pairing is active (QRPA) has been proven in recent publications [37, 49]. Capelli *et al* [37] have made a careful study of constrained Hartree–Fock (CHF), constrained Hartree–Fock–Bogoliubov (CHFB) and QRPA calculations of the excitation energy of the GMR in the light isotopic chains of Ca and Ni. The calculations have reached up to the theoretical neutron drip line of the Skyrme SkM* force, i.e. up to the isotopes $^{76}$Ca and $^{84}$Ni. Admitting that these isotopic chains are known to terminate earlier in experiment than in the predictions of SkM* and of most of the nuclear effective forces, and knowing also that it will be difficult to measure the GMR in even less exotic isotopes, the calculations spanning the whole theoretical isotopic chains are very useful to test the predictions of nuclear forces under extreme isospin conditions (which can take place in astrophysical scenarios [50]), as well as to test the different many-body frameworks employed to deal with the problem. It may be also noted that Khan [51] has recently concluded that knowing the GMR in a single isotope such as $^{208}$Pb may not suffice to extract $K_0$ of nuclear matter and that the whole isotopic chain should be measured in order to have a grasp on the various effects acting on the GMR [51].

From the results of [37] for Ca and Ni, it is seen that the inclusion of pairing (CHFB and QRPA calculations) does not modify significantly the behavior shown by the GMR excitation energies obtained in the CHF calculations along the isotopic chains. In the case of the Ni

chain, the atomic number not being as small as in Ca, the CHFB and CHF values agree fairly well for most isotopes from $^{56}$Ni up to the neutron drip line included, as noted in figure 5 of [37]. Of course, superfluidity is to be taken into account if one wants to describe in detail the excitation spectra or if precise values of the excitation energy within a few hundred keV in specific nuclei are needed for comparison with accurate measurements [37, 51, 52]. It has been pointed out in [37] that the QRPA calculations for isotopes having large neutron numbers become much time consuming and that ensuring proper numerics in such isospin-rich nuclei becomes somewhat difficult due to the weakly bound neutrons. Indeed, the authors of [37] state that in the case of large neutron numbers very accurate QRPA calculations may become almost prohibitive in keeping with the size of the basis.

The GMR is a collective excitation whose average properties in general vary smoothly with the mass number $A$ and are rather insensitive to shell effects, at least for not too light isotopes. Thus, a description of the average properties of this resonance through semiclassical approaches like the extended Thomas–Fermi (ETF) method can be, for some purposes, a practical and interesting alternative. It has been applied in different studies in the nonrelativistic Skyrme–Hartree–Fock framework [46, 47, 53–55]. The results have shown that the average excitation energies of the GMR obtained from scaling and constrained quantal HF calculations are nicely described by the corresponding semiclassical ETF counterparts. The ETF predictions of GMR excitation energies become increasingly closer to the quantal predictions with increasing atomic number, as it can be expected in semiclassical methods. Indeed, in the calculations along the Pb isotopic chain with the Skyrme force shown in figure 12 of [47], the ETF scaling and constrained excitation energies differ from the corresponding quantal values by less than 0.4 MeV and they reproduce quite accurately the change of the quantal results in going from the proton to the neutron drip line. Thus, from the experience in nonrelativistic calculations, we believe that the semiclassical scaling and constrained estimates of the average excitation energy will be a useful and realistic procedure to have a quick representation of the general trends of the GMR along isotopic chains also in the relativistic mean field framework. And in heavy systems such as the Pb isotopes, we expect that the semiclassical calculations of the GMR average excitation energy will yield reliable predictions practically on the quantitative level. Certainly, for a precise microscopic description, the more demanding QRPA calculations would have to be performed.

The semiclassical relativistic extended Thomas–Fermi (RETF) approach [56–60] has recently been applied in scaling and constrained calculations of the GMR energy in stable isotopes in [61, 62]. The results turn out to be in good agreement with the values extracted from full relativistic RPA calculations [61, 62]. Let us mention as a side comment that the RETF scaling procedure has been helpful in obtaining the virial theorem for the relativistic mean field model [61] and that it has allowed self-consistent calculations of the surface contribution $K_{\rm surf}$ to the nuclear incompressibility in the relativistic theory [63]. In this paper we will use the relativistic nuclear mean field model with an isoscalar–isovector coupling mentioned previously together with the RETF approach for describing the average excitation energy of the GMR in the Pb and Zr isotopic chains, through scaling and constrained calculations. The present results are expected to provide a realistic indication on how the density dependence of the symmetry energy impacts the behavior of the excitation energies and widths of the GMR along isotopic chains of heavy and medium mass. In the next section the basic theory is presented, in section 3 the results are discussed and the summary and conclusions are laid in section 4. Some details about the semiclassical RETF calculations are given in the appendices.

## 2. Formalism

A detailed description of the scaling and constrained calculations of the excitation energy of the GMR in the relativistic framework using the RETF approach has been presented elsewhere [61, 62]. Here, we shall restrict ourselves to outline the more relevant expressions, incorporating the new contributions that arise from the mixed $\omega$–$\rho$ meson interaction.

### 2.1. ETF energy density of the relativistic mean field model

The basic model for the present study is the relativistic mean field theory of nucleons and mesons. As in the nonrelativistic problem, the theory can be formulated in the Thomas–Fermi approach. When corrections of order $\hbar^2$ (in gradients of the nucleon densities and of the Dirac effective mass) to the pure Thomas–Fermi contribution are included in the energy density, it is known as the relativistic extended Thomas–Fermi approach [56–60].

The local energy density that we employ in the present work can be written as follows:

$$\mathcal{H} = \mathcal{E} + W\rho + B\rho_3 + \mathcal{A}\rho_p + \frac{1}{2g_s^2}\left[(\nabla\Phi)^2 + m_s^2\Phi^2\right] + \frac{\kappa}{3!}\Phi^3 + \frac{\lambda}{4!}\Phi^4 - \frac{1}{2g_v^2}\left[(\nabla W)^2 + m_v^2 W^2\right] - \frac{1}{2g_\rho^2}\left[(\nabla B)^2 + m_\rho^2 B^2\right] - \Lambda_V B^2 W^2 - \frac{1}{2}(\nabla\mathcal{A})^2, \quad (1)$$

where $\rho = \rho_p + \rho_n$ is the baryon density, $\rho_3 = \frac{1}{2}(\rho_p - \rho_n)$ is the isovector density and the term $\mathcal{E}$ will be described immediately below. The energy density (1) contains scalar $\Phi = g_s\phi_0(\boldsymbol{r})$, vector $W = g_v V_0(\boldsymbol{r})$ and vector–isovector $B = g_\rho b_0(\boldsymbol{r})$ meson fields, as well as the Coulomb field $\mathcal{A} = eA_0(\boldsymbol{r})$. These fields represent, respectively, $\sigma$-meson, $\omega$-meson, $\rho$-meson and photon exchange. The cubic $\kappa\Phi^3$ and quartic $\lambda\Phi^4$ self-interactions of the scalar field soften the EOS of symmetric nuclear matter around the saturation point. In addition, the model is supplemented by a nonlinear mixed coupling between the $\omega$-meson and the $\rho$-meson fields. This $\Lambda_V B^2 W^2$ interaction was introduced in [8] to soften the density dependence of the symmetry energy and of the EOS of neutron matter, which are two quantities that are predicted to be stiff by the majority of relativistic mean field models.

In the quantum approach, the contribution $\mathcal{E}$ to the RMF energy density in equation (1) is given by $\mathcal{E} = \sum_\nu \varphi_\nu^\dagger[-\mathrm{i}\,\boldsymbol{\alpha}\cdot\boldsymbol{\nabla} + \gamma_0(m - \Phi)]\varphi_\nu$. Here, the $\varphi_\nu$ are single-particle Dirac wavefunctions, $\boldsymbol{\alpha}$ and $\gamma_0$ are the usual Dirac matrices and $m$ denotes the rest mass of the nucleons. The RETF representation of $\mathcal{E}$ consists of a pure Thomas–Fermi part $\mathcal{E}_0$ plus a part $\mathcal{E}_2$, which is of order $\hbar^2$ compared to $\mathcal{E}_0$. The nucleon variables of the RETF energy density are the neutron and proton densities ($\rho_n$ and $\rho_p$) instead of the single-particle wavefunctions $\varphi_\nu$. Thereby, $\mathcal{E}$ is a functional of the nucleon densities and of the Dirac effective mass $m^* = m - \Phi$ in the RETF approach. The gradient corrections contained in the $\mathcal{E}_2$ term provide an improved description of the nuclear surface with respect to the Thomas–Fermi treatment with only the $\mathcal{E}_0$ contribution. The reader can find the full RETF expression of the functional $\mathcal{E}$ in appendix A. We also provide there the variational Euler–Lagrange equations derived from equation (1) in the RETF approach for the nucleon densities and for the meson and photon fields.

The energy density $\mathcal{H}$ is to be integrated over space to compute the total energy of the nucleus. By means of partial integrations, and on account of the variational meson field equations given in appendix A, it is possible to write the relativistic energy density of a finite nucleus in the following form:

$$\mathcal{H} = \mathcal{E} + \frac{1}{2}\Phi\rho_s^{\mathrm{eff}} + \frac{\kappa}{3!}\Phi^3 + \frac{\lambda}{4!}\Phi^4 + \frac{1}{2}W\rho + \frac{1}{2}B\rho_3 + \Lambda_V B^2 W^2 + \frac{1}{2}\mathcal{A}\rho_p. \quad (2)$$

Here, we have introduced the effective scalar density $\rho_s^{\rm eff}$ defined as

$$\rho_s^{\rm eff} = \rho_s - \frac{\kappa}{2!}\Phi^2 - \frac{\lambda}{3!}\Phi^3. \tag{3}$$

The form given in equation (2) for $\mathcal{H}$ turns out to be more practical to perform the scaling of the equations in order to compute the excitation energy of the GMR in the scaling formalism.

### *2.2. Energy of the GMR in the scaling approach*

The excitation energy of the isoscalar giant monopole resonance of a finite nucleus of mass number $A$ is customarily written as

$$E_M = \sqrt{\frac{AK_A}{B_M}}, \tag{4}$$

where $K_A$ is called the compression modulus or incompressibility of the finite nucleus and $B_M$ is called the mass or inertia parameter of the monopole oscillation. In the scaling approach, the incompressibility $K_A$ is obtained from the restoring force of the monopole vibration modeled through a scaling transformation of the nucleon densities:

$$\rho_{q\alpha}(\boldsymbol{r}) = \alpha^3 \rho_q(\alpha \boldsymbol{r}). \tag{5}$$

Here, $\alpha$ denotes the scaling parameter and $q = $ n, p refers to neutrons or protons. The meson fields do not scale as simple powers of $\alpha$ because of the finite-range character of the meson interactions; we collect in appendix B the variational field equations for the scaled meson fields of the RMF model with the mixed $\omega$–$\rho$ interaction. Following [61, 62], it is helpful to write the scaled Dirac effective mass $m_\alpha^*(\boldsymbol{r}) = m - \Phi_\alpha(\boldsymbol{r})$ in the form

$$m_\alpha^*(\boldsymbol{r}) \equiv \alpha \tilde{m}^*(\alpha \boldsymbol{r}) \tag{6}$$

because the energy density $\mathcal{E}$ and the scalar density $\rho_s$ of the RETF model scale, respectively, as $\mathcal{E}_\alpha(\boldsymbol{r}) = \alpha^4 \mathcal{E}[\rho_q(\alpha\boldsymbol{r}), \tilde{m}^*(\alpha\boldsymbol{r})] \equiv \alpha^4 \tilde{\mathcal{E}}(\alpha\boldsymbol{r})$ and as $\rho_{s\alpha}(\boldsymbol{r}) = \alpha^3 \rho_{\rm s}[\rho_q(\alpha\boldsymbol{r}), \tilde{m}^*(\alpha\boldsymbol{r})] \equiv \alpha^3 \tilde{\rho}_{\rm s}(\alpha\boldsymbol{r})$. The tilded quantities $\tilde{\mathcal{E}}$ and $\tilde{\rho}_{\rm s}$ have the same expressions as $\mathcal{E}$ and $\rho_{\rm s}$ given in appendix A if one replaces $m^*$ by $\tilde{m}^*$ in them. Taking into account the above, the scaled form of the energy density of the present model becomes

$$\begin{aligned}\mathcal{H}_\alpha(\boldsymbol{r}) = \alpha^3 \Big[ & \alpha\tilde{\mathcal{E}} + \frac{1}{2}\Phi_\alpha \tilde{\rho}_s^{\rm eff} + \frac{1}{3!}\frac{\kappa}{\alpha^3}\Phi_\alpha^3 + \frac{1}{4!}\frac{\lambda}{\alpha^3}\Phi_\alpha^4 \\ & + \frac{1}{2}W_\alpha \rho + \frac{1}{2}B_\alpha \rho_3 + \frac{\Lambda_V}{\alpha^3} B_\alpha^2 W_\alpha^2 + \frac{1}{2}\mathcal{A}_\alpha \rho_p \Big],\end{aligned} \tag{7}$$

with the definition $\tilde{\rho}_s^{\rm eff} = \tilde{\rho}_s - \frac{\kappa}{2!}\frac{\Phi_\alpha^2}{\alpha^3} - \frac{\lambda}{3!}\frac{\Phi_\alpha^3}{\alpha^3}$. All densities and fields on the rhs of (7) depend on the variable $\alpha\boldsymbol{r}$.

The calculation of the first and second derivatives of the scaled energy $E(\alpha) = \int {\rm d}\boldsymbol{r}\, \mathcal{H}_\alpha(\boldsymbol{r})$ with respect to $\alpha$ proceeds along the same lines described in [61, 62]. The final result for the scaling incompressibility is

$$\begin{aligned} K_A^{\rm scal} &= \frac{1}{A}\left[\frac{\partial^2}{\partial\alpha^2}\int {\rm d}(\alpha\boldsymbol{r})\frac{\mathcal{H}_\alpha(\boldsymbol{r})}{\alpha^3}\right]_{\alpha=1} \\ &= \frac{1}{A}\int {\rm d}\boldsymbol{r}\left[-m\frac{\partial\tilde{\rho}_s}{\partial\alpha} + 3\left(\frac{m_s^2}{g_s^2}\Phi^2 - \frac{m_v^2}{g_v^2}W^2 - \frac{m_\rho^2}{g_\rho}B^2 + \frac{\kappa}{3!}\Phi^3\right)\right. \\ &\quad \left. - \left(2\frac{m_s^2}{g_s^2}\Phi + \frac{\kappa}{2}\Phi^2\right)\frac{\partial\Phi_\alpha}{\partial\alpha} + 2\frac{m_v^2}{g_v^2}W\frac{\partial W_\alpha}{\partial\alpha} + 2\frac{m_\rho^2}{g_\rho^2}B\frac{\partial B_\alpha}{\partial\alpha}\right]_{\alpha=1}, \end{aligned} \tag{8}$$

where $(\partial\tilde{\rho}_s/\partial\alpha)_{\alpha=1} = -(\partial\rho_s/\partial m^*)[m^* + (\partial\Phi_\alpha/\partial\alpha)_{\alpha=1}]$. It is interesting to note that all of the nucleonic contributions to $K_A^{\rm scal}$ are summarized in the term with the scalar density and that the massless photon field and the quartic meson couplings such as $\lambda\Phi^4$ and $\Lambda_V B^2 W^2$ do not provide explicit contributions. Expression (8) requires the calculation of the derivatives of the meson fields with respect to the scaling parameter $\alpha$ at equilibrium ($\alpha = 1$). These derivatives can be computed by differentiation of the scaled meson field equations with respect to $\alpha$ and by solving them at $\alpha = 1$, as we describe in appendix B.

We will use the notation $E_M^{\rm scal}$ to refer to the excitation energy of the GMR calculated in the scaling approach, namely

$$E_M^{\rm scal} = \sqrt{\frac{A K_A^{\rm scal}}{B_M}}. \tag{9}$$

The mass parameter of the monopole resonance is given by the expression [62, 64, 65]

$$B_M = \int {\rm d}\boldsymbol{r}\, r^2 \mathcal{H}. \tag{10}$$

We note that in the nonrelativistic limit it reads

$$B_M^{\rm nr} = \int {\rm d}\boldsymbol{r}\, r^2 m\rho = mA\langle r^2\rangle, \tag{11}$$

where $m$ is the nucleon rest mass. Because of the large contribution of the nucleon rest mass term $m\rho$ to the energy density $\mathcal{H}$ in the integrand of equation (10), the value of the excitation energy of the resonance is little modified by using either $B_M$ or $B_M^{\rm nr}$ in the calculations.

### *2.3. Energy of the GMR in the constrained approach*

One can also study the average excitation energy of the giant monopole resonance through constrained calculations [44, 62, 66–69]. For that purpose, one solves the problem associated with the constrained functional

$$\int {\rm d}\boldsymbol{r}[\mathcal{H} - \eta r^2\rho] = E(\eta) - \eta \int {\rm d}\boldsymbol{r}\, r^2\rho. \tag{12}$$

The densities, fields and energy obtained from the solution of the variational equations deduced from equation (12) depend on the value of the parameter $\eta$ at which one performs the calculation. By expanding $E(\eta)$ in a harmonic approximation about its minimum, located at the ground-state rms radius $R_0$ (corresponding to $\eta = 0$), one obtains the compression modulus of the finite nucleus in the constrained approach:

$$K_A^{\rm cons} = \frac{1}{A} R_0^2 \left(\frac{\partial^2 E(\eta)}{\partial R_\eta^2}\right)_{\eta=0}. \tag{13}$$

Here, $R_\eta^2 = \langle r^2\rangle_\eta$ is the square mass radius of the nucleus computed with the density $\rho$ of equation (12). One can show that equation (13) can be rewritten in the following equivalent forms:

$$K_A^{\rm cons} = -4R_0^4 \left(\frac{\partial R_\eta^2}{\partial\eta}\right)^{-1}_{\eta=0} = 4AR_0^4 \left(\frac{\partial^2 E(\eta)}{\partial\eta^2}\right)^{-1}_{\eta=0}. \tag{14}$$

We have used (14) to check the numerical accuracy of our calculations of $K_A^{\rm cons}$. Finally, the excitation energy of the constrained isoscalar monopole vibration is computed as

$$E_M^{\rm cons} = \sqrt{\frac{A K_A^{\rm cons}}{B_M}}. \tag{15}$$

*2.4. Comparison with the expressions in the nonrelativistic sum-rule approach*

We would like to point out that there is a parallelism between the scaling and constrained expressions for the GMR energy derived above for the relativistic model and the known results in the nonrelativistic formalism of sum rules. That is, one can define suitable average excitation energies of the resonance such as

$$E_3 \equiv \sqrt{\frac{m_3}{m_1}} \qquad \text{and} \qquad E_1 \equiv \sqrt{\frac{m_1}{m_{-1}}} \tag{16}$$

in terms of the ratios of the integral moments $m_k = \int_0^\infty \mathrm{d}\omega\, \omega^k S(\omega)$ of the RPA strength function $S(\omega)$. In the nonrelativistic RPA theory of the GMR [44–46], it has been demonstrated that the cubic energy-weighted moment $m_3 = \int_0^\infty \mathrm{d}\omega\, \omega^3 S(\omega)$ of the RPA strength function is exactly equivalent to the second derivative of the energy obtained from a monopole scaling transformation. It is also known that the RPA energy-weighted moment $m_1 = \int_0^\infty \mathrm{d}\omega\, \omega S(\omega)$ is equivalent to

$$m_1 = \frac{2}{m} A \langle r^2 \rangle \tag{17}$$

('Thouless theorem'), and that the exact RPA inverse energy-weighted moment $m_{-1} = \int_0^\infty \mathrm{d}\omega\, S(\omega)/\omega$ can be obtained from a constrained calculation of the Hartree–Fock ground state:

$$m_{-1} = -\frac{1}{2} A \left( \frac{\partial R_\eta^2}{\partial \eta} \right)_{\eta=0} \tag{18}$$

('dielectric theorem'). Taking into account these results and the fact that $m_1 = (2/m^2) B_M^{\mathrm{nr}}$, one sees an interesting analogy between $E_3$ and $E_1$ of the nonrelativistic RPA formalism of sum rules and $E_M^{\mathrm{scal}}$ of equations (9) and (8) and $E_M^{\mathrm{cons}}$ of equations (15) and (14) given previously for the GMR average excitation energy in the relativistic model, though to our knowledge the sum-rule approach has not been derived in the relativistic RPA theory.

It is worth mentioning that the integral moments of the nonrelativistic RPA strength function obey certain inequalities [44–46]. In particular, one has

$$E_1 \leqslant E_x = \frac{m_1}{m_0} \leqslant E_3, \tag{19}$$

where $E_x$ is the centroid energy of the GMR evaluated from the ratio of the $m_1$ moment to the $m_0$ moment. That is, $E_1$ is a lower limit for the mean energy (centroid) of the resonance, whereas $E_3$ is an upper limit. It is clear from the definition of the $m_3$ and $m_{-1}$ moments that $E_3$ and $E_1$ explore different energy domains of the collective excitation, i.e. $E_3$ is more influenced by the high-energy region of the strength function $S(\omega)$, whereas $E_1$ is more sensitive to the low-energy components of $S(\omega)$. It can be shown [44] that the quantity

$$\sigma = \tfrac{1}{2}\sqrt{E_3^2 - E_1^2} \tag{20}$$

provides an upper bound for the width of the giant monopole resonance in the RPA approximation. The calculations carried out for stable nuclei show that $E_3$ and $E_1$ become increasingly close with increasing nuclear mass. Therefore, in a stable heavy nucleus the value of the width $\sigma$ is small and the monopole strength becomes concentrated around a single peak [44], which is the situation found in experiment. Following equation (20) and the above comments, in the discussion of our results the spread between the calculated $E_M^{\mathrm{scal}}$ and $E_M^{\mathrm{cons}}$ values will provide an indication about the width of the GMR.

**Table 1.** Relativistic Hartree–RPA and relativistic extended Thomas–Fermi values obtained with the NL3 model plus the isoscalar–isovector coupling $\Lambda_V$ for the binding energy per particle (MeV), neutron skin thickness $\Delta R_{np} = R_n - R_p$ (fm) and excitation energy of the GMR (MeV) in $^{208}$Pb and $^{90}$Zr. The GMR centroid energies $m_1/m_0$ are taken from [41].

| | Quantal Hartree–RPA | | | Semiclassical RETF | | | |
|---|---|---|---|---|---|---|---|
| Model | $B/A$ | $\Delta R_{np}$ | $m_1/m_0$ | $B/A$ | $\Delta R_{np}$ | $E_M^{\rm cons}$ | $E_M^{\rm scal}$ |
| $^{208}$Pb | | | | | | | |
| NL3.00 | 7.87 | 0.28 | 14.32 | 7.99 | 0.23 | 13.92 | 14.58 |
| NL3.01 | 7.89 | 0.25 | 14.43 | 8.01 | 0.20 | 13.97 | 14.61 |
| NL3.02 | 7.91 | 0.22 | 14.57 | 8.02 | 0.17 | 14.07 | 14.70 |
| NL3.03 | 7.91 | 0.20 | 14.74 | 8.03 | 0.15 | 14.20 | 14.83 |
| $^{90}$Zr | | | | | | | |
| NL3.00 | 8.69 | 0.11 | 18.62 | 8.91 | 0.10 | 19.04 | 19.53 |
| NL3.01 | 8.69 | 0.10 | 18.67 | 8.91 | 0.09 | 19.05 | 19.54 |
| NL3.02 | 8.70 | 0.09 | 18.69 | 8.92 | 0.08 | 19.08 | 19.58 |
| NL3.03 | 8.70 | 0.08 | 18.75 | 8.92 | 0.07 | 19.12 | 19.62 |

## 3. Results and discussions

### *3.1. Comparison of relativistic ETF and Hartree–RPA results*

First, in this section we test with some examples the results of the relativistic extended Thomas–Fermi (RETF) approach vis-á-vis relativistic Hartree and RPA calculations. To this end, we report in table 1 the semiclassical RETF results for the binding energy and the excitation energy of the GMR in the nuclei $^{208}$Pb and $^{90}$Zr. We also include in the comparison the value of the neutron skin thickness $\Delta R_{np} = R_n - R_p$ (the difference between the neutron and proton rms radii of the nucleus) because this quantity is very sensitive to the density dependence of the symmetry energy [7, 12, 70, 71]. The results have been computed with the NL3 mean field interaction [72] supplemented by the nonlinear $\Lambda_V$ coupling between the $\omega$-meson and $\rho$-meson fields [8]. As pointed out in the introduction, this model, through the isoscalar–isovector meson coupling, allows one to change the symmetry energy leaving unchanged the properties of the EOS of symmetric nuclear matter. By modifying the value of $\Lambda_V$ one can investigate the changes in finite nuclei due to the variation of the density dependence of the symmetry energy almost without affecting the previous quality of the model for binding energies and charge radii [8–10, 41, 43].

For the coupling constant $\Lambda_V$ we use the values 0.00, 0.01, 0.02 and 0.03 (models denoted as NL3.00, NL3.01, NL3.02 and NL3.03 in table 1). It is known that the binding energy of nuclei constrains an average between the symmetry energy at saturation and the surface symmetry energy, rather than the individual value of the symmetry energy at saturation [8–12]. Thus, as was done in the earlier literature [8–10, 41, 43], we constrain the symmetry energy $S(\rho)$ of the models to take a value of 25.67 MeV at a Fermi momentum $k_F = 1.15$ fm$^{-1}$ (i.e. at a subsaturation density $\rho \approx 0.10$ fm$^{-3}$). This implies that the coupling constant $g_\rho$ of the NL3 interaction has to be suitably adjusted for each value of the isoscalar–isovector $\Lambda_V$ coupling. As a consequence, the value $S(\rho_0)$ of the symmetry energy at the saturation density $\rho_0$ changes with the $\Lambda_V$ parameter. We find the results $S(\rho_0) = 37.4$, 35.0, 33.2 and 31.7 MeV when we vary $\Lambda_V$ from 0.00 to 0.03. That is, the symmetry energy $S(\rho)$ of the model around saturation becomes softer (it increases more slowly with the nuclear density)

when the value of the $\Lambda_V$ parameter is larger. Further details on the behavior of $S(\rho)$ in the NL3 model supplemented by the $\Lambda_V$ coupling can be found in [10].

Table 1 shows that by increasing the $\Lambda_V$ coupling the neutron skin thickness of a neutron-rich nucleus is significantly reduced, i.e. the models with a softer symmetry energy give rise to smaller neutron skins. Here, this is achieved while maintaining the proton rms radius of the nucleus essentially intact. For example, in the quantal Hartree calculation with the NL3.00 model we find $R_p = 5.466$ fm for $^{208}$Pb and 4.199 fm for $^{90}$Zr, while the respective values using NL3.03 are 5.478 fm and 4.210 fm. The changes in $R_p$ are thus less than 0.5%. Moreover, one sees in table 1 that also the binding energies are little altered by $\Lambda_V$. Both $^{208}$Pb and $^{90}$Zr are slightly more bound at large $\Lambda_V$ but the changes in $B/A$ are again no larger than 0.5%. Thus, the predictions for charge radii and binding energies of the original NL3 model are not seriously compromised by the additional $\Lambda_V$ coupling, which otherwise largely softens the symmetry energy.

From table 1 we observe that in the semiclassical RETF approach the binding energies of $^{208}$Pb and $^{90}$Zr are larger and the neutron skins smaller than in the corresponding quantal Hartree calculations. In principle, this fact should not be considered as a lack of accuracy of the Thomas–Fermi-like methods because semiclassical and quantal calculations must differ by shell effects. It is well known that the semiclassical ground-state calculations by construction smooth out the quantal shell effects and provide the average part of the quantal binding energy [73–75]. Actually, in the semiclassical calculations one works with the particle densities and completely avoids to calculate single-particle wavefunctions. By this same reason, the semiclassical approach yields smooth average densities and energies that do not show the quantum shell oscillations. The nuclear ETF functionals with gradient corrections up to order $\hbar^2$ always produce some overbinding (between a $\sim$2% in heavy nuclei and a $\sim$10% in light nuclei) and yield smaller rms radii (between $\sim$1% and $\sim$4%) than the quantal mean field calculations [53, 56, 57, 74]. The quantal corrections, which are more prominent in magic nuclei (our situation in table 1), can eventually be added perturbatively to the semiclassical binding energies using techniques such as the Strutinsky shell-correction method [75] or the expectation value method [56, 57, 74].

Our focus here is somehow more about the change of the results with the softness of the symmetry energy than on the absolute values themselves. In this respect, one has to note that the quantal and semiclassical results reported in table 1 show both practically the same variation as a function of the $\Lambda_V$ coupling. The binding energies remain similarly constant and the neutron skins decrease by almost the same amount of 0.08 fm in $^{208}$Pb and of 0.03 fm in $^{90}$Zr in both the Hartree and RETF calculations when $\Lambda_V$ is changed from 0.00 to 0.03. Therefore, the RETF approach predicts practically the same variation with $\Lambda_V$ as the quantal Hartree calculations. This implies that the rate of change of the results with the softness of the symmetry energy in the present model is well described by the RETF method. As a further test, which is motivated also because later we will study RETF results along isotopic chains, in figure 1 we plot for Pb isotopes the difference between the value of the neutron skin thickness of the nucleus calculated with $\Lambda_V = 0.00$ and with $\Lambda_V = 0.03$, as a function of the parameter $I = (N - Z)/A$. We observe by comparison with the corresponding quantal Hartree results that the RETF approach performs quite satisfactorily along the Pb isotopic chain in predicting the right size of the modification induced by the change of the symmetry energy of the model.

With regard to the average excitation energies of the GMR, table 1 shows the scaled and constrained values (i.e. $E_M^{\rm scal}$ of section 2.2 and $E_M^{\rm cons}$ of section 2.3) for $^{208}$Pb and $^{90}$Zr calculated in the RETF approach. We compare our RETF results with the values of the centroid energy $m_1/m_0$ of the GMR extracted from the relativistic RPA (RRPA) strength, which have

J. Phys. G: Nucl. Part. Phys. **37** (2010) 075107 M Centelles *et al*

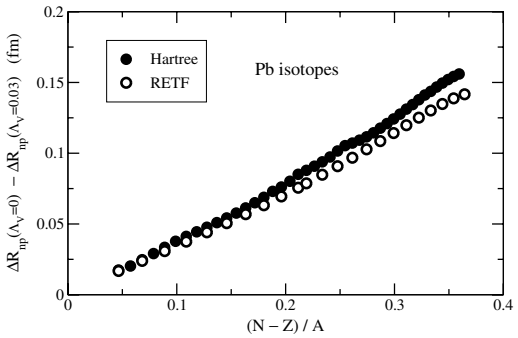


**Figure 1.** Difference between the values of the neutron skin thickness $\Delta R_{np}$ obtained with $\Lambda_V = 0$ and with $\Lambda_V = 0.03$ for lead isotopes. The results of the RETF method are compared with the results of quantal Hartree calculations.

been reported in [41]. We see that for the $^{208}$Pb nucleus, the RRPA centroid energies very nicely lie in between the RETF constrained and scaled estimates, as it is required in the nonrelativistic sum-rule approach to the RPA [44–46] (recall equation (19) of section 2.4). In the case of a lower-mass nucleus such as $^{90}$Zr, the semiclassical excitation energies are not expected to be as successful as for the heavier $^{208}$Pb. Indeed, we see in table 1 that the RETF constrained and scaled estimates in $^{90}$Zr overestimate a little the RRPA centroid energies. The discrepancies are nevertheless moderate, with differences no larger than 2% for $E_M^{\rm cons}$ and 5% for $E_M^{\rm scal}$ with respect to the RRPA $m_1/m_0$ value of $^{90}$Zr. And, as happens in the case of $^{208}$Pb, the semiclassical average excitation energies of $^{90}$Zr as a function of the $\Lambda_V$ coupling display the tendency of the RRPA excitation energies. In summary, we can conclude from the results discussed in the present section that the RETF approach is a reasonable starting point to study the influence of the density dependence of the symmetry energy on the GMR of neutron-rich nuclei.

### *3.2. GMR in heavy neutron-rich nuclei*

As mentioned in the introduction, we found in [47] within the Skyrme–Hartree–Fock framework that the semiclassical calculations are able to describe realistically the tendencies of the excitation energy of the GMR in regions away from the stability valley, especially for heavy nuclei such as the lead isotopes where a semiclassical approach performs better. In the present section we analyze with the RETF approach to the relativistic mean field model the effects of the density dependence of the symmetry energy on the excitation energy of the GMR in heavy neutron-rich nuclei by contrasting the results for the nucleus $^{266}$Pb, which we take as an example of a heavy system with a large neutron excess away from stability, with the results for the stable isotope $^{208}$Pb.

We display in figure 2 for $^{208}$Pb and in figure 3 for $^{266}$Pb the calculated values of the energy per particle $E/A$, the neutron skin thickness $\Delta R_{np} = R_n - R_p$, the compression modulus of the finite nucleus $K_A$ and the average excitation energy $E_x$ of the GMR as a function of the coupling constant $\Lambda_V$ in the relativistic model. We recall that the coupling $\Lambda_V$ induces a change of the density dependence of the symmetry energy. The model has a

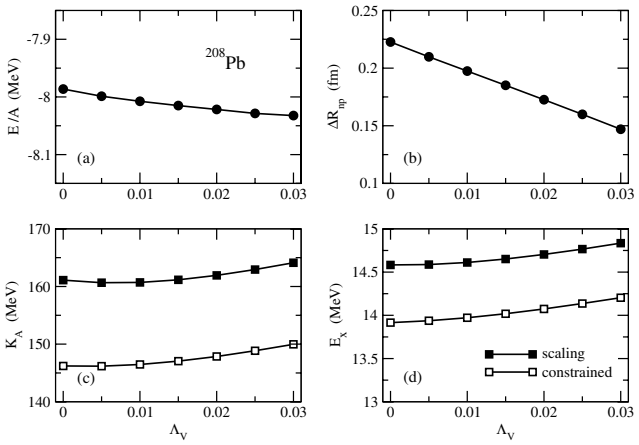


**Figure 2.** Dependence with the value of the isoscalar–isovector coupling $\Lambda_V$ of the energy per particle (a), neutron skin thickness (b), finite nucleus compression modulus (c) and average excitation energy of the GMR (d) for the $^{208}$Pb nucleus.

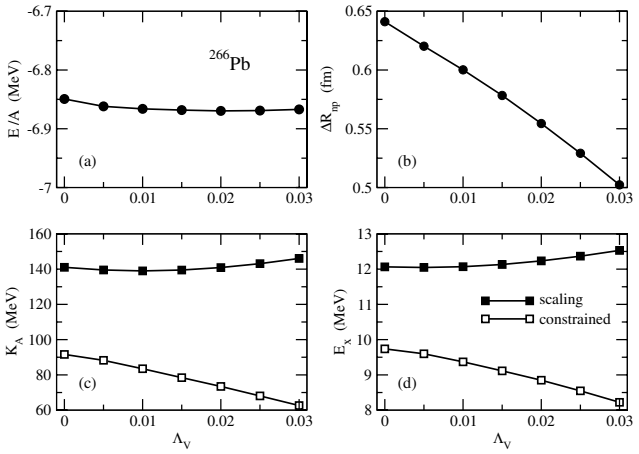


**Figure 3.** Dependence with the value of the isoscalar–isovector coupling $\Lambda_V$ of the energy per particle (a), neutron skin thickness (b), finite nucleus compression modulus (c) and average excitation energy of the GMR (d) for the $^{266}$Pb nucleus.

stiff symmetry energy at $\Lambda_V = 0.00$, while it has a soft symmetry energy at $\Lambda_V = 0.03$. The RMF Lagrangian supplemented by the nonlinear interaction between the $\omega$- and $\rho$-meson fields leaves the binding energy of the nucleus almost independent of $\Lambda_V$, at least for moderate

values of this coupling. We note from the results for $^{266}$Pb in figure 3 that this happens not only in the case of stable nuclei, which we have seen previously for $^{208}$Pb and $^{90}$Zr in table 1, but also in the case of much more neutron-rich nuclei. The neutron thickness $\Delta R_{np}$ decreases almost linearly with an increase of $\Lambda_V$ in both $^{208}$Pb and $^{266}$Pb. The reduction of the $\Delta R_{np}$ value at $\Lambda_V = 0.03$ amounts to about 30% of the original neutron skin thickness at $\Lambda_V = 0.00$. The proton rms radius $R_p$ of $^{208}$Pb and $^{266}$Pb has been found to remain nearly constant with $\Lambda_V$, and therefore the decrease of $\Delta R_{np}$ is due almost exclusively to the decrease of $R_n$. It is worth mentioning that the alluded variation of the neutron skin thickness of $^{208}$Pb in the present calculations is close to roughly a 1% change in the neutron rms radius $R_n$ of this nucleus. That is, the range of variation we have allowed in the density dependence of the symmetry energy by changing $\Lambda_V$ between 0.00 and 0.03 induces a change in $R_n$ of $^{208}$Pb around 1%. In this sense, it is consistent with the uncertainty that will remain in this observable after the PREX experiment at the Jefferson Laboratory [76], which aims to measure $R_n$ of $^{208}$Pb to 1% accuracy via parity-violating electron scattering.

The average excitation energy of the GMR calculated in the RETF approach involves the knowledge of the finite nucleus compression modulus $K_A$, or restoring force of the resonance. We display $K_A$ in figures 2(c) and 3(c) for $^{208}$Pb and $^{266}$Pb, respectively. Let us discuss first the change of $K_A$ with the mass number $A$ in isotopes. We see from the results for $^{208}$Pb and $^{266}$Pb that the finite nucleus compression modulus decreases when $A$ increases. This behavior may be easily understood from the so-called leptodermous expansion of $K_A$ [77]:

$$K_A = K_0 + K_{\rm surf} A^{-1/3} + K_\tau I^2 + K_{\rm Coul} Z^2 A^{-4/3} + \cdots , \tag{21}$$

where $K_0$ is the compression modulus of symmetric infinite nuclear matter and $K_{\rm surf}$, $K_\tau$ and $K_{\rm Coul}$ are the leading surface, volume–symmetry and Coulomb corrections. The coefficients $K_{\rm surf}$, $K_\tau$ and $K_{\rm Coul}$ in the scaling model are negative, and in particular $K_\tau$ may be large [33, 63, 77–80]. Within an isotopic chain, the nuclear charge $Z$ is fixed and therefore the neutron–proton asymmetry $I = (N - Z)/A$ increases when $A$ increases. Then, although the surface and Coulomb contributions in (21) become a little less negative with increasing $A$, the increase of the negative volume–symmetry contribution $K_\tau I^2$ dominates. Therefore, $K_A$ in isotopes decreases with larger $A$. We stress that expansion (21) is provided here for indicative purposes only and that in all results we have computed $K_A$ self-consistently.

The scaling value $K_A^{\rm scal}$ of the finite nucleus incompressibility, given by equation (8) of section 2.2, is displayed in figures 2(c) and 3(c) by the upper curves with solid symbols. For both isotopes $^{208}$Pb and $^{266}$Pb, $K_A^{\rm scal}$ shows an upward trend with larger $\Lambda_V$. This variation of $K_A^{\rm scal}$ with $\Lambda_V$ is due to the softening of the density dependence of the symmetry energy. It modifies the value of $K_\tau$ and consequently $K_A$ (of course, $K_\tau$ does not describe alone the whole effect as there are surface symmetry and other corrections neglected in (21) [63]). The present models have all $K_0 = 271.5$ MeV, while the $K_\tau$ coefficient changes from $-699$ MeV in NL3.00 to $-381$ MeV in NL3.03. The recent empirical extractions of $K_\tau$ suggest $K_\tau$ values in this range. For example, isospin diffusion in nuclear reactions favors the constraint $K_\tau = -500 \pm 50$ MeV [4], the breathing mode of Sn isotopes suggests $K_\tau = -550 \pm 100$ MeV [28] (or $-500 \pm 50$ MeV [79]) and neutron skins of nuclei point to $K_\tau = -500^{+125}_{-100}$ MeV [12].

The excitation energy $E_M^{\rm scal}$ of the monopole oscillation evaluated in the scaling approach is determined by the ratio of the restoring force $K_A^{\rm scal}$ to the mass parameter $B_M$ (section 2). As indicated, to replace $B_M$ by its nonrelativistic limit $B_M^{\rm nr}$ is a very good approximation. In practice, this implies that $B_M$ varies with the parameters of the nuclear interaction essentially in the same way as $\langle r^2 \rangle$ of the nucleus does, see equation (11). When $\Lambda_V$ is increased, $\langle r^2 \rangle$ of the matter distribution of the nucleus decreases because of the reduction of the neutron rms

radius originated by the softer symmetry energy. As a consequence, the mass parameter of the GMR (analogously, the $m_1$ sum rule (17) in the nonrelativistic language) also decreases. This effect combined with the growing tendency of $K_A^{\rm scal}$ with $\Lambda_V$ implies that the scaling excitation energy of the GMR will be enhanced with a softer symmetry energy, which is confirmed in figures 2(d) and 3(d) where $E_M^{\rm scal}$ is plotted. We recall that this enhancement of $E_M^{\rm scal}$ is due to the different density dependence of the symmetry energy alone because the incompressibility $K_0$ of symmetric matter is forced to be the same in all the interactions considered here.

Let us now analyze the results obtained through the constrained calculations described in section 2.3. For the stable nucleus $^{208}$Pb, we see in figure 2 that $K_A^{\rm cons}$ and $E_M^{\rm cons}$ have a similar behavior to the discussed scaling results as a function of the density dependence of the symmetry energy. The separation between $E_M^{\rm scal}$ and $E_M^{\rm cons}$ is indicative of the width of the GMR resonance (see equation (20)), and therefore this quantity is basically constant with the symmetry energy in $^{208}$Pb. In contrast to this situation in the stable $^{208}$Pb nucleus, in the more neutron-rich isotope $^{266}$Pb we see in figure 3 that the change of $K_A^{\rm cons}$ and $E_M^{\rm cons}$ with the symmetry energy exhibits a different pattern from the corresponding scaling results. For $^{266}$Pb, both quantities $K_A^{\rm cons}$ and $E_M^{\rm cons}$ not only do not increase with $\Lambda_V$, but they decrease significantly.

To interpret the reduction of $E_M^{\rm cons}$ and $K_A^{\rm cons}$ with $\Lambda_V$ in $^{266}$Pb, it will be helpful to rewrite the expression $E_M^{\rm cons} = \left(AK_A^{\rm cons}/B_M\right)^{1/2}$ of equation (15) by approximating $B_M$ with its nonrelativistic form $B_M^{\rm nr} = mA\langle r^2\rangle$, and to write $K_A^{\rm cons}$ using the first expression given in equation (14). This results in

$$E_M^{\rm cons} \simeq \sqrt{\frac{2A\langle r^2\rangle/m}{-\frac{1}{2}A\left(\partial R_\eta^2/\partial\eta\right)_{\eta=0}}} \equiv \sqrt{\frac{\overline{m}_1}{\overline{m}_{-1}}}, \tag{22}$$

which in terms of the defined quantities $\overline{m}_1$ and $\overline{m}_{-1}$ has the same form that $E_M^{\rm cons}$ takes in the nonrelativistic RPA formalism of sum rules (i.e. $E_1$ of equation (16)) [44–46]. It is to be noted that the denominator of (22) is very sensitive to the presence of loosely bound nucleons in the nucleus [47], which is precisely the situation that occurs in $^{266}$Pb. When one approaches the neutron drip line, the negative chemical potential $\mu_n$ of neutrons becomes close to vanishing, implying that the system contains weakly bound neutrons. These neutrons are very soft against compression and in the constrained calculations they give rise to a large increase of the absolute value of $\left(\partial R_\eta^2/\partial\eta\right)_{\eta=0}$, i.e. of $\overline{m}_{-1}$ in (22). This effect has been found in [47] in constrained HF (and ETF) calculations for nonrelativistic Skyrme forces, where it can be related to the enhancement of the RPA strength in the low-energy region produced by the increase of the transitions to the continuum at large neutron numbers. The same effect is found in the recently published QRPA and CHFB Skyrme calculations, which take account of the pairing correlations, performed in the light isotopic chains of Ca and Ni [37]. In our present calculations, when the increase of $\overline{m}_{-1}$ at large neutron numbers is accentuated the softer is the symmetry energy (note that parameter sets having a softer symmetry energy have also weaker binding energy of the last bound neutrons [10] and therefore reinforce the effect). This explains the decreasing trend of $E_M^{\rm cons}$ with $\Lambda_V$ in $^{266}$Pb noted in figure 3. The decrease of $K_A^{\rm cons}$ with $\Lambda_V$ seen in the same figure is similarly understood by recalling equation (14) that relates $K_A^{\rm cons}$ to $\left(\partial R_\eta^2/\partial\eta\right)_{\eta=0}^{-1}$.

### *3.3. GMR along the Pb and Zr isotopic chains*

In this section we would like to investigate at which values of the neutron excess of the nucleus the effects coming from the symmetry energy become more relevant in the excitation energies

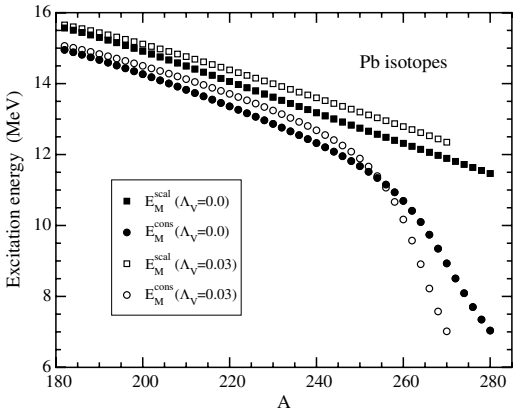


**Figure 4.** Mass-number dependence of the excitation energy of the giant monopole resonance in the Pb isotopic chain for the NL3 model with $\Lambda_V = 0$ (stiff symmetry energy) and $\Lambda_V = 0.03$ (soft symmetry energy), in the scaling and constrained approaches.

of the GMR in isotopic chains of heavy (Pb) and medium (Zr) mass. Within the Skyrme–Hartree–Fock framework, in [47] we analyzed the excitation energy and the resonance width of the GMR in some isotopic chains with the sum-rule approach (i.e. through scaling and constrained calculations). In the case of a small atomic number such as the Ca isotopes, the semiclassical ETF results were able to describe the global variation of the quantal HF excitation energies but could not reproduce them quantitatively. However, the ETF results for the GMR excitation energies become progressively more accurate with a larger atomic number. In the case of the Pb chain, the ETF scaling and constrained excitation energies were found to be in very good agreement with the quantal HF values on the quantitative level from the proton to the neutron drip line (the differences between ETF and quantal values not exceeding 0.4 MeV) [47]. Thus, from the experience in the nonrelativistic calculations, as well as suggested by the comparison of RETF and RRPA results made in table 1, the present semiclassical predictions for the GMR are expected to be sufficiently realistic, and rather accurate quantitatively (compared to quantal calculations) in the case of the Pb isotopes.

We depict in figure 4 the scaling and constrained average excitation energies of the GMR for the Pb isotopic chain. Here we only use the values 0.00 and 0.03 for the nonlinear $\omega$–$\rho$ interaction $\Lambda_V$, representing stiff and soft density dependences of the symmetry energy. In the semiclassical calculations, the vanishing of the neutron chemical potential $\mu_n$ defines the location of the neutron drip line. We see in figure 4 that the latter is reached at a smaller mass number when the model has a soft symmetry energy, in agreement with the earlier observations of [10]. Note that shell effects are absent in these semiclassical predictions of the drip line (a quantal Hartree calculation with NL3 predicts the Pb neutron drip line at $A = 266$). The proton drip line occurs at the neutron number $N$ not much larger than $Z$. Therefore, because one deals with almost symmetric matter, the position of the proton drip line is unaffected by the density dependence of the symmetry energy.

The calculated GMR excitation energies show in figure 4 a downward tendency with increasing mass number $A$ when one proceeds along the isotopic chain, by similar reasons to those pointed out in our previous discussion about the $^{208}$Pb and $^{266}$Pb isotopes. The

downward trend is more noticeable for $E_M^{\rm cons}$ than for $E_M^{\rm scal}$ in the isotopes with larger neutron numbers. The scaling excitation energies $E_M^{\rm scal}$ obtained using a parameter set with a soft symmetry energy ($\Lambda_V = 0.03$) are systematically higher in the whole isotopic chain than if the symmetry energy is stiff ($\Lambda_V = 0.00$). Similar to the scaling results discussed for $^{208}$Pb and $^{266}$Pb, this behavior of $E_M^{\rm scal}$ is a consequence of the fact that the matter radius of the nucleus is smaller and the scaling incompressibility $K_A^{\rm scal}$ larger for a soft symmetry energy.

At variance with the uniformity displayed by the $E_M^{\rm scal}$ results, the constrained estimate $E_M^{\rm cons}$ of the GMR excitation energy has a distinct feature with the symmetry energy below and above $A \simeq 254$. If the mass number is below $A \simeq 254$, $E_M^{\rm cons}$ is larger when the parameter set has a soft symmetry energy. However, this tendency is reversed from $A \simeq 254$ to the neutron drip line when the isotopes are more neutron rich. Actually, in a given nucleus the $\Lambda_V$ parameter reduces its neutron rms radius, which means that the system becomes on average more compact. As long as the nucleus is not very neutron rich, if it is more compact, the effect of the constraining parameter $\eta$ on the nuclear rms radius is less, and therefore the absolute value of $\left(\partial R_\eta^2/\partial\eta\right)_{\eta=0}$ in the denominator of equation (22) for $E_M^{\rm cons}$ is smaller. This explains the larger magnitude of $E_M^{\rm cons}$ at $\Lambda_V = 0.03$, compared to $\Lambda_V = 0.00$, in the Pb isotopes lighter than $A \simeq 254$. But a point is reached in a mass number ($A \simeq 254$ here) where the isotopes are so neutron rich that the last neutrons become very weakly bound. These outer neutrons are very soft against compression. As a result of their specific contribution to $R_\eta^2$ when one applies an external constraint, the absolute value of $\left(\partial R_\eta^2/\partial\eta\right)_{\eta=0}$ increases sharply instead of decreasing. This originates the large reduction of $E_M^{\rm cons}$ seen in figure 4 for the more neutron-rich isotopes. The reduction of $E_M^{\rm cons}$ at large neutron numbers is enhanced when the symmetry energy is soft compared to the case of a stiff symmetry energy because the outer neutrons are more weakly bound in the former case. A comparable decrease of the excitation energy of the GMR, however, is not present in the scaling calculations because the discussed effect does not arise in a self-similar scaling of the density of the nucleus. As we mentioned in section 2.4, the scaling and constrained average energies pertain to different energy regimes of the GMR. While $E_M^{\rm scal}$ informs more about the relatively high-energy contributions to the RPA strength, $E_M^{\rm cons}$ carries more information about the low-energy sector which is the region that shows the more noticeable changes in largely neutron-rich nuclei because of the presence of weakly bound neutrons.

We may take $\sigma = \frac{1}{2}\left[\left(E_M^{\rm scal}\right)^2 - \left(E_M^{\rm cons}\right)^2\right]^{1/2}$ as an estimate of the width of the GMR, in analogy with the nonrelativistic framework [44–46] (see section 2.4). From the separation observed in figure 4 between $E_M^{\rm scal}$ and $E_M^{\rm cons}$, at either $\Lambda_V = 0.00$ or $\Lambda_V = 0.03$, the width of the resonance is expected to be almost independent of the mass number and of the density dependence of the symmetry energy for all of the Pb nuclei located in the region between the proton-rich side of the isotopic chain till $A \simeq 230$–$240$. However, $E_M^{\rm cons}$ starts to show a pronounced departure from $E_M^{\rm scal}$ after $A \simeq 240$ and, as a consequence, the resonance width should display a sharp increase for the Pb isotopes with large neutron numbers. We see from figure 4 that this effect is predicted to be stronger when the nuclear interaction has a soft symmetry energy. As discussed in [47] in nonrelativistic calculations with Skyrme forces, the value of the estimate $\sigma$ of the GMR width provides a qualitative idea about the distribution of the RPA strength. A small width $\sigma$ indicates that the RPA strength of the GMR is basically concentrated in a narrow single peak, while a large width $\sigma$ suggests that the peak is broad, or even that the RPA strength may be fragmented into several peaks. The large value of $\overline{m}_{-1} \propto -\left(\partial R_\eta^2/\partial\eta\right)_{\eta=0}$ (see equation (22)) that one finds in the constrained calculations for the more neutron-rich Pb isotopes points toward an enhancement of the RPA strength in the low-energy region in these nuclei, due to transitions from the last weakly bound single-particle

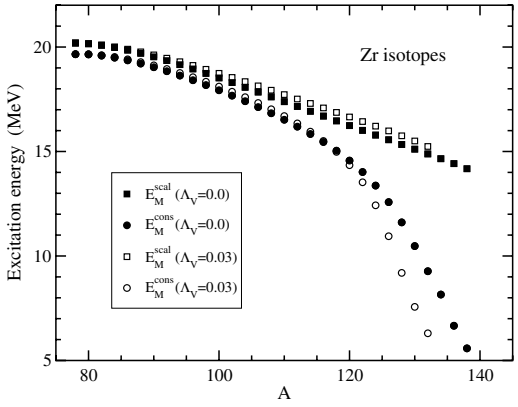


**Figure 5.** Mass-number dependence of the excitation energy of the giant monopole resonance in the Zr isotopic chain for the NL3 model with $\Lambda_V = 0$ (stiff symmetry energy) and $\Lambda_V = 0.03$ (soft symmetry energy), in the scaling and constrained approaches.

levels to the continuum [47]. (This effect, which has a quantal origin, is accounted at least on average by the semiclassical calculations [47].) The discussed scenario is actually confirmed by the QRPA calculations of [37] where the fragmentation as well as the enhancement of the low-energy part of the RPA strength in Ca and Ni isotopes approaching the neutron drip line can be seen in figures 3 and 6.

Lastly, we present in figure 5 the calculated results for the excitation energies of the GMR in the Zr isotopic chain. The variation of the excitation energies obtained in the scaling scheme as a function of the mass number $A$ and of the $\Lambda_V$ coupling is qualitatively similar to the pattern exhibited by the Pb isotopes. That is, the excitation energies $E_M^{\rm scal}$ show a monotonic decrease with increasing mass number, and they are larger when calculated with a soft symmetry energy. The relative differences between the values of $E_M^{\rm scal}$ at $\Lambda_V = 0.03$ and at $\Lambda_V = 0.00$ are smaller compared to the chain of the Pb isotopes because of the smaller isospin content of the Zr isotopes. Concerning the results for the constrained excitation energies in Zr, the value of $E_M^{\rm cons}$ shows a stronger dependence on the mass number $A$ at large neutron numbers than the scaling value $E_M^{\rm scal}$. As long as $A \lesssim 120$, the excitation energy $E_M^{\rm cons}$ for zirconium is to a large extent independent of the symmetry energy. But afterward ($A \gtrsim 120$), $E_M^{\rm cons}$ becomes visibly lower for the soft symmetry energy.

In consonance with the behavior of $E_M^{\rm scal}$ and $E_M^{\rm cons}$ found in figure 5, it is predicted that the width $\sigma$ of the GMR for the Zr nuclei should remain practically constant till $A \simeq 100$. The width $\sigma$ would start increasing moderately between $A \simeq 100$ and $A \simeq 120$ because of the slight gradual separation between $E_M^{\rm scal}$ and $E_M^{\rm cons}$ in these isotopes. Finally, the resonance width would be much enhanced in the region of the most neutron-rich Zr isotopes, where the effect is largely reinforced by having a soft symmetry energy in the nuclear interaction.

## 4. Summary and conclusions

Though the excitation energy of the isoscalar giant monopole resonance is mainly ruled by the compression modulus of symmetric nuclear matter, it is also affected by the symmetry energy

in neutron-rich nuclei. In this paper we have analyzed the influence of the density dependence of the symmetry energy on the average excitation energy of the GMR. In order to do this study, we have used a relativistic mean field model supplemented by an additional $\omega$–$\rho$ nonlinear interaction driven by a coupling constant $\Lambda_V$. This additional coupling allows one to generate different parameter sets that preserve the properties of the symmetric matter and differ among them, only, in the density dependence of the symmetry energy, which is softened by increasing $\Lambda_V$. As a function of the coupling constant $\Lambda_V$, the model predicts in finite nuclei almost the same binding energy and proton rms radius as in the case where $\Lambda_V = 0$, while the neutron rms radius gets significantly reduced.

The excitation energy of the isoscalar giant monopole resonance has been computed using the semiclassical relativistic extended Thomas–Fermi theory. We obtain the energy of the breathing mode in two different ways: through the scaling model and performing constrained calculations. It is known that these calculations with nonrelativistic Skyrme forces nicely reproduce the average energies $E_3$ and $E_1$ obtained from the more microscopic RPA calculations, not only for stable nuclei but also for largely neutron-rich nuclei [47]. In our study, we have calculated the scaling and constrained semiclassical average energies with the relativistic model along the isotopic chains of Pb and Zr. We can also obtain some qualitative information about the distribution of the RPA strength from the resonance width computed using these two semiclassical estimates of the excitation energy.

As is known, the excitation energy of the breathing mode decreases, at least for stable nuclei, following roughly an $A^{-1/3}$ law [77] due to the geometrical enhancement of the mass denominator. However, when the neutron–proton asymmetry increases, departures from this behavior appear. The reason is that the isospin-dependent part of the finite nucleus incompressibility $K_A$ plays a non-negligible role by reducing the restoring force and making nuclei with large neutron numbers softer than the stable isotopes. This effect in the average excitation energy is present in the scaling estimate but it is particularly strong in the constrained calculation. When the neutron–proton asymmetry increases, the outer neutrons become more and more weakly bound starting to behave almost as extremely asymmetric nuclear matter, which is very soft compared to symmetric matter [81]. This effect makes the compression modulus $K_{\rm A}^{\rm cons}$ smaller and, therefore, the average excitation energy of the GMR decreases. As discussed in the case of constrained HF calculations with Skyrme forces [47], this scenario reflects the important contribution to the low-energy part of the RPA strength distribution coming from the particle-hole transitions to the continuum from the weakly bound neutron energy levels in nuclei having large neutron numbers. A similar situation has been found recently by Capelli, Colò and Li [37] in QRPA and constrained HFB Skyrme calculations performed along the light isotopic chains of Ca and Ni.

For a given nucleus the excitation energy of the GMR also depends on the density content of the symmetry energy of the model used to compute it. In stable nuclei the scaled and constrained estimates of the excitation energy are larger for parameter sets that have a symmetry energy with a soft density dependence. In the case of the constrained estimate, this tendency is reversed in the nuclei with large neutron–proton asymmetry. The reason lies in the fact that in these nuclei the outermost and weakly bound neutrons are very compressible and consequently the constrained compression modulus $K_{\rm A}^{\rm cons}$ becomes lower when the density dependence of the symmetry energy is soft (the outer neutrons are then less bound) than when the symmetry energy is stiff. Thus, the average excitation energies based on the inverse energy-weighted sum rule are predicted to be significantly reduced for large neutron numbers when computed with a parameter set that has a softer density dependence of the symmetry energy.

In conclusion, the density dependence of the symmetry energy has a moderate influence on the value of the excitation energy of the isoscalar giant monopole resonance in stable nuclei and in nuclei that are not far from stability. It has a larger impact on the GMR of isotopes with large isospins, where the calculations reveal that the constrained energies become much reduced in models having a soft symmetry energy. The results point toward a considerable enhancement of the low-energy part of the RPA strength and to likely different structures in the excitation spectra of the GMR in unstable neutron-rich nuclei if the nuclear symmetry energy is soft. It may be worth pursuing a detailed characterization of these predictions related to the softness of the symmetry energy by computing the strength distribution in a few selected isotopes at large neutron numbers with the more demanding but more microscopic QRPA theory of the GMR response. Unfortunately, it is difficult that the indicated effects be tested in the laboratory as they become prominent at neutron numbers beyond present reach. Such nuclear systems are otherwise expected to exist under astrophysical conditions, such as those prevailing in the inner crust of neutron stars, where exotic nuclear clusters can be stabilized by an enveloping gas of neutrons and electrons [50]. It is thought that low-energy collective excitations play an important role in astrophysical processes that involve nuclei far from stability [82], and in that context the modification of the low-energy region of the strength distribution of the monopole resonance by the softness of the symmetry energy could have implications.

**Acknowledgments**

MC, XR and XV would like to thank J Piekarewicz for useful conversations. They acknowledge support from the Consolider Ingenio 2010 Programme CPAN CSD2007-00042 and grants FIS2008-01661 from MEC and FEDER, and 2009SGR-1289 from Generalitat de Catalunya. XR also acknowledges grant AP2005-4751 from MEC. SKP and BKS acknowledge the support of CSIR (no 03(1060) 06/EMR-II), Government of India. PDS acknowledges support from the UK Science and Technology Facilities council under grants PP/F000596/1 and ST/F012012/1.

**Appendix A. Equations of the relativistic extended Thomas–Fermi model**

We have introduced the energy density of the relativistic nuclear mean field model supplemented by an isoscalar–isovector mixed $\omega$–$\rho$ interaction in equation (1) of the text. Following [56–59], in the relativistic extended Thomas–Fermi approach the expression of the nucleonic part $\mathcal{E}$ is written as $\mathcal{E} = \mathcal{E}_0 + \mathcal{E}_2$, where

$$\mathcal{E}_0 = \sum_{q=\mathrm{n,p}} \frac{1}{8\pi^2}\left[k_{\mathrm{F}q}\epsilon_{\mathrm{F}q}^3 + k_{\mathrm{F}q}^3\epsilon_{\mathrm{F}q} - m^{*4}\ln\frac{k_{\mathrm{F}q}+\epsilon_{\mathrm{F}q}}{m^*}\right] \tag{A.1}$$

and

$$\mathcal{E}_2 = \sum_{q=\mathrm{n,p}} [C_{1q}(k_{\mathrm{F}q}, m^*)(\nabla\rho_q)^2 + C_{2q}(k_{\mathrm{F}q}, m^*)(\nabla\rho_q\cdot\nabla m^*) + C_{3q}(k_{\mathrm{F}q}, m^*)(\nabla m^*)^2]. \tag{A.2}$$

The leading term $\mathcal{E}_0$ is the contribution of the pure Thomas–Fermi part, while the term $\mathcal{E}_2$ contains the gradient corrections of order $\hbar^2$. The variables $k_{\mathrm{F}q}$, $m^*$ and $\epsilon_{\mathrm{F}q}$ are, respectively, the local Fermi momentum $k_{\mathrm{F}q} = (3\pi^2\rho_q)^{1/3}$, the Dirac effective mass $m^* = m - \Phi$ and the dispersion relation $\epsilon_{\mathrm{F}q} = \left(k_{\mathrm{F}q}^2 + m^{*2}\right)^{1/2}$ of the effective particle, with $q = \mathrm{n}$ for neutrons and $q = \mathrm{p}$ for protons. The coefficients $C_{iq}$ stand for the following analytic functions of $k_{\mathrm{F}q}$ and

$m^* = m - \Phi$:

$$C_{1q} = \frac{\pi^2}{24 k_{\mathrm{F}q}^3 \epsilon_{\mathrm{F}q}^2}\left(\epsilon_{\mathrm{F}q} + 2k_{\mathrm{F}q}\ln\frac{k_{\mathrm{F}q}+\epsilon_{\mathrm{F}q}}{m^*}\right),$$
$$C_{2q} = \frac{m^*}{6 k_{\mathrm{F}q}\epsilon_{\mathrm{F}q}^2}\ln\frac{k_{\mathrm{F}q}+\epsilon_{\mathrm{F}q}}{m^*}, \tag{A.3}$$
$$C_{3q} = \frac{k_{\mathrm{F}q}^2}{24\pi^2\epsilon_{\mathrm{F}q}^2}\left[\frac{\epsilon_{\mathrm{F}q}}{k_{\mathrm{F}q}} - \left(2+\frac{\epsilon_{\mathrm{F}q}^2}{k_{\mathrm{F}q}^2}\right)\ln\frac{k_{\mathrm{F}q}+\epsilon_{\mathrm{F}q}}{m^*}\right].$$

The RETF ground-state densities and meson fields are calculated by solving by a numerical iteration the Euler–Lagrange equations associated with the energy density (1), with the constraint of baryon number conservation (which is imposed through Lagrange multipliers $\mu_q$, the chemical potentials of neutrons and protons):

$$\epsilon_{\mathrm{F}q} + W + \frac{1}{2}[\mathcal{A} + (\mathcal{A}+B)\tau_{3q}] - 2C_{1q}\Delta\rho_q - C_{2q}\Delta m^* - \frac{\partial C_{1q}}{\partial\rho_q}(\nabla\rho_q)^2$$
$$- 2\frac{\partial C_{1q}}{\partial m^*}(\nabla\rho_q\cdot\nabla m^*) - \left(\frac{\partial C_{2q}}{\partial m^*} - \frac{\partial C_{3q}}{\partial\rho_q}\right)(\nabla m^*)^2 = m + \mu_q, \tag{A.4}$$

$$\left(\Delta - m_s^2\right)\Phi = -g_s^2\left(\rho_s - \frac{\kappa}{2!}\Phi^2 - \frac{\lambda}{3!}\Phi^3\right) \equiv -g_s^2\rho_s^{\mathrm{eff}}, \tag{A.5}$$

$$\left(\Delta - m_v^2\right)W = -g_v^2(\rho - 2\Lambda_V B^2 W), \tag{A.6}$$

$$\left(\Delta - m_\rho^2\right)B = -g_\rho^2(\rho_3 - 2\Lambda_V B W^2), \tag{A.7}$$

$$\Delta\mathcal{A} = -\rho_p. \tag{A.8}$$

We have $\tau_{3q} = +1$ for protons and $\tau_{3q} = -1$ for neutrons. The baryon density is $\rho = \rho_p + \rho_n$, while $\rho_3 = \frac{1}{2}(\rho_p - \rho_n)$ is the isovector density of the nucleus. Finally, the RETF expression of the scalar density $\rho_s$ entering equation (A.5) is given by

$$\rho_s = \frac{\delta\mathcal{E}}{\delta m^*} = \frac{\delta\mathcal{E}_0}{\delta m^*} + \frac{\delta\mathcal{E}_2}{\delta m^*} = \rho_{s0} + \rho_{s2}$$
$$= \sum_q \frac{m^*}{2\pi^2}\left[k_{\mathrm{F}q}\epsilon_{\mathrm{F}q} - m^{*2}\ln\frac{k_{\mathrm{F}q}+\epsilon_{\mathrm{F}q}}{m^*}\right]$$
$$- \sum_q\left[C_{2q}\Delta\rho_q + 2C_{3q}\Delta m^* + \left(\frac{\partial C_{2q}}{\partial\rho_q} - \frac{\partial C_{1q}}{\partial m^*}\right)(\nabla\rho_q)^2\right.$$
$$\left. + 2\frac{\partial C_{3q}}{\partial\rho_q}(\nabla\rho_q\cdot\nabla m^*) + \frac{\partial C_{3q}}{\partial m^*}(\nabla m^*)^2\right]. \tag{A.9}$$

## Appendix B. Klein–Gordon equations of the scaled meson fields

In this appendix we illustrate how to calculate the derivatives of the scaled meson fields upon the scaling parameter $\alpha$ that we have used to represent the collective coordinate of the monopole oscillation of the nucleus in the scaling approach. In view of equation (5) for the scaled baryon density $\rho_\alpha$, i.e. $\rho_\alpha(\boldsymbol{r}) = \alpha^3\rho(\alpha\boldsymbol{r})$, and of the field equation (A.6) obeyed by the omega–meson field $W$, the scaled field $W_\alpha$ fulfills the Klein–Gordon equation

$$\left(\Delta_{\boldsymbol{u}} - \frac{m_v^2}{\alpha^2}\right)W_\alpha(\boldsymbol{u}) = -g_v^2\left(\alpha\rho(\boldsymbol{u}) - \frac{2\Lambda_V}{\alpha^2}B_\alpha(\boldsymbol{u})^2 W_\alpha(\boldsymbol{u})\right), \tag{B.1}$$

where we have introduced the coordinate $\boldsymbol{u} \equiv \alpha \boldsymbol{r}$. On differentiating equation (B.1) with respect to the scaling parameter $\alpha$ we have

$$\left(\Delta_u - \frac{m_v^2}{\alpha^2}\right)\frac{\partial W_\alpha}{\partial \alpha} = -g_v^2\left(\rho + \frac{2m_v^2}{g_v^2}\frac{W_\alpha}{\alpha^3} + \frac{4\Lambda_V}{\alpha^3}B_\alpha^2 W_\alpha - \frac{4\Lambda_V}{\alpha^2}B_\alpha W_\alpha \frac{\partial B_\alpha}{\partial \alpha} - \frac{2\Lambda_V}{\alpha^2}B_\alpha^2\frac{\partial W_\alpha}{\partial \alpha}\right). \quad \text{(B.2)}$$

If we now set $\alpha = 1$, the solution of this equation allows us to obtain the value of the derivative $\partial W_\alpha/\partial\alpha|_{\alpha=1}$. One can work out the equations for the scaled isovector $\rho$-meson field in the same way. In practice, one simply has to replace $(W_\alpha, B_\alpha, \rho, m_v, g_v)$ by $(B_\alpha, W_\alpha, \rho_3, m_\rho, g_\rho)$ in equations (B.1) and (B.2).

In the case of the scalar field one has to take account of the terms that arise due to the fact that the scalar density $\rho_s$ is itself a function of the scalar field. Following the same steps as above, from the Klein–Gordon equation

$$\left(\Delta_u - \frac{m_s^2}{\alpha^2}\right)\Phi_\alpha(\boldsymbol{u}) = -\alpha g_s^2 \tilde{\rho}_s^{\rm eff}(\boldsymbol{u}) \quad \text{(B.3)}$$

for the scaled scalar field $\Phi_\alpha$, one readily arrives at the equation

$$\left(\Delta_u - \frac{m_s^2}{\alpha^2}\right)\frac{\partial \Phi_\alpha}{\partial \alpha} = -g_s^2\left(\tilde{\rho}_s^{\rm eff} + \alpha\frac{\partial \tilde{\rho}_s^{\rm eff}}{\partial \alpha} + \frac{2m_s^2}{g_s^2}\frac{\Phi_\alpha}{\alpha^3}\right), \quad \text{(B.4)}$$

whose solution at $\alpha = 1$ provides the value of $\partial\Phi_\alpha/\partial\alpha|_{\alpha=1}$.

## References


[1] Steiner A W, Prakash M, Lattimer J M and Ellis P J 2005 *Phys. Rep.* **411** 325 (arXiv:nucl-th/0410066)
[2] Klähn T *et al* 2006 *Phys. Rev.* C **74** 035802 (arXiv:nucl-th/0602038)
[3] Lattimer J M and Prakash M 2007 *Phys. Rep.* **442** 109 (arXiv:astro-ph/0612440)
[4] Li B A, Chen L W and Ko C M 2008 *Phys. Rep.* **464** 113 (arXiv:0804.3580)
[5] Xu J, Chen L W, Li B A and Ma H R 2009 *Astrophys. J.* **697** 1549 (arXiv:0901.2309)
[6] Bednarek I and Manka R 2009 *J. Phys. G: Nucl. Part. Phys.* **36** 095201 (arXiv:0905.0131)
[7] Brown B A 2000 *Phys. Rev. Lett.* **85** 5296
[8] Horowitz C J and Piekarewicz J 2001 *Phys. Rev. Lett.* **86** 5647
[9] Horowitz C J and Piekarewicz J 2001 *Phys. Rev.* C **64** 062802
[10] Todd B G and Piekarewicz J 2003 *Phys. Rev.* C **67** 044317
[11] Danielewicz P 2003 *Nucl. Phys.* A **727** 233
[12] Centelles M, Roca-Maza X, Viñas X and Warda M 2009 *Phys. Rev. Lett.* **102** 122502 (arXiv:0806.2886)
[13] Warda M, Viñas X, Roca-Maza X and Centelles M 2009 *Phys. Rev.* C **80** 024316 (arXiv:0906.0932)
[14] Baran V, Colonna M, Greco V and Di Toro M 2005 *Phys. Rep.* **410** 335 (arXiv:nucl-th/0412060)
[15] Shetty D V, Yennello S J and Souliotis G A 2007 *Phys. Rev.* C **76** 024606 (arXiv:0704.0471)
[16] Tsang M B, Zhang Y, Danielewicz P, Famiano M, Li Z, Lynch W G and Steiner A W 2009 *Phys. Rev. Lett.* **102** 122701 (arXiv:0811.3107)
[17] Klimkiewicz A *et al* 2007 *Phys. Rev.* C **76** 051603
[18] Trippa L, Colò G and Vigezzi E 2008 *Phys. Rev.* C **77** 061304 (arXiv:0802.3658)
[19] Roy C P, Basu D N and Samanta C 2009 *Phys. Rev.* C **80** 011305 (arXiv:0905.1599)
[20] Khoa Dao T, von Oertzen W and Ogloblin A A 1996 *Nucl. Phys.* A **602** 98
[21] Ozawa A, Suzuki T and Tanihata I 2001 *Nucl. Phys.* A **693** 32
[22] Khoa Dao T, Than H S, Nam T H, Grasso M and Van Giai N 2004 *Phys. Rev.* C **69** 044605
[23] Seweryniak D and Khoo L (ed) 2005 *Nuclei at the Limits (Argonne, USA, 2004) AIP Conf. Proc.* **764**
[24] Gross C J, Nazarewicz W and Rykaczewski K P (ed) 2005 Proc. Conf. ENAM'04 on Exotic Nuclei and Atomic Masses (Pine Mountain, USA, 2004) *Eur. Phys. J.* A **25** s01
[25] Harakeh M N and van der Woude A 2001 *Giant Resonances* (Oxford: Oxford University Press)
[26] Harakeh M N 2002 *Eur. Phys. J.* A **13** 169
[27] Youngblood D H, Clark H L and Lui Y-W 1999 *Phys. Rev. Lett.* **82** 691

[28] Li T *et al* 2007 *Phys. Rev. Lett.* **99** 162503 (arXiv:0709.0567)
[29] Monrozeau C *et al* 2008 *Phys. Rev. Lett.* **100** 042501
[30] Blaizot J P, Berger J F, Dechargé J and Girod M 1995 *Nucl. Phys.* A **591** 435
[31] Farine M, Pearson J M and Tondeur F 1997 *Nucl. Phys.* A **615** 135
[32] Hamamoto I, Sagawa H and Zhang X Z 1997 *Phys. Rev.* C **56** 3121
[33] Colò G, Van Giai N, Meyer J, Bennaceur K and Bonche P 2004 *Phys. Rev.* C **70** 024307 (arXiv:nucl-th/0403086)
[34] Ma Z-Y, Van Giai N, Wandelt A, Vretenar D and Ring P 2001 *Nucl. Phys.* A **686** 173
[35] Todd-Rutel B G and Piekarewicz J 2005 *Phys. Rev. Lett.* **95** 122501 (arXiv:nucl-th/0504034)
[36] Hamamoto I, Sagawa H and Zhang X Z 1998 *J. Phys. G: Nucl. Part. Phys.* **24** 1445
[37] Capelli L, Colò G and Li J 2009 *Phys. Rev.* C **79** 054329
[38] Piekarewicz J 2002 *Phys. Rev.* C **66** 034305
[39] Vretenar D, Nikšić T and Ring P 2003 *Phys. Rev.* C **68** 024310
[40] Agrawal B K, Shlomo S and Au V K 2003 *Phys. Rev.* C **68** 031304
[41] Piekarewicz J 2004 *Phys. Rev.* C **69** 041301 (arXiv:nucl-th/0312020)
[42] Piekarewicz J 2007 *Phys. Rev.* C **76** 031301 (arXiv:0705.1491)
[43] Sil T, Centelles M, Viñas M and Piekarewicz J 2005 *Phys. Rev.* C **71** 045502 (arXiv:nucl-th/0501014)
[44] Bohigas O, Lane A and Martorell J 1979 *Phys. Rep.* **51** 267
[45] Lipparini E and Stringari S 1989 *Phys. Rep.* **175** 103
[46] Gleissl P, Brack M, Meyer J and Quentin P 1990 *Ann. Phys., NY* **197** 205
[47] Centelles M, Viñas X, Patra S K, De J N and Sil T 2005 *Phys. Rev.* C **72** 014304 (arXiv:nucl-th/0502055)
[48] Sil T, Shlomo S, Agrawal B K and Reinhard P-G 2006 *Phys. Rev.* C **73** 034316 (arXiv:nucl-th/0601091)
[49] Khan E, Sandulescu N, Grasso M and Giai N V 2002 *Phys. Rev.* C **66** 024309
[50] Sil T *et al* 2002 *Phys. Rev.* C **66** 045803
[51] Khan E 2009 *Phys. Rev.* C **80** 057302 (arXiv:0907.3423)
[52] Khan E 2009 *Phys. Rev.* C **80** 011307 (arXiv:0905.3335)
[53] Centelles M, Pi M, Viñas X, Garcias F and Barranco M 1990 *Nucl. Phys.* A **510** 397
[54] Li G-Q and Xu G-O 1990 *Phys. Rev.* C **42** 290
[55] Li G-Q 1991 *J. Phys. G: Nucl. Part. Phys.* **17** 1
[56] Centelles M, Viñas X, Barranco M and Schuck P 1993 *Ann. Phys., NY* **221** 165
[57] Centelles M, Viñas X, Barranco M, Marcos S and Lombard R J 1992 *Nucl. Phys.* A **537** 486
[58] Speicher C, Engel E and Dreizler R M 1993 *Nucl. Phys.* A **562** 569
[59] Centelles M, Del Estal M and Viñas X 1998 *Nucl. Phys.* A **635** 193
[60] Centelles M *et al* 1993 *Phys. Rev.* C **47** 1091
[61] Patra S K, Viñas X, Centelles M and Del Estal M 2001 *Phys. Lett.* B **523** 67
[62] Patra S K, Viñas X, Centelles M and Del Estal M 2002 *Nucl. Phys.* A **703** 240
[63] Patra S K, Centelles M, Viñas X and Del Estal M 2002 *Phys. Rev.* C **65** 044304
[64] Nishizaki S, Kurasawa H and Suzuki T 1987 *Nucl. Phys.* A **462** 687
[65] Zhu C and Qiu X-J 1991 *J. Phys. G: Nucl. Part. Phys.* **17** L11
[66] Maruyama T and Suzuki T 1989 *Phys. Lett.* B **219** 43
[67] Boersma H F, Malfliet R and Scholten O 1991 *Phys. Lett.* B **269** 1
[68] Stoitsov M V, Ring P and Sharma M M 1994 *Phys. Rev.* C **50** 1445
[69] Stoitsov M V, Cescato M L, Ring P and Sharma M M 1994 *J. Phys. G: Nucl. Part. Phys.* **20** L149
[70] Typel S and Brown B A 2001 *Phys. Rev.* C **64** 027302
[71] Baldo M, Maieron C, Schuck P and Viñas X 2004 *Nucl. Phys.* A **736** 241
[72] Lalazissis G A, König J and Ring P 1997 *Phys. Rev.* C **55** 540
[73] Ring P and Schuck P 1980 *The Nuclear Many Body Problem* (Berlin: Springer)
[74] Brack M, Guet C and Håkansson H-B 1985 *Phys. Rep.* **123** 275
[75] Brack M and Bhaduri R K 1997 *Semiclassical Physics* (Reading, MA: Addison Wesley)
[76] Kumar K, Souder P A, Michaels R and Urciuoli G M 2003 http://hallaweb.jlab.org/parity/prex
[77] Blaizot J P 1980 *Phys. Rep.* **64** 171
[78] Chossy T and Stocker W 1997 *Phys. Rev.* C **56** 2518
[79] Sagawa H, Yoshida S, Zeng G M, Gu J Z and Zhang X Z 2007 *Phys. Rev.* C **76** 034327 (arXiv:0706.0966)
[80] Piekarewicz J and Centelles M 2009 *Phys. Rev.* C **79** 054311 (arXiv:0812.4499)
[81] Bombaci I and Lombardo U 1991 *Phys. Rev.* C **44** 1892
[82] Paar N, Vretenar D, Khan E and Colò G 2007 *Rep. Prog. Phys.* **70** 691 (arXiv:nucl-th/0701081)

# 4 Elastic electron scattering by nuclei

## 4.1 Introduction

Elastic electron scattering by nuclei has been for many years a very useful tool for experimental studies on the charge distribution in stable nuclei. The exquisite accuracy achieved by these experiments and the systematic measurements performed in the past [Ho56] have allowed to improve substantially our conception of the nucleus. Electrons interact basically through the electromagnetic interaction. Hence, they constitute a "clean" probe for the determination of the nuclear charge distribution in elastic scattering experiments using a nucleus as a target. Protons and neutrons, the nuclear constituents, have totally opposite electric properties. While the former have net electric charge $e$, the latter have net electric charge zero. Therefore, the protons essentially characterize the electromagnetic properties of nuclei and the proton distribution have been frequently considered as equal to the nuclear charge distribution. This approximation is quite accurate depending on the properties of the charge distribution in which one is interested in. On the other side, the isospin asymmetric effects on this scattering measurements are relevant since neutrons affect the proton distribution via the strong interaction. Such effects can be shown, *e.g.*, by the fact that the second moment of the nuclear charge distribution scale in average with $A^{2/3}$ —where $A$ is the mass number. The reason is that the proton distribution depends on the nuclear dynamics governed by the strong interaction and, therefore, the neutron-richness present on the nuclear medium has relevant effects on the charge distribution in nuclei.

Recently, new techniques have been developed to synthesize and perform measurements of nuclear properties on radioactive nuclei. This fact have motivated new projects on elastic electron scattering by exotic nuclei —usually short-lived— envisaged for the next years in Radioactive Ion Beam (RIB) facilities [Ta95, Ge95, Mu01], such as the ELISe experiment at GSI (Germany) [Si07] and the SCRIT project at RIKEN (Japan) [Su05, Wa08]. Therefore, the theoretical investigation of exotic nuclei with models of purported reliability in stable isotopes is a timely and challenging problem. Such effort will test the ability of the established nuclear theory in the domain of exotic nuclei and may provide as well valuable references for future experiments.

In the publication of the theoretical study of elastic electron scattering off stable and exotic nuclei presented in the following section, we have used a set of representative relativistic and non-relativistic mean field nuclear models. All of them have been fitted to accurately describe the ground state properties of stable nuclei. In particular, binding energies and charge radii. The measured quantity in such experiments are the electromagnetic Differential Cross Section (DCS) and the Total Cross Section ($\sigma$). The DCS is an observable that measures the probability distribution as a function of the angle of the outcoming electron once it has been scattered by the target nucleus. Theoretically, we compute the DCS performing the exact phase shift analysis of the Coulomb distortions felt by the electron after the electromagnetic interaction with the nucleus [Sa05]. The accurate phase shift analysis is mandatory to properly deal with the Dirac equation for an incident electron with a given initial energy (beam) under the influence of an electromagnetic potential created by the nucleus (target). The electromagnetic potential is calculated through the self-consistent mean field charge distributions of the nucleus under investigation. First of all, we compare the DCSs as predicted by mean field models against some of measured stable nuclei. In this way we test these models and our methodology in the calculations. Then, we investigate how the DCS evolves along the Sn and Ca isotopic chains, from the proton to the neutron drip lines. Actually, in this case we analyze the theoretical results paralleling in a sense the experimental analysis of scattering data, *i.e.* we parameterize the self-consistent densities using a simple ansatz for them. The advantage of this procedure relies on the simple mathematical expressions one has for the parametrized densities allowing, in principle, a simpler connection with the DCS than using directly the mean-field ones. Specifically, we choose the Helm model [He56] which have only two parameters, one is directly related with the bulk part of the density distribution and the other with the surface. In this sense, we took the mean field predictions as our benchmark for the study of the two isotopic chains allowing us to identify correlations of potential interest between the Helm model parameters and the calculated finite size effects of the nucleus in the DCS, namely the form factor.

# 4.2 Theoretical study of elastic electron scattering off stable and exotic nuclei

PHYSICAL REVIEW C **78**, 044332 (2008)

## Theoretical study of elastic electron scattering off stable and exotic nuclei

X. Roca-Maza,* M. Centelles, F. Salvat, and X. Viñas
*Departament d'Estructura i Constituents de la Matèria and Institut de Ciències del Cosmos, Facultat de Física, Universitat de Barcelona, Diagonal 647, 08028 Barcelona, Spain*
(Received 8 August 2008; published 31 October 2008)

Results for elastic electron scattering by nuclei, calculated with charge densities of Skyrme forces and covariant effective Lagrangians that accurately describe nuclear ground states, are compared against experiment in stable isotopes. Dirac partial-wave calculations are performed with an adapted version of the ELSEPA package. Motivated by the fact that studies of electron scattering off exotic nuclei are intended in future facilities in the commissioned GSI and RIKEN upgrades, we survey the theoretical predictions from neutron-deficient to neutron-rich isotopes in the tin and calcium isotopic chains. The charge densities of a covariant interaction that describes the low-energy electromagnetic structure of the nucleon within the Lagrangian of the theory are used to this end. The study is restricted to medium- and heavy-mass nuclei because the charge densities are computed in mean-field approach. Because the experimental analysis of scattering data commonly involves parameterized charge densities, as a surrogate exercise for the yet unexplored exotic nuclei, we fit our calculated mean-field densities with Helm model distributions. This procedure turns out to be helpful to study the neutron-number variation of the scattering observables and allows us to identify correlations of potential interest among some of these observables within the isotopic chains.

DOI: 10.1103/PhysRevC.78.044332 PACS number(s): 21.10.Ft, 25.30.Bf, 13.40.Gp, 21.60.−n

### I. INTRODUCTION

Elastic electron-nucleus scattering has been for many years a very useful tool to investigate the size and shape of stable nuclei [1–5]. Electrons interact with nuclei basically through the electromagnetic force. If the energy of the electrons is high enough, they become a relatively clean probe to explore precisely the internal structure of nuclei, insensitive to strong interaction effects. In particular, the analysis of electron-scattering data provides most valuable information about the charge distribution in atomic nuclei [6–8].

Developments in accelerator technology and detection techniques nowadays allow experimentation with nuclei beyond the limits of $\beta$ stability. The number of nuclei whose masses have been measured keeps growing [9] and this tendency is expected to continue with the use of radioactive isotope beams (RIB) [10–12]. A new generation of electron-RIB colliders using storage rings is now under construction in RIKEN (Japan) [13,14] and GSI (Germany) [15,16]. These facilities will offer unprecedented opportunities to study the structure of exotic unstable nuclei through electron scattering in the ELISe experiment at the Facility for Antiproton and Ion Research in Germany [17] and the SCRIT project in Japan [18,19]. Therefore, the theoretical investigation of exotic nuclei with models of purported reliability in stable isotopes is a timely and challenging problem. Such effort will test the ability of the established nuclear theory in the domain of exotic nuclei and may as well provide valuable references for future experiments.

In recent literature, several theoretical studies of elastic electron-nucleus scattering in exotic nuclei have been reported [20–26]. Some of these works are concerned with analyzing electron scattering in light nuclei, where exciting exotic phenomena such as the appearence of halos may take place. That is the case of, e.g., $^{6,8}$He [20,22], $^{11}$Li [20,23], $^{8}$B [22,23], $^{12}$O, and $^{28}$S [24] nuclei, where possible effects on scattering from the occurrence of halos have been investigated. Light nuclei require a microscopic treatment of the scattering interaction to properly deal with the underlying shell-model structure [22]. Other works study the variation of the charge form factors along isotopic [20,21,25] and isotonic [26] chains of medium and heavy mass nuclei. It has been found that when the number of neutrons (protons) in these isotopic (isotonic) chains increases, the squared modulus of the charge form factor and the position of its minima show, respectively, an upward trend and a significant inward shifting in the momentum transfer. In addition to electron scattering, it is worth mentioning that proton scattering may be another valuable tool to investigate the changes in the charge density of the nucleus, especially at its interior, as one proceeds to the drip lines along isotopic chains [27].

To investigate the internal structure of nuclear charge densities, the de Broglie wavelength of the probe has to be of the order of 1 fm. This means that the energy of the electron beam has to be of the order of several hundred MeV. Therefore, for accurate theoretical calculations of differential cross sections (DCS) and electric charge form factors, one needs to solve the elastic scattering of Dirac particles in the scalar potential pertaining to the nuclear charge distribution. The simplest approach is the plane-wave Born approximation (PWBA), where one assumes that the initial and final states of the electron can be described by plane waves. Although the PWBA is able to account for important features of scattering, it is not enough accurate for quantitative calculations of the electric charge form factor. A more elaborate method is supplied by the Glauber theory using a relativistic eikonal approximation of the Dirac equation [28]. It has been successfully applied

*roca@ecm.ub.es

 

to a systematic study in elastic electron-nucleus scattering [24–26]. The most sophisticated calculations of electron-nucleus scattering employ the exact phase-shift analysis of the Dirac equation. This method corresponds to the so-called distorted wave Born approximation (DWBA) [29] and was employed, e.g., in Refs. [20,21]. In the present work we apply a modified version of the recently published code ELSEPA [30] to the elastic electron-nucleus scattering problem. This code was originally devised to perform accurate Dirac partial-wave calculations of elastic scattering of electrons and positrons by atoms, positive ions, and molecules in the low-energy domain.

The main input needed for solving the elastic electron-nucleus scattering problem is the charge density of the target nucleus. In the present article we use charge densities obtained with mean-field models for calculating electron scattering off medium- and heavy-mass nuclei. For this purpose, we employ effective nuclear interactions of current use in nuclear structure physics. It is known that the overall trends of the elastic electron-nucleus scattering in medium and heavy nuclei are, in general, reasonably reproduced by the theoretical charge densities obtained in the mean-field approximation. However, different effective interactions predict electric charge form factors and DCS that differ in fine details and describe with different quality the experimental data. In our study we consider the nonrelativistic Skyrme forces SkM* [31] and SLy4 [32] and the covariant models NL3 [33], FSUGold [34], $G2$ [35], and DD-ME2 [36]. They are representative examples of effective interactions that accurately describe the ground-state properties of finite nuclei and some of their collective excitations.

The parameters of the alluded microscopic interactions have been determined from careful calibration to observables such as binding energies, single-particle levels, and charge and diffraction radii of a variety of selected nuclei. The nucleon density distributions of the Skyrme Hartree-Fock and relativistic mean-field theories are obtained by numerical solution of the quantal mean-field variational equations. The effects of the neutrons on the proton density are taken into account, in a self-consistent manner, through the interaction terms of the effective force or Lagrangian. Therefore, no parametrized shapes of the density profiles are implemented. Nevertheless, most of the mean-field calculations of finite nuclei assume point-nucleon densities. The charge density is obtained from the proton pointlike distribution folded with the proton charge form factor [37]

$$\rho_p(r) = \frac{\alpha^3}{8\pi} e^{-\alpha r}. \tag{1}$$

A value $\alpha^2 = 18.29$ fm$^{-2}$ corresponds to a proton root-mean-square (rms) radius of 0.81 fm. This is the standard prescription in the fitting procedure of the parameters of most Skyrme forces and relativistic mean-field interactions to the experimental data of finite nuclei, including charge radii. The covariant models of Ref. [35] are an exception to this fact and, in particular, the interaction $G2$ [35,38] that we will employ in several of our calculations. The effective Lagrangian of $G2$ incorporates the low-energy electromagnetic structure of the nucleon within the theory [35,38]. It is to be emphasized that in $G2$ the charge density is obtained directly from the solution of the mean-field equations and that there is no folding to be performed with external single-nucleon form factors, hereby maximizing the predictive power. In the other mean-field forces considered in our work we will neglect the contribution of the neutron charge form factor [39] to the charge density. This is known to be a reasonable approximation up to moderate-momentum transfers [40], which is the region analyzed in the present study of scattering. Moreover, it ensures consistency with the method applied originally to fit the parameters of these interactions; additional modifications into the charge densities could spoil, e.g., their accurate predictions for charge radii.

It is to be mentioned that the mean-field treatment would reach its limits in the study of exotic light nuclei, where the shell-model structure and halos can become prevailing features [22]. Therefore we do not attempt to treat these light systems in the present work. The development of suitable tools and a unified framework to deal with charge densities and electron scattering in nuclei across the mass table remains an outstanding problem in the field, maybe appropriate for new initiatives like the UNEDF collaboration to build a universal nuclear energy density functional [41].

The present article is organized as follows. Section II is devoted to the theoretical formalism. The mean-field description of finite nuclei in the nonrelativistic and relativistic frames is briefly discussed. The Dirac partial-wave calculation of elastic scattering of electrons by nuclei implemented in the code ELSEPA is summarized. In Sec. III, the elastic electron scattering results obtained from the charge densities of the above-mentioned effective interactions are studied by comparing with available experimental data for several stable nuclei. In Sec. IV we investigate the theoretical predictions for elastic electron-nucleus scattering in the tin and calcium isotopic chains from the proton drip line to the neutron drip line. These calculations are performed with the relativistic mean-field interaction $G2$ [35]. Our conclusions are laid in the final section.

## II. THEORY

In the current section we review the basic features of the Skyrme and relativistic mean-field models that we will employ to compute the theoretical nuclear charge densities. We also summarize the calculation of Dirac distorted waves for elastic electron-nucleus scattering in the code ELSEPA. The reader conversant with effective nuclear mean-field models and with knowledge of the basics of Dirac partial-wave calculations may prefer to proceed directly to the discussion of results that starts in Sec. III.

### A. Mean-field description of nuclei

The mean-field approach assumes that nucleons move independently in a mean-field generated by the other nucleons of the atomic nucleus. Useful tools for mean-field calculations of nuclei are the nonrelativistic Hartree-Fock method with phenomenological interactions and the relativistic mean-field (RMF) Hartree model with effective Lagrangians [42]. These

phenomenological forces and effective Lagrangians usually depend on about 10 adjustable parameters that are fitted to reproduce relevant ground-state properties, such as binding energies and charge radii of a few nuclei.

A common trend of phenomenological interactions used in the mean-field approach is their simple mathematical structure. In the nonrelativistic mean-field models, the Skyrme interactions [43,44] are among those most widely used. Skyrme forces are zero-range interactions that do not require calculations of exchange contributions. These forces have been employed for describing ground-state properties of the atomic nucleus, low-energy excited states, fission and fusion barriers, nucleon-nucleus and heavy-ion potentials, etc. (see, e.g., Ref. [44]). The parameter set SkM* [31] is the classical paradigm of such a model. It is known to yield charge densities in overall agreement with densities inferred from experiment [45]. SLy4 [32] is a more modern version of the Skyrme force that was calibrated with special care for the isospin sector and for predictions of neutron-rich matter that occurs, e.g., in neutron stars.

The RMF theory of hadrons has become another useful tool for the study of bulk and single-particle properties of nuclear matter and finite nuclei [38,46–48]. In the relativistic model, nucleons are treated as Dirac particles that interact by exchanging virtual mesons. The covariant theory automatically takes into account the spin-orbit force, the finite range, and the density dependence of the nuclear interaction. The no-sea approximation, which disregards effects from the Dirac sea of negative energy states, is adopted. The open parameters of the model are the meson coupling constants and some of the meson masses. After fitting them to binding energies, charge radii, and other well-known empirical data of a few selected nuclei, the covariant theory predicts average properties of spherical and deformed nuclei over the whole periodic table in very good agreement with experiment [35,49,50].

The original Walecka Lagrangian [46] contained $\sigma$, $\omega$, and $\rho$ mesons without any meson self-interactions. It was able to predict the correct saturation point of nuclear matter, albeit with a very large incompressibility modulus. The model was refined with the introduction of $\sigma$-meson self-interactions [51]. A parametrization of this type is, e.g., the celebrated NL3 model [33]. These parameter sets properly describe the data about finite nuclei, but often display differences, at densities above the saturation point, with microscopic Dirac-Brueckner-Hartree-Fock calculations of the nuclear matter equation of state [52,53]. A better agreement with the latter calculations at densities up to two to three times the saturation density is achieved by incorporating a quartic vector meson self-interaction in the effective Lagrangian. Another interesting addition is a mixed isoscalar-isovector coupling [54], which allows one to modulate the density dependence of the nuclear symmetry energy. The variation of this coupling leaves the binding energy and proton rms of a finite nucleus almost unaltered, but it considerably modifies the rms radius of the neutron distribution. A representative instance of this type of model is the FSUGold parameter set [34]. This set yields an equation of state that is considerably softer than in NL3 for both symmetric matter and neutron matter. Apart from the binding energies and charge radii of nuclei, FSUGold delivers a satisfactory description of several modes of collective excitations having different neutron-to-proton ratios.

The Lagrangian density associated with the $G2$ parameter set is inspired by effective field theory methods. It contains all couplings consistent with the underlying QCD symmetries up to the order considered in the expansion scheme [35,38]. In contrast to the majority of mean-field models, $G2$ describes the low-energy electromagnetic structure of the nucleon within the theory by means of vector-meson dominance and derivative couplings to the photon, cf. Ref. [35] for details. As indicated above, this means that no additional calculations with external nucleon form factors are needed to obtain the charge density and that the electromagnetic effects of the protons and neutrons are included within the low-energy regime in a unified framework [35]. The $G2$ set explains finite nuclei and nuclear matter with a commendable level of accuracy. It predicts a soft equation of state both around saturation and at high densities that is consistent with recent measurements of kaon production and flow of matter in energetic heavy-ion collisions as well as with observations of masses and radii of neutron stars [55].

Recent formulations of the RMF theory do not introduce mesonic self-interactions but make the coupling constants of the mesons density dependent, like in the DD-ME2 parameter set [36]. These models accurately describe the properties of finite nuclei and, in addition, the associated equation of state of nuclear and neutron matter at suprasaturation agrees with the trends of microscopic Dirac-Brueckner-Hartree-Fock calculations that start from the bare nucleon-nucleon interaction.

Pairing correlations need to be taken into account for the calculation of open-shell nuclei. We will describe them in both nonrelativistic and relativistic frames, through a modified BCS approach that takes into account the continuum by means of quasibound levels due to their centrifugal (neutrons) or centrifugal-plus-Coulomb barriers (protons) [56]. For the Skyrme models used in this work, the pairing correlations are introduced by using a zero-range density-dependent force whose parameters can be found in Ref. [32]. In the case of the covariant NL3, $G2$, and FSUGold models, we describe the pairing correlations by means of a constant matrix element fitted to reproduce the experimental binding energies of some selected isotopic and isotonic chains [56]. In the DD-ME2 parameter set a fixed gap is considered, determined from experimental odd-even mass differences [36].

### B. Description of electron scattering

The ELSEPA code [30] was originally designed for the calculation of elastic scattering of electrons and positrons by atoms, positive ions, and molecules. We have adapted it to handle high-energy electron scattering by nuclei. ELSEPA computes the DCS using the conventional relativistic partial-wave method, which was first formulated by Yennie *et al*. [29]. The projectile electron is assumed to feel the electrostatic field of the nuclear charge distribution. The potential energy of an electron at a distance $r$ from the center of the nucleus is given

by

$$V(r) = -4\pi e \left[ \frac{1}{r} \int_0^r \rho_{\rm ch}(r') r'^2 dr' + \int_r^\infty \rho_{\rm ch}(r') r' dr' \right], \tag{2}$$

where $\rho_{\rm ch}(r)$ denotes the charge density of the nucleus, considered to be spherically symmetrical. At the energies of interest for the electron-nucleus problem, the effect of screening by the orbiting atomic electrons is limited to scattering angles smaller than $1^\circ$ (see, e.g. Ref. [30]), which are well below the angular range covered by the electron-nucleus scattering measurements. Consequently, electron screening is ignored in the present calculation. Because the nuclear charge density is assumed to vanish beyond a certain radius $r_B$ (i.e., the radius of the box where the nuclear charge distribution is calculated), the potential (2) is purely Coulombian, $V(r) = -Ze^2/r$, beyond that radius. Globally it can be regarded as a Coulomb potential with the short-range distortion arising from the finite size of the nucleus, i.e., as a modified Coulomb potential.

The DCS for elastic scattering of spin unpolarized electrons is given by

$$\frac{d\sigma}{d\Omega} = |f(\theta)|^2 + |g(\theta)|^2, \tag{3}$$

where

$$f(\theta) = \frac{1}{2ik} \sum_{\ell=0}^{\infty} \{(\ell+1)[\exp(2i\delta_{\kappa=-\ell-1}) - 1] + \ell[\exp(2i\delta_{\kappa=\ell}) - 1]\} P_\ell(\cos\theta) \tag{4}$$

and

$$g(\theta) = \frac{1}{2ik} \sum_{\ell=0}^{\infty} [\exp(2i\delta_{\kappa=\ell}) - \exp(2i\delta_{\kappa=-\ell-1})] P_\ell^1(\cos\theta) \tag{5}$$

are the direct and spin-flip scattering amplitudes, respectively. Here $k$ denotes the wave number of the projectile electron,

$$c\hbar k = \sqrt{E(E + 2m_e c^2)}, \tag{6}$$

and the functions $P_\ell(\cos\theta)$ and $P_\ell^1(\cos\theta)$ are Legendre polynomials and associated Legendre functions, respectively. The phase shifts $\delta_\kappa$ represent the behavior of the Dirac spherical waves at large $r$ distances (see, e.g., Ref. [57]).

For modified Coulomb potentials, the spherical solutions of the Dirac equation are suitably expressed in the form

$$\psi_{E\kappa m}(\mathbf{r}) = \frac{1}{r} \begin{bmatrix} P_{E\kappa}(r)\Omega_{\kappa,m}(\hat{\mathbf{r}}) \\ i\,Q_{E\kappa}(r)\Omega_{-\kappa,m}(\hat{\mathbf{r}}) \end{bmatrix}. \tag{7}$$

The functions $\Omega_{\kappa,m}(\hat{\mathbf{r}})$ are the spherical spinors, and the radial functions $P_{E\kappa}(r)$ and $Q_{E\kappa}(r)$ satisfy the following system of coupled differential equations [57]:

$$\begin{aligned} \frac{dP_{E\kappa}}{dr} &= -\frac{\kappa}{r} P_{E\kappa} + \frac{E - V + 2m_e c^2}{c\hbar} Q_{E\kappa}, \\ \frac{dQ_{E\kappa}}{dr} &= -\frac{E - V}{c\hbar} P_{E\kappa} + \frac{\kappa}{r} Q_{E\kappa}. \end{aligned} \tag{8}$$

The relativistic quantum number $\kappa$ is defined as $\kappa = (\ell - j)(2j + 1)$, where $j$ and $\ell$ are the total and orbital angular momentum quantum numbers. Note that $j$ and $\ell$ are both determined by the value of $\kappa$; $j = |\kappa| - 1/2$, $\ell = j + \kappa/(2|\kappa|)$. In the numerical calculations, the spherical waves are normalized so that the upper-component radial function $P_{E\kappa}(r)$ oscillates asymptotically with unit amplitude.

For modified Coulomb potentials and $r \to \infty$, we have (see, e.g., Ref. [58])

$$P_{E\kappa}(r) \simeq \sin\left(kr - \ell\frac{\pi}{2} - \eta \ln 2kr + \delta_\kappa\right), \tag{9}$$

where

$$\eta = Ze^2 m_e/(\hbar^2 k) \tag{10}$$

is the Sommerfeld parameter. It is convenient to express the phase shifts $\delta_\kappa$ as $\Delta_\kappa + \hat{\delta}_\kappa$, where $\Delta_\kappa$ is the phase shift of the point-nucleus Coulomb potential and $\hat{\delta}_\kappa$ is the "inner" phase shift of the short-range potential induced by the nuclear charge distribution.

As indicated above, the calculations reported here have been performed using the computer code ELSEPA [30]. It solves the radial Dirac equations using a robust integration algorithm, described in Refs. [58,59], which effectively minimizes the effect of truncation errors. The algorithm starts from a table of values of the function $rV(r)$ at the points $r_i$ of a radial grid, which is provided by the user. This function is replaced by the natural cubic spline that interpolates the tabulated values; thus, in the interval between consecutive grid points, the potential function $rV(r)$ is represented as a cubic polynomial. The radial wave equations (8) are then solved by using the exact power-series expansions of the radial functions [59]. The integration is started at $r = 0$ and extended outwards up to a point $r_m$ that is beyond the starting radius $r_B$ of the Coulomb tail. For $r > r_m$, the field is purely Coulombian, and the normalized upper-component radial Dirac function can be expressed as

$$P_{E\kappa}(r) = \cos\hat{\delta}_\kappa f_{E\kappa}^{(\rm u)}(r) + \sin\hat{\delta}_\kappa g_{E\kappa}^{(\rm u)}(r), \tag{11}$$

where $f_{E\kappa}^{(\rm u)}(r)$ and $g_{E\kappa}^{(\rm u)}(r)$ are the upper components of the regular and irregular Dirac-Coulomb radial functions [58], respectively. As usual, the phase shift $\hat{\delta}_\kappa$ is determined by matching this outer analytical form to the inner numerical solution at $r_m$, requiring continuity of the radial function $P_{E\kappa}(r)$ and its derivative. The Dirac-Coulomb functions are calculated by using the Fortran subroutine described in Ref. [58], which delivers values of the regular and irregular Dirac-Coulomb functions and their derivatives that are accurate to more than 10 decimal figures.

The convergence rate of the series (4) and (5) for the calculation of $d\sigma/d\Omega$ is known to be slow. The summations are optimized by performing them in two steps [30]. First, they are evaluated for the pure Coulomb field, for which the phase shifts $\Delta_\kappa$ are known analytically and the calculation is fast. Second, the point-nucleus results are subtracted from the expansions (4) and (5); the remaining series represent the effect of only the short-range component of the potential and converge more rapidly than the original series. As a consequence, the number of inner phase shifts $\hat{\delta}_\kappa$ one needs to compute is normally much smaller than the number of required Coulomb phase shifts.

In general, ELSEPA gives reliable results for electron energies up to 1 GeV but numerical difficulties can appear at very small scattering angles because the DCS for the bare nucleus is very close to the point nucleus DCS (which is known as the Mott DCS) and consequently diverges. The code evaluates the finite-nucleus DCS only for scattering angles larger than 10 degrees, which is a lower bound of the usually measured electron-nucleus DCS. Depending on the particulars of each calculation, difficulties can also be found in the high-energy regime and for large scattering angles where the DCS takes much smaller values than the Mott DCS. In this case, the nuclear amplitudes almost cancel the Coulomb scattering amplitudes, thus magnifying the numerical errors. In practice, round-off errors become apparent when the nuclear scattering amplitudes are less then $10^{-5}$ times the Coulomb amplitudes (which are themselves small). When there are indications that these errors could be important, ELSEPA discontinues the calculation and the DCS is set to zero.

## III. ELASTIC ELECTRON-NUCLEUS SCATTERING IN STABLE NUCLEI

As stated in the Introduction, we compute the charge-density distributions with selected effective nuclear interactions, namely the Skyrme forces SkM* [31] and SLy4 [32] and the covariant parametrizations NL3 [33], FSUGold [34], *G*2 [35], and DD-ME2 [36]. We obtain the DCS from these mean-field charge densities using the ELSEPA code. Specifically, in the present section we compare the theoretical DCS derived from the mean-field models with available experimental data for elastic electron scattering in $^{16}$O at 374.5 MeV [60], $^{40,42,44,48}$Ca and $^{48}$Ti at 250 MeV, $^{40,48}$Ca at 500 MeV [61], $^{90}$Zr at 209.6 and 302 MeV [62], $^{116,118,124}$Sn at 225 MeV [63], and $^{208}$Pb at 248.2 and 502 MeV [64].

In the conventional analyses of the scattering data measured in experiment, the charge density is usually modeled by means of an analytical function. For instance, two- or three-parameter Fermi distributions are used to this end. The charge density may also be constructed from the eigenfunctions of an adjustable single-particle potential of Woods-Saxon or harmonic oscillator type. Also, nearly model-independent charge densities are obtained from a Fourier-Bessel expansion [65] with unknown coefficients. In all these cases the free parameters in the charge distributions are determined from the measured electron scattering data through a least-squares minimization procedure. In some comparisons with our theoretical predictions we will employ experimental charge densities borrowed from the literature. These densities have been extracted from fits with Fourier-Bessel expansions [6,7]. In the case of the nucleus $^{118}$Sn, for which this type of density is not available, we employ the two-parameter Fermi distribution given in Ref. [63]. The results computed with these "experimental" (fitted) charge densities will be referred to as Exp(fit) in the tables and figures henceforth.

First, we report in Table I the rms radii of the theoretical charge distributions of the nuclei $^{16}$O, $^{40}$Ca, $^{48}$Ca, $^{90}$Zr, $^{118}$Sn, and $^{208}$Pb predicted by the Skyrme and RMF forces used in this work. They are compared with the rms radii of the experimental charge distributions extracted from the analysis of the electron scattering data [6,7,63]. The agreement is seen to be very good. This fact is not surprising because some of the experimental values of the charge radius have been used in the fit of the free parameters of the Skyrme forces and RMF models considered.

TABLE I. Root-mean-square radii (in fm) for the studied charge distributions. Exp(fit) values are calculated from the experimental Fourier-Bessel charge densities [6,7], except for the case of $^{118}$Sn where a Fermi density is used [63].

| Nucleus | Exp(fit) | DD-ME2 | *G*2 | NL3 | FSUGold | SLy4 | SkM* |
|---|---|---|---|---|---|---|---|
| $^{16}$O | 2.74 | 2.73 | 2.73 | 2.73 | 2.69 | 2.80 | 2.81 |
| $^{40}$Ca | 3.45 | 3.46 | 3.46 | 3.47 | 3.44 | 3.51 | 3.52 |
| $^{48}$Ca | 3.45 | 3.48 | 3.45 | 3.47 | 3.47 | 3.54 | 3.54 |
| $^{90}$Zr | 4.26 | 4.28 | 4.25 | 4.28 | 4.26 | 4.30 | 4.29 |
| $^{118}$Sn | 4.67 | 4.63 | 4.62 | 4.63 | 4.63 | 4.65 | 4.63 |
| $^{208}$Pb | 5.50 | 5.52 | 5.50 | 5.52 | 5.52 | 5.52 | 5.51 |

Figure 1 displays the theoretical charge density profiles obtained with the investigated mean-field models as well as the experimental charge distributions for $^{16}$O, $^{90}$Zr, and $^{208}$Pb [6,7]. In general, theoretical and experimental charge densities agree nicely in the fall-off region and differ more in the nuclear interior as a consequence of the shell oscillations of the mean-field densities. Differences in the inner region are more marked in light nuclei where a mean-field approximation

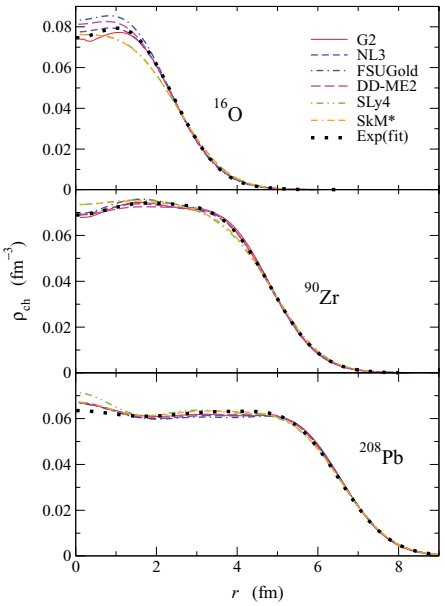


FIG. 1. (Color online) Radial dependence of the charge densities of the stable nuclei $^{16}$O, $^{90}$Zr, and $^{208}$Pb. The predictions of the different mean-field models indicated in the legend are compared with the charge densities fitted experimentally by the Fourier-Bessel analysis [6,7].

may be less justified. In the present case, if we analyze the region of the experimental density of $^{16}$O between the center and about 2 fm, we see that the covariant sets $G2$ and NL3 give a better description, whereas the SkM* and SLy4 forces tend to underestimate it and the DD-ME2 and FSUGold sets tend to overestimate it. A detailed inspection of the mean-field charge densities shows that they differ not only among themselves in the nuclear interior but also in the surface region. As discussed in Ref. [45], the inner density is normally larger for nuclei with larger surface diffuseness. From Fig. 1 we see that for medium and heavy nuclei the Skyrme charge density, in particular the one predicted by SLy4, is larger in the interior and consequently more diffuse at the surface than the RMF distributions. Differences regarding the surface diffuseness between non-relativistic and relativistic charge densities are related to the different density dependence of the effective interactions [45].

The comparison between theoretical and experimental charge densities shall be connected with the discussion of the DCS and the electric charge form factors, which are the quantities measured in real experiments. Figure 2 shows the DCS for elastic electron scattering in $^{16}$O at 374.5 MeV, $^{90}$Zr at 302 MeV, and $^{208}$Pb at 502 MeV, which we choose as representative examples to illustrate the predictions of the different mean-field models. To improve readability, the curves calculated with NL3 and SkM* are not displayed in the figure. In the three scattering processes, one observes that the experimental data are similarly reproduced by all of the considered mean-field charge densities at small scattering angles, up to the first diffraction minimum. The statement is more valid for lead, where models and data keep close up to the second, or even third, diffraction minimum. The case which is seen to pose more difficulties to the mean-field models at all scattering angles is, not surprisingly, the lightest investigated nucleus, $^{16}$O. From the considered interactions, only the parameter set $G2$ is able to reproduce the experimental data of $^{16}$O at 374.5 MeV closely at all scattering angles. As one might expect from the discussion of Fig. 1, the deviations among the DCS predicted by the various mean-field models, and the discrepancies with respect to experiment, become more prominent at the largest scattering angles in the three processes studied in Fig. 2. One detects a significant difference between the nonrelativistic Skyrme interactions and the RMF models used here. It is seen that the SLy4 interaction yields DCS values that, in general, are smaller than those calculated using the charge densities of the covariant sets (the same happens with the Skyrme force SkM*). This trend is especially clear in $^{16}$O and $^{90}$Zr, if one just excludes the region immediately after the first diffraction minimum where a crossing of the DCS values predicted by some of the models takes place.

One of the most effective quantities to characterize elastic electron-nucleus scattering is the electric charge form factor $F(q)$. The momentum transfer $q$ is related to the scattering angle $\theta$ in the laboratory frame by

$$c\hbar q = 2E \sin(\theta/2). \tag{12}$$

In PWBA the electric-charge form factor is computed as the Fourier transform of the charge density. In the present work

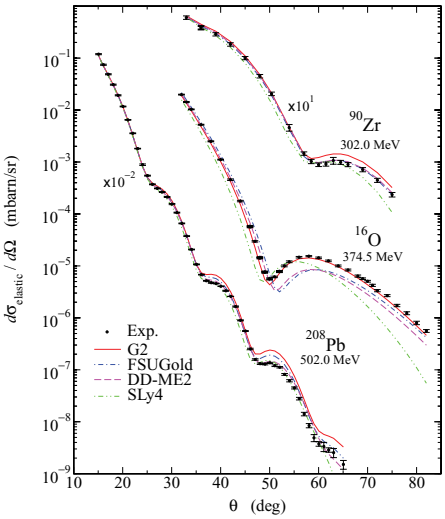


FIG. 2. (Color online) Elastic DCS for electron-nucleus scattering in $^{16}$O, $^{90}$Zr, and $^{208}$Pb as a function of the scattering angle $\theta$, at the energies shown. The results from the mean-field models indicated in the legend are compared with the measured DCS (Exp) [60–62] and with the DCS calculated in the ELSEPA code from the charge densities fitted experimentally by the Fourier-Bessel analysis [Exp(fit)] [6,7].

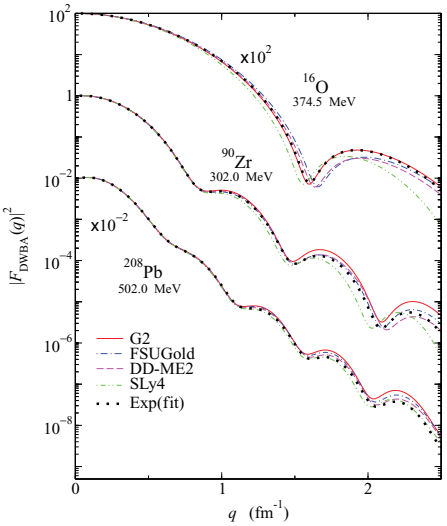


FIG. 3. (Color online) Squared charge form factor for $^{16}$O, $^{90}$Zr, and $^{208}$Pb as a function of the momentum transfer $q$ at the electron beam energies shown. It has been obtained by applying Eq. (13) as described in the text, both for the mean-field models indicated in the legend and for the experimentally fitted charge densities [Exp(fit)] [6,7].

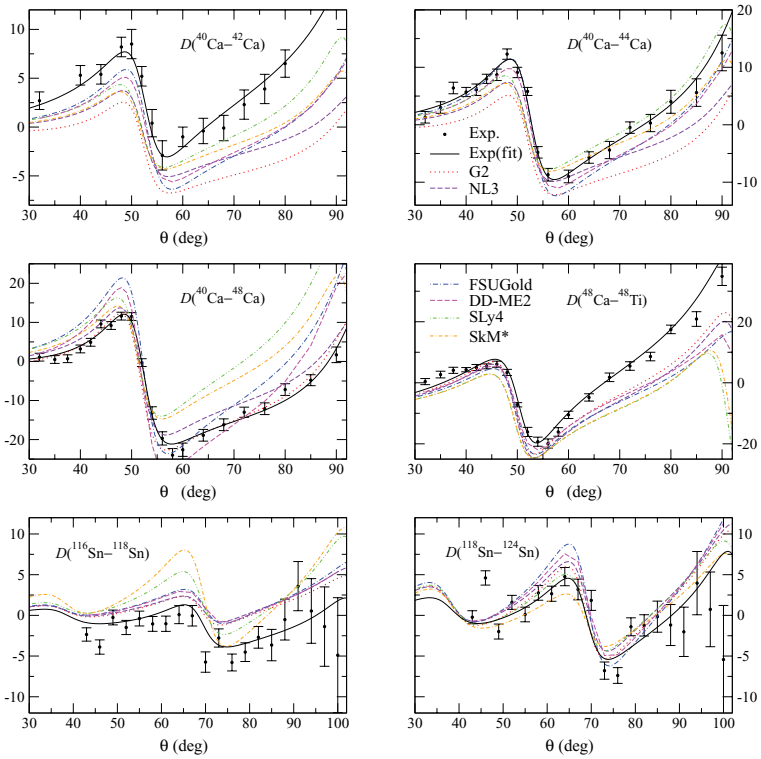


FIG. 4. (Color online) Relative differences of DCS in pairs of neighbor nuclei at 250 MeV for Ca and Ti and at 225 MeV for Sn. The results from mean-field models are compared with the measured RDDCS (Exp) and with the RDDCS calculated in the ELSEPA code from the charge densities fitted experimentally [Exp(fit)] in Refs. [61,63]. Note that in the present figure the vertical scales are linear and that all of them have been magnified by a factor 100.

we obtain $|F(q)|^2$ at a given beam energy as

$$|F(q)|^2 = \left(\frac{d\sigma}{d\Omega}\right)\left(\frac{d\sigma_M}{d\Omega}\right)^{-1}, \tag{13}$$

where $d\sigma/d\Omega$ is the DCS calculated from the DWBA analysis and $d\sigma_M/d\Omega$ is the Mott DCS. Equation (13) goes beyond the first Born approximation to the charge form factor because, instead of the PWBA for the DCS of the point nucleus, the exact Mott DCS is used. It will be referred to as $F_{\mathrm{DWBA}}(q)$ in what follows. We will extract the squared charge form factor from experiment using the same expression (13), by inserting the DCS obtained from the experimentally fitted charge densities on its right-hand side.

Figure 3 displays the $q$ dependence of $|F_{\mathrm{DWBA}}(q)|^2$ for the nuclei $^{16}$O, $^{90}$Zr, and $^{208}$Pb at the electron beam energies 374.5, 302, and 502 MeV, respectively. Results are calculated from the considered mean-field models and from the experimental charge density (as in Fig. 2, the curves obtained with NL3 and SkM* are not shown). As it may be expected from our previous analysis of the DCS, the experimental values of $|F(q)|^2$ are well reproduced in the low-momentum transfer region by all of the discussed mean fields. However, some discrepancies appear between the theoretical predictions and the experimental data at large-momentum transfers (or, equivalently, at large scattering angles). They are an indication that the theoretical mean-field models describe differently the central region of the experimental charge density [60], which we have addressed in the discussions of Fig. 1.

A more exigent test of the mean-field charge densities than the DCS themselves is provided by the analysis of the relative differences of DCS values between pairs of neighbor nuclei (RDDCS). The RDDCS are defined as

$$D(A-B) = \frac{(d\sigma/d\Omega)_A - (d\sigma/d\Omega)_B}{(d\sigma/d\Omega)_A + (d\sigma/d\Omega)_B}. \tag{14}$$

We explore the following cases where experimental values are available: $^{40}$Ca-$^{42}$Ca, $^{40}$Ca-$^{44}$Ca, $^{40}$Ca-$^{48}$Ca, and $^{48}$Ca-$^{48}$Ti [61], as well as $^{116}$Sn-$^{118}$Sn and $^{118}$Sn-$^{124}$Sn [63]. The theoretical predictions for the RDDCS (14) from the mean-field charge densities are displayed against experiment in Fig. 4, where a factor of 100 has been introduced for the sake of clarity. Notice that the vertical scale of this figure is

TABLE II. Normalized square weighted difference ($d_w^2$) between the calculated and measured DCS values. Exp(fit) values are calculated from the experimental Fourier-Bessel charge densities [6,7], except for the case of $^{118}$Sn where a Fermi density is used [63]. The energy $E$ of the incident electrons is in MeV.

| Nucleus | $E$ | Exp(fit) | DD-ME2 | $G2$ | NL3 | FSUGold | SLy4 | SkM* |
|---|---|---|---|---|---|---|---|---|
| $^{16}$O | 374.5 | 11.1 | 88.7 | 13.1 | 38.6 | 206 | 191 | 194 |
| $^{40}$Ca | 250 | 7.18 | 3.15 | 16.2 | 13.9 | 0.84 | 24.4 | 24.3 |
| | 500 | 3.48 | 1.49 | 42.9 | 19.7 | 5.79 | 40 | 39 |
| $^{48}$Ca | 250 | 6.66 | 4.85 | 9.74 | 7.14 | 4.08 | 14.9 | 13.6 |
| | 500 | 3.19 | 1.11 | 17 | 3.53 | 2.57 | 21.84 | 18.5 |
| $^{90}$Zr | 209.6 | 0.78 | 0.87 | 2.21 | 1.36 | 0.65 | 6.53 | 5.36 |
| | 302 | 0.86 | 0.91 | 9.92 | 3.27 | 0.67 | 9.35 | 7.19 |
| $^{118}$Sn | 225 | 5.43 | 18.4 | 34.8 | 25.5 | 31.8 | 2.75 | 4.2 |
| $^{208}$Pb | 248.2 | 30.6 | 44.4 | 154 | 74.8 | 89.5 | 89.2 | 61 |
| | 502 | 21.2 | 14.1 | 186 | 50.5 | 61.1 | 95.9 | 76.5 |

linear instead of logarithmic. In general, all the considered models describe fairly well the experimental RDDCS values for small scattering angles. The agreement with experiment deteriorates when the scattering angle increases, pointing out again some possible deficiencies in the inner region of the theoretical charge density distributions.

To make a more quantitative analysis of the electron scattering DCS derived from the mean-field charge densities, we introduce a normalized square weighted difference ($d_w^2$), or comparison magnitude, with respect to the DCS measured in experiment. For each nucleus and electron beam energy, it is defined as

$$d_w^2 = \frac{1}{N}\sum_{i=1}^{N}\left[\frac{(d\sigma/d\Omega)_i^{\rm exp} - (d\sigma/d\Omega)_i^{\rm calc}}{\delta(d\sigma/d\Omega)_i^{\rm exp}}\right]^2. \qquad (15)$$

In this expression, the quantities $(d\sigma/d\Omega)_i^{\rm calc}$, $(d\sigma/d\Omega)_i^{\rm exp}$, and $\delta(d\sigma/d\Omega)_i^{\rm exp}$ are, respectively, the calculated DCS, the measured DCS, and the uncertainty of the latter. The sum in Eq. (15) runs over all the $N$ available data for the given scattering process.

In Table II we report, for several elastic electron-nucleus reactions, the $d_w^2$ values (15) from theory in comparison with the $d_w^2$ obtained from the charge densities fitted experimentally. One realizes that the $d_w^2$ of the DCS computed with the theoretical charge densities take sizably varying values, depending on the scattering process and nuclear model. Nevertheless, for all the considered electron-scattering processes, there are Skyrme forces or RMF parametrizations that yield a $d_w^2$ of similar quality to the experimental charge density. In particular, the RMF sets DD-ME2 and FSUGold give, on the average, the best overall agreement with the considered experimental data. The Skyrme forces SkM* and SLy4 provide a similar description, but globally this description is slightly worse than in the case of the RMF parametrizations, except for the nucleus $^{118}$Sn.

We have also analyzed the $d_w^2$ values of the relative differences between differential cross sections (14) in pairs of neighbor nuclei. The corresponding results are collected in Table III. For all the mean fields considered in the present study, the predicted $d_w^2$ values are larger than the $d_w^2$ values computed with the charge densities that are fitted to experiment. Looking globally at the results presented in Table III, the agreement obtained between theoretical and experimental RDDCS is not significantly worse than the agreement found in the case of the DCS analyzed previously in Table II. But, in the DCS analysis, it has been seen in Table II that for each scattering process there is always one or various specific interactions that are able to come very close to experiment, whereas in Table III this does not happen in any of the studied RDDCS in pairs of neighbor nuclei.

## IV. ELECTRON SCATTERING ALONG ISOTOPIC CHAINS

Different tendencies of the square of the charge form factor as a function of the momentum transfer have been

TABLE III. Normalized square weighted difference ($d_w^2$) between calculated and measured relative differences of DCS in pairs of neighbor nuclei. The beam energy per electron is 250 MeV for the Ca isotopes and $^{48}$Ti, and 225 MeV for the Sn isotopes.

| $D(A-B)$ | Exp(fit) | DD-ME2 | $G2$ | NL3 | FSUGold | SLy4 | SkM* |
|---|---|---|---|---|---|---|---|
| $D(^{40}\text{Ca}-^{42}\text{Ca})$ | 0.56 | 9.1 | 28.3 | 16 | 11.1 | 9.11 | 12.9 |
| $D(^{40}\text{Ca}-^{44}\text{Ca})$ | 1.14 | 4.5 | 29.6 | 12.2 | 3.88 | 7.08 | 9.13 |
| $D(^{40}\text{Ca}-^{48}\text{Ca})$ | 1.06 | 16.4 | 4.89 | 7.74 | 38.5 | 94.1 | 49.3 |
| $D(^{48}\text{Ca}-^{48}\text{Ti})$ | 2.49 | 18 | 19.6 | 31 | 37.8 | 71.8 | 64.9 |
| $D(^{116}\text{Sn}-^{118}\text{Sn})$ | 2.05 | 8.05 | 7.8 | 9 | 10.1 | 13.2 | 18.5 |
| $D(^{118}\text{Sn}-^{124}\text{Sn})$ | 4.03 | 5.35 | 6.98 | 7.5 | 9.22 | 7.05 | 7.18 |

studied in earlier literature for isotopic [20,21,25] and isotonic [26] chains of medium and heavy nuclei. Our aim here is to perform an analysis, quantitative whenever possible, that could eventually be useful for future electron-scattering measurements in RIB facilities.

We will be concerned with the study of electron scattering in isotopic chains of medium and relatively heavy systems, which will be exemplified by the cases of the Ca and Sn isotopes. Many of these nuclei lie in the region of the nuclear chart that is likely to be explored employing RIB facilities. Some of them may be investigated in future electron-scattering experiments, such as ELISe [17] and SCRIT [18,19]. For the purpose of our study, we are interested in predicting the trends of the variation along the isotopic chains of the electric charge form factor in the low-momentum transfer regime. Our calculated mean-field charge densities will be parameterized by means of the Helm model [66], often used in the analysis of experimental data, with a view to gain deeper physical insights and to elucidate possible correlations among scattering observables within the isotopic chains.

We have seen in the previous section that in the region of small $q$ values the experimental results are almost equally well reproduced by the calculations with the different theoretical mean-field models considered. In our subsequent study of electron scattering in the tin and calcium chains, as a representative reference, we will work with the charge densities predicted by the covariant interaction $G2$ [35,38]. This model was constructed as an effective hadronic Lagrangian consistent with the symmetries of quantum chromodynamics. As mentioned, the model describes the low-energy electromagnetic structure of the nucleon using vector-meson dominance and provides directly the charge density of the nucleus so no external single-nucleon form factors are required to compute the latter [35]. $G2$ is also a reliable parameter set for calculations of ground states of nuclei and, at the same time, for predictions of the nuclear equation of state up to supranormal densities and of some properties of neutron stars [35,38,55]. Calculations of the squared charge form factor done in PWBA with the set $G2$ for stable isotopes have been reported elsewhere [35].

For each nucleus in an isotopic chain we compute the associated DCS via the DWBA calculation using the $G2$ charge density. The electron beam energy in all the investigated scattering processes is fixed at 500 MeV. In practice, the energy dependence of the electric charge form factor defined in Eq. (13) is seen to be considerably weak for low-momentum transfers, the regime addressed in our analysis. We have verified numerically that $|F_{\rm DWBA}(q)|^2$ of high-energy electron scattering depends little on the electron beam energy for momentum transfers up to 1–1.5 fm$^{-1}$ (the precise value depends on the nucleus). This happens even for a heavy system like $^{208}$Pb, where the departure from the point-nucleus assumption of the Mott DCS used on the right-hand side of Eq. (13) is more significant. We illustrate the situation in Fig. 5, where we display $|F_{\rm DWBA}(q)|^2$ at several beam energies for electron scattering off $^{118}$Sn and $^{208}$Pb.

Before proceeding to the presentation of the results in the tin and calcium isotopic chains, we briefly summarize in the next subsection how we determine the parameters of the Helm model charge-density distributions.

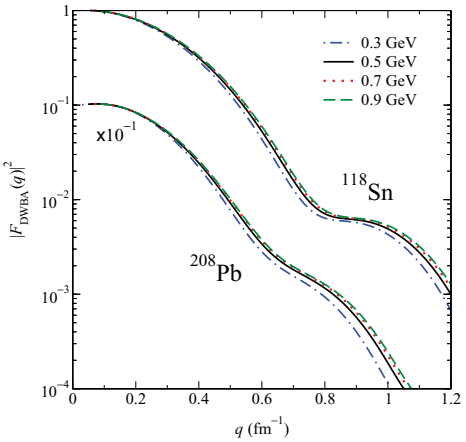


FIG. 5. (Color online) Squared charge form factor of $^{118}$Sn and $^{208}$Pb, derived from the covariant mean-field model $G2$, for the indicated electron beam energies. The figure points out that the sensitivity of the charge form factor extracted through Eq. (13) to the beam energy in high-energy elastic electron-nucleus scattering is rather small, even when the atomic number of the target is large as in $^{208}$Pb.

### A. Equivalent Helm charge densities

Valuable insights into the study of electron scattering often stem from consideration of modeled charge densities and electric charge form factors. Moreover, these parameterized forms are instrumental in experimental data analyses. A notable case is the so-called Helm model, whose original version [66] has later been extended in various ways for more accurate descriptions of the experimental charge densities [67–69]. In the simpler version of the model, two chief features of the nuclear charge density, namely the position and the thickness of the surface, can be related explicitly to the electric charge form factor obtained in PWBA. The Helm charge density is obtained from the convolution of a constant density $\rho_0$ in a hard sphere of radius $R_0$ (the diffraction radius) with a Gaussian distribution of variance $\sigma^2$ (whose square root relates to the nuclear surface thickness):

$$\rho^{(H)}(\vec{r}) = \int d\vec{r}\,' f_G(\vec{r}-\vec{r}\,')\rho_0\Theta(R_0-r), \tag{16}$$

where

$$f_G(r) = (2\pi\sigma^2)^{-3/2}e^{-r^2/2\sigma^2}. \tag{17}$$

The rms radius of the Helm density is readily obtained from Eqs. (16) and (17). It can be expressed in terms of $R_0$ and $\sigma$ as

$$\langle r^2\rangle_H^{1/2} = \sqrt{\frac{3}{5}\left(R_0^2+5\sigma^2\right)}. \tag{18}$$

The corresponding electric charge form factor in PWBA is given by

$$F^{(H)}(q) = \int e^{i\vec{q}\cdot\vec{r}}\rho^{(H)}(\vec{r})d\vec{r} = \frac{3}{qR_0}j_1(qR_0)e^{-\sigma^2q^2/2}, \tag{19}$$

where $j_1(x)$ is a spherical Bessel function.

The diffraction radius $R_0$ of the Helm density is usually fixed as follows. One requires that the first zero of Eq. (19) occurs at $q_{\min}R_0$, where $q_{\min}$ corresponds to the first minimum of the modulus of the PWBA form factor [$F_{\rm PWBA}(q)$ hereinafter] associated to the original charge distribution that the Helm density attempts to describe:

$$R_0 = \frac{4.49341}{q_{\min}}. \tag{20}$$

The variance $\sigma^2$ of the Gaussian is chosen to reproduce the height of the second maximum of $|F_{\rm PWBA}(q)|$, located at $q_{\max}$:

$$\sigma^2 = \frac{2}{q_{\max}^2}\ln\left[\frac{3j_1(q_{\max}R_0)}{q_{\max}R_0F_{\rm PWBA}(q_{\max})}\right]. \tag{21}$$

For moderate values of $qR_0$, the Helm charge form factor $F^{(H)}(q)$ reproduces well the actual charge form factor, with the exception of the regions closest to its zeros [66]. The relative difference between $F^{(H)}(q)$ and the actual charge form factor becomes progressively manifest as the momentum transfer grows. The applicability of the Helm model near the drip lines is to be explored. The extent to which it may be appropriate away from stability, for the purposes of our study, will be validated later from the numerical point of view in connection with the discussion of the calculations in the Sn and Ca chains.

### B. Tin and calcium isotopic chains

We are interested in the study of elastic electron scattering in the Ca and Sn chains. The calculated DCS and squared charge form factors $|F_{\rm DWBA}(q)|^2$ show, for the lightest nuclei considered here (calcium isotopes), a relatively well-marked first minimum. This first minimum, however, practically disappears for the heavier nuclei analyzed (tin isotopes). (This fact can also be told from the previous Figs. 2 and 3 for $^{16}$O, $^{90}$Zr, and $^{208}$Pb.) In the latter case, the form factor $|F_{\rm DWBA}(q)|^2$ of Eq. (13) still shows an inflection point (IP) in the low-momentum transfer region, a point where the curvature changes sign. In the absence of an explicit minimum at low-momentum transfer, these IP are the best candidates to characterize along the isotopic chain relevant properties of the electric charge form factor in the small-$q$ region.

We determine for each isotope an equivalent Helm distribution from the calculated mean-field charge density. In the PWBA the distortion of the electron wave functions due to the Coulomb potential of the nucleus is neglected. The effect of the Coulomb attraction felt by the electrons can be simulated by replacing the momentum transfer $q$ by an effective value [66]

$$q_{\rm eff} = q\left(1 + c\frac{Z\alpha}{qR_{\rm ch}}\right), \tag{22}$$

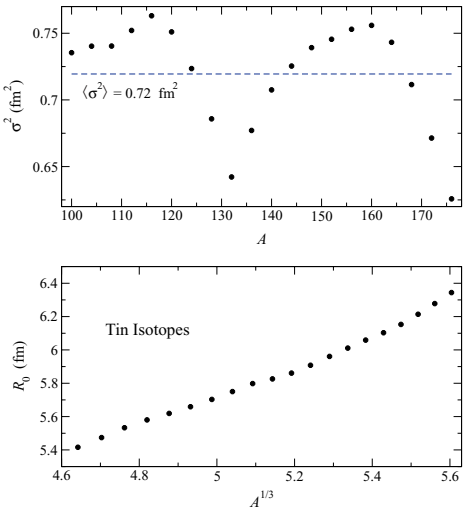


FIG. 6. (Color online) Mass-number dependence of the Helm parameters $\sigma^2$ (upper panel) and $R_0$ (lower panel) predicted by the covariant mean-field model $G2$ in the Sn isotopic chain. The average value of $\sigma^2$ is depicted by a horizontal dashed line.

where $R_{\rm ch} = \sqrt{3/5}R$ is the rms of the charge density assuming a hard sphere distribution of radius $R = r_0A^{1/3}$. In Ref. [66] the value of the constant $c$ is taken to be 3/2. Here we leave $c$ as a free parameter. It is optimized so that the rms radii of the equivalent Helm charge densities (18), with $R_0$ and $\sigma$ determined by Eqs. (20) and (21), and with $q$ replaced by $q_{\rm eff}$, best reproduce along the isotopic chain the mean field rms charge radii obtained with the RMF parametrization $G2$. Proceeding in this way, we find $c \approx 0.15$ for the tin isotopes and $c \approx 0.12$ for the calcium isotopes.

We first investigate the tin isotopic chain. The calculated Helm parameters $R_0$ and $\sigma^2$ are displayed in the lower and upper panels of Fig. 6, respectively. It is seen that $R_0$ steadily increases with the mass number $A$ and that it roughly follows the typical $A^{1/3}$ law. On the contrary, the change of the variance $\sigma^2$ with mass number shows a nonuniform character along the isotopic chain, related to the underlying shell structure. It oscillates around a mean value $\sigma^2 \simeq 0.72$ ($\sigma \simeq 0.85$). It is to be noted that $\sigma^2$ displays local minima at the doubly magic isotopes $^{132}$Sn and $^{176}$Sn (neutron drip line nucleus). This fact points out a stiffer nuclear surface for neutron-rich nuclei with double-closed major shells, in agreement with earlier literature [67].

The upper panel of Fig. 7 depicts the radial dependence of the mean-field charge-density profiles computed with the $G2$ covariant interaction for the isotopes $^{100}$Sn, $^{132}$Sn, and $^{176}$Sn. We have selected these examples to illustrate the evolution of the results along the isotopic chain from one drip line to another. Though the three isotopes share the same atomic number, one notices outstanding variations in the calculated

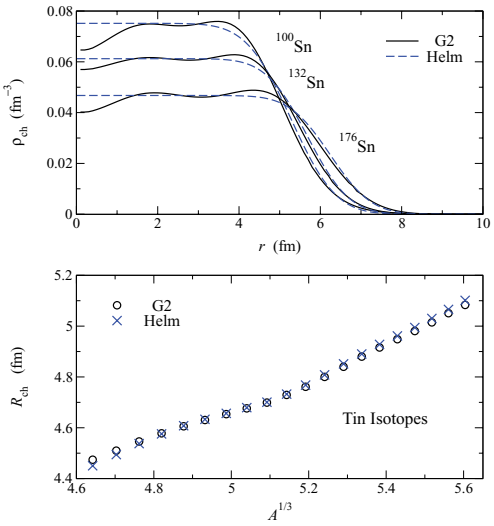


FIG. 7. (Color online) Charge densities (upper panel) and charge radii (lower panel) in the Sn isotopic chain, according to the covariant model $G2$ and to the determined Helm distributions.

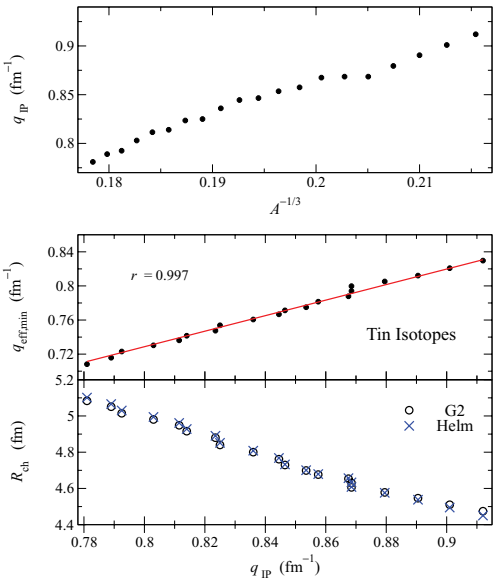


FIG. 8. (Color online) Results predicted by the $G2$ effective interaction for 500-MeV electron scattering in the Sn isotopic chain. (Upper panel) Mass-number dependence of the momentum transfer at the first inflection point ($q_{IP}$) of the squared charge form factor in DWBA. (Middle panel) Correlation of the effective momentum transfer at the first minimum of the squared charge form factor in PWBA ($q_{eff,min}$) with the value of $q_{IP}$. A linear fit of the results is shown and the correlation coefficient $r$ is indicated. (Lower panel) The change of the charge radii calculated with $G2$ and with the corresponding Helm densities is depicted against the value of $q_{IP}$.

mean-field charge densities of these isotopes, both in the surface region and, especially, in the interior region. This fact reflects the important influence of the changing neutron number on driving the structure of the charge density along the isotopic chain. This influence is encoded in the interaction terms of the covariant Lagrangian of $G2$ through the exchanged mesons and the couplings to the photon, and it is accounted for self-consistently by the mean-field calculations. In the same figure we compare the fitted Helm charge densities and the original $G2$ charge densities for the three discussed tin isotopes. At the interior of these nuclei, we see that the uniform density of the Helm model averages the oscillations of the self-consistent quantal densities obtained with the $G2$ interaction. In spite of the fact that the surface falloff of the Helm densities is of Gaussian type, the agreement at the surface region between the mean-field charge densities and their Helm equivalents is fairly good as one proceeds along the isotopic chain from stability to the neutron and proton drip lines. This provides some confidence on using the Helm model as determined in the present work when the drip lines are approached in the Sn chain. The lower panel of Fig. 7 illustrates the mass number dependence of the mean field and the equivalent Helm rms charge radii. Our approach leads to an excellent agreement between the Helm values and the mean-field values in the Sn chain. One appreciates some slight discrepancies only for isotopes very close to the drip lines. The rms charge radii of both calculations follow the expected linear trend with $A^{1/3}$. One observes some departure from the $A^{1/3}$ behavior to slightly lower values in the isotopes close to $A = 132$. This is finally the reason why the variance $\sigma^2$ decreases around $A = 132$ in Fig. 6 [also see Eq. (18)].

We now analyze the evolution along the isotopic chain of the momentum transfer $q_{IP}$ corresponding to the first inflection point of $|F_{DWBA}(q)|^2$ and the variation of $|F_{DWBA}(q_{IP})|^2$, calculated for an electron beam energy of 500 MeV. We discuss possible correlations with the parameters $R_0$ and $\sigma$ of the equivalent Helm density. Two noticeable findings of this study are displayed in Fig. 8. In the upper panel of the figure it is seen that the change of the momentum transfer $q_{IP}$ with mass number in the Sn isotopic chain approximately follows an $A^{-1/3}$ law. Thus, the position of the first minimum of the square of the modulus of the electric charge form factor is shifted toward smaller $q$ values as the number of neutrons in the isotopic chain increases, a feature also noted in Ref. [25]. Another interesting result is that the momentum transfer $q_{IP}$ turns out to be almost proportional to the effective momentum transfer $q_{eff}$ corresponding to the corrected first minimum of $|F_{PWBA}(q)|$ computed with the mean-field charge density. The situation is illustrated in the middle panel of Fig. 8. Recalling Eq. (20), this correlation allows one to establish a straightforward relationship between $q_{IP}$ and the

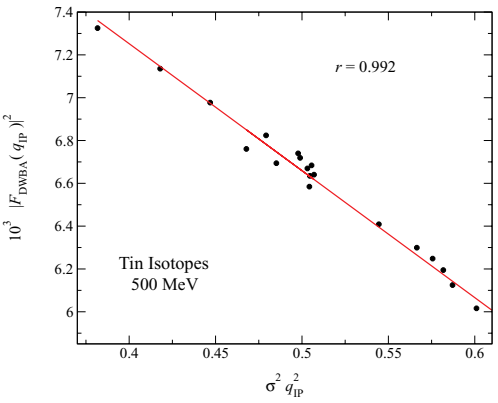


FIG. 9. (Color online) Correlation along the Sn isotopic chain of the squared charge form factor in DWBA, at its first inflection point ($q_{IP}$), with the product of the Helm parameter $\sigma^2$ and $q_{IP}^2$. The results are computed with the $G2$ effective interaction for scattering by 500-MeV electrons. Note that each point of the figure corresponds to a different isotope and that the mass number increases from right to left.

Helm parameter $R_0$ in the tin isotopic chain:

$$R_0 \approx \frac{4.934}{q_{IP}}. \tag{23}$$

We also find that the rms charge radii of the tin isotopes exhibit a considerable linear correlation with the momentum transfer $q_{IP}$, as depicted in the lower panel of Fig. 8. These correlations could, in principle, provide an alternative way to obtain the parameter $\sigma$ of the equivalent Helm charge densities directly through Eq. (18), taking into account the relationship (23) between $R_0$ and $q_{IP}$.

Figure 9 displays the evolution in the Sn chain of $|F_{DWBA}(q_{IP})|^2$ (the value of the DWBA squared charge form factor calculated at $q_{IP}$) as a function of $\sigma^2 q_{IP}^2$. The addition of neutrons along the isotopic chain in general brings about an increase of the value of $|F_{DWBA}(q_{IP})|^2$, also documented in the literature [20,21,23–25]. Furthermore, we notice that an interesting linear correlation arises between the quantities $|F_{DWBA}(q_{IP})|^2$ and $\sigma^2 q_{IP}^2$ as one moves from the proton-rich side of the isotopic chain to the neutron-rich side. This correlation may be qualitatively understood in the following terms. If for guidance we consider the expression (19) of the electric charge form factor in the adopted Helm model, we see that the natural variables to investigate the variation of the charge form factor are $qR_0$ and $\sigma^2 q^2$. But, as stated in Eq. (23), the value of $qR_0$ at the first inflection point of $|F_{DWBA}(q)|^2$ is practically independent of the mass number in the whole isotopic chain. Therefore, the mass-number variation of $\sigma^2 q_{IP}^2$ is left as the principal source for the $A$ dependence of the value of the squared charge form factor at $q = q_{IP}$. It is then reasonable that the change with $A$ of $|F_{DWBA}(q_{IP})|^2$ and $\sigma^2 q_{IP}^2$ is correlated along the isotopic chain, a feature confirmed by Fig. 9. As a physical insight, helped by Eq. (23), the product

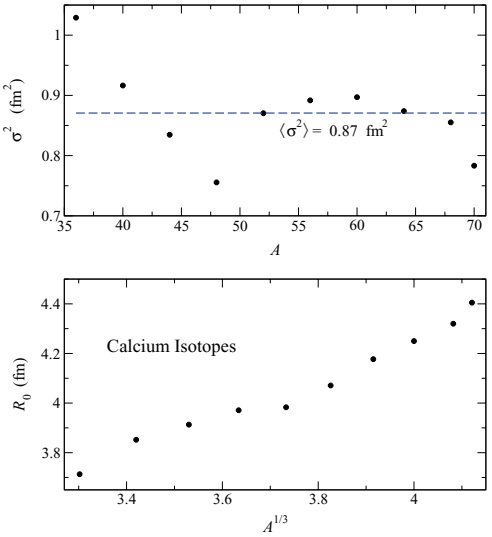


FIG. 10. (Color online) Same as described in the caption to Fig. 6 for the Ca isotopic chain.

$\sigma^2 q_{IP}^2$ can be recast as proportional to $\sigma^2/R_0^2$, which is the ratio between the surface width and the mean location of the surface of the underlying nuclear charge density.

Similar results to those discussed above for tin have been obtained in the study of the calcium isotopic chain. They are presented in Figs. 10–13. We first have modeled the

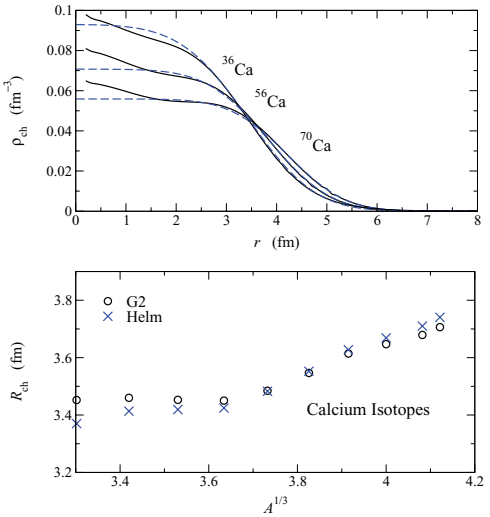


FIG. 11. (Color online) Same as described in the caption to Fig. 7 for the Ca isotopic chain.

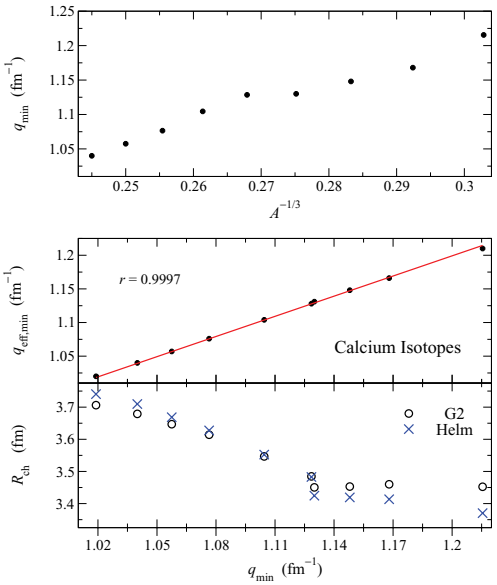


FIG. 12. (Color online) Same as described in the caption to Fig. 8 for the Ca isotopic chain.

calculated mean-field densities of the calcium chain by the simpler form of Helm densities. The mass-number evolution of the parameters of the Helm charge densities is illustrated in Fig. 10. The shrinkage of the Helm parameter $\sigma$ at magic neutron numbers, noticed in the tin chain, is a feature also present in the calcium isotopes for the magic neutron numbers $N = 28$ and 50. However, the effect at $N = 20$ is completely washed out, in agreement with the result of Ref. [67]. The mean-field charge densities of $^{36}$Ca, $^{56}$Ca, and $^{70}$Ca calculated

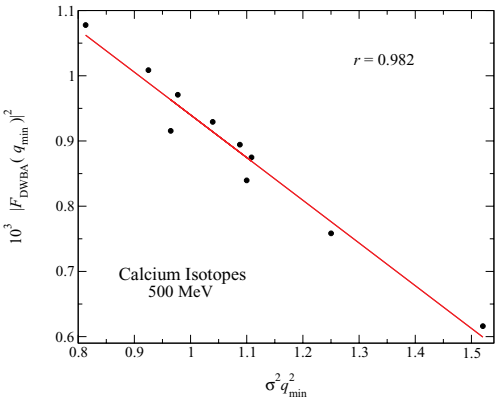


FIG. 13. (Color online) Same as described in the caption to Fig. 9 for the Ca isotopic chain.

with $G2$, along with the equivalent Helm profiles, are displayed in the upper panel of Fig. 11. As in the case of the tin chain, the effects of the addition of neutrons are very manifest in the mean-field charge density, as one can appreciate from the changes in the interior and surface regions of the density distributions of the shown Ca isotopes. One also sees that the Helm densities manage to follow on average these changes. The Helm profiles are found to reproduce closely the surface region of the mean-field densities, including the isotopes at the proton- and neutron-rich sides of the calcium chain. Discrepancies are observed in the interior region of the density distributions. In the lower panel of Fig. 11 we display, as a function of $A^{1/3}$, the variation in the calcium chain of the rms radii of the mean-field and Helm charge densities. Compared to the case of Sn, this lighter chain presents more significant departures from the $A^{1/3}$ behavior. Also, the agreement of the rms radii of the Helm model with the self-consistent $G2$ values is less good. This is more visible in approaching the drip lines, especially at the proton drip line.

Analogous correlations to those previously discussed in the case of tin, between the value of $q$ at the first minimum (or IP) of $|F_{DWBA}(q)|^2$ with (i) the mass number, (ii) the first minimum of $|F_{PWBA}(q)|$, and (iii) the rms radius of the charge distributions, are similarly found in the analysis of the calcium isotopes. They are displayed in Fig. 12. In the present case, however, a significant departure of the radii $R_0$ and $R_{ch}$ from the $A^{1/3}$ law is observed as one moves toward the proton drip line. These deviations may be largely due to the fact that, in approaching the proton drip line, the protons are more loosely bound and therefore the charge density extends to larger distances compared with the stable nuclei above $^{40}$Ca. The effect is much more prominent in calcium than in tin because of the lower Coulomb barrier due to its smaller atomic number. In turn, the same effect may originate that the Helm parameter $\sigma$ of $^{40}$Ca, measuring the surface thickness of the nucleus, does not decrease as compared with the heavier neighbor nuclei (see upper panel of Fig. 10). We plot in Fig. 13 the square of the DWBA charge form factor computed for 500-MeV electrons at its first minimum against the value of the product $\sigma^2 q_{min}^2$. In calcium, as in the case of the tin isotopes, an outstandingly linear correlation exists between both quantities.

Finally, to validate the consistency of our analysis with Helm density equivalents, we compute in test cases the squared DWBA electric charge form factor both with the Helm profiles and with their original mean-field charge densities. The results, as a function of the momentum transfer $q$, in a few isotopes of calcium and tin are compared in Fig. 14. The cases shown in the figure are chosen to illustrate the situation from the proton to the neutron drip lines, but similar conclusions are found for the other isotopes of these chains. In the range of $q$ values up to $\approx$1.5 fm$^{-1}$ in the calcium isotopes and up to around $\approx$1 fm$^{-1}$ in the tin isotopes, one observes an excellent agreement between the results for $|F_{DWBA}(q)|^2$ obtained using the mean-field charge densities and using the equivalent Helm charge densities. A similar situation is found in the nuclei that lie near the drip lines: the agreement between the Helm and the mean field results is slightly worse but without sizable differences compared to the more stable nuclei. This scenario

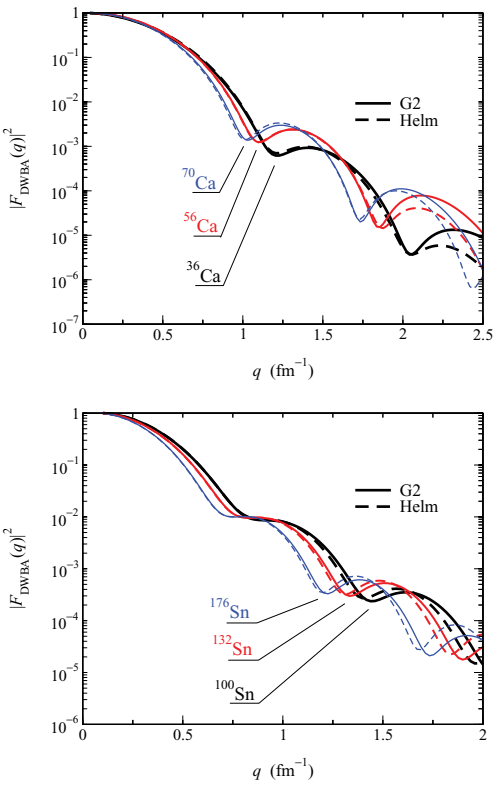


FIG. 14. (Color online) Comparison in Ca and Sn isotopes between the squared charge form factor in DWBA calculated with the charge densities of the $G2$ mean-field interaction (solid lines) and with the equivalent Helm charge densities (dashed lines). Notice that the vertical and horizontal scales for calcium and tin are different.

points out that the electron-nucleus scattering results in the low-momentum transfer region computed with mean-field charge densities, are very well simulated by equivalent Helm densities with the $R_0$ and $\sigma$ parameters obtained according to the method described above. As the value of the momentum transfer increases, expectably, the discrepancies between the actual calculations with $G2$ and the adjusted Helm model become evident.

Let us now concentrate on the results pertaining to the self-consistent calculations with $G2$ that are shown in Fig. 14. One can observe that, as mentioned earlier, the first minimum that is visible in the squared charge form factor of calcium sinks away in tin. Its fingerprint in tin is recognized as an inflection point. The second and further minima of $|F_{\rm DWBA}(q)|^2$ remain, however, clearly identifiable in the tin isotopes. With the progressive addition of neutrons in either of the two isotopic chains, it may be seen from Fig. 14 that the first minimum of $|F_{\rm DWBA}(q)|^2$, or its signature, becomes slightly more marked. This effect is, however, much less noticeable than the discussed effect on the first minimum induced by changing $Z$. One also observes that the location of the minima or inflection points of the squared charge form factor is gradually pushed toward lower-momentum transfers as the nucleus becomes more and more neutron rich. This effect has been noted in previous literature [20,21,23–25], and for the first minimum we have described it in more detail in the upper panels of Figs. 8 and 12. The same trend (inwards shift of the minima or IP) occurs with increasing atomic number (compare the scales of the $q$ axis for Ca and Sn in Fig. 14). In general, the inwards displacement of the momentum transfer of the minima is accompanied by a simultaneous increase of the height of the maxima of the squared charge form factor.

## V. SUMMARY AND CONCLUSIONS

We adapted the ELSEPA code [30] for calculations of elastic electron-nucleus scattering. The predictions obtained from the charge densities computed with various selected Skyrme forces and modern relativistic mean-field parameter sets have been compared with existing experimental data about elastic electron scattering in several stable nuclei.

A suitable quantitative comparison among the theoretical predictions is established by introducing, for each nucleus and beam energy, a normalized square weighted difference. Although all the considered effective interactions describe qualitatively well the experimental DCS data, the quantitative analysis in terms of the $d_w^2$ with respect to experiment shows some differences among the various theoretical DCS, especially for large scattering angles. These differences are related mainly with the different behavior of the mean-field densities in the inner region of the nuclei. For the investigated nuclei and energies, one always finds a theoretical charge distribution whose $d_w^2$ is at least similar, and in some cases better, than the one obtained with the experimental charge density that has been fitted to reproduce the measured DCS data. Among the nuclear interactions analyzed, the DCS values calculated with the charge densities obtained from the covariant DD-ME2 and FSUGold parameter sets are the ones that tend to give overall better agreement with the experimental values considered.

A more challenging test on theory is provided by the analysis of the experimental data about relative differences of DCS between pairs of neighbor nuclei. The calculations based on the mean-field charge densities reasonably follow the global trends shown up by the experimental measurements. The quantitative analysis, however, as in the case of the previously investigated DCS, highlights some deficiencies of the mean-field densities in their inner region.

We have used the mean-field charge densities obtained with the relativistic $G2$ parametrization, by the reasons discussed previously, as the input baseline to study the elastic electron-nucleus scattering along the tin and calcium isotopic chains. Calculations have been performed from the proton to the neutron drip lines. Our aim has been to extract general trends, according to current mean-field theories of nuclear structure, about the behavior that may be expected from real

electron-nucleus scattering experiments in exotic nuclei, in the low-momentum transfer region. Such experiments are envisaged at FAIR [17] and the SCRIT [18,19] project in the nearby future, using exotic nuclei provided by radioactive isotope beams. We have confined our study to medium and heavy mass isotopes where the mean-field approach can be applied. Surely, the experimental program will investigate not only heavy exotic nuclei but it will address also scattering from light exotic nuclei. The theoretical investigation of these light nuclei, however, demands a sophisticated microscopic treatment of scattering to deal with the underlying shell-model structure and the possible occurrence of halos, which is beyond the methodology of the mean-field study of the present work.

First, we have computed for each isotope of the investigated chains the squared electric charge form factor. It has been obtained as the ratio between the DWBA DCS calculated with ELSEPA and the Mott DCS. We have checked that $|F_{\rm DWBA}(q)|^2$ defined in this way is relatively independent of the energy of the electron beam up to momentum transfers $q \approx 1$–$1.5$ fm$^{-1}$, even for nuclei as large as $^{208}$Pb. Second, we have fitted the mean-field charge densities by two-parameter Helm distributions. In doing so, we have adjusted the effective momentum transfer correction to reproduce the mean-field rms charge radii, on average, along the isotopic chain. We have made an *a posteriori* check that a DWBA calculation of the elastic electron scattering using as input the equivalent Helm charge density, is in excellent agreement with the results computed with the original mean-field charge density up to momentum transfers $q \approx 1$–$1.5$ fm$^{-1}$.

We have paid special attention to the value of the square of the DWBA electric charge form factor at the momentum transfer where its first minimum, in medium-mass nuclei, or its first inflection point, in heavier nuclei, appears. We have studied how it evolves along the isotopic chains of tin and calcium. Interesting linear correlations between the value of the momentum transfer at the first minimum (or IP) of $|F_{\rm DWBA}(q)|^2$ with the mass number of the isotopes of the chain, with the effective momentum transfer at the first minimum of $|F_{\rm PWBA}(q)|^2$, and with the rms radius of the charge distribution, have been discussed. Also, a linear correlation between $|F_{\rm DWBA}(q)|^2$ and $\sigma^2 q^2$ computed at the first minimum or IP, where $\sigma$ is the Helm parameter that accounts for the surface thickness of the nuclear density, has been found in the studied chains.

The analysis described in the present article could potentially be useful for future electron-nucleus elastic-scattering experiments. If the experimental data are available for two or more isotopes of a given chain, the aforementioned linear correlations would provide, for an unknown nucleus of the chain, a hint on the value expected for the square of the experimental electric charge form factor at its first minimum and for the momentum transfer where the latter occurs. The parameters of the Helm charge density distribution of the unknown isotope could be estimated by means of correlations such as those displayed in Figs. 8 and 12, with the help of Eqs. (20) and (18). Also, if the value of the squared modulus of the form factor is determined experimentally at its first minimum, the charge density in the Helm model can be sketched from similar correlations to Figs. 8 and 12, together with the correlation of the type depicted in Figs. 9 and 13. The use of more elaborated versions of the Helm model [67–69] that take into account the central depression of the charge density should allow one to extend the domain of validity of our method up to larger values of the momentum transfer. Work in this direction will be undertaken.

## ACKNOWLEDGMENTS

We are very grateful to Professor P. Ring for supplying us with the code for finite nuclei calculations with the model DD-ME2. We thank Professor D. W. L. Sprung for reading a preliminary version of the manuscript and for valuable comments. This work has been partially supported by Grants Nos. FIS2005-03142 and FPA2006-12066 from MEC (Spain) and FEDER and by Grant No. 2005SGR-00343 from Generalitat de Catalunya, as well as by the Spanish Consolider-Ingenio 2010 Programme CPAN CSD2007-00042. One of us (X.R.) also acknowledges Grant No. AP2005-4751 from MEC (Spain).

[1] R. Hofstadter, Rev. Mod. Phys. **28**, 214 (1956).
[2] T. W. Donnelly and J. D. Walecka, Annu. Rev. Nucl. Part. Sci. **25**, 329 (1975).
[3] T. W. Donnelly and I. Sick, Rev. Mod. Phys. **56**, 461 (1984).
[4] E. Moya de Guerra, Phys. Rep. **138**, 293 (1986).
[5] I. Sick, Prog. Part. Nucl. Phys. **47**, 245 (2001).
[6] H. de Vries, C. W. de Jager, and C. de Vries, At. Data Nucl. Data Tables **36**, 495 (1987).
[7] G. Fricke, C. Bernhardt, K. Heiling, L. A. Schaller, L. Shellenberg, E. B. Shera, and C. W. de Jager, At. Data Nucl. Data Tables **60**, 177 (1995).
[8] I. Angeli, At. Data Nucl. Data Tables **87**, 185 (2004).
[9] *Proceedings of the ENAM'04 Conference, Pine Mountain (USA), 2004*, edited by C. J. Gross, W. Nazarewicz, and K. P. Rykaczewski, Eur. Phys. J. A **25**, s01 (2005).
[10] I. Tanihata, Prog. Part. Nucl. Phys. **35**, 505 (1995).
[11] H. Geissel, G. Müzenberg, and R. Riisager, Annu. Rev. Nucl. Part. Sci. **45**, 163 (1995).
[12] A. Mueller, Prog. Part. Nucl. Phys. **46**, 359 (2001).
[13] T. Suda, K. Maruyama, and I. Tanihata, RIKEN Accel. Prog. Rep. **34**, 49 (2001).
[14] K. Katayama, T. Suda, and I. Tanihata, Phys. Scr., T **104**, 129 (2003).
[15] An International Accelerator Facility for Beams of Ions and Antiprotons, GSI report 2006. http://www.gsi.de/GSI-Future/cdr/.
[16] H. Simon, in *Proceedings of the International Workshop XXXII on Gross Properties of Nuclei and Nuclear Excitations*, Hirschegg (Austria), 2004, edited by M. Buballa, J. Knoll, W. Nörenberg, B.-J. Schaefer, and J. Wambach (GSI, Darmstad, 2004), p. 290.
[17] H. Simon, Nucl. Phys. **A787**, 102 (2007).
[18] T. Suda and M. Wakasugi, Prog. Part. Nucl. Phys. **55**, 417 (2005).

[19] M. Wakasugi, T. Emoto, Y. Furukawa, K. Ishii, S. Ito, T. Koseki, K. Kurita, A. Kuwajima, T. Masuda, A. Morikawa, M. Nakamura, A. Noda, T. Ohnishi, T. Shirai, T. Suda, H. Takeda, T. Tamae, H. Tongu, S. Wang, and Y. Yano, Phys. Rev. Lett. **100**, 164801 (2008).

[20] A. N. Antonov, D. N. Kadrev, M. K. Gaidarov, E. Moya de Guerra, P. Sarriguren, J. M. Udias, V. K. Lukyanov, E. V. Zemlyanaya, and G. Z. Krumova, Phys. Rev. C **72**, 044307 (2005).

[21] P. Sarriguren, M. K. Gaidarov, E. M. de Guerra, and A. N. Antonov, Phys. Rev. C **76**, 044322 (2007).

[22] S. Karataglidis and K. Amos, Phys. Lett. **B650**, 148 (2007).

[23] C. A. Bertulani, J. Phys. G **34**, 315 (2007).

[24] Zaijun Wang and Zhongzhou Ren, Phys. Rev. C **70**, 034303 (2004).

[25] Zaijun Wang and Zhongzhou Ren, Phys. Rev. C **71**, 054323 (2005).

[26] Zaijun Wang, Zhongzhou Ren, and Ying Fan, Phys. Rev. C **73**, 014610 (2006).

[27] K. Amos, S. Karataglidis, and J. Dobaczewski, Phys. Rev. C **70**, 024607 (2004).

[28] A. Baker, Phys. Rev. **134**, B240 (1964).

[29] D. R. Yennie, D. G. Ravenhall, and R. N. Wilson, Phys. Rev. **95**, 500 (1954).

[30] F. Salvat, A. Jabalonski, and C. J. Powell, Comput. Phys. Commun. **165**, 157 (2005).

[31] J. Bartel, P. Quentin, M. Brack, C. Guet, and H.-B. Håkansson, Nucl. Phys. **A386**, 79 (1982); M. Brack, C. Guet, and H.-B. Håkansson, Phys. Rep. **123**, 275 (1985).

[32] E. Chabanat, P. Bonche, P. Haensel, J. Meyer, and R. Schaeffer, Nucl. Phys. **A635**, 231 (1998).

[33] G. A. Lalazissis, J. König, and P. Ring, Phys. Rev. C **55**, 540 (1997).

[34] B. G. Todd-Rutel and J. Piekarewicz, Phys. Rev. Lett. **95**, 122501 (2005).

[35] R. J. Furnstahl, B. D. Serot, and H.-B. Tang, Nucl. Phys. **A615**, 441 (1997); [Erratum-*ibid*. **A640**, 505 (1998)].

[36] T. Niksić, D. Vretenar, P. Finelli, and P. Ring, Phys. Rev. C **66**, 024306 (2002).

[37] W. Greiner and J. Reinhardt, *Quantum Electrodynamics* (Springer-Verlag, Berlin/Heidelberg, 1992).

[38] B. D. Serot and J. D. Walecka, Int. J. Mod. Phys. E **6**, 515 (1997).

[39] W. Bertozzi, J. Friar, J. Heisenberg, and J. W. Negele, Phys. Lett. **B41**, 408 (1972).

[40] E. Garrido and E. Moya de Guerra, Nucl. Phys. **A650**, 387 (1999).

[41] UNEDF SciDAC Collaboration, http://www.unedf.org.

[42] M. Bender, P.-H. Heenen, and P.-G. Reinhard, Rev. Mod. Phys. **75**, 121 (2003).

[43] D. Vautherin and D. M. Brink, Phys. Rev. C **5**, 626 (1972).

[44] Li Guo-Quiang, J. Phys. G **17**, 1 (1991).

[45] W. A. Richter and B. A. Brown, Phys. Rev. C **67**, 034317 (2003).

[46] B. D. Serot and J. D. Walecka, Adv. Nucl. Phys. **16**, 1 (1986).

[47] P.-G. Reinhard, Rep. Prog. Phys. **52**, 439 (1989).

[48] B. D. Serot, Rep. Prog. Phys. **5**, 1855 (1992).

[49] Y. K. Gambhir, P. Ring, and A. Thimet, Ann. Phys. (NY) **198**, 132 (1990).

[50] P. Ring, Prog. Part. Nucl. Phys. **37**, 193 (1996).

[51] J. Boguta and A. R. Bodmer, Nucl. Phys. **A292**, 413 (1977).

[52] Y. Sugahara and H. Toki, Nucl. Phys. **A579**, 557 (1994).

[53] M. Del Estal, M. Centelles, X. Viñas, and S. K. Patra, Phys. Rev. C **63**, 024314 (2001).

[54] C. J. Horowitz and J. Piekarewicz, Phys. Rev. Lett. **86**, 5647 (2001); Phys. Rev. C **64**, 062802(R) (2001).

[55] P. Arumugam, B. K. Sharma, P. K. Sahu, S. K. Patra, Tapas Sil, M. Centelles, and X. Viñas, Phys. Lett. **B601**, 51 (2004).

[56] M. Del Estal, M. Centelles, X. Viñas, and S. K. Patra, Phys. Rev. C **63**, 044321 (2001).

[57] M. E. Rose, *Relativistic Electron Theory* (Wiley, New York, 1961).

[58] F. Salvat, J. M. Fernandez-Varea, and W. Williamson Jr., Comput. Phys. Commun. **90**, 151 (1995).

[59] F. Salvat and R. Mayol, Comput. Phys. Commun. **74**, 358 (1993).

[60] I. Sick and J. S. McCarthy, Nucl. Phys. **A150**, 631 (1970).

[61] R. F. Frosch, R. Hofstadter, J. S. McCarthy, G. K. Nöldeke, K. J. van Oostrum, M. R. Yearian, B. C. Clark, R. Herman, and D. G. Ravenhall, Phys. Rev. **174**, 1380 (1968).

[62] Phan Xuan Ho, J.-B. Bellicard, A. Bussiere, Ph. Leconte, and M. Priou, Nucl. Phys. **A179**, 529 (1972).

[63] A. S. Litvinenko, N. G. Shevchenko, A. Yu. Buki, G. A. Savitsky, V. M. Khvastunov, A. A. Khomich, V. N. Polishchuk, and I. I. Chkalov, Nucl. Phys. **A182**, 265 (1972).

[64] J. L. Friar and J. W. Negele, Nucl. Phys. **A212**, 93 (1973).

[65] B. Dreher, J. Friedrich, K. Merle, H. Rothhaas, and G. Luhrs, Nucl. Phys. **A235**, 219 (1974).

[66] R. H. Helm, Phys. Rev. **104**, 1466 (1956).

[67] J. Friedrich and N. Voegler, Nucl. Phys. **A373**, 192 (1982).

[68] J. Friedrich, N. Voegler, and P. G. Reinhard, Nucl. Phys. **A459**, 10 (1986).

[69] D. C. Zheng, N. Yamanishi, and D. W. L. Sprung, Nucl. Phys. **A550**, 89 (1992).

# 5 DDME$\delta$: Relativistic mean field interaction with density dependent meson-nucleon vertices

## 5.1 Introduction

Structure properties of nuclei described in the framework of effective mean-field interactions are remarkably successful over almost the entire periodic table [Va72, De80, Fu97, La97, Ty99, Ni02, Go03, Sa03, To05, La05, Ba08]. Relativistic and non-relativistic versions of this approach enable an effective description of the nuclear many-body problem as an energy density functional. These energy functionals are usually adjusted to a variety of finite nuclei and infinite nuclear matter properties. Although all these effective interactions are based on the mean-field approach, some differences will generally appear between them due to the specific ansatz on the density dependence adopted by each interaction. As we have discussed in previous chapters, an illustrative example of this situation is the symmetry energy. This is a nuclear property whose density dependence is far to be fully determined and, as a consequence, the predictions of existing functionals differ widely between them. For these reasons, one of the main goals in Nuclear Physics is to build a universal density functional theory [UNEDF, La04] based on microscopical calculations. This functional should be able to explain as many as possible measured data within the same parameter set. Attempts on this direction have been already taken. One of the first steps in building such an energy functional was developed with Skyrme-like interactions in the Hartree-Fock framework [Go03, Sa03]. One aim of these calculations was to describe microscopically measured nuclear masses with the highest accuracy ever. The results were very precise but they could not achieve a better accuracy than, *e.g.*, microscopic-macroscopic approaches [Mo95, Du95]. For that reason, there is still ongoing work for the improvement in their theoretical treatment.

With the same goal, in the more recent past a different approach was tried. Baldo, Schuck and Viñas employed the same route as in condensed matter physics and constructed a functional (BCP1) [Ba08] where the bulk part is based on the fully microscopic calculations of Reference [Ba04]. In this more fundamental calculations, Baldo and collaborators investigate the nuclear and infinite neutron matter on the basis of the Bethe-

Brueckner approach [Ba99]. Their results for the Equation of State (EoS) of symmetric and neutron matter are believed to be among the most accurate in the literature. Then, the BCP1 functional took as a benchmark the calculations of Reference [Ba04] by means of a polynomial fit. In this way an accurate and analytic EoS as a function of neutron and proton densities were constructed covering the whole range from symmetric nuclear matter to pure neutron matter in density ranges from zero to about two times saturation density. Subsequently a finite range surface term dependent on three parameters together with the strength of the spin-orbit term (four parameters in total) were added to the bulk part of the functional. The pairing correlations needed to describe open-shell nuclei were accounted by a density dependent $\delta$-force. Adjusting these free parameters to some selected nuclear experimental data yielded excellent results for nuclear masses and reasonable charge radii of the whole nuclear chart.

On the other hand, self-consistent mean-field calculations starting from relativistic Lagrangians have been very successful in describing nuclear properties [Fu97, La97, Ty99, Ni02, To05, La05]. They arise from a microscopic treatment of the nuclear many-body problem in terms of nucleons and mesons carrying the effective interaction between nucleons. Moreover, since the theory is relativistically invariant and the field and nucleon equations of motion are solved self-consistently, they preserve causality and provide a self-consistent description of the spin-orbit term of the nuclear effective force and of the bulk and surface parts of the interaction. Recently, the relativistic mean field framework have been extended to include the density dependence of the meson-nucleon vertices(see *e.g.* [Hof1]). The extension is based on the Density Dependent Relativistic Hadron Field (DDRHF) theory and the ansatz for the specific density dependence of the meson-nucleon vertices is mapped from Dirac-Brueckner calculations where the in-medium interaction is obtained from nucleon-nucleon potentials consistent with scattering experiments. Therefore, if this ansatz is adopted, the effective theory contains information on the density dependence of the meson-nucleon vertices as suggested by first-principle calculations. Although a fit of the free parameters is still needed, this fact allows to constrain the different possibilities and keeps the compatibility, at least theoretically, with more fundamental calculations of infinite nuclear matter. These models have shown improvements with respect to previous relativistic mean-field models in the description of asymmetric nuclear matter, neutron matter and nuclei far from the stability valley [Ty99, Ni02, La05].

As mentioned, there exist *ab initio* calculations of the nuclear EoS over a wide range of nucleon densities, *i.e.* far from densities currently reachable at the laboratory. In this sense, apart from the experimental data needed in the fitting procedure for determining an effective interaction, further steps on building a universal density functional may need to implement such *ab initio* information as it was done in the BCP1 model. Therefore, this EoS calculated from first principles can be understood as a temporary benchmark at supra- and sub-saturation densities of the energy per particle at different asymmetries. Furthermore, from a theoretical point of view, consistency is desirable between predictions of both theories. Regrettably, to make them compatible is not only a problem of including

the EoS derived from realistic nucleon-nucleon potentials within the fitting procedure. It is also a problem of taking into account the proper density dependence in the different terms of the functional. For that, first-principle calculations are also thought to be the best candidate to help in building a universal energy density functional, at least the bulk part of it since many-nucleon calculations are not feasible yet. Hence, from an effective and self-consistent treatment of the nuclear many body problem, we propose here a novel fit of an improved relativistic mean-field interaction with explicit density dependence of the meson-nucleon vertices compatible with fully microscopical calculations (Density Dependent Meson Exchange interaction based on microscopical calculations: DDME$\delta$). The relativistic mean field model DDME$\delta$ is an extension of the DDME model developed by Ring and collaborators [Ni02, La05] based on the DDRHF theory. The DDME model has the following degrees of freedom: the proton, the neutron and three mesons carrying the nuclear interaction, namely $\sigma$, $\omega$ and $\rho$ mesons. In addition to these degrees of freedom, we include a new one, the $\delta$ meson. The reaon for it is motivated in References [Hu96, Hu98] where Huber *et al.* stressed that mean-field models which neglect the $\delta$ meson are likely to miss an important ingredient in describing properly very asymmetric nuclear matter. Therefore, the $\delta$ meson will be appropiate for the description of nuclei with large asymmetries —as the exotic nuclei planned to be studied experimentally at Rare Ion Beam Facilities [RBFa]— or astrophysical objects. In that way, we improve the theoretical description of the nucleus as compared with the DDME model by taking into account that new degree of freedom.

After establishing the DDME$\delta$ model, we compare binding energies, charge radii, two-neutron separation energies and neutron skins in spherical nuclei as predicted by the novel effective interaction with the experiment and with two very different models, BCP1 [Ba08] and DDME2 [La05].

## 5.2 Density Dependent Hadron Field Theory

### 5.2.1 Lagrangian and equations of motion

The density dependent relativistic hadron field theory in which DDME$\delta$ is based has been formulated and broadly discussed in References [Le95, Fu95, Hof1]. Here we will present the essential features of the mean-field equations of motion derived from such theory. The relativistic Lagrangian includes the neutron and the proton represented as Dirac spinors $\mathbf{\Psi} = \begin{pmatrix} \psi_p \\ \psi_n \end{pmatrix}$, the four mesons ($\sigma$, $\omega$, $\rho$ and $\delta$) carrying the effective nuclear strong interaction represented by the fields $\Phi_\sigma$, $A_\mu^{(\omega)}$, $\mathbf{A}_\mu^{(\rho)}$ and $\mathbf{\Phi}_\delta$ and, finally, the photon field $A_\mu^{(\gamma)}$ accounting for the electromagnetic interaction. The index $\mu$ indicates the time- and space-like components of the vector fields and the bold face indicates the vector nature of a field in the isospin space. As mentioned, the $\delta$ meson should be included if one wants to follow the theoretical indications pointed out by Huber *et al.* [Hu96, Hu98] for a proper

decription of asymmetric nuclear matter inside the mean-field approach and so we do. The Lagrangian can be splitted as follows,

$$\mathcal{L} = \mathcal{L}_{_N} + \mathcal{L}_M + \mathcal{L}_{int} \tag{8}$$

where, $\mathcal{L}_{_N}$ is the nucleonic free Lagrangian, $\mathcal{L}_M$ is the mesonic free Lagrangian and $\mathcal{L}_{int}$ is the Lagrangian describing the interactions. Their algebraic expressions are,

$$\mathcal{L}_{_N} = \bar{\mathbf{\Psi}}\left(i\gamma_\mu\partial^\mu - M\right)\mathbf{\Psi} \tag{9}$$

$$\begin{aligned}\mathcal{L}_M &= \frac{1}{2}\sum_{i=\sigma,\delta}\left(\partial_\mu\Phi_i\partial^\mu\Phi_i - m_i^2\Phi_i^2\right) \\ &\quad -\frac{1}{2}\sum_{j=\omega,\rho,\gamma}\left(\frac{1}{2}F^{(j)}_{\mu\nu}F^{(j)\mu\nu} - m_j^2A^{(j)}_\mu A^{(j)\mu}\right)\end{aligned} \tag{10}$$

$$\begin{aligned}\mathcal{L}_{int} &= \bar{\mathbf{\Psi}}\Gamma_\sigma(\bar{\mathbf{\Psi}},\mathbf{\Psi})\mathbf{\Psi}\Phi_\sigma + \bar{\mathbf{\Psi}}\Gamma_\delta(\bar{\mathbf{\Psi}},\mathbf{\Psi})\boldsymbol{\tau}\mathbf{\Psi}\mathbf{\Phi}_\delta \\ &\quad -\bar{\mathbf{\Psi}}\Gamma_\omega(\bar{\mathbf{\Psi}},\mathbf{\Psi})\gamma_\mu\mathbf{\Psi}A^{(\omega)\mu} - \bar{\mathbf{\Psi}}\Gamma_\rho(\bar{\mathbf{\Psi}},\mathbf{\Psi})\gamma_\mu\tau\mathbf{\Psi}\mathbf{A}^{(\rho)\mu} \\ &\quad -e\bar{\mathbf{\Psi}}\hat{Q}\gamma_\mu\mathbf{\Psi}A^{(\gamma)\mu}\end{aligned} \tag{11}$$

where $M$ is the nucleon mass (commonly taken as 939 MeV), the field strength tensor for the vector fields is,

$$F^{(j)}_{\mu\nu} = \partial_\mu A^{(j)}_\nu - \partial_\nu A^{(j)}_\mu, \tag{12}$$

$\hat{Q} = (1-\tau_3)/2$ is the electric charge operator ($\tau_3$ is the third component of the Pauli matrices $\boldsymbol{\tau}$) and $e$ the electromagnetic coupling constant. The meson-nucleon vertices are denoted by $\Gamma_k$ for $k = \sigma$, $\omega$, $\rho$ and $\delta$. They will depend generally on the nucleon field $\mathbf{\Psi}$ but, since covariance is required, the dependence should reduce to a scalar operator of the form $\hat{\rho}(\bar{\mathbf{\Psi}},\mathbf{\Psi})$. At this point, one should take a prescription for the specific expression of this Lorentz-invariant operator. The prescription $\hat{\rho}^2 = \hat{j_\mu}\hat{j^\mu}$ —where $\hat{j_\mu} = \bar{\mathbf{\Psi}}\gamma_\mu\mathbf{\Psi} = \hat{\rho}\hat{u}_\mu$ is the nucleon vector current and $\hat{u}_\mu$ a four velocity ($\hat{u}_\mu\hat{u}^\mu = \mathbf{1}$)— has been chosen since its expectation value at the ground state is just the nucleon density $\rho$. Hence, the connections with other theories will be more natural.

Next, the variational derivatives of $\mathcal{L}$ respect to $\bar{\mathbf{\Psi}}$ should be performed in order to calculate the mesonic equations of motion and the Dirac equation for the nucleons,

$$\begin{aligned}\delta S &= 0 \\ &= \int dx^4\left(\frac{\delta\mathcal{L}}{\delta\bar{\mathbf{\Psi}}}\right) \\ &= -\partial_\mu\left(\frac{\partial\mathcal{L}_{_N}}{\partial(\partial_\mu\bar{\mathbf{\Psi}})}\right) + \frac{\partial\mathcal{L}_n}{\partial\bar{\mathbf{\Psi}}} + \frac{\partial\mathcal{L}_{int}}{\partial\bar{\mathbf{\Psi}}} + \frac{\partial\mathcal{L}_{int}}{\partial\hat{\rho}}\frac{\partial\hat{\rho}}{\partial\bar{\mathbf{\Psi}}}\end{aligned} \tag{13}$$

where the latter term is,

$$\frac{\partial\hat{\rho}}{\partial\bar{\mathbf{\Psi}}} = \gamma_\mu\Psi u^\mu \tag{14}$$

The equation of motion for the nucleons,

$$\left[\gamma_\mu(i\partial^\mu - \hat{\Sigma}^\mu) - M^*\right]\mathbf{\Psi} = 0 \tag{15}$$

where $M^* \equiv M - \hat{\Sigma}^s$ is the effective Dirac nucleon mass and $\hat{\Sigma}^\mu$ and $\hat{\Sigma}^s$ are the vector and scalar self-energies defined as follows,

$$\hat{\Sigma}^s \equiv \Gamma_\sigma(\hat{\rho})\Phi_\sigma + \Gamma_\delta(\hat{\rho})\boldsymbol{\tau}\boldsymbol{\Phi}_\delta \tag{16}$$

$$\hat{\Sigma}^\mu \equiv \hat{\Sigma}^{\mu(0)} + \hat{\Sigma}^{\mu(r)} \tag{17}$$

here, (0) indicates the usual definition of the vector self-energy and $(r)$ the rearrangement vector self-energy,

$$\hat{\Sigma}^{\mu(0)} \equiv \Gamma_\omega(\hat{\rho})A^{(\omega)\mu} + \Gamma_\rho(\hat{\rho})\mathbf{A}^{(\rho)\mu} + e\hat{Q}A^{(\gamma)\mu} \tag{18}$$

$$\hat{\Sigma}^{\mu(r)} \equiv -\frac{\partial\Gamma_\sigma(\hat{\rho})}{\partial\hat{\rho}}\Phi_\sigma\bar{\boldsymbol{\Psi}}\boldsymbol{\Psi} + \frac{\partial\Gamma_\omega(\hat{\rho})}{\partial\hat{\rho}}A^{(\omega)\mu}\bar{\boldsymbol{\Psi}}\gamma_\mu\boldsymbol{\Psi} - \frac{\partial\Gamma_\delta(\hat{\rho})}{\partial\hat{\rho}}\boldsymbol{\Phi}_\delta\bar{\boldsymbol{\Psi}}\boldsymbol{\tau}\boldsymbol{\Psi} + \frac{\partial\Gamma_\rho(\hat{\rho})}{\partial\hat{\rho}}\mathbf{A}^{(\rho)\mu}\bar{\boldsymbol{\Psi}}\gamma_\mu\boldsymbol{\tau}\boldsymbol{\Psi} \tag{19}$$

The rearrangement term is a contribution to the vector self-energy typical of the DDRHF models which is due to the density dependence of the meson-nucleon vertices. The equations of motion for the mesons are,

$$\left(\partial^\mu\partial_\mu + m_\sigma^2\right)\Phi_\sigma = \Gamma_\sigma(\hat{\rho})\bar{\boldsymbol{\Psi}}\boldsymbol{\Psi} \tag{20}$$

$$\partial_\mu F^{(\omega)\mu\nu} + m_\omega^2 A^{(\omega)\nu} = \Gamma_\omega(\hat{\rho})\bar{\boldsymbol{\Psi}}\gamma^\nu\boldsymbol{\Psi} \tag{21}$$

$$\left(\partial^\mu\partial_\mu + m_\delta^2\right)\boldsymbol{\Phi}_\delta = \Gamma_\delta(\hat{\rho})\bar{\boldsymbol{\Psi}}\boldsymbol{\tau}\boldsymbol{\Psi} \tag{22}$$

$$\partial_\mu\mathbf{F}^{(\rho)\mu\nu} + m_\rho^2\mathbf{A}^{(\rho)\nu} = \Gamma_\omega(\hat{\rho})\bar{\boldsymbol{\Psi}}\gamma^\nu\boldsymbol{\tau}\boldsymbol{\Psi} \tag{23}$$

$$\partial_\mu F^{(\gamma)\mu\nu} = e\bar{\boldsymbol{\Psi}}\left(\frac{1-\tau_3}{2}\right)\gamma^\nu\boldsymbol{\Psi} \tag{24}$$

### 5.2.2 Mean-Field equations

The Hartree mean-field equations are obtained by taking the ground-state expectation value on both sides of the meson field equations of motion (Equations 20-24), then calculating the mean-field self energies and finally introducing them in the Dirac Equation (15). Using Wick's theorem ($\hat{\rho} = \rho + C(\hat{\rho})$ with $\langle 0|C|0\rangle = 0$) one can see by expanding the meson-nucleon vertices in a Taylor series that,

$$\Gamma(\hat{\rho}) = \Gamma(\rho) + C(\hat{\rho})\partial_\rho\Gamma(\rho) + ... \quad \rightarrow \quad \langle 0|\Gamma(\hat{\rho})|0\rangle = \Gamma(\rho) \tag{25}$$

Next, one assumes that the meson fields can be decomposed in a stationary part and a time dependent and fluctuating part of vanishing ground state expectation value,

$$\Phi_i(\mathbf{r},t) \rightarrow \Phi_i(\mathbf{r}) + \delta\Phi_i(\mathbf{r},t) \qquad i = \sigma,\delta \tag{26}$$

$$A^{(j)\mu}(\mathbf{r},t) \rightarrow A^{(j)\mu}(\mathbf{r}) + \delta A^{(j)\mu}(\mathbf{r},t) \qquad j = \omega,\rho,\gamma \tag{27}$$

and therefore,

$$\langle 0|\Phi_i(\mathbf{r},t)|0\rangle \rightarrow \Phi_i(\mathbf{r}) \qquad i = \sigma,\delta \tag{28}$$

$$\langle 0|A^{(j)\mu}(\mathbf{r},t)|0\rangle \rightarrow A^{(j)\mu}(\mathbf{r}) \qquad j = \omega,\rho,\gamma \tag{29}$$

Finally, the assumption of time reversal symmetry implies that the space-like parts of the vector potentials vanish, so $A^{(j)\mu}(\mathbf{r}) \to A^{(j)0}(\mathbf{r})$. Hereinafter $\Phi_i$ and $A^{(j)0}$ will denote the static classical meson fields. Then, the mean-field equations to be solved read,

$$\left(-\partial^i\partial_i + m_\sigma^2\right)\Phi_\sigma = \Gamma_\sigma(\rho)\rho^s \tag{30}$$

$$\left(-\partial^i\partial_i + m_\omega^2\right)A^{(\omega)0} = \Gamma_\omega(\rho)\rho \tag{31}$$

$$\left(-\partial^i\partial_i + m_\delta^2\right)\Phi_\delta = \Gamma_\delta(\rho)\rho_3^s \tag{32}$$

$$\left(-\partial^i\partial_i + m_\rho^2\right)A^{(\rho)0} = \Gamma_\omega(\rho)\rho_3 \tag{33}$$

$$-\partial^i\partial_i A^{(\gamma)0} = e\rho_p \tag{34}$$

where the ground-state expectation value of the different densities are defined as,

$$\rho^s \equiv \langle 0|\bar{\mathbf{\Psi}}\mathbf{\Psi}|0\rangle = \rho_n^s + \rho_p^s \tag{35}$$

$$\rho \equiv \langle 0|\bar{\mathbf{\Psi}}\gamma_0\mathbf{\Psi}|0\rangle = \rho_n + \rho_p \tag{36}$$

$$\rho_3^s \equiv \langle 0|\bar{\mathbf{\Psi}}\tau_3\mathbf{\Psi}|0\rangle = \rho_n^s - \rho_p^s \tag{37}$$

$$\rho_3 \equiv \langle 0|\bar{\mathbf{\Psi}}\gamma_0\tau_3\mathbf{\Psi}|0\rangle = \rho_n - \rho_p \tag{38}$$

using the subindex $n$ or $p$ to indicate whether we are considering neutrons or protons respectively. The Dirac equation for the nucleons becomes,

$$\left[\gamma_\mu(i\partial^\mu - \Sigma_{_N}^\mu) - (M - \Sigma_{_N}^s)\right]\psi_{_N} = 0 \qquad N = n, p \tag{39}$$

where the effective mass, in terms of protons and neutrons, is defined as $M_{_N}^* \equiv M - \Sigma_{_N}^s$ where $N = n, p$. Finally, the non-zero contributions to the density dependent mean-field self-energies are,

$$\Sigma_{_N}^s(\rho) = \Gamma_\sigma(\rho)\Phi_\sigma + \tau_{_N}\Gamma_\delta(\rho)\Phi_\delta \tag{40}$$

$$\Sigma_{_N}^{0(0)}(\rho) = \Gamma_\omega(\rho)A^{(\omega)0} + \tau_{_N}\Gamma_\rho(\rho)A^{(\rho)0} + e\frac{1-\tau_{_N}}{2}A^{(\gamma)0} \tag{41}$$

$$\Sigma^{0(r)}(\rho) = -\frac{\partial\Gamma_\sigma(\rho)}{\partial\rho}\Phi_\sigma\rho^s + \frac{\partial\Gamma_\omega(\rho)}{\partial\rho}A^{(\omega)0}\rho - \frac{\partial\Gamma_\delta(\rho)}{\partial\rho}\Phi_\delta\rho_3^s + \frac{\partial\Gamma_\rho(\rho)}{\partial\rho}A^{(\rho)0}\rho_3 \tag{42}$$

where $\tau_n = +1$ for neutrons and $\tau_p = -1$ for protons.

### 5.2.3 Infinite asymmetric nuclear matter

In the infinite nuclear matter system under the relativistic Hartree description, all the equations of motion simplify since translational invariance should be fulfilled and because the electromagnetic field is neglected. The solutions of the Dirac equations for protons and neutrons are the usual plane-wave Dirac spinors [Bj65]. The infinite matter reduction of the meson field equations of motion are,

$$\Phi_\sigma = \frac{\Gamma_\sigma(\rho)}{m_\sigma^2}\rho^s \tag{43}$$

$$A^{(\omega)0} = \frac{\Gamma_\omega(\rho)}{m_\omega^2}\rho \tag{44}$$

$$\Phi_\delta = \frac{\Gamma_\delta(\rho)}{m_\delta^2}\rho_3^s \tag{45}$$

$$A^{(\rho)0} = \frac{\Gamma_\rho(\rho)}{m_\rho^2}\rho_3 \tag{46}$$

and the nucleon and scalar densities can be computed as follows,

$$\rho_{_N} = \frac{2}{(2\pi)^3}\int_{|k|<k_{F_n}} d^3k = \frac{{k_{F_n}}^3}{3\pi^2} \tag{47}$$

$$\begin{aligned}\rho_{_N}^s &= \frac{2}{(2\pi)^3}\int_{|k|<k_{F_n}} \frac{M_{_N}^*}{E_{_N}} d^3k \\ &= \frac{M_{_N}^*}{2\pi^2}\left[k_{F_n}E_{F_n} - {M_{_N}^*}^2 \ln\left(\frac{k_{F_n}+E_{F_n}}{M_{_N}^*}\right)\right]\end{aligned} \tag{48}$$

where the Fermi energy of a proton or a neutron is $E_{F_{_N}} = \sqrt{{\mathbf{k}_{F_{_N}}}^2 + {M_{_N}^*}^2}$. Now, we calculate the energy density ($e$) and pressure ($p$) from the energy-momentum tensor,

$$T^{\mu\nu} = \sum_i \frac{\partial\mathcal{L}}{\partial(\partial_i\phi_i)}\partial^\nu\phi_i - g^{\mu\nu}\mathcal{L} \tag{49}$$

where $\phi_i$ runs for all possible fields,

$$\begin{aligned}e = \langle 0|T^{00}|0\rangle &= \frac{1}{4}\left[3E_{F_n}\rho_n + M_n^*\rho_n^s\right] + \frac{1}{4}\left[3E_{F_p}\rho_n + M_p^*\rho_p^s\right] \\ &\quad + \frac{1}{4}\left[m_\sigma^2{\Phi_\sigma}^2 + m_\omega^2{A^{(\omega)0}}^2 + m_\delta^2{\Phi_\delta}^2 + m_\rho^2{A^{(\rho)0}}^2\right]\end{aligned} \tag{50}$$

$$\begin{aligned}p = \frac{1}{3}\sum_{i=1}^{3}\langle 0|T^{ii}|0\rangle &= \frac{1}{4}\left[E_{F_n}\rho_n - M_n^*\rho_n^s\right]\frac{1}{4}\left[E_{F_p}\rho_p - M_p^*\rho_p^s\right] \\ &\quad - \frac{1}{2}\left[m_\sigma^2{\Phi_\sigma}^2 - m_\omega^2{A^{(\omega)0}}^2 + m_\delta^2{\Phi_\delta}^2 - m_\rho^2{A^{(\rho)0}}^2\right] \\ &\quad + (\rho_n+\rho_p)\,\Sigma^{(r)0}\end{aligned} \tag{51}$$

From the last expressions we can see that the energy density is not affected by rearrangement terms, *i.e.* derivatives of the nucleon-meson vertices do not appear explicitely in the energy density. On the contrary, the pressure receives a contribution from the zero-component of the vector (rearrangement) self-energy. We have checked that the pressure as calculated through the energy-momentum tensor coincides with the thermodynamical definition: $p = \rho^2[\partial(e/\rho)/\partial\rho]$ and that the energy-momentum tensor is conserved $\partial_\mu T^{\mu\nu} = 0$.

### 5.2.4 Density dependence of the meson-nucleon vertices

Here we would like to describe the specific density dependence of the meson-nucleon vertices we have chosen for the novel interaction DDME$\delta$. As we have pointed out, our goal is to go a step further in the process of building a universal energy density functional in

the relativistic frame. To this end, we recall that we want to describe the nuclear dynamics at the mean-field level trying to reproduce fully microscopical calculations and keep, if not improve, the accuracy of mean-field models in describing finite nuclei properties.

Basically, one can use two strategies to select a good ansatz. From a phenomenological point of view, (a) one could check with different parametrizations and select the one which best reproduces the data used in the fit. Notice that this strategy does not ensure density powers compatible with first-principle calculations. And, from a more fundamental point of view, (b) one could set the mean-field self-energies equal to the Dirac-Brueckner (DB) ones in infinite nuclear matter and find a compatible parametrization of the density dependence of the meson-nucleon vertices. This is possible since the scalar and vector self-energies obtained from DB calculations can be related to the meson-nucleon vertices of the DDRHF theory [Jo98]. As we would like to reproduce first-principle calculations with the DDME$\delta$ interaction, the natural choice would be the strategy (b) but it has some negative aspects. Generally, the mean-field mapping to Dirac-Brueckner meson-nucleon vertices assumes that the self-energies are not momentum dependent and set the momentum value at the Fermi surface. As a result of this mapping, the mean-field EoS is not able to reproduce the fully microscopic EoS and a momentum correction of the different meson-nucleon vertices is required. This correction can be estimated theoretically but it is more accurate if corrected by a fit. Furthermore, we also would like to keep low the number of free parameters in our model to ensure a high predictability power and, in this respect, the density dependence of the meson-nucleon vertices suggested by DB calculations have a larger number of parameters than typical relativistic mean-field models. All these facts, convinced us that a mixed strategy between (a) and (b) was the more convenient one. In this way, we follow (as in the DDME model) closely what was done in Reference [Ty99] and extend the method to include the delta meson.

In the semi-phenomenological approach adopted in the above mentioned work, the density dependence of the $\sigma$ and $\omega$ couplings is extracted from first-principle calculations,

$$\Gamma_i(\rho) = g_i(\rho_0) f_i(x) \quad \text{for} \quad i = \sigma, \omega \tag{52}$$

where $\rho_0$ is the symmetric nuclear saturation density and $f_i(x = \rho/\rho_0)$ correspond to the ansatz for the meson-nucleon vertices,

$$f_i(x) = a_i \frac{1 + b_i(x + d_i)^2}{1 + c_i(x + d_i)^2} \tag{53}$$

apart from $a_i$, all parameters appearing in the latter expression are in principle free. By definition of $\Gamma_i(\rho)$, $a_i$ is constrained since $\Gamma_i(\rho_0) = g_i(\rho_0)$ should be fulfilled. Then, further constraints to keep the number of parameters small are taken: $f_\sigma''(x = 1) = f_\omega''(x = 1)$ and $f_i''(x = 0) = 0$. The latter condition ensures that the rearrangement terms do not diverge at zero density. With all these constraints, the free parameters to be adjusted for the $\sigma$- and $\omega$-ansatzs are reduced from eight to three ($b_\sigma$, $c_\sigma$ and $c_\omega$). Finally, since the behavior in density of such couplings as predicted by DB calculations is quite similar (see

*e.g.* Figure 1 of Reference [Ho01]) we also added a sixth constraint, $c_\sigma = c_\omega$. In the case of the $\delta$- and $\rho$-nucleon vertices, DB calculations also suggest a density dependence like (53) but for simplicity, the ansatz chosen for the $\rho$-nucleon vertex is,

$$\Gamma_\rho(\rho) = g_\rho(\rho_0) e^{-a_\rho(x-1)} \tag{54}$$

where the exponential dependency is showed qualitatively by DB calculations (see *e.g.* upper panel in Figure 2 of Reference [Ho01]) since it was seen that the strength of the $\rho$-nucleon coupling becomes very small at high densities. Finally, the density dependence for the $\delta$-nucleon vertex is fixed to reproduce the mass splitting between protons and neutrons in pure neutron matter as predicted by the DB calculations of Reference [Da07] and, therefore, it does not enter directly in the minimization procedure. Hence, based also on qualitative suggestions of first-principle calculations and with the aim of keeping the number of free parameters low, we found that the simplest ansatz able to reproduce the above mentioned proton-neutron effective mass splitting is,

$$\Gamma_\delta(\rho) = g_\rho(\rho_0) \left[ e^{-a_\delta(x-1)} + b_\delta(x-1) \right] \tag{55}$$

In Figure 12 we depict two different parametrizations for this ansatz in order to reproduce the data of Reference [Da07]. The first fit sets the parameter $b_\delta$ to zero and the second one releases it. As it can be seen from this figure, we found that at least two parameters characterizing the density dependence of the $\delta$ vertex were needed to reproduce the above mentioned data.

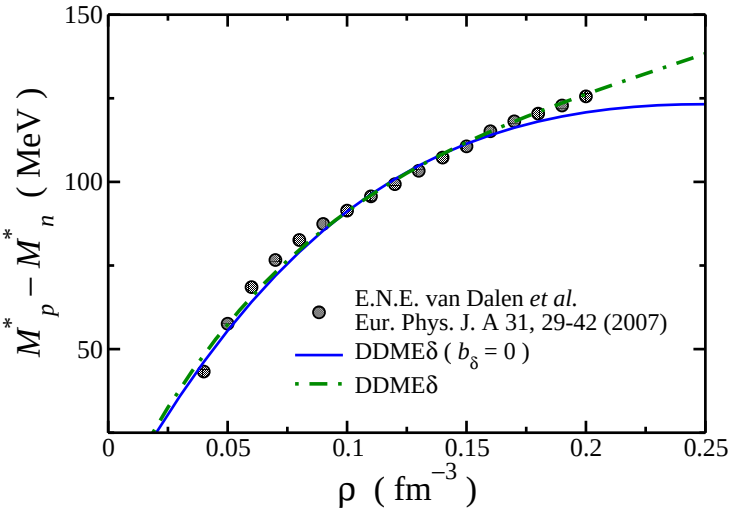


Figure 12: Proton-neutron effective mass splitting as a function of the nucleon density. The value of the different parameters are displayed in Table 4.

## 5.3 Fitting procedure: $\chi^2$ definition and results

The fit has been performed through a "modified" $\chi^2$ test. We have defined the individual $\chi^2$ of each magnitude $\mathcal{O}$ as follows,

$$\chi^2 = \frac{1}{n_{\rm data}} \sum_{i=1}^{n_{\rm data}} w_i^2 \left( \mathcal{O}_i^{\rm model} - \mathcal{O}_i^{\rm ref} \right)^2 \tag{56}$$

where $n_{\rm data}$ is the number of data points and $w_i$ the weights associated to each $\mathcal{O}_i^{\rm ref}$. The nuclear observables used for the fit are the mass and charge radius of $^{16}$O, $^{40}$Ca, $^{48}$Ca, $^{72}$Ni, $^{90}$Zr, $^{116}$Sn, $^{124}$Sn, $^{132}$Sn, $^{204}$Pb, $^{208}$Pb, $^{210}$Po and $^{214}$Pb. In the standard definition of a $\chi^2$ test, the weights $w_i$ should be inversely proportional to the experimental errors. But, as DDME$\delta$ is a mean-field model which is supposed to be more accurate as heavier is the nucleus, we have preferred to account for this fact and have used instead a constant weight. In doing this, we favor —through the $\chi^2$ definition— a smaller relative error of the model in the fitted masses and charge radii as heavier is the nucleus.

On the other side, the first-principle calculations introduced in the $\chi^2$ test are the EoS of symmetric and pure neutron nuclear matter of Reference [Ba04]. In this calculations, there is no associated error and, thus, we have introduced a relative error-like magnitude to equaly-weight the symmetric and pure neutron EoS at each density. The specific weights for each magnitude are listed in Table 3 indicating the inverse of its value (error-like magnitude associated to each property) and the number of data points involved in each magnitude. In the particular case of the EoS calculation, it is also indicated the density range included in the fitting procedure. The total $\chi^2$ is, thus,

$$\chi^2_{\rm tot} = \chi^2_m + \chi^2_{r_{\rm ch}} + \chi^2_{\rm sym.} + \chi^2_{\rm neut.} \tag{57}$$

We made the minimization of the $\chi^2_{\rm tot}$ by means of a variable metric method included in the MINUIT package [Mi96]. We note that during the fitting procedure, at each step of the minimization, we re-fix the $\delta$-meson parameters to reproduce the proton-neutron effective mass splitting. This is because of the fact that the mean-field equations are solved self-consistently and, therefore, the $\delta$-nucleon parametrization of the vertex affect the value of the $\sigma$, $\omega$ and $\rho$ fields during the fit of the latter. Specifically, although the proton-neutron mass splitting is not directly related with the $\omega$- and $\rho$-meson fields,

$$M_p^* - M_n^* = 2 \left( \frac{\Gamma_\delta(\rho)}{m_\delta} \right)^2 (\rho_n^s - \rho_p^s) \tag{58}$$

where $\rho_{_N}^s = \rho_{_N}^s[M_{_N}^*(\Gamma_\sigma, \Gamma_\delta), \rho_{_N}]$, one can see that it is related through the scalar density with the $\sigma$ meson coupling and that, due to the self-consistency, to the $\omega$ and $\rho$ couplings. This feature turns out to be quite useful since fixing the $\delta$ meson-nucleon vertex parameters reduces the $\rho$ free-parameter space and, as a consequence, the strength of the $\rho$ meson field (namely $g_\rho(\rho_0)$) is noticeably constrained in the fit. In order to check this constraint on the $\rho$-meson, one can calculate the correlation coefficient ($\mathcal{C}_{ij}$) between $g_\delta(\rho_0)$ and

$g_\rho(\rho_0)$ parameters which account for the strength of the $\rho$-nucleon and $\delta$-nucleon vertices as follows,

$$\mathcal{C}_{ij} = \frac{M_{ij}}{\sqrt{M_{ii}M_{jj}}} \quad \text{where} \quad M_{ij}^{-1} \equiv \frac{\partial^2 \chi^2_{\rm tot}}{\partial g_i \partial g_j} \tag{59}$$

where $M_{ij}$ defines the error matrix and, therefore, the error associated to the $i$-th parameter is $e_i = \sqrt{M_{ii}}$. A correlation coeficient $\mathcal{C}_{ij} = 1$ means that the parameters $g_i$ and $g_j$ are completely correlated and $\mathcal{C}_{ij} = 0$ that no correlation holds at all. In orther to perform that calculation, we have taken the DDME$\delta$ parameter set (after the fit) allowing these two parameters to change slightly from the minimum and calculate numerically how depends the $\chi^2$ on such a changes. This have given us an estimation of the correlation coefficient between them. Specifically, we have found,

$$\mathcal{C}_{ii} = 1 \quad \text{and} \quad \mathcal{C}_{g_\rho g_\delta} = \mathcal{C}_{g_\delta g_\rho} \approx 0.9 \tag{60}$$

From this estimation, one can see that the strong correlation noticed during the fitting procedure between $g_\delta(\rho_0)$ and $g_\rho(\rho_0)$ is confirmed by its correlation coefficient. Hence, a reduction of the possible values that $g_\rho(\rho_0)$ can take is tightly constrained if $g_\delta(\rho_0)$ is fixed (as in the case of our fit).

Our strategy allows us to keep the number of free parameters unaltered by adding the $\delta$ meson to our treatment. It is also worth to remember that adding the $\delta$-meson has improved our theoretical picture of the bulk properties of the nucleus, in particluar, on the EoS of asymmetric nuclear matter. The $\chi^2_{\rm tot}$ for DDME$\delta$ is almost 50, the partial

| $\mathcal{O}$ | $w_i = 1/e_i$ | $n_{\rm data}$ | $\rho_{\rm min.} \rightarrow \rho_{\rm max.}$ (fm$^{-3}$) | $\chi^2$ | Reference |
|---|---|---|---|---|---|
| Mass | 1/0.50 MeV$^{-1}$ | 12 | | 8.61 | [Au03] |
| Charge radii | 1/0.01 fm$^{-1}$ | 10 | | 6.51 | [An04] |
| Neutron EoS | $1/(0.01 \times \mathcal{O}_i)$ | 30 | $0.01 \rightarrow 0.30$ | 8.70 | [Ba04]$^\dagger$ |
| Symmetric EoS | $1/(0.03 \times \mathcal{O}_i)$ | 30 | $0.01 \rightarrow 0.30$ | 26.0 | [Ba04]$^\dagger$ |
| $M_p^* - M_n^*$ | $1/(0.03 \times \mathcal{O}_i)$ | 25 | $0.05 \rightarrow 0.25$ | 1.00 | [Da07] |

Table 3: Specifications of the $\chi^2$ definition used to obtain DDME$\delta$.$^\dagger$ where some points have been interpolated form the original calculations of that reference in order to perform the fit.

contributions to it are listed in Table 3 and the parameter set in Table 4 where the free (bold faced) and constrained parameters (normal) are indicated. The results for some properties of the infinite system at saturation are shown in Table 5 and the results for the finite nuclei included in the fit can be found in Table 6 where the self-consistent results for masses include a microscopic estimate for the center of mass correction substracted from the total binding energy,

$$E_{\rm cm} = -\frac{\langle P^2_{\rm cm} \rangle}{2MA} \tag{61}$$

where $P_{\rm cm}$ is the total momentum of a nucleus with A nucleons. Regarding the charge radius, it is calculated as follows,

$$R_{\rm ch} = \sqrt{\langle r_p^2 \rangle + 0.8^2} \tag{62}$$

Moreover, all calculations of open shell nuclei in the fit account for the pairing correlations treated in the BCS approach [Va73] fixing the pairing gap to the experiment (three-point formula [Be00]).

| meson | $m$ (MeV) | $g(\rho_0)$ | $a$ | $b$ | $c$ | $d$ |
|---|---|---|---|---|---|---|
| $\sigma$ | **563.3526** | **10.2248** | 1.3257 | **0.3170** | **0.5208** | 0.8000 |
| $\omega$ | 783.0000 | **12.2047** | 1.3257 | 0.3170 | 0.5208 | 0.8000 |
| $\delta$ | 983.0000 | 7.1657 | 0.4866 | 0.2756 | | |
| $\rho$ | **799.0793** | **6.5802** | **0.4094** | | | |

Table 4: Parameters of the relativistic mean-field effective interaction DDME$\delta$. The free parameters entering in the minimization procedure are in bold face. For further details see the text.

| Property | $\rho_0$ (fm$^{-3}$) | $e_0$ (MeV) | $K_0$ (MeV) | $J$ (MeV) | $L$ (MeV) | $M_N^*$ (MeV) |
|---|---|---|---|---|---|---|
| Value | 0.153 | -16.22 | 251.1 | 31.82 | 48.72 | 575.65 |

Table 5: Nuclear saturation properties as predicted by DDME$\delta$

Finally, we also present graphically (Figures 13, 14, and 15) the results obtained with the new effective interaction DDME$\delta$ as compared with fitted properties and with DDME$\delta(b_\delta = 0)$ (shown in Figure 12 in the case of the proton-neutron mass splitting), BCP1 [Ba08] and DDME2 [La05]. We include here the information about the analogous fit DDME$\delta(b_\delta = 0)$ which sets the parameter $b_\delta = 0$ to show the effects that different ansatz of $\delta$ meson-nucleon vertex have in the EoS and in the fitted finite nuclear properties. The comparison with DDME2 is motivated by the fact that, as DDME$\delta$, it is based on the DDRHF albeit it does not include the $\delta$ meson. And, finally, the comparison between DDME$\delta$ and BCP1 is quite interesting since, by construction of both functionals, they share almost the same EoS up to $\rho \approx 0.25$ fm$^{-3}$. In Figure 13 one can see graphically the accuracy achieved by the new interaction DDME$\delta$ in the fit of the microscopic calculations of Baldo and collaborators [Ba04]. From that figure one can conclude that, at least along the density-range considered here, DDME-like models are quite compatible with first-principle calculations. There are no doubts about that since DDME2 was only fitted to some selected nuclear observables and to well stablished properties of the infinite nuclear matter at saturation. Therefore,the DDME2 interaction does not include any

| Element | $A$ | $B^{\mathrm{DDME}\delta}$ | $B^{\mathrm{exp.}}$ | $R_{\mathrm{ch}}^{\mathrm{DDME}\delta}$ | $R_{\mathrm{ch}}^{\mathrm{exp.}}$ |
|---|---|---|---|---|---|
| O | 16 | 129.00 | 127.62 | 2.69 | 2.70 |
| Ca | 40 | 343.85 | 342.05 | 3.42 | 3.48 |
| Ca | 48 | 415.31 | 415.99 | 3.46 | 3.48 |
| Ni | 72 | 612.57 | 613.15 | 3.89 | |
| Zr | 90 | 783.12 | 783.89 | 4.25 | 4.27 |
| Sn | 116 | 986.12 | 988.68 | 4.59 | 4.63 |
| Sn | 124 | 1048.16 | 1049.96 | 4.64 | 4.68 |
| Sn | 132 | 1103.66 | 1102.85 | 4.69 | |
| Pb | 204 | 1606.64 | 1607.51 | 5.47 | 5.48 |
| Pb | 208 | 1637.19 | 1636.43 | 5.48 | 5.50 |
| Pb | 214 | 1662.78 | 1663.29 | 5.54 | 5.56 |
| Po | 210 | 1648.00 | 1645.21 | 5.52 | 5.53 |

Table 6: DDME$\delta$ results for the binding energies and charge radii used in the fit

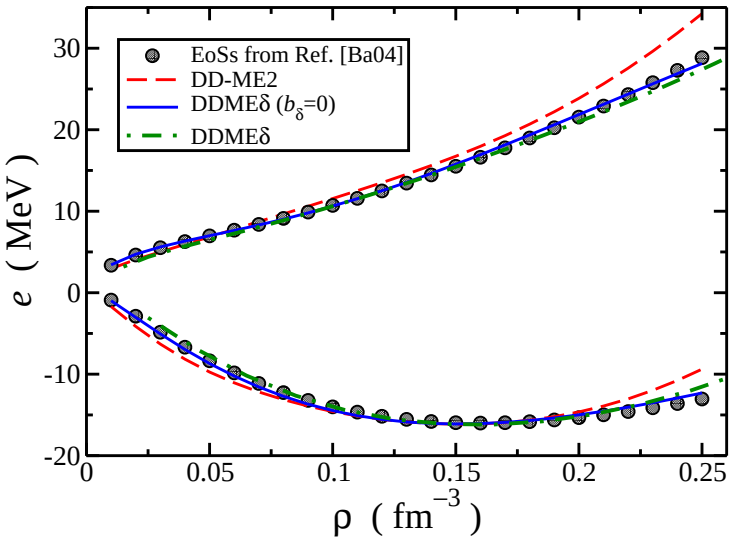


Figure 13: DDME$\delta$ symmetric and pure neutron matter EoS as a function of the nucelon density along the fitted. Results are compared with DDME$\delta$($b_\delta = 0$) and DDME2 [La05].

information on first-principle calculations in the fitting procedure and, then, ignores the density dependence of the EoS of symmetric and pure neutron matter as predicted by more fundamental calculations. Nevertheless, it is important to notice that the ansatz for the density dependence of the nucleon-meson vertices in both, DD-ME2 and DDME$\delta$ interactions, are suggested by DB calculations. This fact may partially justify the accuracy showed by DD-ME2 in describing the EoS of Reference [Ba04]. Hence, keeping the same type of ansatzs in DDME$\delta$ and performing a fit including the calculations of Ref-

erence [Ba04] lead us to a very good agreement with the above mentioned microscopical calculations. Regarding the fitted binding energies, we present in Figure 14 a comparison

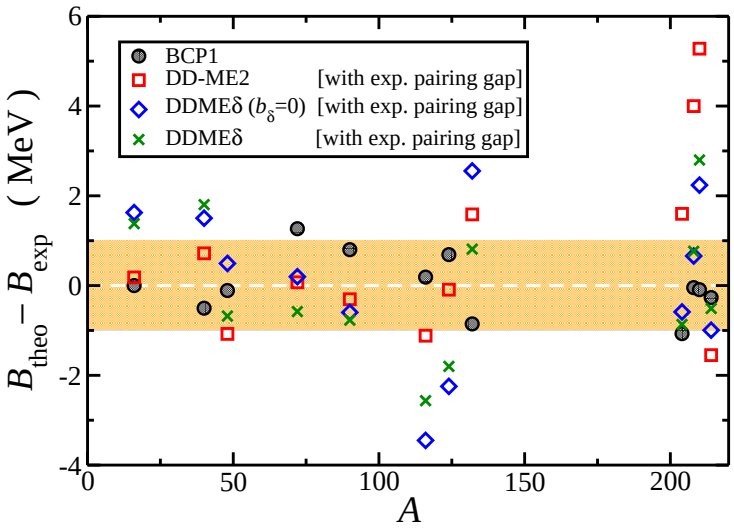


Figure 14: Difference between theoretical and experimental binding energies as a function of the mass number. DDME$\delta$ results as compared with DDME$\delta(b_\delta = 0)$, DDME2 [La05] and BCP1 [Ba08]. The orange region correspond to twice the fixed weight used in the fit (see Table 3).

between the above mentioned nuclear interactions. As it has been indicated, the pairing correlations are calculated in the BCS approach in the constant gap approach deduced from experimental masses [Va73]. The important features to be fulfilled by a nuclear model is that of showing small deviations from zero and in the case of mean-field models to be more accurate as heavier is the nucleus. BCP1 seems to account for both properties better than DDME-like interactions where all of them, although accurate, get a bit worse for heavier nuclei. We present in Figure 15 the same type of plot but for the results of the fitted charge radii. In this case, DDME-like models display smaller deviations from experiment than BCP1. Generally, DDME$\delta$ does not improve the accuracy achieved by DDME2 or BCP1 for finite nuclei but is worth to say that its precision in describing these particular finite nuclear properties is comparable to the former models. We will see in the next section if this conclusion extends further in DDME$\delta$ predictions.

## 5.4 Applications

In this section, we present various predictions obtained with the DDME$\delta$ functional. Specifically, we calculate the charge radii and binding energies of nuclei known to be spherical (our code does not include deformations at present). DDME$\delta$ achieves essentially the same accuracy as other models based on the same theoretical grounds such as DDME2 [La05]. For the present calculations, we have changed the prescription for the

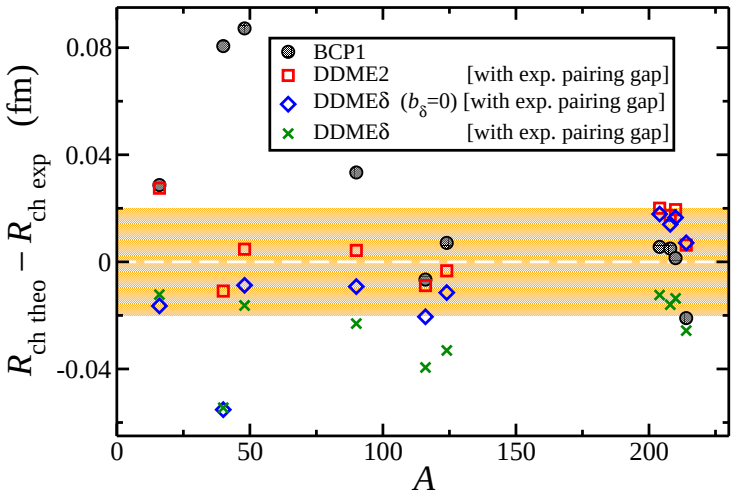


Figure 15: Difference between theoretical and experimental charge radii as a function of the mass number. DDME$\delta$ results as compared with DDME$\delta$($b_\delta = 0$), DDME2 [La05] and BCP1 [Ba08]. The orange region correspond to twice the fixed weight used in the fit (see Table 3).

pairing calculations. Within the BCS approach, for simplicity, we compute this time the pairing correlations assuming a constant pairing strenght [Es01]. The results obtained with DDME$\delta$ interaction for the binding energies of the 161 measured nuclei with spherical shape reach a good level of accuracy. Indeed, the root mean square deviation,

$$\sigma_{\rm rms} = \sqrt{\frac{1}{n}\sum_i^n \left(\mathcal{O}_i^{\rm theo} - \mathcal{O}_i^{\rm exp}\right)^2} \tag{63}$$

is $\sigma_{\rm rms} = 2.9$ MeV. It is a bit larger than in DDME2 ($\sigma_{\rm rms} = 2.1$ MeV) or BCP1 ($\sigma_{\rm rms} = 1.8$ MeV) models but still within the same level of accuracy. Looking at Figure 16, no particular trends can be disentangled in any case apart from the typical oscillations due to a non-perfect description of the shell structure. Probably, a more sophisticated approach for the pairing correlations will improve the results but, in any case, it will be a correction smaller than $\approx 12/\sqrt{A}$ MeV which is a good estimate of the average pairing energy.

In the case of Figure 17 where predictions for the charge radius of 86 measured nuclei having spherical shape are depicted for the same interactions, similar conclusions can be drawn. The accuracy in describing the charge radii of all those models is quite similar although here, different patterns can be seen. In the case of BCP1, a great part of the charge radius are overestimated while in the case of DD-ME2 the average trend is closer to the line defining the zero deviation from the experiment. Finally and just having an opposite behavior, DDME$\delta$ systematically underestimates most of the charge radii shown in this figure. As a general trend of all models, the deviations from experiment are highly reduced as heavier is the nucleus.

Next, we show in Figure 18 the two-neutron separation energy ($S_{2n}(N) = B(N,Z) -$

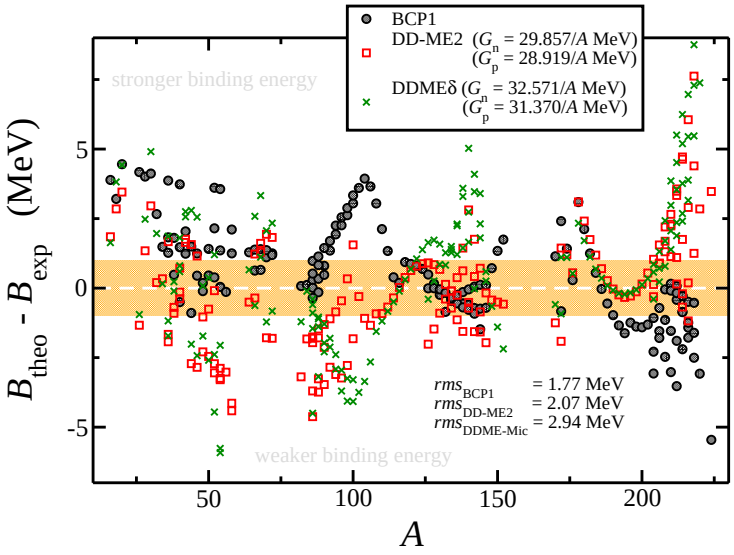


Figure 16: Binding energies of 161 spherical nuclei as a function of the mass number. DDME$\delta$ is compared against the experiment [Au03] and the models BCP1 and DD-ME2.

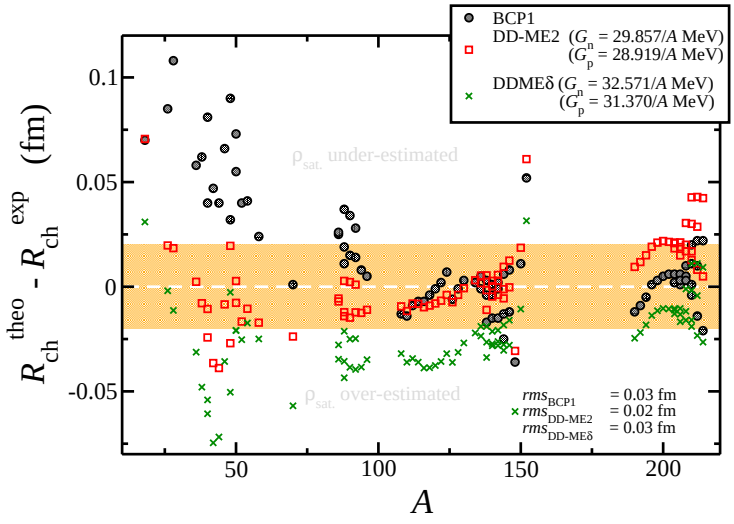


Figure 17: Charge radii of 86 spherical nuclei as a function of the mass number. DDME$\delta$ is compared against the experiment [Au03] and the models BCP1 and DD-ME2.

$B(N-2,Z)$) for experimentaly available Sn isotopes [Au03] and as predicted by the DDME$\delta$ model. One can see from this figure that the novel DDME$\delta$ interaction accurately reproduces the experimental data including the shell effects at the magic number $N$=82. We can not show the experimental $S_{2n}(N)$ in the case of the double-magic nuclei $^{100}$Sn since there is no data for $^{98}$Sn.

As a final application, we show in Figure 19 the neutron skin thickness of 25 stable nuclei measured using antiprotonic atoms [Tr01]. The results obtained with DDME$\delta$ are compared against the experiment and the DD-ME2 interaction. The experimental data

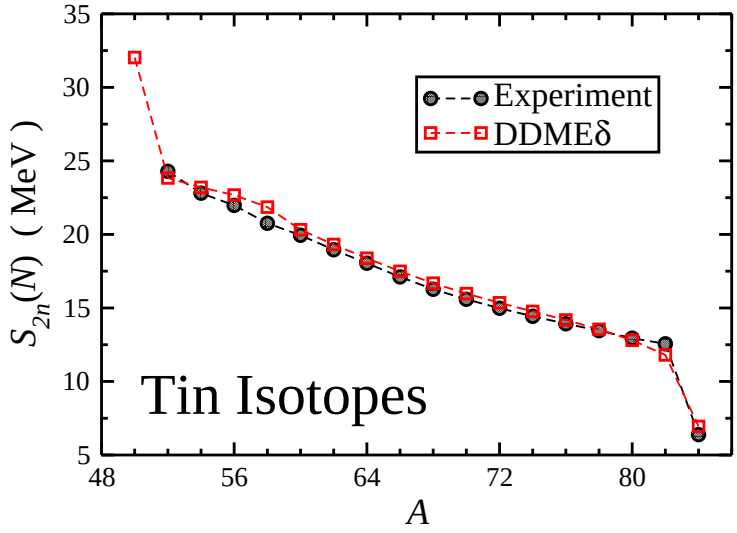


Figure 18: The two-neutron separation energy as a function of the neutron number for the Tin Isotopes. We show the predictions of the DDME$\delta$ interaction as compared with the experiment.

is fairly well reproduced by both interactions as one can see from the figure. In chapter one, we concluded that this experiment [Tr01] pointed towards a relatively soft (small) density derivative of the symmetry energy at saturation ($L$) as compared with other experimental indications. We also showed that the neutron skin thickness predictions of different mean-field models are linearly correlated to $L$. Hence, the obtained results indicate that the predicted value for $L$ of both mean-field interactions (around 50 MeV) is consistent with these measurements. Furthermore, both predictions and our derivations from the experimental data on neutron skins of the parameter $L$ are also in agreement with the accurately calibrated Thomas-Fermi (mean-field) model of Reference [My96, My98] which include in its fitting procedure binding energies of 1654 nuclei and predicts a $L =$ 49.9 MeV.

## 5.5 Outlook

Mean-field models are commonly fitted to some saturation properties of the nuclear EoS and some selected finite nuclei properties of spherical nuclei. DDME$\delta$, in addition, reproduces also first-principle calculations along a relatively wide range of densities and describes in a proper theoretical basis the neutron-proton number differences through the $\rho$ and $\delta$ mesons. For all these reasons, the study of excited states using this novel interaction, could provide useful insights on our understanding of the nuclear dynamics.

As mentioned in chapter three, studies of collective excitations are of fundamental interest in nuclear structure physics. Applying the DDME$\delta$ functional to these excitations can provide an interesting and fruitful phenomenological framework for interpreting

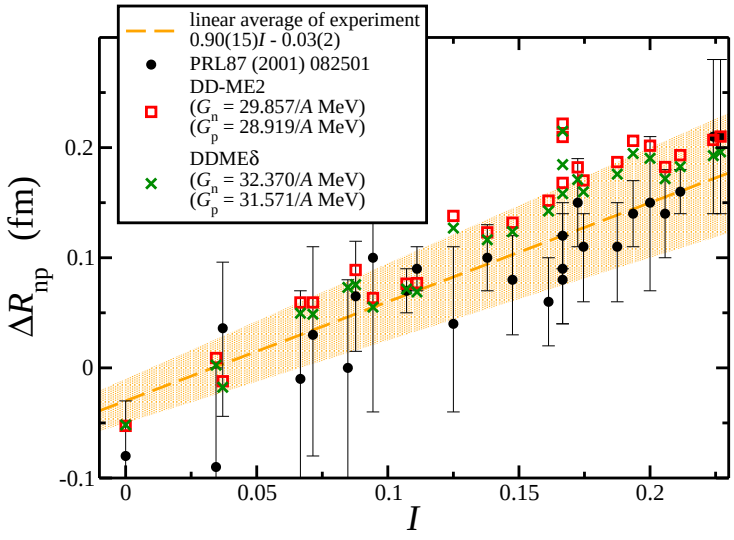


Figure 19: Neutron skin thickness of different nuclei as a function of the asymmetry coefficient ($I = (N - Z)/A$). DDME$\delta$ is compared against the experiment of Reference [Tr01] and the model DD-ME2.

observed properties of nuclei and to relate them with the Equation of State of symmetric and asymmetric matter. An illustrative example is the $L = 0$ mode of the nuclear collective motion, the so-called isoscalar Giant Monopole Resonance (GMR). The frequency of this mode is directly related to the compressibility of the nucleus. For stable nuclei, where the neutron-proton asymmetry is not higher than $\alpha \equiv (N - Z)/A < 0.25$, the determination of the GMR energy is one of the most direct ways to access to the compressibility modulus of nuclear matter ($N = Z$). Furthermore, available data on the Giant Dipole Resonances and Pygmy Dipole Resonances have allowed to obtain recently valuable constraints on the density dependence of the nuclear symmetry energy [Tr08, Kl07]. Therefore, it will be interesting to investigate theoretically with DDME$\delta$ how the density dependence of the symmetry energy is related to the nuclear collective modes and whether future experiments on exotic nuclei could provide narrower constraints on this property.

# Summary and Conclusions

Physical properties of nuclei, such as the mass, neutron and proton distributions, collective excitations, fission properties, etc. are influenced by the isospin dependence of the nuclear strong interaction. In this sense, the effects of the isospin asymmetry in stable and exotic nuclei should be taken into account for a quantitative description of these systems. The symmetry energy and its density dependence account for the effects observed in nuclei with proton-neutron differences. Therefore, the accurate characterization of this property entails profound consequences in studying the nucleus. It also impacts on diverse areas such as nuclear astrophysics and tests of the Standard Model via atomic parity violation. Unfortunately, the characterization of this property remains elusive to date. Basically, it is due to the lack of experimental data on nuclei with large isospin asymmetries as well as the lack of theoretical calculations based on first principles in the case of a finite nucleus.

The experimental situation will change considerably within the next years. The advent of new techniques to synthesize and perform experiments with exotic nuclei will allow this change. Facilities such as HIFRL@CSR [Xi02, Xi05] (China), Spiral2@GANIL [Sa01] (France), FAIR@GSI [FAIR, Si04] (Germany), FRIB@MSU [FRIB] (USA) or RIBF@RIEKEN [Su01] (Japan) plan to perform a wide variety of experiments on nuclei far from the stability valley. The study of those nuclei, which usually have large isospin asymmetries, is thought to provide a better understanding of the nuclear dynamics and, in particluar, of the density dependence of the symmetry energy. Furthermore, observational data from astrophysical objects and processes, such as neutron stars, proto-neutron stars, cooling processes, supernova dynamics, etc., could be crucial in constraining the nuclear EoS in density ranges and isospin asymmetries unreachable in Earth-Laboratories.

This situation have motivated the studies presented along this Thesis where some aspects of the isospin dependence of the nuclear force have been investigated. Our aim was to understand the effects that such dependence produce on different nuclear observables of both, stable and exotic nuclei. For this purpose we have focused in the first chapters on the influence of the density dependence of the (bulk) symmetry energy on the neutron skin thickness of nuclei, the Giant Monopole Resonance along isotopic chains and on the structure and composition of the outer crust of a neutron star. As mentioned, the bulk symmetry energy is the contribution to the nuclear EoS due to the differences between the number of protons and neutrons. Previous works than the ones presented here have already shown that this property entails important consequences on nuclear isospin dependent observ-

ables [Br00, Ty01, Hor1, To05, St05, La07, Ba05, Ch05, Che5, Li08, Sh07, Fa06, Pi07].

In the publication entitled "Nuclear Symmetry Energy Probed by Neutron Skin Thickness of Nuclei", we relate the symmetry energy in a finite nucleus with the symmetry energy of the EoS at subsaturation densities. This general correlation, was applied to extract constraints on the density dependence of the symmetry energy from neutron skin measurements. In this respect, we were specially interested on how the largest uniformly-measured data set of neutron skins [Tr01] using antiprotonic atoms may help on constraining such quantity. The constraints derived from this study were in good agreement with other derivations from heavy ion reactions, pygmy dipole and giant dipole resonances and favor a rather soft symmetry energy at subsaturation densities. Within the same spirit, in the publication "Neutron skin thickness in the droplet model with surface width dependence: Indications of softness of the nuclear symmetry energy", we presented a correlation between the density derivative of the symmetry energy at saturation ($L$) and the symmetry energy at saturation ($J$) over the surface stiffness coefficient ($Q$). We first showed, based on the grounds of the Droplet Model[My74, My77], that the ratio $J/Q$, as predicted by different nuclear models, drives the neutron skin thickness of nuclei. Then, we stated a linear correlation between $L$ and $J/Q$, a fact that enabled us to rewrite the DM formula for the neutron skin thickness calculation in terms of the density dependence of the symmetry energy at saturation $L$. Finally, using the same experimental data on neutron skins mentioned above, we found compatible constraints on $L$ as compared with our previous indications and with those based on other experiments as the ones mentioned above. In the last contribution —accepted for publication in *Physical Review C*— presented in the first chapter of this thesis, "Analysis of bulk and surface contributions in the neutron skin of nuclei", we study the neutron skin of nuclei following form theoretical calculations with relativistic and non-relativistic interactions. Experimental measurements on neutron skins may imply model dependent assumptions about its bulk and surface nature, we exemplify this situation analyzing the methods and results of the neutron skin data in 26 antiprotonic atoms used in our previous works [Tr01]. Discussing then the suitability of different definitions of the nuclear charge radii usually employed in the experimetal determination of such observable, we realized that the equivalent sharp radius is a magnitude to discern between the bulk and surface nature of a density distribution more suitable than the half density parameter. Subsequently, this study enabled a theoretical investigation using different and successful nuclear models which helped us to set upper and lower bounds on such commonly-used parameters and, therefore, to the bulk and surface contributions of the neutron skin thickness.

Next, we investigate the influence of the density dependence of the symmetry energy on the structure and composition of a neutron star crust using some of the more sophisticated nuclear mass models available in the literature. The publication presented in this Thesis is entitled "Impact of the symmetry energy on the outer crust of non-accreting neutron stars". The neutron-rich nuclei present in the outer crust are on average more dilute than their more symmetric counterparts because of the development of a neutron skin.

As a result, these nuclei become sensitive to the symmetry energy below nuclear matter saturation density and affect the composition of the crust. Specifically, the realistic mass tables showed that models with a smaller derivative of the symmetry energy with respect to the baryon density at nuclear sub-saturation predict nuclei that are more neutron rich than models with a bigger derivative. Apart from that, it was also our aim to elucidate how the different ingredients accounting for the stability of the neutron star throughout the outer layer of its crust compete between them. For that reason, on a Liquid Drop Formula basis, we derive in a simple and analytical way some interesting features of the essential physics of the outer crust. Namely, the competition between the Coulomb energy accounted by the degenerate free Fermi gas of electrons, corrected by the ion lattice, and the symmetry energy coming from the large asymmetries of such ions embedded in the lattice. The analytical picture of the problem turned out to be enlightening in all discussions about the important physics thought to hold in the outer crust.

The third chapter is devoted to "The influence of the symmetry energy on the giant monopole resonance of neutron-rich nuclei analyzed in Thomas-Fermi theory", a work accepted to be published in *Journal of Physics G*. The experiments on giant ressonances have been extensively used as a measure of the compressibility modulus of symmetric nuclear matter ($K_0$). Not exempt from uncertainties closely related to those of the density dependence of the symmetry energy [Da02, Pi04, Co04], we investigated the average excitation energy of the GMR on stable and exotic nulclei and how it depends on the symmtery energy. Specifically, we studied the average excitation energy of the Giant Monopole Resonance (GMR) along two isotopic chains by applying the relativistic extended Thomas-Fermi method. The range of analyzed asymmetries brought us to notice different areas of influence of the symmetry energy on that observable. While in the case of stable (symmetric) nuclei, a moderate effect of the symmetry energy on the excitation energy is observed. For large asymmetries, the stiffness of the symmetry energy is likely to be reflected in the properties of the excitation spectra. Nevertheless, it may be worth to contrast our results through a study of the influence of the density dependence of the symmetry energy on the grounds of a more fundamental —and more demanding— theory as it is the Quasi-particle Random Phase Approximation of the GMR response.

"Theoretical study of elastic electron scattering off stable and exotic nuclei" is the title of the publication presented in the fourth chapter. We have also studied theoretically the electron elastic scattering off stable and exotic nuclei. A process which have regained new interest due to the recent developments on Radioactive Ion Beams. Actually, the ELISe [Si07] and SCRIT [Su05, Wa08] experiments, planned at GSI (Germany) and RIKEN (Japan) respectively, will take advantage of such technical developments and study elastic electron scattering off exotic nuclei. Our main goal on that topic was to provide theoretical predictions along isotopic chains trying to identify correlations of potential interest for the upcoming experiments as well as to check current nuclear models with already measured cross section. To that end, we solve the problem of an electron in a central field by means of a partial wave expansion of the electron outcoming wave

function. In other words, once we have computed the charge distribution of a nucleus, the exact solution of the corresponding Dirac equation is calculated. This fact allows us to concentrate on the only ingredient which is model dependent in our study: the nuclear electric charge distribution. In the way to partially avoid this dependency on the theory, we employ nuclear models of very different nature. Then, with the experience gained in the study of stable nuclei, we extend our study to unmeasured regions including nuclei with large isospin asymmetries. Specifically, we analyze the evolution of the differential cross section as the neutron number increases until the neutron drip is reached, fixing the proton number first to 20 and then to 50. We also fitted the self-consistent charge distributions obtained from the nuclear models through the so-called Helm density (dependent on two parameters with a clear physical interpretation) in an attempt to find a relation between the input, *i.e.* electromagnetic potential of the nucleus, and the output, *i.e.* the differential cross section. This procedure turned out to be helpful to study the neutron-number variation of the scattering observables and allowed us to identify a linear correlation of potential interest among the electromagnetic form factor and a combination of the Helm parameters.

Finally, inspired in density functional theory methods, we constructed an improved mean-field effective interaction (DDME$\delta$) to describe the nuclear EoS and the splitting of the proton and neutron effective masses as predicted by first-principle calculations. The effective mass splitting is an isospin dependent magnitude which can be predicted by fully microscopical calcualtions. In this sense, the DDME$\delta$ functional account for the magnitude and density content of the isospin dependence part of the nuclear strong interaction accordingly with *ab initio* calculations. Furthermore, in the fitting procedure we neglected all possible parameterizations falling away from the typical accuracy showed by such kind of models in describing basic properties of finite nuclei such as the mass or the charge radius. In other words, using available theoretical and experimental information, we tried to best account from an effective picture for the nuclear EoS and finite properties of nuclei along the stability valley. Our results on finite nuclei properties achieved the same level of accuracy as other mean-field models but with the theoretical advantage of including the $\delta$ meson. In this respect, DDME$\delta$ introduce an important degree of freedom usually neglected by mean-field calculations and suggested as important by fully microscopical calculations in describing the asymmertic EoS and finite nuclei with large isospin asymmetries. Furthermore, DDME$\delta$ reproduces the *ab initio* calculations of Reference [Ba04] —believed to be among the most accurate in the literaure— and with a high predictive power since are only based on realistic nucleon-nucleon potentials consistent with scattering experiments.

In general, the density dependence of the symmetry energy has been shown to impact on Earth nuclei and astrophysical objects as the neutron skin thickness of nuclei, the Giant Monopole Resonance of nuclei with large asymmetries, the elastic electron scattering of exotic nuclei or the crust of a neutron star. This important property of the nuclear EoS have been also investigated from a more fundamental point of view trying to characterize it

as well as to go a step further in understanding its nature from first-principle calculations.

Laboratory experiments relevant for nuclear physics and astrophysics in general, have grown significantly in recent years. A huge amount of nuclei ranging from the $\beta$-stability line to the neutron drip line have been now measured. In addition, with the prospects of the Radioactive Ion Beam experiments more neutron rich nuclei will be measured. In this light, it is likely that some theoretical problems on physics related with isospin dependent observables, will be no more hindered by the lack of relevant experimental data on very asymmetric nuclei. On the other hand, fully microscopical calculations are very important since it is possible that some isospin-related phenomena have been misunderstood because of the lack of appropriate theoretical calculations. All in all, the isospin dependence of the nuclear strong interaction plays a crucial role in the nuclear dynamics involving a large number of different observables, among them all those derived form nuclei which are constituted by a large isospin asymmetry. We, therefore, are hopeful that our calculations and stated correlations may supply theoretical hints on further experiments or theoretical investigations of neutron skins, Giant Monopole Resonances or elastic electron scattering off exotic nuclei as well as having provided an enlightening view —through the improved effective mean field interaction— of the role of the isovector part of the nuclear force and its importance to go further in our understanding of the nuclear dynamics, at least from an effective picture. Last but not least, we are also hopeful that our numerical and analytical calculations of the structure and composition of the outer crust of a neutron star had helped to clarify how sensitive are these astrophysical objects on the density content of the nuclear symmetry energy.

Along this Thesis, we have presented several studies on the influence of the isospin asymmetry in different nuclear properties and, in particular, on the symmetry energy and its density dependence. However, there are still many studies and applications that one can investigate. Among the most interesting in our opinion are the following:

- The investigation of the bulk and surface origin of the neutron skin thickness of $^{208}$Pb in mean-field models. Motivated by the upcoming experiment at the Jefferson Laboratory which aims to provide an accurate and model-independent determination of the neutron skin of $^{208}$Pb [Mi02], this study could determine, very precisely, the density derivative of the symmetry energy at saturation ($L$) universally in mean-field models. The accurate characterization of this property has been identified as one of the most outstanding questions in Nuclear Physics [Br00, Bao8, Ty01, Hor1, To05, St05, La07, Ba05, Ch05, Che5, Li08, Sh07, Fa06, Pi07]. .

- The study of the structure and composition of the inner crust and the outer core of a neutron star with the accurately calibrated DDME$\delta$ interaction. In this way we will be able to provide an almost full description of the structure and composition of a neutron star within the same nuclear interaction. It could also provide interesting physical insights on neutron stars as well as in nuclear physics.

- The theoretical study of elastic electron scattering along isotonic chains. Motivated by the advent of new experiments of elastic electron scattering planned in Radioactive Ion Beam Facilities for the study of nuclei far from the stability valley [Si07, Su05, Wa08], the study of isotonic chains will complement the work presented here under the title "Theoretical study of elastic electron scattering off stable and exotic nuclei". And, therefore, could provide an interesting overview of the established nuclear mean field approach in the domain of exotic nuclei as well as valuable references for future experiments.

- The study of exited states and deformations using the new DDME$\delta$ functional. Mean-field models are commonly fitted to some saturation properties of the nuclear EoS and some selected finite nuclei properties of spherical nuclei. DDME$\delta$, in addition, reproduces also first-principle calculations along a relatively wide range of densities and describes in a proper theoretical basis the neutron-proton number differences through the $\rho$ and $\delta$ mesons. For all these reasons, the study of deformations and excited states using this novel interaction, could provide useful insights on our understanding of the nuclear dynamics.

# Resum, conclusions i perspectives

El nucli atòmic està composat de neutrons i protons lligats per mitjà de la interacció nuclear forta. Degut a les seves propietats (veure taula 1), el neutró i el protó poden ser considerats com la mateixa partícula en dos estats d'isospí diferents (nombre quàntic analog al espí). Nuclis amb diferent nombre de neutrons que de protons —és a dir, amb una certa asimetria d'isospí— existeixen de manera natural a la Terra, a les estrelles i poden ser sintetitzats en el laboratori. Les propietats d'aquests nuclis estan, en major o menor mesura, governades per la dependència en l'isospí de la interacció nuclear forta i constitueixen avui en dia un tema de recerca molt interessant en física nuclear i astrofísica [St05, Bao8]. En general, aquestes propietats dels nuclis com poden ser la massa, les distribucions de neutrons i protons, les excitacions col.lectives, les propietats de fisió, els fluxes de materia i de moment en col.lisions d'ions pesats, etc. no estan completament caracteritzades per la teoria nuclear actual. En aquest sentit, les contribucions a les propietats dels nuclis originades per les asimetries d'isospí són un dels ingredients importants a tenir en compte per arribar a una descripció més precisa de l'experiment. Aquest fet ha motivat un fort interès i una gran activitat per part de la comunitat científica en aquesta nova branca d'investigació anomenada Física de l'Isospí. Els treballs presentats en aquesta Tesi, composada per diferents publicacions i treballs acceptats per a ser publicats a més d'una última secció a on el treball que presentem es preveu enviar a publicar en els propers mesos, han estat motivats per l'estudi d'aquestes propietats dels nuclis en que les diferències en el nombre total de protons i de neutrons poden jugar un paper important. La majoria de treballs han estat focalitzats en l'estudi de l'energia de simetria i la seva dependecia en densitat, dues propietats molt importants de l'Equació d'Estat (EoS) nuclear. En concret, es tracta de la contribució més important a l'energia total d'un sistema infinit de protons i neutrons deguda a la asimetria d'isospí que pugui presentar. L'acurada caracterització d'aquesta part de l'EoS nuclear és considerada una de les qüestions més importants a tractar en la Física Nuclear actual [Br00, Bao8, Ty01, Hor1, To05, St05, La07, Ba05, Ch05, Che5, Li08, Sh07, Fa06, Pi07].

Experimentalment, tot i que hi han mesures precises en diversos observables nuclears, hi ha una mancança en la precisió en què es mesuren aquells observables sensibles a les asimetries d'isospí, sobretot pel que fa a les asimetries grans. Justament, són aquests observables els que ens ajudarien a caracteritzar millor la dependencia en isospí de la interacció nuclear forta. En aquesta direcció s'estan movent molts laboratoris arreu del

Món. Recentment, s'han desenvolupat tècniques experimentals per sintetitzar nuclis lluny de la vall d'estabilitat i explorar així zones del mapa del nuclis (veure Figura 5) de les quals ara mateix no disposem de cap informació més que prediccions teòriques [RBFa]. Majoritàriament aquestes zones corresponen a nuclis que en molts dels cassos mostren asimetries d'isospí grans i que en general són anomenats exòtics. Donada aquesta falta de coneixement de la interacció nuclear forta en els dominis dels nuclis exòtics es preveu portar a la pràctica diferents experiments aprofitant aquests recents desenvolupaments en tècniques experimentals per sintetitzar nuclis inestables.

Pel que fa a la teoria moderna del nucli, després de molts avenços aconseguits desde que James Chadwick va descobrir el neutró en 1932 [Ch32], la connexió entre la interacció nucleó-nucleó derivada de l'experiment i el sistema de molts nucleons lligats que formen el nucli no és encara transparent. Degut a això, s'està duent a terme un esforç important en diverses direccions, tant per caracteritzar com per entendre millor la interacció nuclear forta i en particular la seva dependència en l'isospí. Aquí podríem destacar dos grans grups, aquells que es dediquen a un estudi més fenomenològic del nucli, tractant de recórrer el camí desde la caracterització de la interacció nuclear en el medi fins a la interacció nucleó-nucleó, i aquells que recorren el camí contrari. El punt d'intersecció, lamentablement, encara no està ben definit.

Motivats per tota aquesta situació, ens endinsem al llarg d'aquesta Tesi en l'estudi dels efectes de la asimetria d'isospí en els nuclis estables i exòtics. Per desenvolupar aquest estudi, ens vam fixar —en molts dels projectes en què ens hem involucrat— en la contribució a l'Equació d'Estat (EoS) deguda a la asimetria d'isospí. En concret a la contribució que es coneix com a energia de simetria i que és crucial en molts processos nuclears i astrofísics. Aquesta propietat i la seva dependència en densitat constitueixen un dels temes més importants i candents en la física nuclear moderna. Tant és així, que la seva complerta caracterització es considerada per molts països i projectes d'investigació com un dels grans problemes a resoldre en el futur proper (veure per exemple http://www.er.doe.gov/np/nsac/nsac.html).

En concret, en aquesta Tesi, presentem un bloc ben definit de treballs que tractan d'entendre i caracteritzar l'energia de simetria i la seva dependència en densitat a través de l'estudi de diferents observables nuclears sensibles en nuclis estables i exòtics. A més, incorporem a l'últim capítol un nou ajust d'una interacció efectiva basada en càlculs relativistes de camp mig que té cura de tractar el més acuradament possible la asimetria d'isospí així com d'incorporar a traves del seu ajust, no només informació experimental sinó que també de les indicacions teòriques basades en càlculs més fonamentals.

En el primer capítol de la Tesi presentem dos publicacions i un treball acceptat per publicar a "*Physical Review C*" tot estudiant la relació entre l'energia de simetria i l'anomenada pell de neutrons ("neutron skin"). La pell de neutrons, és un observable nuclear que depèn de la diferencia quadràtica mitjana entre els radis predits per les distribucions de neutrons respecte a la de protons. En la primera publicació establim una relació entre l'energia de simetria $a_4(A)$ d'un nucli pesat i l'energia de simetria de volum

(de l'Equació d'Estat; EoS) $c_{\rm sym.}(\rho)$ a una densitat donada $\rho_A$. Aquesta relació, valida per tot model de camp mig, ens permet estudiar els lligams que estableix l'experiment de la referència [Tr01] (que mesura la pell de neutrons en atoms antiprotonics) en $c_{\rm sym.}(\rho)$ mitjançant l'expressió analítica per la pell de neutrons derivada en el "Droplet Model" (DM) [My74, My77]. Els resultats obtinguts ($L = 75 \pm 25$ MeV and $K_\tau = -500 \pm^{125}_{100}$ MeV) ens permeten obtenir uns lligams similars a d'altres estudis realitzats i basats en diferents tècniques i experiments per algunes de les propietats de de l'EoS relacionades amb la dependència en densitat de l'energia de simetria. En el segon treball, estudiem les contribucions de superfície i de volum en la pell de neutrons predites per una col.lecció representativa de models nuclears efectius. Per fer aquesta descomposició, també recorrem a la formula analítica derivada del DM. Constatem amb aquest estudi que tant les contribucions de volum com les de superfície a la pell de neutrons són importants i que, per tant, assumir que la pell de neutrons es genera bàsicament per una discrepància o a la part de volum o a la de superfície de la distribució de neutrons respecte a la de protons, pot donar lloc a estimacions de la pell de neutrons esbiaixades i depenents del model. A més, també hem establert una nova correlació lineal entre la pell de neutrons d'un nucli pesat i el quocient de l'energia de simetria a saturació $J$ amb el coeficient que dona comte de la resistència que oposa el sistema a la separació dels neutrons en front dels protons $Q$ —terme dominant de les contribucions de volum i superfície a la pell de neutrons— per tot el conjunt de models emprat. Aquest fet ens porta a establir una nova correlació entre la derivada en densitat de l'energia de simetria $L$, que ja es coneixia que estava relacionada linealment amb la pell de neutrons per nuclis pesants universalment por tot model de camp mig [Br00], i el quocient $J/Q$. Fent servir novament els resultats de l'experiment [Tr01] que mesura la pell de neutrons en àtoms antiprotonics intentem obtenir lligams sobre el coeficient $J/Q$ i, posteriorment, amb la derivada en densitat de l'energia de simetria a saturació $L$. Concloem d'aquest ultim anàlisi que aquests experiments, juntament amb les aproximacions i mètodes emprats, prediu un valor per $L$ a la banda baixa en comparació amb altres extraccions d'aquesta propietat de l'EoS nuclear ($L \approx 30 - 80$). Finalment, fem un estudi estadístic dels valors de $L$ predits per diferents experiments i mètodes obtenint una finestra de $L = 45 - 75$ MeV força compatible amb els resultats que hem obtingut en les dues primeres publicacions presentades en aquesta Tesi. Per acabar, en aquest primer capítol estudiem de nou les contribucions de superfície i volum a la pell de neutrons però des d'una perspectiva més propera als anàlisis fets servir típicament a l'experiment per extreure el valor d'aquest observable. Usualment, a l'experiment s'assumeix una dependència analítica definida per les distribucions de protons i neutrons. A més a més, es pot arribar a assumir que la diferencia entre les distribucions de neutrons respecte a la de protons depèn només de les diferencies a la part de volum o superfície d'ambdues distribucions —com ja hem esmentat abans. D'altra banda, també s'ha demostrat que fent servir les dades de l'experiment [Tr01] es poden reproduir les dades experimentals assumint els dos casos extrems que acabem d'explicar amb aproximadament la mateixa qualitat [Tr01, Sw05]. Motivats per aquesta

situació, el que fem en aquest ultim treball és fer una anàlisi anàloga al que es pot fer a l'experiment però fent servir com a base càlculs teòrics. Primer de tot expliquem alguns fonaments sobre l'experiment [Tr01] per entendre millor els seus resultats en els valors obtinguts per a la pell de neutrons. Estudiem també d'entre les definicions més populars per caracteritzar els radis quadràtics mitjos d'una distribució, quin és el que distingeix millor entre les contribucions de superfície i volum de la pròpia distribució arribant a la conclusió que el "equivalent sharp radius" és una quantitat més adient per distingir la contribució de volum que no pas el freqüentment utilitzat "half-density radius" de la distribució de Fermi. A continuació, ajustem les distribucions de neutrons i protons per una densitat de Fermi (dos paràmetres) per les prediccions de diferents models nuclears en les pells de neutrons dels mateixos nuclis estudiats a l'experiment [Tr01] i estudiem les seves contribucions de superfície i volum. El mateix fem en el cas de les cadenes d'isòtops de l'estany i el plom per veure com evolucionen aquestes contribucions al anar incrementant la asimetria entre el número de protons i neutrons en el nucli. D'aquest estudi s'observa que tant la contribució de volum com la de superfície a la pell de neutrons són importants per la descripció dels resultats predits pels respectius models nuclears utilitzats i que, com ja havíem vist en els treballs anteriors, la seva suma per donar la pell de neutrons segueix una correlació lineal amb la asimetria d'isospí en tots els models emprats mentre que per separat, tot i que que s'aprecien tendències comunes, no es pot veure cap comportament fàcilment quantitzable. Especific a les cadenes d'isòtops, trobem que en nuclis molt rics en neutrons els efectes de capes poden ser importants per entendre les diferents contribucions a la pell de neutrons.

El següent capítol, el dediquem a l'estudi de la sensitivitat en la composició i estructura de l'escorça més exterior d'una estrella de neutrons en la dependència en densitat de l'energia de simetria del qual tenim publicats els resultats. En el nostre estudi utilitzem alguns dels models nuclears més precisos en la predicció de masses que hi ha a la literatura a més de dos models relativistes de camp mig amb propietats molt diferents en quant al comportament en densitat de l'energia de simetria. Complementàriament, també proposem un "Toy Model" per copsar d'una manera més clara i entenedora la física important que es dóna en aquesta capa externa de l'estrella de neutrons. Dels nostres resultats observem que a les condicions de densitat i pressió que es donen en l'escorça exterior de l'estrella es poden formar nuclis molt rics en neutrons. Degut a això, el comportament d'aquests nuclis be molt influenciat per la dependència en densitat de l'energia de simetria del model nuclear utilitzat per predir la composició i estructura de l'estrella. La conclusió principal d'aquest estudi es que la competició entre l'energia deguda al gas d'electrons lliures presents per assegurar la neutralitat de l'estrella i l'energia de simetria dels nuclis presents a l'escorça exterior de la mateixa determinen la composició, i en concret la asimetria d'isospí que tenen els nuclis d'aquesta capa més externa de l'estrella de neutrons. En altres paraules, un podria afirmar tenint en compte les correlacions mostrades en els treballs anteriors que la composició de l'escorça externa de l'estrella de neutrons conte nuclis més asimètrics (més exòtics) com major sigui la pell de neutrons del $^{208}$Pb.

L'influencia que exerceix la dependència en densitat de l'energia de simetria pel cas de nuclis rics en neutrons en l'energia mitjana d'excitació de la Ressonància Monopolar Gegant (GMR), és el tema d'estudi del treball que presentem en el tercer capítol i que està acceptat per publicar a "*Journal of Physics G*". La GMR és una excitació col.lectiva del nucli que dona com a resultat un espectre d'energies que es utilitzat per determinar amb molta precisió ( 2%) la incompressibilitat nuclear de l'EoS de la matèria simètrica a saturació $K_0$. La incertesa amb la que s'obté el valor de $K_0$ està estretament lligada a la incertesa que existeix en la dependència en densitat de l'energia de simetria en els models nuclears actuals [Da02, Pi04, Co04]. D'altra banda, en la referencia [Kh09] s'afirma que per una determinació més precisa d'aquesta incompressibilitat és necessita mesurar experimentalment la GMR a tota una cadena d'isòtops i que, per tant, l'energia de simetria juga un paper rellevant en aquest sentit. Motivats per l'estudi de l'energia de simetria en aquesta excitació col.lectiva i degut a que no existeixen càlculs teòrics a la bibliografia sobre el valor de les energies d'excitació d'aquestes ressonàncies en nuclis amb grans asimetries d'isospí, hem volgut analitzar la influencia que l'energia de simetria té en aquests nuclis basant els nostres càlculs en la teoria de Thomas-Fermi (veure apèndix d'aquest treball). Les conclusions que es deriven d'aquest estudi apunten a que, efectivament, les energies d'excitació d'aquesta ressonància depenen fortament del valor de la derivada en densitat de l'energia de simetria $L$ pel cas de nuclis molt rics en neutrons (els quals encara no és possible mesurar avui en dia) i que per nuclis més a prop del vall de l'estabilitat, aquesta influencia és menys pronunciada com s'entén del fet que $K_0$ està determinada amb molt bona precisió per experiments en nuclis estables, és a dir, nuclis amb asimetries d'isospí petites o nul.les. Els nostres càlculs, a més, poden aportar informació sobre processos físics en què entren en joc nuclis molt rics en neutrons com els que podríem trobar a l'escorça de les estrelles de neutrons. Els resultats que presentem, també poden servir de guia per propers experiments o càlculs teòrics basats en altres mètodes.

Al capítol quart presentem un treball publicat a on dediquem els nostres esforços a l'estudi de la dispersió elàstica d'electrons per nuclis estables i exòtics. Motivats pel desenvolupament de noves tècniques experimentals que permetran l'estudi de nuclis exòtics en els propers anys i en particular pels projectes programats per dur a terme experiments de dispersió elàstica d'electrons [Si07, Su05, Wa08], hem volgut realitzar un estudi sistemàtic del que els models nuclears actuals prediuen per aquests nuclis que es preveuen estudiar. A més, també investiguem com evoluciona la secció eficaç d'aquests processos al llarg de cadenes d'isòtops per poder extreure correlacions que puguin ser d'utilitat tan a l'experiment com a d'altres càlculs teòrics. Per dur a terme els càlculs necessaris resolem exactament l'equació de Dirac i per tant l'única magnitud depenent del model és el potencial nuclear que pateixen els electrons del feix incident. La interacció és bàsicament electromagnètica i per tant, la distribució dels protons al nucli permet calcular aquest potencial casi amb total precisió pels nostres propòsits. Tot i això, el neutrons també juguen un cert paper ja que posseeixen una distribució de càrrega elèctrica no nul.la i, en major mesura, influencien mitjançant la interacció nuclear forta la distribució de protons

i (de manera indirecte) el potencial electromagnètic generat pel nucli. Aquest estudi ens ha permès testejar la metodologia emprada, estudiar les prediccions de diferents models teòrics en nuclis actualment mesurats i comprovar les seves prediccions. A continuació hem estudiat les cadenes d'isòtops de l'Sn i el Pb basats en un model que té una especial cura a l'hora de tenir en compte els efectes electromagnètics del neutró a la distribució de càrrega nuclear. Com a resultat, hem extret una correlació prou significativa entre els paràmetres de la distribució d'Helm [He56] emprada per modelitzar (en analogia amb l'experiment) la distribució de càrrega predita pel model abans esmentat amb el primer mínim de la secció eficaç diferencial.

Finalment, a la secció cinquena, presentem una nova interacció relativista de camp mig amb dependència explicita en densitat de les constants d'acoblament basada en la Teoria Relativista de Camps Depenent de la Densitat per Hadrons. En general, els models relativistes de camp mig que estan disponibles a la literatura i que poden ser entesos com a funcionals de la densitat, són models efectius que neixen d'un Lagrangià que té com a graus de llibertat físics el protó i el neutró i donen compte de la interacció nuclear mitjançant tres camps mesònics els quals representen els mesons anomenats $\sigma$, $\omega$ i $\rho$ que fan de portadors de la interacció nuclear forta. Aquests models efectius estan típicament ajustats a algunes propietats de nuclis finits tals com masses o radis de càrrega i en molts casos també a algunes propietats de l'Equació d'Estat (EoS) de matèria simètrica a la saturació nuclear. Tot i la seva relativa simplicitat comparats amb altres models nuclears, aquest tipus de models han demostrat la seva precisió en la descripció de diferents processos i propietats nuclears no només en nuclis estables sinó que també en nuclis lluny de la vall d'estabilitat [Va72, De80, Fu97, La97, Ty99, Ni02, Go03, Sa03, To05, La05, Ba08]. D'altra banda, existeixen càlculs més fonamentals com els càlculs basats en primers principis dels quals no s'inclou gairebé cap informació en els fits abans esmentats i que tampoc és té en compte les seves indicacions referents a la inclusió d'un grau de llibertat molt important per la descripció de l'EoS de matèria asimètrica. Es tracta del mesó $\delta$. Aquests models més fonamentals estan basats en les teories i tècniques de molts cossos més avançades i fan servir el potencial nucleó-nucleó extret de l'experiment per calcular la interacció nuclear en el medi. Aquests càlculs basats en primers principis —que només són possibles per l'EoS nuclear i no pas per càlculs de nuclis finits— constitueixen la connexió més neta que coneixem actualment entre la interacció nuclear forta en el medi i de la interacció nucleó-nucleó. Per tant, fer servir aquesta informació per construir una nova força nuclear a on a més es tingui en compte el mesó $\delta$ i que reprodueixi amb la mateixa qualitat que els altres models relativistes de camp mig les propietats dels nuclis finits és el repte que ens hem plantejat en aquest treball. Els resultats obtinguts reprodueixen els de matèria neutrónica i simètrica de la Referencia [Ba04] en un rang bastant ample de densitats (fins dos cops la densitat de saturació). També reprodueixen en el mateix rang de densitats la diferencia de masses efectives entre protons i neutrons tal i com són predites pels càlculs més fonamentals de la Referència [Da07]. Finalment, amb aquesta nova força, s'aconsegueix obtenir el mateix nivell de precisió obtingut anteriorment per d'altres models

relativistes de camp mig en propietats com les energies de lligam, radis de càrrega o pells de neutrons.

Com a conclusió general derivada de tots aquests treballs, podem dir que la dependència en l'isospí de la interacció nuclear forta juga un paper molt important en la dinàmica nuclear i aquest fet afecta notablement a molts observables nuclears, en especial aquells que es mesuren en nuclis amb asimetries d'isospí moderades o grans. Per tant, esperem que els nostres càlculs en la pell de neutrons, la ressonància monopolar gegant, la composició i estructura de les estrelles de neutrons o la dispersió elàstica d'electrons per nuclis exòtics així com la nova interacció nuclear construïda amb la intenció d'entendre millor la interacció nuclear de sistemes asimètrics en isospí ajudin a anar una mica més enllà en la nostre comprensió de la dinàmica nuclear, al menys desde un punt de vista efectiu.

Finalment, tot i que al llarg d'aquesta Tesi hem presentat diferents resultats sobre la influència de la asimetria d'isospí en propietats nuclears de sistemes estables i exòtics per mitjà moltes vegades de l'energia de simetria i la seva dependència en densitat, encara queden molts estudis i aplicacions interessants per investigar en aquesta mateixa direcció. De les més importants segons la nostra opinió són:

- La investigació de l'origen de la pell de neutrons del plom $^{208}$Pb en models de camp mig. Degut a que durant aquest any està previst un experiment al Jefferson Laboratori el qual proporcionara una mesura d'alta precisió a la pell de neutrons del $^{208}$Pb [Mi02] i que aquesta mesura posara un lligam molt estret al valor de $L$ en els models nuclears de camp mig [Br00], l'estudi de l'origen de la pell de neutrons del plom $^{208}$Pb és un problema interessant i que podria ser d'ajuda a l'extracció del valor de la pell de neutrons a l'experiment.

- L'estudi de l'estructura i composició de l'escorça interna i del nucli extern d'una estrella de neutrons amb la nova interacció DDME$\delta$. Aquest estudi ens permetria tenir una EoS quasi complerta per l'estrella i ens permetria testejar la nova força.

- L'estudi de la dispersió elàstica d'electrons en cadenes d'isòtons. Aquest treball complementaria la visió teòrica que ja hem donat amb l'estudi de cadenes d'isòtops i podria constituir una part interessant dels càlculs de referència que haurien de disposar en el futur proper experiments amb nuclis exòtics planejats a Alemanya i al Japó [Si07, Su05, Wa08].

- L'estudi d'estats excitats i deformacions amb la nova interacció presentada a l'ultim capítol d'aquesta Tesi. Degut a les característiques especials amb que s'ha construït aquesta interacció: reprodueix càlculs de primers principis, inclou els graus de llibertat suggerits per càlculs més fonamentals i manté la precisió dels models relativistes de camp mig en la descripció de les propietats de nuclis finits; seria molt interessant explorar les seves prediccions en el cas d'excitacions col.lectives o estendre el

rang de prediccions al tots els nuclis coneguts experimentalment (incloent per tant deformacions i d'altres característiques).

# Bibliography


[An04] I. Angeli, At. Data and Nucl. Data Tables 87 (2004) 185.

[Au03] G. Audi and A.H. Waspra, Nucl. Phys. A 729 (2003) 337.

[Ba04] M. Baldo, C. Maieron, P. Schuck and X. Viñas, Nucl. Phys. A 736 (2004) 241.

[Ba05] V. Baran, M. Colonna, V. Greco and M. Di Toro, Phys. Rep. 410 (2005) 335.

[Ba08] M. Baldo, P. Schuck and X. Viñas, Phys. Lett. B 663 (2008) 390.

[Ba34] W. Baade and F. Zwicky Phys. Rev. 46 (1934) 76.

[Ba71] G. Baym, C. Pethick, and P. Sutherland, Astrophys. J. 170 (1971) 299.

[Ba99] For a pedagogical introduction, see, in: Nuclear Methods and the Nuclear Equation of State, in: M. Baldo (Ed.), Int. Rev. Nucl. Phys., vol. 9, World Scientific, Singapore, 1999.

[Bao8] Bao-An Li, Lie-When Chen and Che Ming Ko, Phys. Rep. 464 (2008) 113.

[Be00] M. Bender, K. Rutz, P.-G. Reinhard and J.A. Maruhn, Eur. Phys. J. A 8 (2000) 59-75

[Be37] H.A. Bethe and R.F. Bacher, Rev. Mod. Phys. 8 (1937) 165.

[Bj65] J.D. Bjorken and S.D. Drell, *Relativistic Quantum Fields* (McGraw-Hill, New York, 1965)

[Br00] B.A. BrownPhys. Rev. Lett. 85 (2000) 5296.

[Br67] K.A. Brueckner, S.A. Coon, J, Dobrowski, Phys. Rev. 168 (1967) 1184.

[Ch05] L.W. Chen, C. M. Ko and B. A. Li, Phys. Rev. Lett. 94 (2005) 032701

[Ch32] J. Chadwick, Nature 129 (1932) 312.

[Ch98] E. Chabanat, P. Bonche, P. Haensel, J. Meyer and R. Schaeffer, Nucl. Phys. A635 (1998) 231 (1998).

[Che5] L.W. Chen, C. M. Ko and B. A. Li, Phys. Rev. C 72 (2005) 064309.

[Co04] G. Colo, N. Van Giai, J. Meyer, K. Bennaceur, P. Bonche, Phys. Rev. C 70 (2004) 024307.

[Da02] P. Danilelewicz, R. Lacey, W.G. Lynch, Science 298 (2002) 1592.

[Da07] E.N.E. van Dalen, C. Fuchs and Amand Faessler, Eur. Phys. J. A 31 (2007) 29.

[De80] J. Dechargé, D. Gogny, Phys. Rev. C 21 (1980) 1568.

[Du95] J. Duflo and A. Zuker, Phys. Rev. C 52 (1995) R23.

[Du98] R.C. Duncan Astrophys. J. 498 (1998) L45.

[Es01] M. Del Estal, M. Centelles, X. Viñas and S. K. Patra, Phys. Rev. C 63 (2001) 044321.

[Fa06] M. A. Famiano et al., Phys. Rev. Lett. 97 (2006) 052701.

[FAIR] An International Accelerator Facility for Beams of Ions and Antiprotons, *GSI report* 2006. http://www.gsi.de/GSI-Future/cdr/.

[Fu04] R.J. Furnstahl, Lect. Notes Phys. 641 (2004) 1.

[Fu06] C. Fuchs and H.H. Wolter, Eur. Phys. J. A 30 (2006) 5-21.

[Fu95] C. Fuchs, H. Lenske and H.H. Wolter, Phys. Rev. C 52 (1995) 3043.

[Fu97] R.J. Furnstahl, Brian. D. Serot and Hua-Bin Tang, Nucl. Phys. A 615 (1997) 441.

[FRIB] Facility for Rare Isotope Beams at Michigan State University, http://www.frib.msu.edu/about/msu-frib-proposal.

[Ge95] H. Geissel, G. Müzenberg, and R. Riisager, Annu. Rev. Nucl. Part. Sci. 45 (1995) 163.

[Go03] S. Goriely,M. Samyn, M. Bender, and J.M. Pearson, Phys. Rev.C 68 (2003) 054325.

[Ha49] O. Haxel *et al.*, Phys. Rev. 75 (1949) 1766.

[Ha77] M.N. Harakeh, K . van der Borg, T Ishimatsu, H.P. Morsch, A . van der Woude and F .E . Bertrand . Phys. Rev. Lett. 38 (1977) 676.

[He56] R. H. Helm, Phys. Rev. 104 (1956) 1466.

[Ho56] R. Hofstadter, Rev. Mod. Phys. 28 (1956) 214.

[Ho01] C.J. Horowitz, S.J. Pollock, P.A. Souder and R. Michaels, Phys. Rev. C 63 (2001) 025501.

[Hof1] F. Hofmann, C.M. Keil and H. Lenske, Phys. Rev. C 64 (2001) 034314.

[Hor1] C. J. Horowitz and J. Piekarewicz, Phys. Rev. Lett. 86 (2001) 5647.

[Hu96] H. Huber, F.Weber and M.K. Weigel, Nucl. Phys. A 596 (1996) 684.

[Hu98] H. Huber, F.Weber, M.K. Weigel and C. Schaab, Int. J. Mod. Phys. E 7 (1998) 301.

[Jo98] F. de Jong and H. Lenske, Phys. Rev. C 57 (1998) 3099.

[Kh09] E. Khan, Phys. Rev. C 80 (2009) 057302.

[Kl07] A. Klimkiewicz, *et al.*, Phys. Rev. C 76 (2007) 051603(R).

[Ko98] C. Kouveliotou *et al.*, Nature (London) 393 (1998) 235.

[La97] G.A. Lalazissis, J, König ans P. Ring, Phys. Rev. C 55 (1997) 540.

[La04] G.A. Lalazissis, P. Ring, and D. Vretenar (Eds.), *Extended Density Functionals in Nuclear Structure Physics*, Lecture Notes in Physics 641 (Springer-Verlag, Berlin/Heidelberg, 2004)

[La05] G.A. Lalazissis, T. Nikšić, D. Vretenar and P. Ring, Phys. Rev. C 71 (2005) 024312.

[La07] J. M. Lattimer and M. Prakash, Phys. Rep. 442 (2007) 109.

[Le95] H. Lenske and C. Fuchs, Phys. Lett. B 345 (1995) 355.

[Li08] B. A. Li, L.W. Chen, and C. M. Ko, Phys. Rep. 464 (2008) 113.

[Lu03] D. Lunney, J.M. Pearson and C. Thibault, Rev. Mod. Phys. 75 (2003) 1021.

[Ma49] M.G. Mayer, Phys. Rev. 75 (1949) 1964.

[Ma55] M.G. Mayer and J.H.D. Jensen. *Elementary Theory of Nuclear Shell Structure*. Wiley, New York, 1955.

[Mi96] F. James, MINUIT- Function Minimization and Error Analysis (1998); CERN Program Library entry **D506**; Package Revision 1.1.1.1 (1996).

[Mi02] R. Michaels *et al.*, Jefferson National Accelerator Facility Proposal E-00-003, 2002, http://www.jlab.org/exp_prog/generated/halla.html

[Mo95] P. Moller, J.R. Nix, W.D. Myers, and W.J. Swiatecki, At. Data Nucl. Data Tables 59 (1995) 185.

[Mu01] A. Muller, Prog. Part. Nucl. Phys. 46 (2001) 359.

[My69] W.D. Myers and W.J. Swiatecki, Ann. Phys. N.Y. 55 (1969) 395.

[My74] W.D. Myers and W.J. Swiatecki, Ann. Phys. N.Y. 84 (1974) 186.

[My77] W.D. Myers, Droplet Model of Atomic Nuclei (Plenum, New York, 1977).

[My96] W.D. Myers and W. J. Świątecki, Nucl. Phys. A 601 (1996) 141.

[My98] W.D. Myers and W. J. Świątecki Phys. Rev. C 57 (1998) 3020.

[Ni02] T. Nikšić, D. Vretenar, P.Finelli and P. Ring, Phys. Rev. C 66 (2002) 024306.

[Pa07] N. Paar, D. Vretenar, E. Khan and G. Colò, Rep. Prog. Phys. 70 (2007) 691.

[Pi04] J. Piekarewicz, Phys. Rev. C 69 (2004) 041301.

[Pi05] A.L. Piro, J. 634 (2005) L153.

[Pi07] J. Piekarewicz, Phys. Rev. C 76 (2007) 031301(R).

[RBFa] Radioactive Beam Facilities: Operating, Under Construction or Proposed; http://www.rarf.riken.go.jp/rarf/np/nplab.html

[Ri96] P. Ring, Prog. Nucl. Phys. 37 (1996) 193-263.

[Sa01] M.-G. Saint-Laurent et al. Final report SPIRAL PHASE-II (2001) in: http://pro.ganil-spiral2.eu/spiral2/origin-of-spiral2/spiral-phase-ii-european-rtt-final-report/view

[Sa03] M. Samyn, S. Goriely, and J. M. Pearson, Nucl. Phys. A 725 (2003) 69.

[Sa05] F. Salvat, A. Jabalonski, and C. J. Powell, Comput. Phys. Commun. 165 (2005) 157.

[Sh07] D.V. Shetty, S. J. Yennello, and G. A. Souliotis, Phys. Rev. C 76 (2007) 024606.

[Si04] H. Simon, in Proceedings of the International Workshop XXXII on Gross Properties of Nuclei and Nuclear Excitations, Hirschegg (Austria), 2004, edited by M. Buballa, J. Knoll, W. Norenberg, B.-J. Schaefer, and J.Wambach (GSI, Darmstad, 2004) 290.

[Si05] T. Sil, M. Centelles, X. Viñas and J. Piekarewicz, Phys. Rev. C 71 (2005) 045502.

[Si07] H. Simon, Nucl. Phys. A 787 (2007) 102

[St05] A.W. Steiner et al., Phys. Rep. 411 (2005) 325.

[Su01] T. Suda, K. Maruyama, and I. Tanihata, *RIKEN Accel. Prog. Rep.* 34 (2001) 49.

[Su05] T. Suda and M. Wakasugi, Prog. Part. Nucl. Phys. 55 (2005) 417.

[Sw05] W.J. Świątecki, A. Trzcińska and J. Jastrębski, Phys. Rev. C (2005) 047301.

[Ta95] I. Tanhihata, Prog. Part. Nucl. Phys. 35 (1995) 505.

[Ty01] S. Typel and B. A. Brown, Phys. Rev. C 64 (2001) 027302.

[To05] B.G. Todd-Rutel and J. Piekarewicz, Phys. Rev. Lett. 95 (2005) 122501.

[Tr01] A. Trzcińska, J. Jastrzebski, P. Lubiński, F. J. Hartmann, R. Schmidt, T. von Egidy, and B. Kos, Phys. Rev. Lett. 87 (2001) 082501.

[Tr08] L. Trippa, G. Colò and Enrico Vigezzi, Phys. Rev. C 77 (2008) 061304(R)

[Ty99] S. Typel and H.H. Wolter, Nucl. Phys. A 656 (1999) 331

[UNEDF] Universal Nuclear Energy Density Functional, SciDAC collaboration; http://unedf.org/.

[Va72] D. Vautherin, D.M. Brink, Phys. Rev. C 5 (1972) 626.

[Va73] D. Vautherin, Phys. Rev. C 7 (1973) 296.

[Wa07] A. L. Watts and T. E. Strohmayer, Astrophys. Space Sci. 308 (2007) 625.

[Wa08] M. Wakasugi, T. Emoto, Y. Furukawa, K. Ishii, S. Ito, T. Koseki, K. Kurita, A. Kuwajima, T. Masuda, A. Morikawa, M. Nakamura, A. Noda, T. Ohnishi, T. Shirai, T. Suda, H. Takeda, T. Tamae, H. Tongu, S. Wang, and Y. Yano, Phys. Rev. Lett. 100 (2008) 164801.

[We35] C.F. von Weizsäcker, Zeit. f. Phys. 96 (1935) 431.

[Yo77] D.H.Youngblood, C .M. Rosza, J.M. Moss, D.R. Brown and J.D. Bronson, Phys. Rev. Lett. 39 (1977) 1188.

[Yo77] D.H. Youngblood, H.L. Clark, Y.W. Lui, Phys. Rev. Lett. 82 (1999) 691.

[Xi02] J.W. Xia *et al.*, The heavy ion cooler-storage-ring project (HIRFL-CSR) at Lanzhou, Nucl. Instr. and Meth. A 488 (2002) 11.

[Xi05] J.W. Xia, W.L. Zhan, B.W. Wei and CSR group, Cooler storage ring at china institute of modern physics, Proc. PAC05 (2005) 271.